Fatigue crack growth rate threshold of laser powder bed fusion Ti-6Al-4V

by
Nur Mohamed Dhansay

Dissertation presented for the degree of
Doctor of Philosophy
in the Faculty of Engineering at
Stellenbosch University

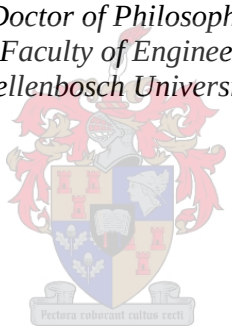

Supervisor: Prof Thorsten Hermann Becker
Co-supervisor: Prof Kim Vanmeensel

December 2021

Declaration

By submitting this thesis electronically, I declare that the entirety of the work contained therein is my own, original work, that I am the sole author thereof (save to the extent explicitly otherwise stated), that reproduction and publication thereof by Stellenbosch University will not infringe any third party rights and that I have not previously in its entirety or in part submitted it for obtaining any qualification.

Date: December 2021

Abstract

Typically, producing Ti-6Al-4V through the laser powder bed fusion (LPBF) technique, results in the material having large residual stresses and martensitic microstructure. These stresses and microstructure have been shown to result in Ti-6Al-4V having poor fatigue properties. However, the insight into the fatigue failure mechanisms caused by the residual stress and microstructure has been limited.

LPBF is one of many additive manufacturing (AM) techniques in which parts are built in a layer-wise manner with the use of powdered material and consolidated through high power laser melting. This allows for complex geometries and previously impossible geometries to be manufactured with minimal material wastage. Many industries are aware of the potential in this manufacturing technique and have shown interest in it becoming a viable option for the manufacturing of some of their components. In particular, the use of LPBF produced Ti-6Al-4V is of interest to the aerospace and biomedical industries. This is because Ti-6Al-4V is already well established in many existing industries. For LPBF produced Ti-6Al-4V to be a viable option in industry, researchers need to have an adequate understanding of the material and the implications for its mechanical properties.

Fatigue property investigations have largely focused on the fatigue life approach (crack initiation) and Paris regime (region II, crack propagation). However, in recent years, the near-threshold regime (region I, crack propagation) has become of interest, albeit limited in approach. The consensus within literature shows that the large tensile residual stresses, martensitic microstructure and porosity results in poor fatigue properties. Unfortunately, the insight into the fatigue fracture mechanisms brought about by the residual stress and microstructure is not yet well established. Furthermore, the near-threshold fatigue crack growth rate regime (FCGR) experiences crack closure mechanisms which result in premature near-threshold values. The majority of the near-threshold investigations on LPBF produced Ti-6Al-4V do not account for the crack closure mechanisms and therefore produce premature results. As a result of the low crack growth rates achieved in the near-threshold regime, a window into observing the fatigue crack initiation mechanisms is obtained. More specifically, how the fatigue crack initiation mechanisms are influenced by residual stress, martensitic microstructure and changing microstructural morphology. Literature has shown that porosity acts as crack initiation sites and reduce the fatigue life of a component. Furthermore, surface and near-surface porosity have been shown to have a more severe impact on fatigue life than internal porosity. It is through using the near-threshold FCGR approach in which one can calculate the allowable pore size under operational loads.

Using the load-shedding technique to obtain near-threshold FCGRs, the results showed anisotropic behaviour dependent on residual stress levels and *R-ratios*. The fatigue fracture mechanisms were predominantly governed by transgranular quasi-cleavage mechanisms. Furthermore, the fracture is directed by PBG morphology which results in anisotropic crack-closure effects. In addition, primary α lath orientation is governed by the crystallographic texture of the PBG which influences the mechanisms of crack propagation. With the increase in grain size, the presence of β improves the near-threshold FCGRs in the duplex anneal (DA) condition due to the superior plastic flow abilities more than in the as-fabricated and stress relief conditions.

This study investigates the near-threshold FCGRs of LPBG produced Ti-6Al-4V in the as-fabricated, stress relief and bi-modal conditions in three build orientations. In addition, crack closure mechanisms are accounted for by implementing variable *R-ratio* testing. This research presents the influencing mechanisms of residual stress and microstructure on fatigue behaviour.

Obsomming

Gewoonlik veroorsaak die vervaardiging van Ti-6Al-4V deur middel van die laser poeierbed fusie (LPBF) tegniek dat die materiaal groot respannings en ‘n martensitiese mikrostruktuur het. Daar is getoon dat hierdie spanning en mikrostruktuur veroorsaak dat Ti-6Al-4V swak vermoeidheideienskappe het. Insig in die meganismes van vermoeidheid faling, wat veroorsaak word deur die resspanning en mikrostruktuur, is egter beperk.

LPBF is een van vele tegnieke van additiewe vervaardiging waar parte laagvormig gebou word uit metaalpoeier deur konsolidasie met ‘n hoë-drywing laser. Dit maak voorsiening vir die vervaardiging van komplekse vorms, voorheen onmoontlike vorms en minimale vermorsing van die materiaal. Baie nywerhede is bewus van die potensiaal van hierdie vervaardigingstegniek en toon ook belangstelling in hierdie lewensvatbare alternatief vir die vervaardiging van sommige van hul komponente. Die gebruik van LPBF-geproduseerde Ti-6Al-4V is van belang vir die lugvaart- en biomediese industrieë omdat hierdie metaal gevestig is in hierdie industrieë.Vir LPBF-geproduseerde Ti-6Al-4V om 'n lewensvatbare opsie in die industrie te wees, moet navorsers voldoende kennis dra oor die materiaal en die proses-afhanklike meganiese eienskappe.

Navorsing van vermoeidheidseienskappe het voorheen grootliks gefokus op die benadering tot vermoeidheidslewe (dws. Die ontstaan van krake) en Parys-regime (dws. deel II van die kraakgroeiekurwe). In onlangse jare het die nabye drempelregime (dws. deel I van die kraakgroeiekurwe) egter van belang geword, al is dié benadering beperk. Die literatuur stem ooreen dat die groot resspannings en martensitiese mikrostruktuur swak vermoeidheidseienskappe tot gevolg het. Ongelukkig is die meganismes van vermoeidheidfaling wat deur die resspanning en mikrostruktuur veroorsaak word, nog nie goed vasgestel nie. Die regime van naby-drempel vermoeidheidskraak groeikoers (VKGK) ondervind verder dat kraak-sluitingsmeganismes tot voortydige naby-drempelwaardes lei. Die meerderheid van die studies waarin naby-drempelwaardes van LPBF-geproduseerde Ti-6Al-4V ondersoek is, neem nie krakingsmeganismes in ag nie en dus is die resultate onvoldoende. As gevolg van die lae kraak groeitempo wat in die nabye drempelregime behaal word, word 'n ingangspunt gevind om die meganismes vir die ontstaan van vermoeidheidskrake waar te neem. Meer spesifiek - hoe die meganisme vir die onstaan van krake beïnvloed word deur resspannings, martensitiese mikrostruktuur en veranderende mikrostrukturele morfologieë. Literatuur toon dat porositeit dien as skeurinisiëring en dus lei tot die vermindering van die lewensduur van 'n komponent. Verder is aangetoon dat oppervlak- en naby-oppervlakporositeit 'n ernstiger invloed op die lewensvermoeidheid het as die interne porositeit. Dit is deur middel van die naby-drempel VKGK-benadering waarin 'n mens die toegelate poriegrootte kan bereken onder operasionele vragte.

Nabye-drempel-VKGK, verkry deur die beurtkragtegniek, toon aan dat anisotropie in die materiaal van resspanningsvlakke en R-verhoudings afhang. Die vermoeidheidsfaling meganismes is hoofsaaklik beheer deur transgranulêre, kwasi-splytsingsmeganismes. Breuk rigting word deur voorafgaande-beta korrelgrense beïnvloed wat anisotropiese kraak-sluitingseffekte tot gevolg het. Verder word primêre alfa-korreloriëntasie bepaal deur die orientasie van die voorafgaande-beta korrel waaruit dit vorm en dus word die meganismes van kraakverspreiding beïnvloed. Die toename in korrelgroottte na ‘n uitgloei hittebehandeling, asook die teenwoordigheid van beta fase, verbeter die nabye-drempel-VKGK’s van die bimodale mikrostruktuur as gevolg van die beter plastiese vloei-vermoëns .

Hierdie studie ondersoek die naby-drempel-VKGK's van LPBG geproduseerde Ti-6Al-4V in die onverwerkte-, spanningverligde- en bimodale mikrostruktuur in drie bou-oriëntasies. Daarbenewens word die sluitingsmeganismes in ag geneem deur die implementering van veranderlike R-verhoudingstoetse. Hierdie navorsing verduidelik die meganisme waarmeë die resspanning en mikrostruktuur die drempelgedrag beïnvloed.

Acknowledgements

In the name of Allah, The Most Beneficent, The Most Merciful

I thankfully acknowledge funding from the Department of Science and Innovation through the Collaborative Program in Additive Manufacturing (CPAM)

To my parents Dawood and Nurjehaan Dhansay: for their sacrifices, guidance, and support throughout my life, especially during the PhD and Covid pandemic, where extra assistance was required. My brothers Hayder and Fayaadh Dhansay, my in-laws Adila Adam and Ilhaam Sahabodien. Thank you for your support and words of guidance and wisdom. To the Dhansay and Jaffer family. Thank you for the support and understanding while the last few years of my life were immersed in the PhD.

To my main supervisor Professor Thorsten Becker: thank you for your guidance, support, understanding, motivation, insights and allowing for the opportunity to conduct my experiments in Belgium. To my co-supervisor, Professor Kim Vanmeensel: thank you for your guidance, help and support; for talking sense into me when I needed it; for welcoming and introducing me to Belgium, more specifically Leuven, and all the experiences I gained while living there.

To my amazing, worldwide, office family: Dr Gerrit Ter Haar, Dr Melody Neeves (nee van Rooyen), Dr Maria Luz Montero Sistiaga, (soon to be Dr) Suraj Jadav, (soon to be Dr) Guichuan Li. Thank you to all of you. Honestly, you all mean the world to me, and have shown friendships I never thought were possible. You are all amazing people and have supported me through this project in more ways than I can ever say thank you in. The conversations, the laughter, the highs, the lows, you were all there for me, and I wouldn't have been able to do this without any of you. To the friends I made in Leuven: Aljaz, Pierre, Bensu, Evita, Bey, Matteo, Thomas, Christel, Chola, Antonio. Thank you for being part of the journey. The lunches in the cafeteria, outside Arenberg castle, ESAT. The jogs that I joined…. sometimes.

To Christel and Paul from the metallography lab in Leuven. To the Mechanical engineering workshop in Stellenbosch, Mr Cobus and Ferdie Zietsman and the staff members. I am truly honoured to have worked alongside you all and appreciate the kindness you have shown me. You have all played a critical role in my research.

To my STUDAX family: Koen, Cheng-Ming, Kleopatra, Annalisa, Montse, Nicola (both), Jinglin, Noami, Gianmario, Elana, Hala. Thanks to all of you. You made it feel like I was living with family and made it feel like home when returning from campus.

To my life-long friends: Kathija, Fatima, Sameeha, Muhammad, Jehaan/Janine, Nabilah, Iedrus, Lameez, Nerita, Muhammad. You have all been there from before the PhD journey, and helped me along in your own ways. Thank You. To Aunty Zubeida Brey: for reading through my PhD for grammar purposes.

Dedication

"Acquire knowledge and impart it to the people." Al-Tirmidhi

To my family that we lost during the Covid-19 pandemic: Aunty Yasmine and Sharmilah. May you be granted the highest place in Jannah, Ameen.

Table of contents

List of figures

List of tables

Page

List of abbreviations

3D	Three-dimensional
AF	As-fabricated
AM	Additive manufacturing
ASTM	American society for testing and materials
BCC	Body centre cubic
BM	Bi-modal
BOR	Burger's orientation relationship
CMM	Coordinate measuring machine
CMOD	Crack-mouth opening displacement
CP	Commercially produced
CPAM	Collaborative programme in additive manufacturing
CSIR	Council for Scientific and Industrial Research
CT	Compact tension
CTOD	Crack-tip opening displacement
DA	Duplex anneal
EBSD	Electron back scatter diffraction
ELI	Extra low interstitials
EPBF	Electron powder-bed fusion
EPFM	Elastic plastic fracture mechanics
FCGR	Fatigue crack growth rate
FM	Fracture mechanics
HAZ	Heat affected zone
HCF	High cycle fatigue
HCP	Hexagonal closed packed
HIP	Hot isostatic pressing
HT	Heat treated
ISO	International organization for standardization
LEFM	Linear elastic fracture mechanics
LENS	Laser engineered net shaping
LPBF	Laser powder-bed fusion

NDT	Non-destructive testing
OICC	Oxidation induced crack closure
PBG	Prior beta grain
PICC	Plasticity induced crack closure
PM	Powder metallurgy
RICC	Roughness induced crack closure
SEM	Scanning electron microscope
SIF	Stress intensity factor
SLM	Selective laser melting
SR	Stress relief
SSTR	Solid solution temperature region
STL	Standard tessellation language
UV	Ultra-violet
VAR	Vacuum arc remelting
X-CT	X-ray computed tomography
XRD	X-ray diffraction

Nomenclature

a	Nominal crack/flaw length
a_c	Critical crack length
a_i	Initial crack length
a_f	Final crack length
a_n	Notch length
B	Compact tension specimen thickness
C	y-intercept of Paris curve
da/dN	Change in crack length per a load cycle
E	Youngs modulus of elasticity
h	Hatch spacing
HF	Hydrofluoric acid
HNO_3	Nitric acid
K	Stress intensity
K_{cl}	Closure stress intensity
K_{IC}	Plane strain fracture toughness mode I
K_{max}	Maximum stress intensity
K_{min}	Minimum stress intensity
K_{op}	Opening stress intensity
m	Slope of Paris curve
N	Number of fatigue cycles
P	Applied load
P_{max}	Maximum applied load
P_{min}	Minimum applied load
r	Radial distance from crack tip
r_c	Cyclic plastic zone size
r_{max}	Maximum plastic zone size
r_p	Plastic zone size
R	Load-ratio
R_c	Critical load-ratio
SN	Fatigue life/Stress life

t	thickness
$TiCl_4$	Titanium tetrachloride
v	Scan speed
W	Effective width on compact tension specimen
Y	Compliance factor
α	Alpha phase
α_p	Primary alpha phase
β	Beta phase
ΔK	Cyclic stress intensity
ΔK_{eff}	Effective cyclic stress intensity
ΔK_{th}	Near-threshold stress intensity
$\Delta\sigma$	Cyclic stress
δ	Crack tip opening displacement
σ	Stress
σ_y	Yield strengthααα
ε_f	Elongation to failure
θ	Angle
λ	Wavelength
ϕ	Scan rotation

1 Introduction

This dissertation concerns an investigation into the near-threshold fatigue crack growth rate behaviour of laser powder bed fusion (LPBF), previously known as selective laser melted (SLM), produced Ti-6Al-4V titanium alloy. The interest in Ti-6Al-4V lies in the alloy's effective properties such as high strength, relatively low density, high corrosion resistance and excellent biocompatibility (Agius *et al.*, 2018; Becker *et al.*, 2020). Furthermore, Ti-6Al-4V has the ability to have a variety of mechanical properties, through the manipulation of its microstructural state. This has resulted in Ti-6Al-4V being the workhorse material in various industries. In addition, the Ti-6Al-4V alloy is typically found in dynamic loading applications in which fatigue damage and failure occurs. With the emerging interest in the LPBF manufacturing technique from industry, and the already established use of Ti-6Al-4V, it is important for the LPBF produced Ti-6Al-4V fatigue behaviour and structural integrity to be investigated.

LPBF is known as a powder bed additive manufacturing (AM) technique in which parts are produced, using powdered material, in a line-by-line and layer-by-layer fashion via the consolidation method of laser-produced heat (Santos *et al.*, 2006). This technique allows for complex part geometries to be produced which previously were not possible when using conventional manufacturing methods (Murr *et al.*, 2009). Along with capabilities of producing complex part geometries, LPBF reduces material wastage substantially by producing near net-shape parts (de Beer *et al.*, 2016). It is well-established that the LPBF process causes high residual stresses, a brittle martensitic microstructure, porosity as well as rough surface finishes (Mercelis & Kruth, 2006; Xu *et al.*, 2015; Kasperovich *et al.*, 2016; Fei Cao *et al.*, 2018). Typically, these properties have been shown to have a negative influence on fatigue behaviour and the structural integrity of a component. Of the titanium alloys in use today, Ti-6Al-4V is the most widely used alloy in industry for applications in the aerospace, automotive and biomedical fields, amongst many others (Donachie, 2000). It stands to reason that if the most popular titanium alloy, Ti-6Al-4V, were to be produced via the LPBF technique, many industries would stand to benefit.

The aerospace industry uses Ti-6l-4V for various applications such as airframe skins, structural components, and gas turbine engine components. However, it is the turbine blade from a turbine engine that is of interest as these experiences the most fatigue type loadings. Currently, the aerospace industry has a high buy-to-fly ratio for machined titanium parts, where ratios as high as 9:1 are common within the industry (Jeanette Clark, 2012). Approximately 16% of an aircraft's airframe weight consists of titanium products as it is compatible with carbon fibre composites. Thus, the titanium parts manufactured via LPBF for aircraft components may largely reduce the high buy-to-fly ratio within the industry. Furthermore, Ti-6Al-4V is biocompatible with the human body as well as providing good bone integration with the implant, making the alloy suitable for medical

implants. Combining the use of X-ray computed tomography (X-CT) scans of a patient's affected area and the intricate geometrical manufacturing capabilities of LPBF, unique implants can be easily manufactured for specific requirements. For LPBF (and AM) to be accepted for application in these important industries, it is of great significance that there is an in-depth understanding of the material's mechanical properties (du Preez & Booysen, 2016).

2 Background of project

2.1 Introduction

With regards to conventionally manufactured Ti-6Al-4V, it is well established that the material is sensitive to the process conditions, which result in different mechanical properties, such as, fatigue properties (Vrancken, 2016; Li *et al.*, 2016; Becker *et al.*, 2020). For the remainder of the investigation, conventionally manufactured Ti-6Al-4V refers to Ti-6Al-4V in which the production techniques such as thermomechanical processing, forgings and castings were used and no alternate AM techniques. In these fatigue properties (and mechanical properties in general) differences are brought about by microstructural features such as alpha (α) grain size, α grain morphology as well as the presence of beta (β) phase (Becker *et al.*, 2020). Typically, conventionally manufactured Ti-6Al-4V has three distinct types of microstructure, namely, lamellar, bi-modal and equiaxed. Each type of microstructure has its structural benefits and drawbacks.

Which microstructure is best from a fatigue perspective is still contested within the literature. Investigations by Zuo et al (2008) and Niinomi et al (1999) found that bi-modal microstructures had higher high cycle fatigue (HCF) strengths than lamellar microstructures (Wu *et al.*, 2013a). Ivanova et al (2002) and Peters and Lutjering (2001) showed that a bi-modal microstructure had higher HCF strength than equiaxed microstructure. Peters and Lutjering (2001) further showed that a lamellar microstructure has a higher HCF strength than an equiaxed microstructure. However, Nalla et al (2002) and Hines and Lutjering (1999) found that lamellar microstructures have a higher HCF strength than bi-modal microstructures. While this is contested, bi-modal microstructures are known to be used in the aerospace industry for applications in the low temperature stages of turbine engines (Nalla, Boyce, *et al.*, 2002). While these differences exist within literature, it is generally understood that the α grain size plays an influential role in the near-threshold FCGRs (Lawson *et al.*, 1999; Everaerts *et al.*, 2016). However, others have also noted the importance of primary α_p size, morphology, colony size, lath size, α_p content (volume fraction, V_α) and α grain connectivity (Wu *et al.*, 2013b; Kumar *et al.*, 2018; Oberwinkler *et al.*, 2010).

The as-fabricated (AF) microstructure of LPBF Ti-6Al-4V produces a significantly different microstructure to that typically found within conventionally manufactured Ti-6Al-4V, i.e. very fine α' martensitic laths and no presence of β phase. As a result of the layer-by-layer technique, previous layers undergo partial remelting, resulting in columnar prior β grains (PBG) growing in the build direction (Kelly & Kampe, 2004). This causes the PBG to play a role in anisotropic behaviour. Furthermore, the α' laths form in relation to the PBG morphology, which can further result in microstructural anisotropy (Thijs *et al.*, 2010; Tarik Hasib *et al.*, 2020). However, the α' forms a weak crystallographic texture due to it having twelve possible variants, based on the parent PBG and Burger's Orientation Relationship (BOR)

(Simonelli *et al.*, 2014; Ter Haar & Becker, 2021). The general consensus regarding the fatigue properties of LPBF Ti-6Al-4V in the literature shows that microstructure, residual stress and porosity play an influential role in fatigue properties. However, it is only well established that porosity plays a significant role in aiding crack initiation while it is unclear as to what the influencing mechanisms of residual stress and microstructure are.

The investigation by Leuders et al (2012) was conducted using the fatigue life approach (*SN*) as well as near-threashold FCGRs and Paris regime FCGRs. Two build orientations were considered as well as four different microstructural conditions, i.e., AF, below β-transus anneal, hot isostatic pressing (HIP) and above β-transus anneal. The focus of the investigation was to investigate the effect of residual stress, LPBF microstructure, microstructural characterisation and porisity on the fatigue life and FCGR behaviour. They concluded that residual stress is the primary influence on near-threshold FCGRs (and Paris regime) with microstructural influences being secondary and porosity having the least influence (on FCGRs). Furthermore, Leuders et al (2012) observed that the build orientations produced noticeably different results, i.e. anisotropic behaviour. In addition, the annealed microstructure produced near-threshold FCGRs superior to the AF condition, showing a morphological influence. However, the investigation was conducted at a single load-ratio (*R-ratio*) of 0.1, which means that crack closure mechanisms are at a significant level and are known to produce premature near-threshold FCGRs results. As a result, there cannot be an intrinsic observation on the influence of residual stress, LPBF microstructure, microstructural morphological change and anisotropy on near-threshold FCGRs.

The investigation by Wycisk et al (2014) also considered the *SN* approach as well as near-threshold FCGRs in a stress-relieved (SR) condition. They focused on the influence of LPBF production defects on fatigue life and near-threshold FCGRs. Their SR LPBF Ti-6Al-4V condition produced similar near-threshold FCGRs to those reported by Leuders et al (2012) in the annealed conditions. They found that scatter observed in the *SN* approach could be attributed to the defect type, size and location. Furthermore, they postulated that the *SN* approach is dominated by the initiation phase and is related to the material's microstructure. As previously mentioned, one of the methods to better understand the initiation phase is to investigate the near-threshold FCGRs. However, as with Leuders et al (2012), Wycisk et al (2014) conducted the near-threshold FCGRs investigations at an *R-ratio* of 0.1, meaning that the material's intrinsic near-threshold FCGRs was not observed.

In both studies of Kumar et al (2018; 2019), they considered two build orientations with two different build parameters. In one set of parameters in the SR condition, Kumar et al (2018) found that there was observable anisotropic behaviour, while in another set of parameters, there was no significant observable anisotropic behaviour. The set of parameters specifically altered the prior β grain (PBG) shape. For the various annealed conditions investigated by Kumar and Ramamurty (2019),

they found that anisotropic behaviour had diminished significantly when compared to the SR condition which displayed anisotropic behaviour, i.e. observed near-threshold FCGRs that are independent of the PBG structure. They further highlighted that it is the α lath size which influences the near-threshold FCGR regime.

In the investigation by Tarik Hasib et al (2020), they considered three build orientations and four microstructural conditions, i.e. AF and three annealed conditions. They found that there were negligible anisotropic effects for all three orientations in all four conditions. They also highlighted that it is the α'/α thickness which is the primary influencing factor on near-threshold FCGRs. Tarik Hasib et al (2020) also considered the crack closure via compliance methods to obtain a $\Delta K_{eff,th}$ and found that the AF condition did not have a measurable crack closure. However, all three annealed conditions had measurable crack closure.

The literature above highlights various issues concerning near-threshold FCGRs of LPBF Ti-6Al-4V. There seems to be a consensus regarding residual stress, microstructure and porosity having an important role in fatigue behaviour. However, the insight regarding their mechanisms on near-threshold FCGRs is currently lacking. Furthermore, the observations regarding anisotropic behaviour seem to vary from one investigation to another, highlighting that process parameters influence mechanical properties, in this case near-threshold FCGRs. Finally, with regards to LPBF Ti-6Al-4V, variable *R-ratio* near-threshold FCGR testing has not been conducted and thus no investigation into the intrinsic ΔK_{th} has been conducted.

This study sprouts from the collaborative programme in additive manufacturing (CPAM) initiative in South Africa. The CPAM initiative is based on the need to qualify AM produced Ti-6Al-4V for aerospace and biomedical applications, of which fatigue is a critical component. In addition, the author previously conducted an investigation while studying towards a Master of Science of Engineering (Dhansay, 2015), which investigated the fracture mechanics based fatigue and toughness characteristics of LPBF Ti-6Al-4V. Dhansay's (2015) previous work showed that an intricate link between porosity, residual stress, and microstructure exists, which affects the mechanical properties. Furthermore, these contributors have been shown to be dependent on the specific LPBF processes (such as process parameters, scan strategies and post processing procedures). Consequently, this also results in a variety of mechanical/fatigue properties for LPBF Ti-6Al-4V with no significant insight into the mechanisms influencing fatigue properties. Thus, in this research, the interest lies in establishing this link with respect to fatigue properties, specifically focusing on near threshold fatigue crack growth rates. It is hypothesised that by establishing such a link, a better understanding of these properties in relation to the specific LPBF process can be attained. In particular, it proposes that an investigation into fatigue crack growth rate threshold is required to identify the influencing mechanisms of the fatigue failure of LPBF Ti-6Al-4V.

The aim of this dissertation is to identify the mechanisms of residual stress and microstructure on the near threshold FCGRs of LPBF Ti-6Al-4V. Furthermore, it is to identify the sources of crack closure effects and once reduced/eliminated, the effect of the microstructural condition on the intrinsic ΔK_{th} behaviour of LPBF Ti-6Al-4V. In order for this to be obtained, extrinsic factors will need to be reduced by implementing variable *R-ratio* near-threshold testing.

2.2 Project aim

The purpose of this investigation is to better understand the fatigue structural integrity of LPBF Ti-6Al-4V. This forms part of a steppingstone for the readiness of AM (LPBF) produced Ti-6Al-4V to be accepted for use in aerospace and biomedical industry components. In particular, the aim of the investigation is to provide an explanation on the influencing mechanisms of residual stress and microstructure on near-threshold FCGRs of LPBF produced Ti-6Al-4V.

While the intent behind this investigation is for the eventual acceptance of LPBF Ti-6Al-4V in industries, it is beyond the scope of this dissertation for it to actually occur. Rather, the idea is that this dissertation will help in the understanding of and progress in the structural integrity of near-threshold fatigue behaviour of LPBF Ti-6Al-4V with the aim of it eventually being accepted by industry. Chapter 5 has been reserved to detail the motivation behind this research, the scope of what is intended to be completed and the limitations thereof.

2.3 Layout of dissertation

For the reader's benefit, a brief summary of each chapter is given below. The dissertation follows a "standard" report style which covers chapter headings such as Introduction, Background, Literature review, Motivation, Methodology, Results, Discussion and Conclusions. The dissertation's layout aims to progress in a logical order as follows:

Chapter 3 describes the relevant background information required to understand the dissertation. This includes information such as linear elastic fracture mechanics (LEFM) and the fatigue crack propagation approaches along with the concept of crack closure.

Chapter 4 delves into specific literature which focuses on the fatigue properties of LPBF Ti-6Al-4V. This includes fatigue thresholds, fatigue crack growth rates as well as the stress life approach.

Chapter 5 details the motivation behind this investigation and states the central hypothesis of the dissertation. The outcome is the justification of the techniques implemented in the investigation

Chapter 6 describes the experimental procedures conducted in this project as well as the equipment used to conduct the experiments.

Chapter 7 presents all the results obtained from the tests conducted. These include micrographs, residual stress, near-threshold fatigue crack growth rates, fractographic analysis and tensile properties.

Chapter 8 discusses and analyses the results. In particular, the influence of residual stress, the influence of microstructural morphology, the critical parameters, a comparison to conventional Ti-6Al-4V and the application of near-threshold fatigue data are discussed.

Chapter 9 concludes the project based on the main discussion points. The future work arising from this investigation is also summarised.

3 Background reading

The aim of this chapter is to make the reader aware of the key concepts and definitions which are fundamental to the understanding of this dissertation. Given that this dissertation is investigating the near-threshold fatigue of LPBF produced Ti-6Al-4V, it then follows that the foundational information of this chapter will focus on these three areas i.e., Fatigue, LPBF and Ti-6Al-4V. The chapter begins with the broader topic of AM, and how it is categorised. It then focuses on LPBF and its concepts. The following subsection introduces titanium and its alloys with a special focus on Ti-6Al-4V and its uses. Thereafter, a subsection providing the relevant information on understanding the mechanical property of fatigue (the main focus of this project) is described.

3.1 Additive manufacturing

3.1.1 Introduction

The objectives of this study incorporate material that has been manufactured by one of the AM techniques i.e., LPBF. AM is defined as "*the process of joining materials to make objects from 3D model data, usually layer upon layer, as opposed to subtractive manufacturing methods"* (ASTM, 2019). The following subsections give a brief history of AM to inform the reader as to how the ideas behind AM progressed over time and developed into its current significance. Thereafter, the various AM techniques are described with a special focus on LPBF as well as some challenges faced using this AM technique.

3.1.2 AM categories

While there are various categories of the AM processes, they all share the same concept of adding material to the manufacturing process as opposed to subtracting material. The manner in which these materials are added, the types of material used, the energy source used for consolidation, are all part of what divides AM processes into various categories (Basak & Das, 2016; Debroy *et al.*, 2018). The ASTM 52900 "Additive manufacturing - General principles – Terminology" (ASTM, 2015) and ISO 17296-2 "Additive manufacturing – General principles – Part 2: Overview of process categories and feedstock" (ISO, 2015) define seven categories of AM. These are material extrusion, material jetting, binder jetting, powder bed fusion, directed energy deposition, vat photopolymerization, and sheet lamination. This dissertation is specifically concerned with powder bed fusion which is defined as "an AM process in which thermal energy selectively fuses regions of a powder bed" (ASTM, 2015).

While there are seven categories of AM processes, one can also break down the production approach of any AM technology into seven steps (Gibson *et al.*, 2010). These are (i) the CAD model, (ii) conversion to standard tessellation language

(STL) file, (iii) the transfer to the AM machine and STL file manipulation, (iv) the machine setup, (v) the building process, (vi) the removal of the printed part, and (vii) post processing procedures.

3.1.3 Powder bed fusion

As previously mentioned, this category makes use of either a laser beam or an electron beam. The laser method has widely been called selective laser melting (SLM) over the years, but there have been other names such as direct metal printing, laser beam melting, direct metal laser sintering and laser powder bed fusion (LPBF). The variation in names typically comes from preferences by companies who manufacture the printing machines. However, the ASTM and ISO standards define it as LPBF and will likewise be referred to as LPBF for the remainder of this dissertation.

In the LPBF process, the manufacturing chamber is under an inert gas atmosphere (typically argon), to prevent oxidation of the metals at high temperatures. Generally, the chamber consists of two platforms, one where the build occurs, and one as a reservoir for the powder material. Powder is taken from the reservoir, scraped across the build platform which has dropped by one layer (0.02-0.1mm) and any excess material is scraped into an overflow chamber for recycling. A laser beam, which is guided by a set of mirrors onto the build platform's material, selectively melts powder according to the G-code information. The mirror system is known as a *f*-θ lens, which allows for the laser's focal point to align with the build platform surface (Vrancken, 2016). Once the laser has consolidated the selected area(s), the build platform drops by one layer in height, material is scraped from the reservoir platform and the cycle repeats until the 3D part is complete. A schematic of the process is shown in Figure 3-1.

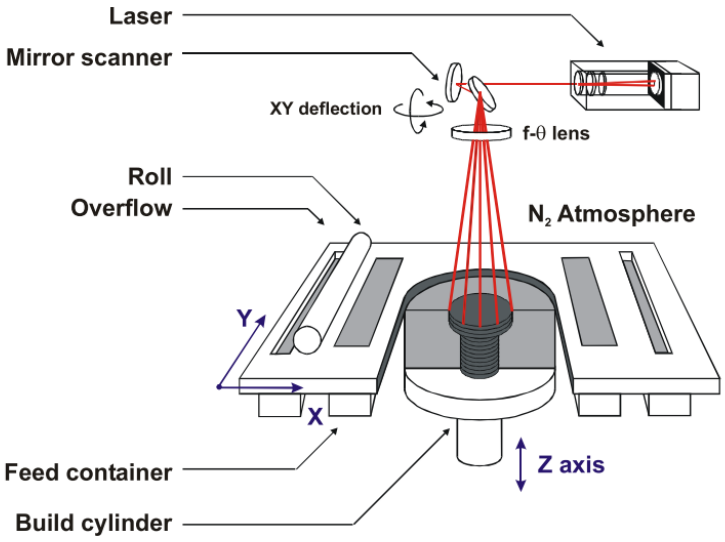

Figure 3-1: The typical LPBF process (Kruth *et al.*, 2005)

Depending on the laser beam's power, diameter, scan speed, scan spacing, scan pattern and even the material layer thickness (process parameters), the resulting 3D part will be affected.

3.1.4 Process parameters

This subsection will briefly describe the parameters affecting the LPBF process. However, for a more detailed discussion on this, the reader is directed to the work of Thijs (Thijs, 2014). There are a few parameters to consider when using the LPBF process. Typically, the parameters are varied for the purpose of producing a fully dense part. Thus, it is of benefit to understand the effect of the process parameters to obtain an optimised part.

The laser in itself has a few parameters to consider: the maximum laser power (P), laser beam wavelength (λ), laser intensity distribution, laser spot diameter and laser temporal mode (Thijs, 2014).

The laser power is limited by the laser hardware installed in the printer (Vrancken, 2016). Laser powers between 100-200 W are generally used in lab scale machines, however, there are machines which provide up to 1 kW of laser power (Sistiaga, 2019). The power is required to sufficiently melt the material. Currently there is research being conducted on having even higher laser power.

The Nd/Yb:YAG laser beams are the most commonly used beams for the LPBF process (Thijs, 2014). They usually has a wavelength between 1063-1070 nm as this corresponds well with most printing alloys' levels of absorption (Sistiaga, 2019).

The laser intensity distribution mainly has two types (i) Gaussian intensity distribution and (ii) top-hat intensity distribution. The Gaussian is typically used in low power applications and the top-hat in high power applications (Sistiaga, 2019). These distributions also affect the size of the laser spot diameter.

The laser temporal mode considers two scenarios, (i) a continuous beam or (ii) a pulsed beam (Thijs, 2014). In (i), the power output will be constant over the material whereas in (ii) high power outputs are used in short bursts (Thijs, 2014). The latter is commonly used in processes such as selective laser erosion (Thijs, 2014).

The remaining process parameters consider the movement of the laser over the material. These are the scan speed (v) [mm/s], hatch spacing (h) and layer thickness (t) [μm] (Sistiaga, 2019). If the scan speed is too high, there may not be enough time for the laser to melt the selected area of material (Vrancken, 2016). Similarly, if the laser scan speed is too slow, the material may be exposed to the laser for too long, causing some material to vaporise. The hatch space refers to the centre-to-centre distance of the laser scan vector. There will be an overlap region based on the laser spot diameter size. The minimum layer thickness will be dependent on the particle

size of the powder material. Depending on the power output required for full melt penetration of the material, the maximum layer thickness will also be limited. These parameters, combined with the laser power, form the energy density (E) [J/mm^3] equation:

$$E = \frac{P}{v\ x\ h\ x\ t} \tag{3-1}$$

This equation becomes useful when comparing parts that were manufactured using different process parameters (Vrancken, 2016). Specific material will have an optimum energy density range required for fully dense parts, and thus the remaining process parameters may be altered while keeping the energy density within the optimal range.

3.1.5 Residual stress

As a result of the high energy laser beams being made use of in LPBF to melt metal (as well as other AM techniques), followed by rapid cooling, large thermal gradients are introduced into a part (Mercelis & Kruth, 2006). These gradients cause residual stress to remain in a part after manufacture. Studies have shown that these stresses affect the mechanical properties of the part. This has led to a great drive to reduce thermal gradients during manufacture as well as relieving the residual stress after manufacture via heat treatments (Shiomil *et al.*, 2004; Mercelis & Kruth, 2006).

The large thermal gradients caused by the manufacturing process can be broken down into two mechanisms which cause residual stress (Mercelis & Kruth, 2006). The first mechanism is known as the temperature gradient mechanism. This occurs when the laser spot rapidly heats up the affected material area, but the surrounding material is not under the laser spot and thus has a lower temperature, causing a temperature gradient. The material heated up by the laser wants to expand, but the surrounding cooler material inhibits this expansion resulting in compressive strains. The second mechanism takes place during cooling. The area, which was under the laser spot, now cools down as the laser moves away. As it cools, it now wants to contract, however, the surrounding material inhibits this contraction and induces large tensile stresses at the surface of the material. The temperature gradient mechanism process is shown in Figure 3-2.

When using LPBF to manufacture a part, the effect of residual stress on a part needs to be considered. As previously mentioned, residual stress affects mechanical properties. However, there are further implications of residual stress which may affect the design process. These include the reduction of the residual stress via shrinkage and bending deformation when a part is removed from the base plate (wire cut) (Mercelis & Kruth, 2006). This is problematic from a design perspective as the actual part would differ from the designed part. There are methods to reduce

residual stress during manufacture, such as heating the base plate and scan strategy to reduce temperature gradients.

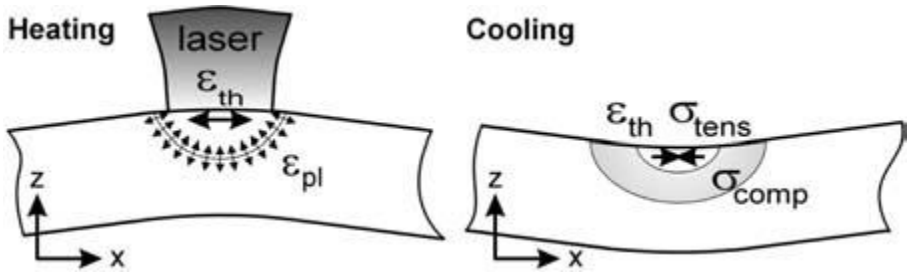

Figure 3-2: temperature gradient mechanism process (Mercelis & Kruth, 2006).

3.1.6 Porosity which leaves pores

Part of the LPBF process is the presence of inherent defects such as porosity. The formation of porosity is typically of two shapes i.e., spherically shaped pores and irregular shaped pores/defects. Spherical pores are caused by entrapped gases within the molten material (melt pool) (Vilaro *et al.*, 2011; Agius *et al.*, 2018). As a result of the rapid cooling and solidification of the melt pool, the gas does not have sufficient time to escape and becomes entrapped in the now solid material (Vilaro *et al.*, 2011; Agius *et al.*, 2018). It has also been identified that porosity formation is influenced by the process parameters (Agius *et al.*, 2018). For high energy densities, Gong et al (2012) found that spherical porosity form whereas at lower energy densities, irregular shaped porosity forms. Frazier (2014) further explains that porosity nucleates at solid-liquid interfaces during solidification when N, H and O are absorbed in the melt pool (high energy density). For the irregular shaped porosity, Vilaro et al (Vilaro *et al.*, 2011) and Gong et al (Gong *et al.*, 2012) showed that low energy densities cause the irregular shapes. This is because the low energy density causes a lack of fusion/melting and reheating of the previous layers, which results in the incorrect fusion of layers (Kasperovich *et al.*, 2016; Agius *et al.*, 2018). The severity of porosity is briefly discussed in section 3.4.3.

Another source of porosity is the inert atmosphere (Agius *et al.*, 2018). During the building process, the inert gas is not stagnant within the build chamber, but rather flows over the build platform. Inadequate gas-flow does not remove sufficient amounts of condensate (vapourised powder). These condensates are now present on the build platform which reduces the effectiveness of the laser beam in relation to the predefined parameter set. As a result, there will be an increase in the likelihood of lack-of-fusion defects, i.e., irregular shaped pores. Kong et al (Kong *et al.*, 2011) and Ferrar et al (Ferrar *et al.*, 2012) also reported that gas-flow across the build-plate is not uniform, causing a build-plate locational dependency. This was further confirmed by Ladewig et al (2016) who found lack-of-fusion defects in areas on the build-plate where inadequate gas-flow rates occurred.

3.1.7 Surface roughness

LPBF (and AM in general) material tends to have a rough surface finish (Edwards *et al.*, 2013; Edwards & Ramulu, 2014). Surface roughness formation can be divided into two phenomena, (i) the staircase effect, and (ii) Spatter (Stoffregen *et al.*, 2013; Li *et al.*, 2016; Ly *et al.*, 2017; Khairallah *et al.*, 2017). With regards to the staircase effect, the layer-by-layer process and the curvature of the printed part results in the surface of the part having a staircase-like pattern. A schematic of the staircase effect is shown in Figure 3-3. One of the methods to reduce the staircase effect is to have thinner layers, however, process time and other process related factors can be affected by this. When considering particles which have not been fully melted, it seems to be a phenomenon which is more apparent in the powder bed fusion (PBF) techniques (Li *et al.*, 2016). This can be reduced to the spatter effect which commonly occurs in PBF and is related to the melt pool, which in turn is related to the laser power, layer thickness, particle size and scan speeds (Khairallah *et al.*, 2017).

Spatter is the splashing or ejection of powder particles and molten material in the vicinity of the laser melt pool (Matthews *et al.*, 2016; Khairallah *et al.*, 2017). One of the mechanisms which produce spatter is recoil-pressure (Gladush & Smurov, 2011). The recoil-pressure occurs under high energy inputs where material vaporises and produces a micro vapour jet (Ly *et al.*, 2017). This vapour jet (recoil pressure) agitates the melt pool, resulting in droplets of molten material being ejected from the melt pool. A significant amount of these ejected droplets fall back onto the consolidation area which can increase surface roughness as well as porosity, amongst other things. A second mechanism causing spatter is vapour driven entrainment of powder particles. The vapour jet interacts with the surrounding gas and due to the pressure differential, the surrounding gas accelerates towards the vapour jet stream. The gas acceleration transports particles along with it, of which some are deposited in the melt pool vicinity and partially melt. These mechanisms lead to the build layer (the surface is the final build layer) having a combination of partially melted particles on the surface (from entrainment) and areas of porosity (from droplet ejection), resulting in surface roughness.

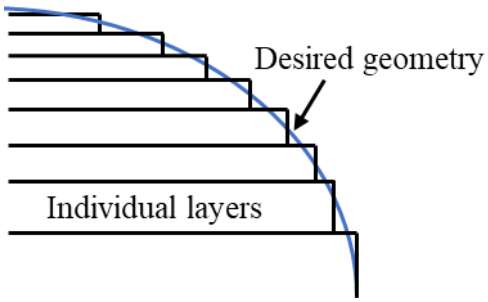

Figure 3-3: Schematic of the staircase effect. Adapted from Brooks et al (2012).

3.1.8 Summary

The above section briefly described the simplicity of a generally accepted seven step process for AM technologies and the complexity of the manufacturing process parameters was also highlighted. The shortcomings of the LPBF were briefly described with a focus on residual stress and defects.

With the basics of the manufacturing process described, it is necessary to have an understanding of the materials, particularly Ti-6Al-4V, used in LPBF and an understanding of why it is used in LPBF in the first place.

3.2 Titanium

3.2.1 Introduction

The objectives of this study are to better understand the mechanisms involved in the fatigue behaviour of Ti-6Al-4V manufactured by LPBF. A brief background to titanium and its alloys is presented here along with its use in industry. Thereafter, Ti-6Al-4V is focused on along with its unique microstructure in LPBF.

3.2.2 Properties

Titanium is an allotropic metal with a β-transus temperature at 882.5°C (Lutjering & Williams, 2007). Below this transus temperature, titanium has a hexagonal closed packed (HCP) crystal structure, also known as the α-phase. Above the transus temperature, titanium exists as a body centred cubic (BCC) crystal structure, also known as the β-phase. These two phases have different effects on the material properties. Figure 3-4 shows the titanium crystal structures.

Titanium, in its commercially pure state (α-phase), is non-heat treatable, however, it has medium strength, good creep resistance at high temperatures, good corrosion resistance and weldability (Leyens & Peters, 2007).

Titanium is commonly categorised as α, α+β and β phase (Donachie, 2000; Leyens & Peters, 2003; Lutjering & Williams, 2007). There are α-stabilising alloying elements which increase the β-transus temperature and, similarly, β-stabilising alloying elements which reduce the β-transus temperature.

Elements such as aluminium, gallium, germanium, carbon, oxygen and nitrogen are α-stabilising alloying elements (Donachie, 2000). By definition, an α-phase alloy would contain zero to less than 10% β-stabilising element in volume fraction (Boyer *et al.*, 1994). α-phase alloys tend to have high creep strength, oxidation resistance at high temperatures, as well as low levels of fabricability at room temperature (Donachie, 2000; Boyer *et al.*, 1994). This is due to the limited availability of slip systems for dislocation glide (Vrancken, 2016; Boyer *et al.*, 1994).

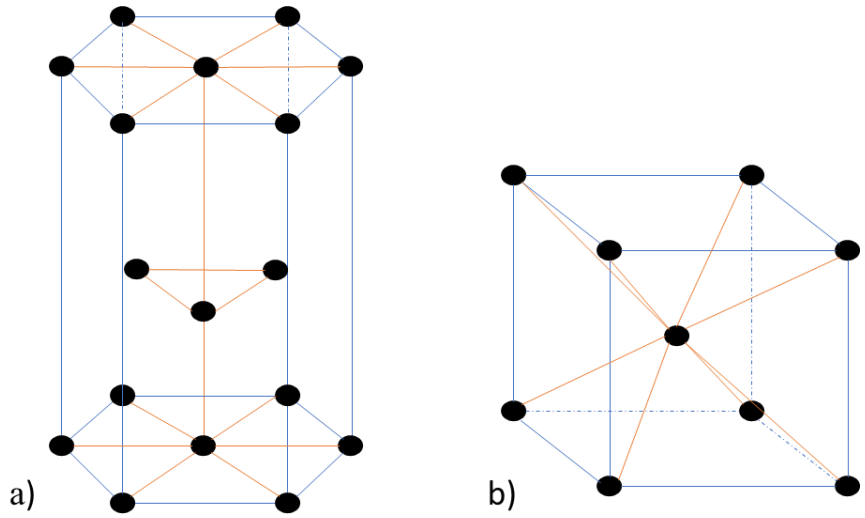

Figure 3-4: Crystal structure of titanium a) Hexagonal closed packed and b) Body centred cubic.

Elements such as molybdenum, iron, vanadium, chromium and manganese are *β*-stabilising alloying elements (Donachie, 2000). The *β*-phase can be retained at room temperature when quenching from above the transus temperature (Dunne *et al.*, 2007). These typically improve the strength of the material, responses to heat treatment and improved fabricability at room temperature, amongst others (Donachie, 2000).

If titanium has a volume fraction between 10 and 50% of *β*-stabilising elements, below the transus temperature, it is considered an *α*+*β* alloy (Donachie, 2000; Boyer *et al.*, 1994). Mechanical properties of the *α*+*β* alloy can be tailored via thermomechanical processing by adjusting the volume fractions, sizes and morphology of the *α* and *β* phases (Lutjering & Williams, 2007; Vrancken, 2016).

3.2.3 Ti-6Al-4V

The advantage of having titanium alloys containing both *α* and *β* phase, is that it's desirable properties from both the *α*-phase and *β*-phase can now be obtained at room temperature. This allows for increased strength, formability and creep resistance in comparison to an *α*-phase titanium alloy. Furthermore, there is the ability to achieve desirable properties through thermomechanical processes. In addition, the lightweight nature of titanium and its alloys allows for it to replace heavier, less cost effective material.

Ti-6Al-4V is the most commonly used *α*+*β* titanium alloy (Boyer *et al.*, 1994). It accounts for approximately 45% of the world's titanium production (André *et al.*, 2005; Donachie, 2000; Boyer *et al.*, 1994). Furthermore, this alloy is most popular in aerospace applications, which use more than 80% of industry's use of the alloy (Vrancken, 2016). Typically in aerospace applications, Ti-6Al-4V is used for

critical components such as turbine blades, fan discs and housing, airframes, fuselage, floor support structures, landing gear components, and assemblies for the tail and wing components (Boyer, 1996; Bache, 2003; Everaerts, 2017; Boyer *et al.*, 1994). As previously mentioned, the mechanical properties of α+β alloy can be tailored via thermomechanical processing. There are generally three distinct morphologies exhibited by α+β alloys through thermomechanical processing. Namely, fully lamellar, fully equiaxed and bi-modal, as shown in Figure 3-5 (Lutjering & Williams, 2007; Rack & Qazi, 2006).

For the formation of a lamellar morphology, an anneal above the β transus is required (Lutjering & Williams, 2007), (Rack & Qazi, 2006; Leyens & Peters, 2003). This is followed by a cooling procedure. Upon cooling, α plates nucleate and form at the β grain boundaries. As the cooling progresses, there is secondary α, which nucleates. The α plates follow the BOR, resulting in parallel plates. When groups of adjacent and parallel plates, separated by a thin layer of β are formed, they are referred to as α colonies (Vrancken, 2016). Depending on the cooling rate experienced, the α lamellae size, α colony size as well as the α layer thickness will be influenced (Lutjering & Williams, 2007). This in turn will significantly influence the mechanical properties of the alloy. This morphology is typically referred to as a Widmanstätten or basket weave structure.

Equiaxed structures have axes of approximate equal length of their α phase crystals. The α phase is surrounded by a β phase at the grain boundaries. These typically form triple points with surrounding crystals. Obtaining the equiaxed structure requires a lamellar "starting" structure to undergo a deformation step in the α+β phase (Simonelli, 2014). A recrystallisation anneal followed by a slow cooling is then performed to allow for the breakup of original α lamellae and dislocations which form the equiaxed grains (primary α) (Lutjering & Williams, 2007; Simonelli, 2014; Vrancken, 2016).

The bi-modal microstructure contains equiaxed primary α grains as well as transformed β grains (Lutjering & Williams, 2007). Within the β grains is a lamellar matrix of α+β (Lutjering & Williams, 2007). This structure is formed by performing an annealing heat treatment high in the α+β region, allowing for secondary α platelets to form within the β grains. To retain the secondary α platelets, a rapid cooling rate is required. This is typically achieved through water quenching. A final, lower temperature anneal, is implemented to eliminate micro-segregates, residual stress as well as to allow for the growth of primary and secondary α grains.

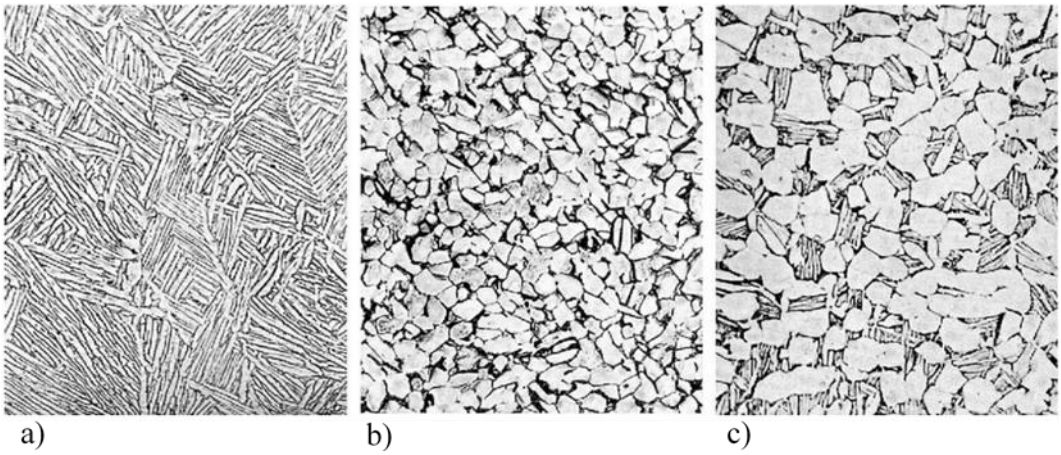

Figure 3-5: The three distinct microstructures of Ti-6Al-4V a) Lamellar, b) equiaxed and c) bi-modal (Rack & Qazi, 2006)

While it has been mentioned that there are three distinct microstructures for Ti-6Al-4V, there is actually a fourth unique microstructure brought about by AM, and more specifically, LPBF. This is discussed in Section 3.2.5.

3.2.4 Bi-modal

Although it was mentioned that there are three distinct microstructures, a special focus on the bi-modal microstructure is given as this is a microstructure used within this dissertation.

As a result of the microstructural sensitivity of α + β alloys, and the resultant mechanical properties, it is commonly contested within literature as to which microstructure produces the best properties. Typically, lamellar structures produce high fracture toughness and have excellent creep as well fatigue crack growth resistance (Leyens & Peters, 2003). The equiaxed microstructure tends to show higher ductility and fatigue strength (crack initiation). Generally, a microstructure which has excellent fatigue strength (resistance to crack initiation) has diminished crack growth resistance and a microstructure which has good crack growth resistance, has diminished fatigue strength. The bi-modal microstructure combines the properties of the previous two microstructures and achieves a balance of the advantages, i.e. good fatigue strength and fatigue crack growth rate resistance, amongst others.

However, there are microstructural parameters to consider which will have an influence on the properties. These include α_p content (volume fraction), α_p grain size, α grain connectivity, α grain morphology and the β phase matrix (Saxena & Radhakrishnan, 1998; Oberwinkler *et al.*, 2010; Wu *et al.*, 2013b). In addition, the α phase morphology can be of more than one type i.e., equiaxed, elongated and Widmanstätten. Several studies have shown that the Widmanstätten α phase

structure produces the best FCGR resistance (Saxena & Radhakrishnan, 1998). However, Saxena and Radhakrishnan (1998) also showed that the type of β phase, i.e. metastable or transformed, also affects the FCGRs. For example, equiaxed α_p phase in a metastable β matrix obtains a higher FCGR resistance than elongated α_p phase in the metastable β matrix. However, an elongated α_p phase in the transformed β matrix becomes slightly superior than the equiaxed α_p phase in a transformed β matrix (Saxena & Radhakrishnan, 1998). The reasons given for superior FCGR resistance are due to crack bifurcation, which disperses strain energy, as well as crack deflection, which reduces the effective ΔK and results in lower FCGRs (Saxena & Radhakrishnan, 1998).

It is possible that the dispute within literature regarding where the bi-modal microstructure lies with regards to lamellar and equiaxed, is due to the variability of its properties depending on α_p phase morphology and the β phase matrix.

3.2.5 LPBF produced Ti-6Al-4V

In addition to Ti-6Al-4V being the most commonly used titanium alloy, it is also one of the main alloys used for commercial LPBF (Vrancken, 2016). Owing to the alloy having a relatively high cost for the base material, reducing material wastage is sought. Thus, with AM technologies, where high material usage and low material wastage is common practice, the success of Ti-6Al-4V's use in AM technologies is achieved.

It has been well documented that LPBF Ti-6Al-4V (as well as EPBF) forms columnar prior β grain structures which are, for the most part, directed along the build height direction (Kelly & Kampe, 2004; Thijs *et al.*, 2010). These are caused by the partial remelting of underlying layers in which there are no nucleation barriers to solidification (Rombouts *et al.*, 2006; Thijs *et al.*, 2010), resulting in columnar/epitaxial growth (Rombouts *et al.*, 2006; Thijs *et al.*, 2010). There is generally a slant in the columnar grain direction, resulting in a $\langle 001 \rangle_\beta$ texture (parallel to Z-axis), which is influenced by the local heat transfer direction, which in turn is due to the scanning strategy (Thijs *et al.*, 2010). As seen in Figure 3-6 (a), the ZX/ZY plane, the PBG has a high aspect ratio, i.e. a large length in comparison to its thickness. The width of the PBG generally corresponds to the hatch spacing (Simonelli, 2014). As a result of of the length of the columnar-shaped PBG affinity to the Z-axis (build direction), the PBG is considered to be morphologically textured (Ter Haar & Becker, 2021). Figure 3-6 (b) shows the XY-plane or cross-section of the PBG which shows an equiaxed PBG shape.

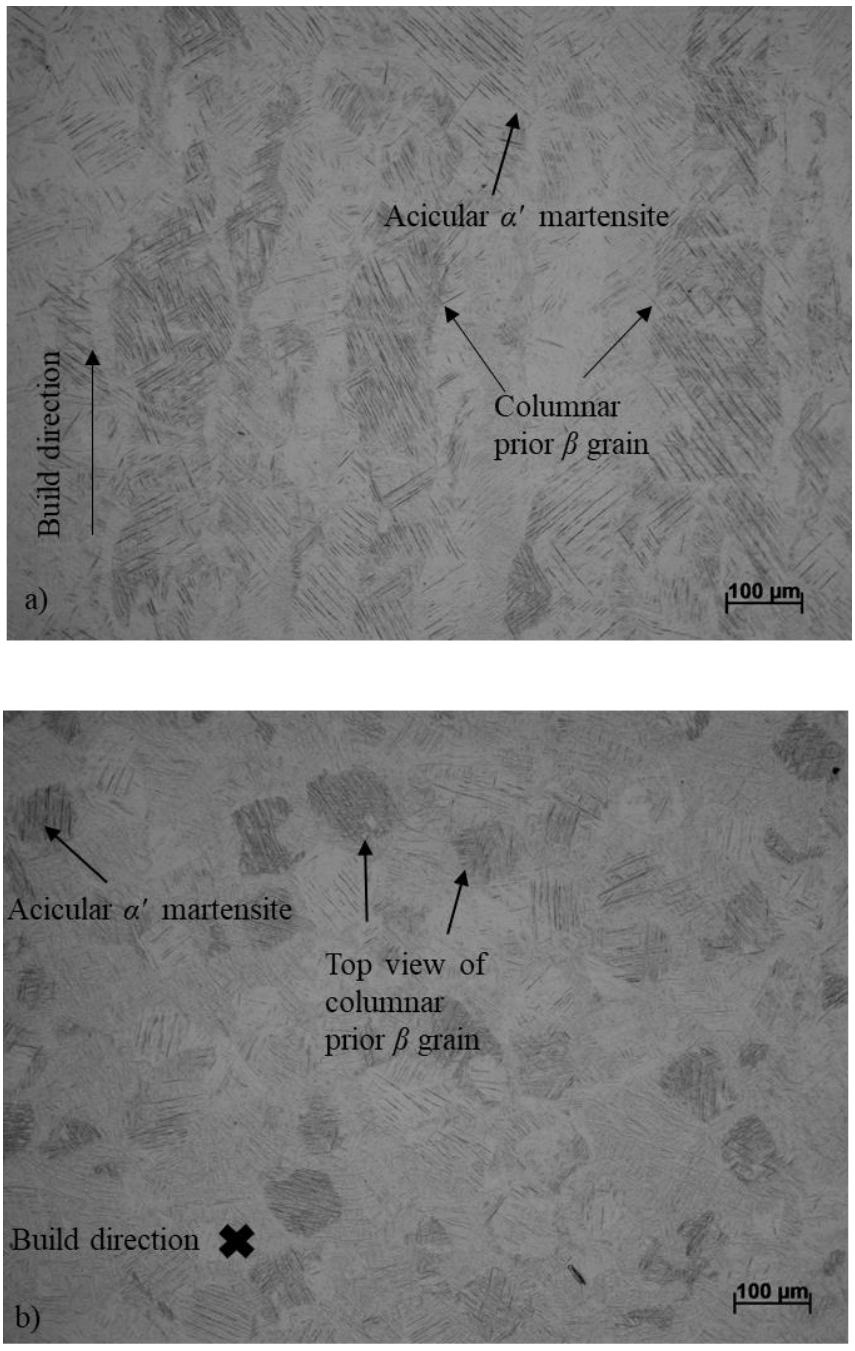

Figure 3-6: AF microstructure a) Front view, b) top view

Although Ti-6Al-4V is considered an $\alpha + \beta$ titanium alloy, the LPBF produced Ti-6Al-4V is typically fully martensitic, i.e. α' and no β-phase present. This is because the retained β-phase at room temperature Ti-6Al-4V, is influenced by the cooling rate from the β-phase field (Glavicic *et al.*, 2003; Simonelli, 2014). The phase diagram for Ti-6Al-4V is shown in Figure 3-7 below. The LPBF process has both rapid heating as well as rapid cooling. This rapid heating into the β-phase field and

cooling from the β-phase field causes the microstructure to not retain any β-phase (Glavicic *et al.*, 2003; Simonelli, 2014). Furthermore, there is a temperature at which α' martensite forms, which is exceeded during the LPBF process (Ahmed & Rack, 1998; Al-Bermani *et al.*, 2010). Within the PBG, the non-equilibrium structure exists, described as a fine acicular α' martensitic microstructure (Thijs *et al.*, 2010). The α' martensite has an HCP crystal structure, which forms in relation to the BOR within a single parent PBG (Burgers, 1934; Ter Haar & Becker, 2021). The BOR results in the grains being oriented at $\{0001\}_{\alpha}//\{101\}_{\beta}$ and $\langle 2\bar{1}\bar{1}0\rangle_{\alpha}//\langle 111\rangle_{\beta}$. As a result of the BOR, there are twelve possible variants for the α' (HCP) crystals to orientate themselves along, resulting in a weak crystallographic texture (Simonelli, 2014; Ter Haar & Becker, 2021). The α' grains are known to be organised within the PBG at different lath angles but seem to have a dominant affinity at ~ 45° to the Z-axis. This is a result of the $\langle 001\rangle_{\beta}//Z$ axis and the $\{334\}_{\beta}$, $\{344\}_{\beta}$ habit planes for α' lath formation, i.e. the PBG habit planes have an ~ 45° affinity (Ter Haar & Becker, 2021).

The mechanical properties of LPBF Ti-6Al-4V, particularly fatigue properties, will be discussed in Section 4.

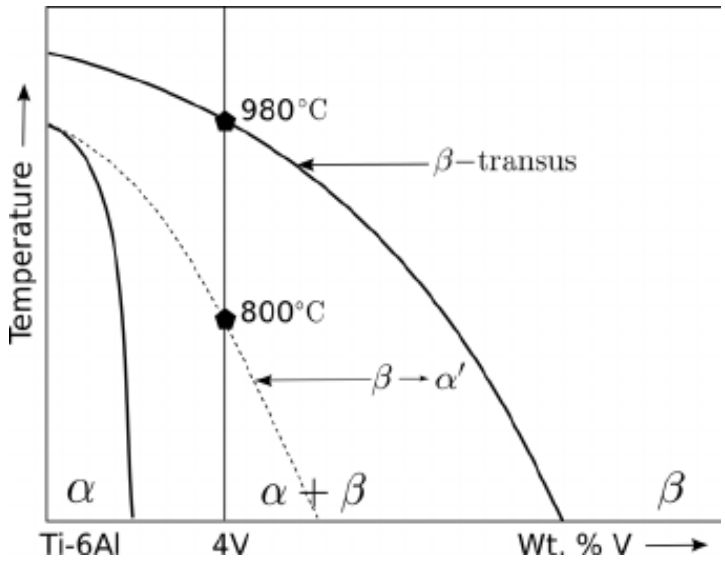

Figure 3-7: Phase diagram for Ti-6Al-4V (Babu, 2008)**.**

3.2.6 Summary

This section highlighted the basic background of Ti-6Al-4V. The more intricate concepts of α and β phase structures were introduced along with their general properties and categories. This led into the Ti-6Al-4V alloy, which can have its properties tailored through thermomechanical processing, resulting in its successful use within various industries. Finally, the link between LPBF and Ti-6Al-4V and its unique microstructure was briefly discussed.

With the concepts of LPBF and Ti-6Al-4V clarified in the above sections, the use of Ti-6Al-4V within industry presents its own challenges. As previously mentioned, Ti-6Al-4V is the workhorse titanium alloy as well as having success in manufacturing through the LPBF process. One of the main challenges is that of fatigue. It is estimated that approximately 90% of mechanical failures are caused by fatigue (Campbell, 2008). Furthermore, it is the primary cause of failure in military aircraft turbine engines (Ritchie *et al.*, 1999). Therefore, the following subsection will address the issue of fatigue by discussing the key concepts, definitions and how it can be used within industry for design and in-service operations.

3.3 Fatigue

3.3.1 Introduction

Fatigue behaviour is what connects this investigation with LPBF and Ti-6Al-4V. As previously mentioned, fatigue is one of the most common causes of mechanical failure (Campbell, 2008). Fatigue can be defined as the accumulation of crack damage caused by fluctuating stresses well below the yield point of the material. Fatigue forms part of the study of fracture mechanics which is a specialisation within solid mechanics. The investigation of this study revolves around the understanding of fatigue. This section starts off with a brief history of fatigue to show the progression of understanding towards fatigue and part integrity. This leads into the study of fracture mechanics to understand the effect of a crack within a system. Thereafter, it is explained how the understanding/interpretation of fatigue behaviour can be used within industry for design and in-service purposes. The incorporation of fatigue and LPBF Ti-6Al-4V will be addressed in Section 3.4, in the literature review.

3.3.2 Background

Understanding fatigue and its implications has taken many years. It was in 1842 when an incident on a locomotive axle occurred which promoted the research into fatigue behaviour (Schütz, 1996). Over a century later, in 1988, one of the most well-known fatigue failure incidents occurred to the Aloha airlines flight 243. During this flight, part of the upper fuselage had ripped off, exposing passengers and crew members to the open air. Figure 3-8 shows the, now landed, aircraft with a missing portion of its fuselage. Upon investigation, it was found that a combination of corrosion, corrosion fatigue, large number of flights (large number of pressurisation and depressurisation) and poor aircraft maintenance had led to the disaster (Schütz, 1996). Fatigue type loading is experienced in aircraft, such as variable airflow speeds over wings, landing gear experiencing take-off, flight and landing, fuselage pressurisation and depressurisation, the use of their engines, amongst others. In more recent times, in April 2018 and February 2021, aircrafts had experienced fatigue failure of their turbine blades during flight (Hemmerdinger, 2021). Highlighting that even today, with nearly two centuries of research into

fatigue, there are still incidences which occur that show a better understanding of the phenomenon is required.

Figure 3-8: Flight Aloha 243's missing fuselage (Airways, 2020)

3.3.3 Stress-life approach

Initial studies on fatigue used the fatigue life/endurance limit approach, also known as the Wohler or S-N curves where S and N refers to the stress and cycles respectively. A cyclic stress is applied to a part in equation (3-2):

$$\Delta\sigma = \sigma_{max} - \sigma_{min} \tag{3-2}$$

Where σ_{max} is the maximum cyclic stress and σ_{min} is the minimum cyclic stress. When a part is subjected to a cyclic stress high enough to initiate a crack, it will propagate until it reaches a critical length a_c where-after rapid brittle full fracture occurs at a specific number of cycles. The number of cycles to fracture at a specific cyclic stress can be presented on a SN graph such as in Figure 3-9. As the cyclic stress is decreased, more fatigue cycles are required to cause failure by fatigue fracture. With the SN approach, it is often mentioned that there is an endurance limit to the fatigue strength, i.e. below a certain cyclic stress, no fatigue will occur, and the endurance/fatigue limit of the material has been reached. However, this mainly true for steel and its alloys but is not representative for most non-ferrous alloys where no endurance limit exists (Carvill, 1993; Campbell, 2008). This means that fatigue will always occur if sufficient fatigue cycles are reached. At lower cyclic stresses and higher fatigue cycles, the SN curve tends to follow Basquin's Law in equation (3-3):

$$\Delta\sigma_0 N_f^b = Constant \tag{3-3}$$

Where *b* is the fatigue strength exponent (slope on Basquin's Law poration of S-N curve).

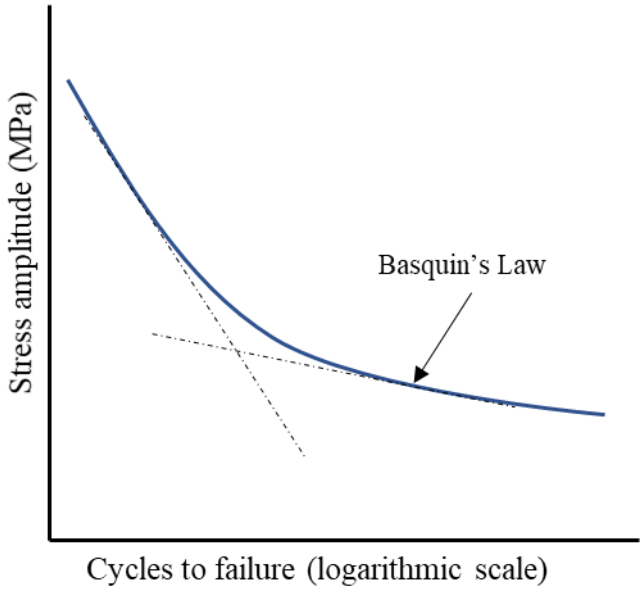

Figure 3-9: Typical *SN* graph of stress-life approach

This approach allows for designers to know approximately how many cycles to failure a material can withstand, or which cyclic stresses will not cause failure and design accordingly. However, this method results in overly conservative designs as it tries to avoid fatigue entirely and has to replace parts subjected to fatigue loading regularly for safety purposes, leading to higher costs. Furthermore, testing procedures require one sample to fracture in order to obtain one data point, which can be an expensive process. In addition, this approach is mainly concerned with the cyclic stress and cycles to failure while not monitoring the crack propagation occurring throughout the process. This approach is largely dependent on initial flaw size, whether it is in the form of a notch, porosity or rough surface etc. The fatigue results will be affected by this in accordance with the initial crack size and its location in the material.

As a result of the technological constraints, fatigue testing had test frequency limitations (Everaerts, 2017). It was for this reason that materials were deemed to have an "infinite" life if no failure occurred below 10^7 cycles. However, with the development of technology and test frequency capabilities, the generally accepted "infinite" life of a material does not truly exist. Furthermore, the endurance limit contains an initiation phase and propagation to failure. This is not distinguished in

the test method. There are various opinions as to how long the fatigue life spends within the initiation phase and propagation to failure phase. Some have claimed that the initiation phase can be above 90% of the cycles to failure. Thus, it is important to investigate these phases to provide a better understanding of fatigue behaviour.

The understanding of a crack and its propagation falls within the discipline of fracture mechanics. It was through Paris and Erdogan (1963), using fracture mechanics, that fatigue crack propagation became better understood.

3.3.4 Linear elastic fracture mechanics

Linear elastic fracture mechanics (LEFM) is one of the divisions of fracture mechanics in which, globally, the material needs to behave in an elastic manner and only small-scale yielding is acceptable (Anderson, 2005). If large scale yielding is present, the material will require analysis under elastic plastic fracture mechanics (EPFM) or any other acceptable technique. LEFM's fundamental teaching introduces the Griffith theory (critical energy release rates) for brittle fracture (Karihaloo & Xiao, 2003). Another teaching of LEFM is the Irwin's theory for brittle failure. Irwin's theory introduces the concept of the stress intensity factor (SIF) approach, which is the approach used in this investigation.

LEFM is concerned with three modes of failure, i.e. mode I (opening), mode II (in-plane shear) and mode III (out-of-plane shear), shown in Figure 3-10. Mode I loading is used in this investigation as this is the most frequent mode of crack propagation in engineering structures (Bertram Broberg, 1999). Furthermore, cracks tend to orientate themselves into mode I, i.e. align itself perpendicular to the applied load (Anderson, 2003). In addition, standardised testing methods, such as the ASTM standards are typically for mode I type loading. Typically, when mode II and mode III are tested, they are mixed with mode I, i.e. mixed mode I+II and mixed mode I+III. In the scenario of mixed mode, it is common practice to reduce the analysis to an equivalent mode I scenario.

To quantify crack tip damage, LEFM used the concept of a stress intensity factor (SIF). This considers the stress field in front of the crack tip. When there is a notch (or crack) in a material, the applied stress/load to the material needs to flow around the notch, causing the stress flow to intensify around the notch, as shown in Figure 3-11. If the radius of the notch is very sharp (like a crack) and/or the length of the notch is increased, the stress flow around the notch would become more intensified. The SIF is denoted by the parameter *K* and is defined in equation (3-4) by:

$$K_I = Y\sigma\sqrt{\pi a} \tag{3-4}$$

Where σ is the applied stress, Y is a geometrical constant and a is the crack length. The subscript I denotes mode I loading conditions.

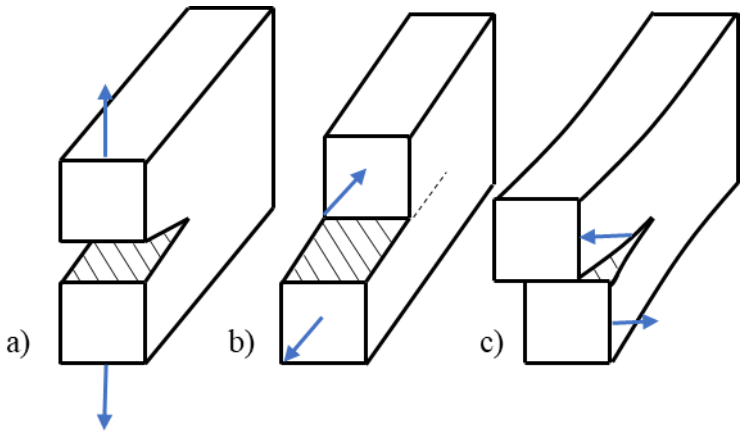

Figure 3-10: The three modes of failure a) Mode I, b) Mode II and c) Mode III.

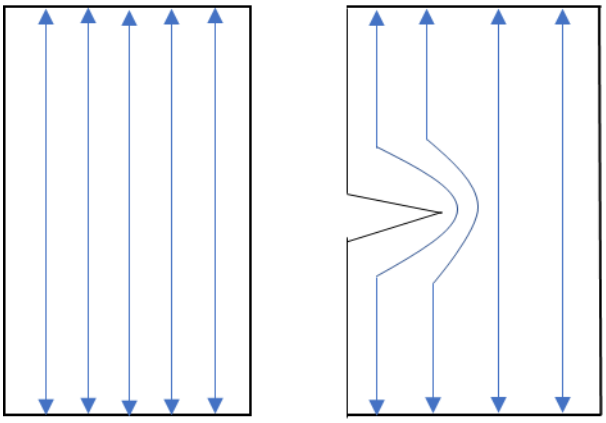

Figure 3-11: Load flow lines.

3.3.5 Crack propagation

By using the above concept of fracture mechanics SIF (K), Paris and Erdogan (Paris & Erdogan, 1963) related the change in crack length per a load cycle (da/dN) to a cyclic SIF, ΔK (John Andrew Newman, 2000). The cyclic SIF can be seen in Figure 3-12. The ratio between K_{min} and K_{max}, R, is referred to as the *R-ratio* or load ratio.

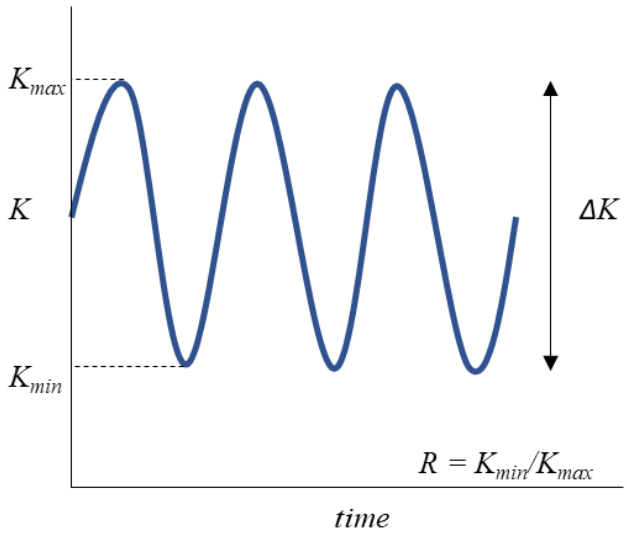

Figure 3-12: Change in stress intensity factor (ΔK) versus time.

Paris and Erdogan (Paris & Erdogan, 1963) found that there is a specific behaviour exhibited by material when monitoring the *da/dN* (crack propagation rate) and ΔK. This behaviour can both be visually and quantitatively represented on a fatigue crack growth rate curve, as shown in Figure 3-13. The curve is plotted on a log-log scale in which the crack growth per a cycle, *da/dN*, is on the y-axis and ΔK on the x-axis. As can be seen in Figure 3-13, the curve has three portions to it which correlate to the three phases of fatigue. The first region is known as the threshold region (initiation) in which the crack growth curve has an asymptotic behaviour. Below this threshold, ΔK_{th}, is the point at which a crack will not propagate and provides insight into the initiation of a crack. The second region is where the stable crack propagation occurs, and follows the Paris law:

$$\frac{da}{dN} = C\Delta K^m \tag{3-5}$$

Where *C* and *m* are typically considered material constants. However, studies on steels have shown that the *C* and *m* values are also affected by the specimen size (Ritchie, 2005). The Paris law, in Equation (3-5), is a power function but follows a linear curve on a log-log scale. As the crack growth rate increases, it approaches a critical stress intensity known as the fracture toughness, K_{IC}. As the K_{max} of ΔK approaches K_{IC}, the crack growth becomes unstable, which is the third region of the graph, and also displays an asymptotic crack growth rate.

The ΔK_{th} region is the region of interest for this project and will be described in more detail later.

The crack propagation phase is where stable crack growth occurs and is commonly referred to as the Paris regime (Paris & Erdogan, 1963; Fatemi, 2006). This phase

is not as influenced by microstructural effects as the initiation phase (Ekberg, 2004). Depending on the material and it's ductility, this fatigue phase produces striations on the fracture surface due to the fatigue loading (Campbell, 2008). Each striation represents one fatigue cycle (Totten, 2008). As the crack approaches a critical length under the fatigue loading, the crack propagation becomes unstable and eventually fast fracture occurs.

One of the factors which may affect the crack growth rate behaviour of a material is temperature. Some metals, such as 7050-T7452 alloy show a crack growth temperature dependency, i.e. for higher temperatures, there is higher crack growth rates (Zhu *et al.*, 2018). However, for Ti-6Al-4V, studies have shown that for room temperature, 150°C, 250°, and 345°C, no significant change in crack growth rates were observed (Arakere *et al.*, 2002; Zhu *et al.*, 2018). Typically, Ti-6Al-4V is used in low temperature applications of turbine engines such as the intake stages (Nalla *et al.*, 2002).

The approach of monitoring fatigue crack propagation behaviour has opened up a newer, less conservative approach to design through better understanding the issue of fatigue, rather than designing by avoiding the problem of fatigue.

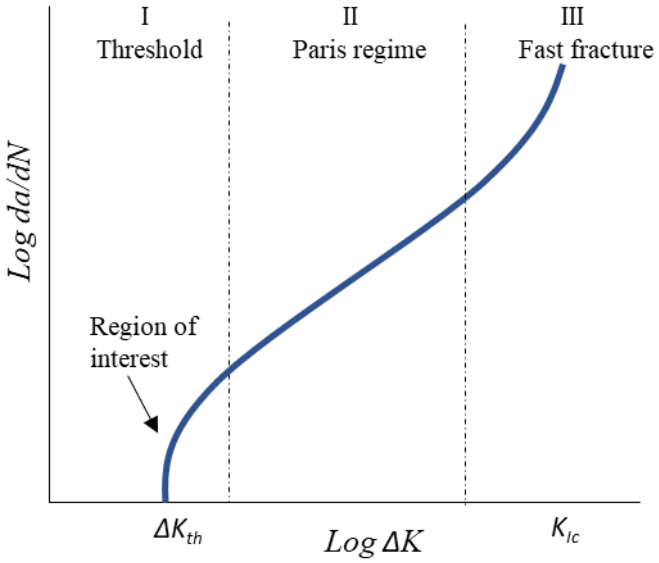

Figure 3-13: The three regions of a fatigue crack growth rate curve (Newman, 2000)

3.3.6 Damage tolerant/Fitness for purpose designs

Unlike the S-N approach where parts are replaced frequently to avoid fatigue crack propagation, the Paris approach allows for damage tolerant designs where fatigue crack propagation is likely to occur. There exists a quantitative relationship between the fatigue stress, flaw size and toughness of the material whereby the part may be

assessed on its fitness for purpose (Tait, 2012). Two terms are required to determine the third e.g. if the crack length is known based on non-destructive testing (NDT) methods, and the fatigue stress, one can use equation (3-4) to solve for K_I. This K_I can be compared with K_{IC} to determine how far away from fracture it is. Furthermore, if the initial crack size is known, the final crack size which will cause fracture can be determined by knowing the fatigue stress and fracture toughness. This is useful as the Paris equation i.e. equation (3-5) can be rearranged and integrated to form:

$$N_f = \int_{a_i}^{a_f} \frac{da}{C(\Delta\sigma Y\sqrt{\pi a})^m} \tag{3-6}$$

Where a_i is the initial crack length and a_f is the final crack length. Equation (3-6) can be used to solve the number of cycles to failure. This allows for the determination of the required inspection periods of the part. In summary, using this fracture mechanics approach can answer questions such as (Tait, 2012):

- What is the critical crack size at service loads?
- How safe is the system if it contains a crack?
- How long might it take for a crack to grow from initial to critical size?
- How often should a particular structure be inspected?

While the above considers the K_{IC} values for design purposes, K_{th} can also be used in conjunction with K_{IC} for designs which require long fatigue lives. In many scenarios (such as LPBF), defects, porosity cannot be avoided. By characterising the flaws as a crack, fatigue crack propagation can be avoided if $\Delta K < \Delta K_{th}$ (John Andrew Newman, 2000).

Using these LEFM methods to design for fatigue has allowed for structural weight reduction (as well as cost) without sacrificing safety. Typically, one could increase the area in which the fatigue load will be applied, but this means an increase in weight which poses a problem for applications where lightweight structures are required. When designing by ΔK_{th}, one requires a significant understanding of the factors affecting ΔK_{th}.

3.3.7 Crack closure

One of the factors affecting ΔK_{th} is crack closure. This occurs when the opposing crack flanks come into contact with each other before the minimum load is reached (Lawson *et al.*, 1999; Newman, 2000; Boyce & Ritchie, 2001). There are numerous crack closure mechanisms affecting fatigue, however, the most likely mechanisms are roughness-induced crack closure (RICC), plasticity-induced crack closure (PICC) and oxidation-induced crack closure (OICC). For the RICC, asperities are

caused as the crack propagates, the asperities then come into contact with each other before the minimum load is reached causing the crack closure. PICC is caused by deformation in the plastic wake of the crack flanks so thar they prematurely come into contact with each other. For OICC, oxide layers and debris stop the crack flanks from getting closer to each other. These closure mechanisms are displayed in Figure 3-14. These premature crack closures cause the crack not to be fully driven by ΔK but rather a ΔK_{eff} which is equal to:

$$\Delta K_{eff} = K_{max} - K_{cl} \tag{3-7}$$

Equation (3-7) shows that calculating ΔK_{th} using the applied ΔK instead of the actual experienced ΔK_{eff} will produce inaccurate fatigue results. Figure 3-15 shows how the ΔK_{eff} looks within a fatigue cycle. The fatigue results obtained will be influenced by the crack closure effects which are extrinsic properties of the material and not the intrinsic fatigue property. The effect ΔK_{eff} will have on the results can be explained using the *R-ratio* (load-ratio) effect. When increasing *R-ratio*, the range between K_{min} and K_{max} becomes smaller, thus the applied ΔK approaches and possibly equals the ΔK_{eff}. This results in a more intrinsic ΔK_{th}. The effect increasing *R-ratio* has on fatigue propagation as well as ΔK_{th} can be seen in Figure 3-16.

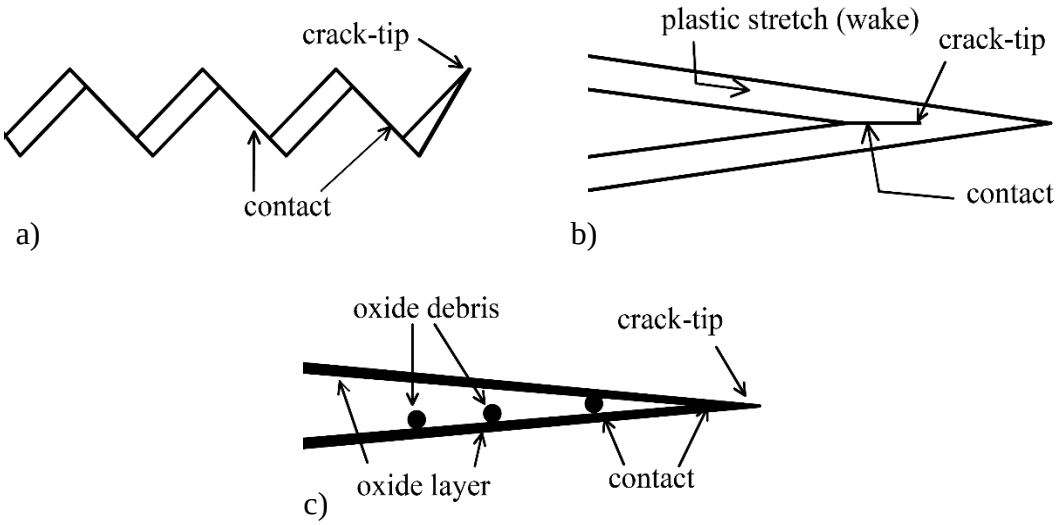

Figure 3-14: Schematics of three crack closure mechanisms a) RICC, b) PICC and c) OICC (Newman, 2000)**.**

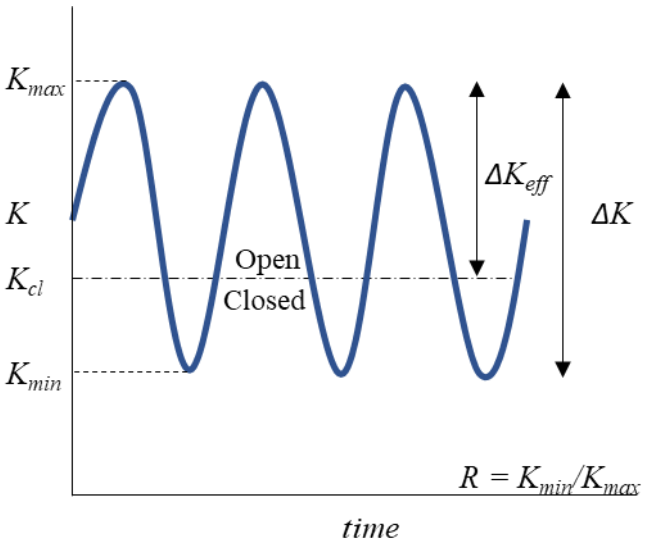

Figure 3-15: Schematic of ΔK_{eff} and crack closure in a fatigue cycle

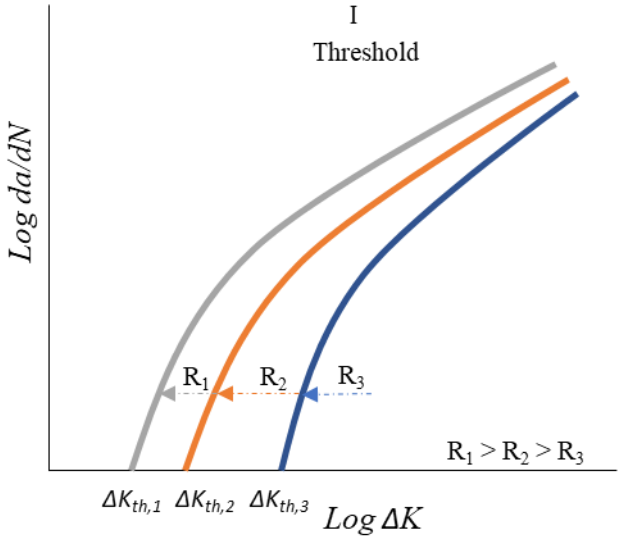

Figure 3-16: The effect of *R-ratio* on ΔKth.

The effect of *R-ratio* on fatigue behaviour can be divided into two parts: (i) increases the FCGR and (ii) reduces the ΔK_{th}. The particular ΔK_{th} effect can also be seen better on a ΔK_{th} versus *R-ratio* graph, as seen in Figure 3-17. In the idealised representation, shown in Figure 3-17 a) and b), there exists a critical *R-ratio*, R_c, in which the ΔK_{th} becomes independent of both *R-ratio*. This is as $K_{min} = K_{cl}$, which in turn means that $\Delta K_{eff,\,th} = \Delta K_{,\,th}$ at $R > R_c$. However, realistically, ΔK_{th} data with respect to *R-ratio* can sometimes behave similarly to that represented in Figure 3-17 b). It is important to note that other data sets found in the literature on various titanium alloys, aluminium alloys and steels vary from that represented in Figure

3-17. While the idealised independence of ΔK_{th} on *R-ratio* differs to that of experiments, the ΔK_{th} based on experiments generally shows a behavioural change before and after a certain R_c. For $R < R_c$, the ΔK_{th} is considered to be in a global crack "closure-affected" region, i.e. affected by extrinsic and intrinsic properties, and for $R > R_c$, the ΔK_{th} is considered to be in a global crack "closure-free" region, i.e. affected by intrinsic properties. This is seen in Figure 3-17 b). This means that for $R < R_c$, it is highly likely that the RICC, PICC and OICC mechanisms are influencing the ΔK_{th} results. However, it is debated as to how severe each mechanism's influence on ΔK_{th} actually is. Furthermore, the type of FCGR threshold test employed may also have a role to play in "closure-affected" results.

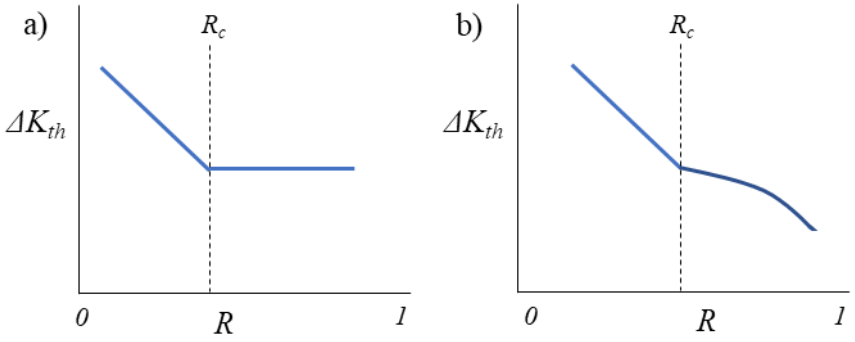

Figure 3-17: The idealised effect of (a) *R-ratio* on ΔK_{th}, and typical effect of (b) *R-ratio* on ΔK_{th}. Adaped from Boyce and Ritchie (2001).

The above explanation highlights the fact that the concept of crack closure should also be considered when designing for fatigue. Crack closure affects ΔK_{th} but not for Paris regime FCGR, However, both are used in design as well as damage tolerant applications.

3.3.8 Summary

The above subsection is a brief background as to how fatigue loading and its consequences became apparent in the 19th century and how today it is still of great concern. The initial fatigue testing method, the Wohler/*SN* approach, was described and highlighted the fact that the method is used to design components by trying to avoid the problem of fatigue. This leads to a non-cost-effective approach. Thereafter, the concepts of fracture mechanics, SIF, Paris regime, ΔK_{th} were discussed and it was explained how these concepts are used in design and damage tolerant design purposes. Finally, the concept of crack closure was discussed and its effect on fatigue behaviour, highlighting the importance of fatigue on AM and Ti-6Al-4V.

3.4 Implications of LPBF Ti-6Al-4V fatigue performance

The following section mainly summarises the works of Li et al (Li *et al.*, 2016) and Agius et al's (Agius *et al.*, 2018) review on the fatigue performance of AM Ti-6Al-4V. This section specifically focuses on the implications of residual stress, LPBF microstructure, porosity and surface roughness on the fatigue life of LPBF Ti-6Al-4V.

3.4.1 Residual stress

It has been found that most fatigue failures start at the surface of the part (Campbell, 2008). Thus, factors such as surface finish, surface porosity and residual stress state at the surface of the part have a significant effect on the fatigue life performance of the material.

It is often described that fatigue is a tensile process. However, fatigue is also common in shear stress cases, such as in torsional loading. One of the methods of improving the fatigue life performance of a part is to shot peen it. This entails shooting the surface of the material with steel balls at a high velocity to induce compressive residual stresses at the surface of the material. This method is widely used for the purpose of retarding the formation and propagation of fatigue cracks (Avcu *et al.*, 2020). It is also one of the more effective ways of improving fatigue life (Benedetti *et al.*, 2017). However, this is only effective at the surface layers and will not inhibit sub-surface crack initiation (Singla *et al.*, 2021).

The relationship to LPBF Ti-6Al-4V is that the process induces large tensile residual stress at the surface of the material (Mercelis & Kruth, 2006; Vrancken *et al.*, 2014). Furthermore, depending on the process parameters, the geometry of the manufactured part and build orientation, the levels of residual stress will be affected (Mercelis & Kruth, 2006; Vrancken *et al.*, 2014). As a result of the tensile residual stress at the surface of the part, it is easier for cracks to initiate and eventually propagate to failure. Furthermore, with LPBF there is porosity and surface roughness which act as stress raisers/concentrations and, coupled with residual stress, will accelerate the crack initiation phase. In addition, because residual stress has been found to be influenced by build orientation, this can also lead to anisotropy in crack initiation. Generally, it is of significance to reduce a residual stress level via various process parameters or post processing treatments. However, in comparison to microstructural effects and porosity/defects, the effect of residual stress is not as severe.

3.4.2 LPBF microstructure

Studies have reported that 85% of the fatigue life of a component can be attributed to the crack initiation phase (Wu *et al.*, 2020). If a material is to initiate a crack purely from the material (no defects/porosity or surface roughness), the crack initiation can be associated with strain localisation as well as basal plane facets

(Bantounas *et al.*, 2010; Li *et al.*, 2016; Wu *et al.*, 2020). Simply put, if a material has good plastic flow capabilities (ductility), it will reduce strain localisation and improve fatigue life performance. Furthermore, one of the methods to increase the fatigue life is to refine the microstructure which reduces the slip length and improves fatigue life performance (Li *et al.*, 2016). The LPBF microstructure produces a largely brittle material due to the α' martensitic microstructure. Furthermore, within the hierarchical α' lath structures, there is a mismatch of strain between the laths which results in strain localisation at their interfaces (Ter Haar & Becker, 2021). This strain localisation can act as a crack initiation site. It is found that the primary α' laths have an ~ 45° orientation affinity to the build direction (Simonelli, 2014; Ter Haar & Becker, 2021). These primary α laths have been shown to promote crack initiation (Dunstan *et al.*, 2020; Tan *et al.*, 2020). This is due to the ~ 45° lath being aligned with the maximum shear stress axis (45°) as well as the lath at ~ 45° having the longest slip distance in comparison to a lath with a different angle. The PBG boundaries have also shown to inhibit deformation due to poor $\alpha' - \alpha'$ slip transmissibility across PBG. For slip crossing PBG, it has been observed to occur at near-parallel basal planes and lath angles.

3.4.3 Porosity

It has become well established that porosity acts as crack initiation sites which reduces the fatigue strength of the material, i.e. accelerate the initiation phase. The size, location and shape of the porosity play an influential role. Porosity can form in various ways, such as shrinkage due to the alloy's freezing range. However, when considering the LPBF process, porosity typically forms due to entrapped gas (spherical shape) or caused by lack of fusion (irregular shape) (Vilaro *et al.*, 2011; Panwisawas *et al.*, 2015; Agius *et al.*, 2018). Furthermore, these two types of porosity can occur at the surface of the material or sub-surface. The surface's lack of fusion porosity has shown to be the most detrimental to fatigue life while gas pores are considered to be the least detrimental. In addition, the larger the size of the porosity, the larger the initial flaw size, the quicker the crack initiation phase will be (Thorsten H. Becker & Dhansay, 2020). It was further found that a small gas pore is less likely to initiate a crack than a large sub-surface lack of fusion porosity. HIP treatments are used to reduce porosity which have shown to improve fatigue life of parts.

With regards to the fatigue behaviour of a material, porosity is an important factor to consider. In particular, porosity has been shown to be detrimental for crack initiation (Tammas-Williams *et al.*, 2017; Thorsten Hermann Becker & Dhansay, 2020). However, multiple investigations have shown that porosity does not have a significant influence on crack propagation (Leuders *et al.*, 2012; Poulin *et al.*, 2019; Becker *et al.*, 2021). This is because the porosity only causes a localised stress concentration which does not provide a sufficient increase in crack driving force. Thus, porosity will not be discussed based on the experimentation of this investigation.

Although the above mentions that the lack of fusion porosity is more detrimental to fatigue life than the gas porosity, the severity of a pore on fatigue life has more complexity to it. The work conducted on flaw characterisation by Anderson (2003), shows that a pore can have an interaction with a neighbouring pore. It is shown that if two flaws are coplanar, their interactions magnify the stress intensity between them. However, if the flaws are parallel, then it provides a shielding effect between the two by reducing the stress intensity. An investigation by Tammas-Williams et al (2017) showed a large increase in stress intensity for pores near the surface in comparison to sub-surface porosity with depths larger than one pore diameter. Investigations on high strength steels conducted by Murakami et al (1989; 1989; 1994) showed that the effect of non-metallic inclusions near the free surface on fatigue strength is similar to that of a notch or crack. This would be similar to the effect of surface roughness on fatigue behaviour.

3.4.4 Surface roughness

Surface roughness is one of the main factors, such as porosity, which is detrimental to the fatigue life of a part (Yadollahi & Shamsaei, 2017; Molaei & Fatemi, 2018; Molaei *et al.*, 2020). Typically, parts which have a larger surface roughness result in parts with lower fatigue life (Molaei *et al.*, 2020). The roughness can be considered as a topography of peaks and valleys on the surface of the material. These act as micro-notches, resulting in stress concentrations which cracks can more easily initiate from. However, because these micro-notches are all around the surface, the part is susceptible to multiple crack initiations (Molaei *et al.*, 2020). These cracks, initially, grow independently until they are large enough to interact with the surrounding cracks and form one large crack (Molaei *et al.*, 2020). Reducing the surface roughness via machining and polishing, in some cases, has shown to improve the fatigue life by almost four times (Chan *et al.*, 2013; Torries *et al.*, 2018). However, some investigations also show no significant difference in fatigue life between a rough surface and machined surfaces (Yadollahi & Shamsaei, 2017). This is because during the machining process, while the surface has become more smooth, internal defects/porosity may now have been brought to the surface of the material (most detrimental location). Furthermore, this porosity may be larger than the surface roughness micro notch, resulting in a larger stress concentration. However, crack origination from surface porosity is typically a single dominant crack whereas surface roughness cracks tend to have multiple crack sites (Yadollahi & Shamsaei, 2017).

3.5 Chapter summary

The aim of this chapter was to introduce the reader to the concepts and definitions required for the understanding of this investigation. The three main concepts are AM (specifically LPBF), Ti-6Al-4V titanium alloy and fatigue behaviour. The chapter began with the various techniques of AM according to the ASTM 52900 (ASTM, 2015) and a special focus on LPBF and it’s process parameters. A

background on titanium and it's α and β-phase was discussed. A special focus on Ti-6Al-4V, an $\alpha + \beta$ alloy, it's microstructures and its use within industry was discussed along with its use in LPBF. Finally, the concepts of fatigue, such as: SIF, Paris regime, ΔK_{th} were explained and it was shown how they are used for design purposes.

4 Previous studies on the fatigue behaviour of LPBF Ti-6Al-4V

This chapter considers various studies which have focused their investigations on the fatigue of LPBF Ti-6Al-4V and/or mechanisms relating to fatigue and LPBF. While there are many more investigations found within literature than which will be addressed in this section, the literature which is considered the most relevant for the purpose of this dissertation will be focused on. The purpose of using the selected literature is: (i) Their main focus is the fatigue behaviour of LPBF Ti-6Al-4V, (ii) the specific literature is sufficient to highlight the current understandings of fatigue behaviour of LPBF Ti-6Al-4V, and (iii) the specific literature is sufficient to highlight the gap(s) within literature. The individual investigations are briefly discussed to highlight the current understanding of fatigue of LPBF Ti-6Al-4V as well as identify key themes, gaps, contrasting views and questions which may arise from reviewing the literature. The final subsection summarises the understanding of fatigue of LPBF Ti-6Al-4V and highlights the need for further investigation on this topic.

4.1 Introduction

While there are many studies which consider the fatigue behaviour of LPBF Ti-6Al-4V, concepts such as crack closure (*R-ratio*) and the influencing mechanisms of residual stress and microstructure aren't typically investigated thoroughly enough. In order for residual stress to be relieved, heat treatments are often applied. Not only does this reduce/eliminate the residual stress, but also alters the microstructure. Often it is the case that the new observations made on stress relieved components reflects not only the effect of residual stress, but also a change in microstructure. In addition, there are mechanisms such as surface roughness and porosity which also influence fatigue behaviour. The prevailing understanding, however, is that these two mechanisms are stress raisers and cause premature crack initiation.

Extensive research on conventionally manufactured Ti-6Al-4V exists, in particular, the effects of microstructure and fatigue properties (Nalla, *et al.*, 2002; Nalla, *et al.*, 2002; Leyens & Peters, 2003; Oberwinkler, 2011). Some of these understandings can be extended to LPBF produced Ti-6Al-4V. However, the layer-wise manufacturing process results in residual stress and microstructural condition's which influence fatigue properties and requires further investigation (Leuders *et al.*, 2012). The following investigations, which will be discussed in this section, show the current understanding on LPBF Ti-6Al-4V and fatigue behaviour:

- Van Hooreweder et al (2012)
- Leuders et al (2012)

- Edwards and Ramulu (2014; 2015)
- Cain et al (2015)
- Kunz et al (2019)
- Xu et al (2019)
- Kumar et al (2018; 2019)
- Tarik Hasib et al (2020)

The various publications use different build orientations in their studies. Figure 4-1 shows the designations given to the orientations and will be used accordingly in what follows. The orientation naming's convention first uses the plane normal and then the crack growth direction. The purpose of using these orientations is a result of the respective crack planes and build directions, the PBG shape, the crack front interaction with the PBG, α lath angles and residual stress. These are described in brief detail in section 6.2.3.

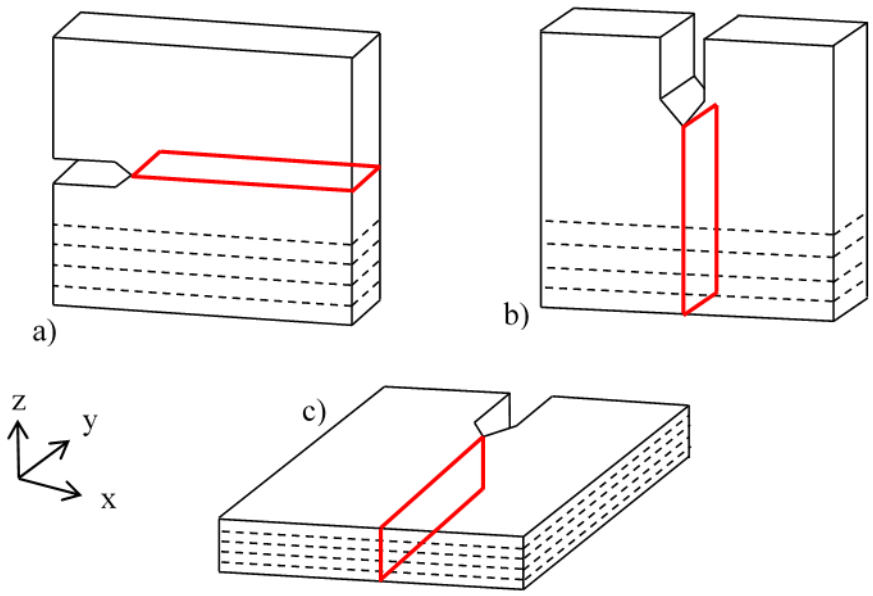

Figure 4-1: Three build orientation a) Z-X, b) X-Z and c) X-Y. Crack planes are in red and build layers are dashed lines.

4.1.1 Van Hooreweder

The investigation conducted by Van Hooreweder et al (2012) focused on the fracture toughness and FCGR (Paris regime) on LPBF Ti-6Al-4V. This investigation compared the LPBF Ti-6Al-4V with vacuum arc remelted (VAR)

standard oxygen mill annealed Ti-6Al-4V. The specific LPBF machine was an in-house LPBF machine, however, with scan parameters that are given and shown in Table 4-1.

Table 4-1: Scan parameters

Laser power, P (W)	Scan speed, *v* ($mm.s^{-1}$)	Track distance, *h* (µm)	Layer thickness, *t* (µm)
250	1600	60	30

A bi-directional scanning strategy was used. The specimens manufactured were of CT specimen geometry. The tests conducted followed the ASTM E399 standard test method for linear-elastic plane-strain fracture toughness of metallic materials (ASTM, 2020) and ASTM E647 standard test method for measurement of fatigue crack growth rates (ASTM, 2015). Specimens were tested in that AF condition.

The fracture toughness results show that the K_{IC} of the LPBF Ti-6Al-4V is 75 % that of the VAR Ti-6Al-4V. Van Hooreweder et al (2012) describe that the most likely reason for this difference is due to the martensitic microstructure causing an increase in brittleness and, therefore, lower fracture toughness.

The FCGR between VAR and LPBF Ti-6Al-4V showed comparable results to each other as well as other FCGR results found within the literature. Van Hooreweder et al (2012) concluded that the reason for the acceptable FCGR of LPBF is: "due to the high density of grain boundaries acting as obstacle points for crack propagation."

For LPBF Ti-6Al-4V and its fatigue properties, there are concerns such as build orientation, residual stress and *R-ratio*. However, this investigation by Van Hooreweder et al (2012) did not investigate these concerns. It is likely that due to this investigation being one of the earliest studies concerning the fatigue properties of LPBF Ti-6Al-4V, that not all of the concerns relating to fatigue properties could be addressed.

4.1.2 Leuders et al (2012)

Leuders et al (2012) investigated the relationship between microstructure and defect property's relationship on cyclic loading of LPBF produced Ti-6Al-4V. This was initially one of the more detailed studies on fatigue behaviour of LPBF Ti-6Al-4V. The investigation considered the FCGR (Paris regime), near-threshold FCGR as well the *SN* approach. Two build orientations were used in the FCGR type test, namely, Z-X and X-Z for compact tension (CT) specimens. Four conditions were investigated, i.e. AF, annealed below the *β*-transus, annealed above the *β*-transus and HIPed below the *β*-transus. Only one orientation was tested in the *SN* approach in all four conditions. Specimens were manufactured using a SLM 250^{HL} machine,

using a 400W yttrium fibre laser. Powder particles of 40µm and a layer thickness of 30µm were used. No further build information was given.

Their results indicated that the fatigue properties generally show a difference between the AF and the remaining post processed conditions in Figure 4-2 and Table 4-2 (Leuders *et al.*, 2012). For the FCGR results, there is a clear improvement in the post processed results compared to the AF, i.e. a shift to right (lower FCGR), particularly the near-threshold FCGR. Furthermore, in both orientations and for all post processed conditions, the FCGRs are comparable to each other as well as to reference material. It is further observed that there is an anisotropic behaviour between the two orientations in the AF conditions, particularly at higher ΔK values. For the entire testing range, the Z-X orientation's AF condition has the lowest near-threshold FCGRs as well as the highest FCGRs for a given ΔK and is not comparable to conventionally manufactured Ti-6Al-4V within their study. However, the X-Z orientation at higher ΔK values is comparable to the reference and post processed material of the study. Furthermore, it is noticeable that anisotropic behaviour has diminished if not been eliminated in the post-process conditions, i.e. both orientations have a FCGR as within the reference material. When considering the fatigue strength, there is also an improvement in the post-processed conditions compared to the AF condition. However, in all three post-processing conditions, their fatigue strengths (*SN* approach) are not comparable to those in the FCGR results. This indicates that the primary influencing mechanisms differ between FCGR and fatigue strength.

Leuders et al (2012) mention that the main influencing factor on FCGR and near-threshold FCGR is the residual stress, showing that a heat treatment below the β-transus improves the near-threshold FCGR by a factor of about three (Leuders *et al.*, 2012). The second influencing factor is the microstructure, i.e. the grain shape and size which have all been thoroughly investigated for multiple titanium alloys. They stress, however, that the impact of layer-wise manufacturing, residual stress, porosity, and AF microstructure have not yet been captured. It is further mentioned that the effect of porosity on the FCGR is minimal, as the HIPed condition is comparable to the other post-process conditions. However, porosity is the main influencing factor on fatigue strength as the HIPed condition performed the best by over an order of magnitude when comparted to the remaining conditions. This is due to the porosity acting as stress raisers and reducing the initiation phase of the material's fatigue strength.

While Leuders et al (2012) argued that residual stress is the primary influence on FCGR and that the microstructure is secondary, the variable of crack closure/ *R-ratio* was not considered. While the arguments and evidence brought by Leuders et al (2012) supports their conclusion, there are more variables of fatigue properties to consider when drawing the conclusions. Since testing for FCGR was tested at R = 0.1, results will be affected by crack closure mechanisms. This means that results are affected by extrinsic properties and are not indicative of the true intrinsic fatigue properties. The residual stress measurements shown in their investigations indicate

between 90 – 265 MPa in the x-direction and 235 – 775 MPa in the y-direction for the AF condition. These directions would be representative of propagation direction and loading direction respectively. Since the larger residual stresses are acting in the load direction, it is possible that these stresses are adding to the applied load and the actual *R-ratio* is $R > 0.1$ rather than $R = 0.1$. Thus, the comparison may not actually be $R = 0.1$ AF versus $R = 0.1$ anneal, but rather $R > 0.1$ AF versus $R = 0.1$ anneal. A question that becomes relevant here is if testing were to be conducted at higher *R-ratio*s, would the claim of residual stress as the primary influence and microstructure the secondary influence on FCGR behaviour, still hold true.

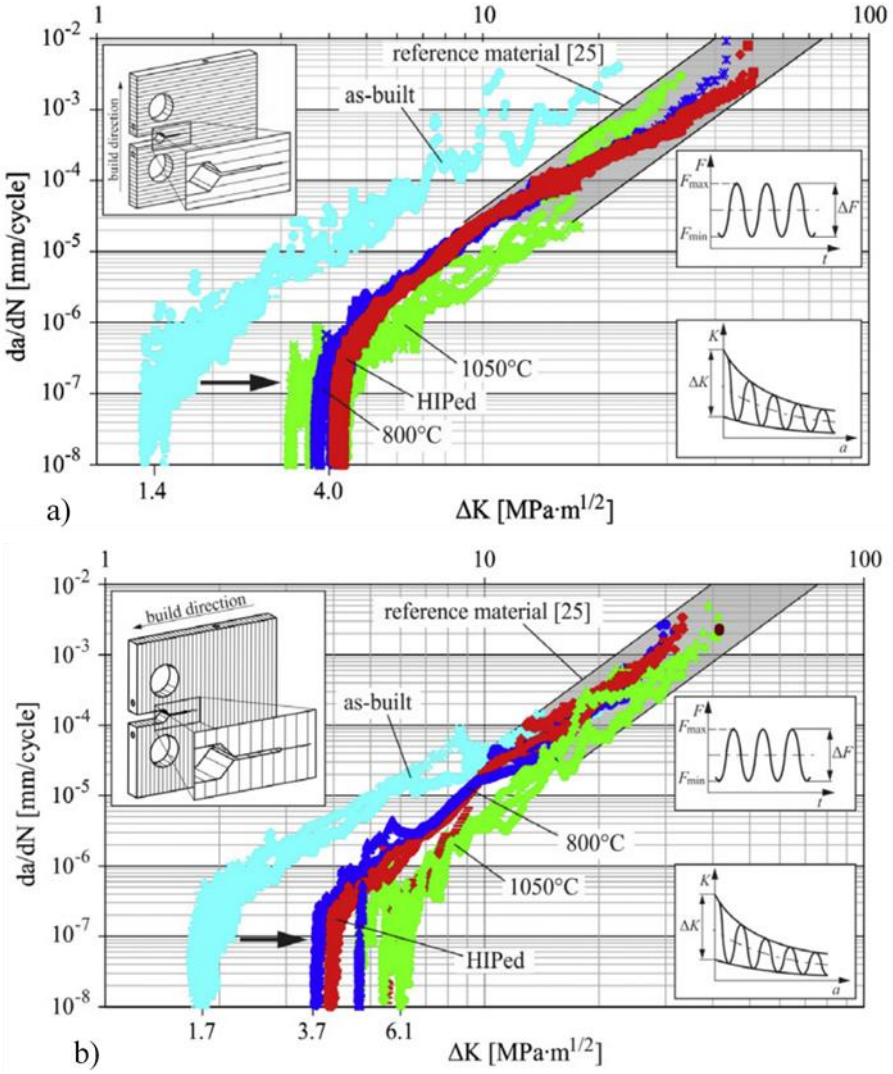

Figure 4-2: Leuders et al's (2012) FCGR results a) YZX orientation b) ZYX orientation

Table 4-2: Post processing parameters and fatigue life at 600 MPa (Leuders *et al.*, 2012)

Condition	As-fabricated	Anneal 1	Anneal 2	HIPed
Temperature (°C)	-	800	1050	920(@ 100bar)
Time (h)	-	2	2	1
Atmosphere	-	Argon	Vacuum	Argon
Cycles to failure	27000	93000	290000	2000000

In addition to the above, Leuders et al (2012) conducted an anneal at 800°C in which there was grain growth (seen in their study), an increase in β content (seen in their study) and decomposition of α' grains. However, this isn't discussed with regards to improvement of fatigue properties, but rather the residual stress is given as the primary concern. Furthermore, Leuders et al (2012) concludes that this heat treatment does not change the microstructure.

Although Leuders et al (2012) considered two build orientations and showed the similarities and differences between these two in the results, they did not address or provide the reasons as to "why" there are these differences and similarities.

It is worth noting that within the works of van Hooreweder et al (2012), the AF fatigue properties were comparable to that of conventional Ti-6Al-4V. In Leuders et al's (2012) investigation, however, the AF LPBF Ti-6Al-4V did, for the most part, not compare well to conventional Ti-6Al-4V, except for one orientation at higher ΔK values. Interestingly, van Hooreweder (2012) mentions that it is likely the microstructure which gives it acceptable fatigue properties, while Leuders et al (2012) mention that the residual stress is the primary concern in weakening the fatigue properties and microstructure is a secondary concern.

4.1.3 Edwards and Ramulu (1)

Edwards and Ramulu (2014) investigated the fatigue strength (S-N approach) of LPBF Ti-6Al-4V. The investigation was further broken down into build orientation effects and surface finish. Specimens were manufactured on an MTT 250 machine with a 200W fibre laser. The machine utilised a multi-directional scanning strategy of 67° per layer with a speed of 200mm/s. The layer thickness was kept at 50µm. Pre-alloyed grade 23 Ti-6Al-4V spherical powder was used with a diameter of 30µm.

They considered three build orientations, namely, (i) "horizontal" where one orientation's profile height is parallel to the x-axis and another to the y-axis, and (ii) "X-Z" where the profile height is parallel to the z-axis. No heat treatments were conducted in this investigation. A set of specimens in all three orientations was left completely AF, and another set had a machined surface finish. The target cycle

count for this investigation was set at 200000 cycles. Results are shown in Figure 4-3.

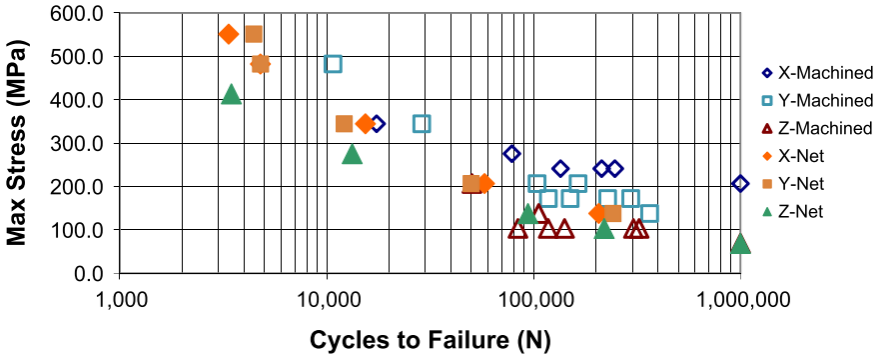

Figure 4-3: Fatigue S-N curves comparing as fabricated and machined conditions as well as build orientation (Edwards & Ramulu, 2014)

Edwards and Ramulu (2014) found that the fatigue performance of LPBF Ti-6Al-4V was 75 % lower than the wrought material to which it was compared. Their reasoning for this was due to the inherent porosity, residual stress and surface finish of the LPBF process. However, it was not clear as to the severity of each mechanism's influence on fatigue life. Furthermore, in their specific study, they did not observe a significant difference between the AF and machined specimen's fatigue life. The explanation given was that the initial internal porosity were now brought to the surface due to the machining process, and likely played a dominant role in crack initiation and premature failure. It was also found that the effect of build orientation was significant, but the extent of the influence from porosity, microstructure and surface roughness required more investigation.

The main highlighting point of this study, which is a recurring theme within the literature, is that for anisotropic behaviour and poor fatigue properties, the reason given is due to a combination of residual stress, microstructure, porosity and surface finish. While these reasons hold true, the investigations into the mechanisms of the influencing factors does not yet seem to be well investigated within literature.

4.1.4 Edwards and Ramulu (2)

In a later study by Edwards and Ramulu (2015), they considered the effect of build orientation on the FCGR and fracture toughness on LPBF Ti-6Al-4V. CT specimens were used in this study and manufactured in three build orientations, i.e. two in the Z-X orientation but rotated on the build platform and X-Y, shown in Figure 4-4. It was not mentioned which specific machine was used to build the specimens, however, it is assumed that the machine was used as in the previous study (Edwards & Ramulu, 2014), as the same building parameters were given. Specimens were tested in the AF condition with no post processing conducted. FCGR testing was conducted according to the ASTM E647 and fracture toughness

according to the ASTM E561 “standard test method for KR curve determination” (plane stress) (ASTM, 2020).

It was found that the AF LPBF fracture toughness (plane stress) for all three orientations, is lower than that of wrought, cast as well as EBM Ti-6Al-4V. They attribute this to the brittle martensitic microstructure. They also argued that specimens with crack planes perpendicular to build layers, produce a higher fracture toughness than those of planes parallel to the build layer. For the FCGR, there was no perceivable difference between the three orientations. However, it was found that that FCGR for the LPBF Ti-6Al-4V performed better (slower) than for the wrought material but with more erratic behaviour. It was also mentioned that it is likely that residual stresses overshadow the influences of build orientation and microstructural directionality.

Edwards and Ramulu (2015) make mention of ΔK_{th} and give a value to this for all three orientations, i.e. of the order 6 MPa.m$^{0.5}$. However, their FCGR testing was only for the Paris regime and fracture toughness. On inspection, their ΔK_{th}, seems to be based off their lowest *da/dN-ΔK* data points as opposed to a crack growth rate of 10^{-10} m/cycle. This is a bit confusing as there is no specific discussion surrounding it not being a “real” near-threshold based on a type of test or a near-threshold obtained through curve fitting methods. Furthermore, this ΔK_{th} is said to be lower than that for wrought material, based on Boyer et al’s (1994) titanium material handbook. However, various literature, such as Leuders et al (2012) and Nalla et al (2002), amongst others, show that $\Delta K_{th} \sim 6$ MPa.m$^{0.5}$ is actually high, particularly for such a fine AF microstructure produced from LPBF.

In this work, no anisotropic behaviour was observed between the different orientations. This is of interest as the previous work of Edwards and Ramulu (2014) on the *SN* approach had a significant anisotropic behaviour. Furthermore, in the works of Leuders et al (2012), they found anisotropic behaviour in the AF condition between the Z-X and X-Z orientations. Highlighting that within the literature, there are different observations with regards to any anisotropic behaviour of LPBF Ti-6Al-4V.

One of the possible reasons as to why no anisotropic behaviour was observed in this study (at least for two of the three orientations) is because two of the orientations are identical. As shown in Figure 4-4, the X-Z and Y-Z orientation are both what is considered Z-X orientation in this dissertation. It is unclear as to why two Z-X orientations were considered, however, one could expect anisotropic behaviour between the Z-X and X-Y, but this did not occur. It is possible that this may be due to their selected scan strategy.

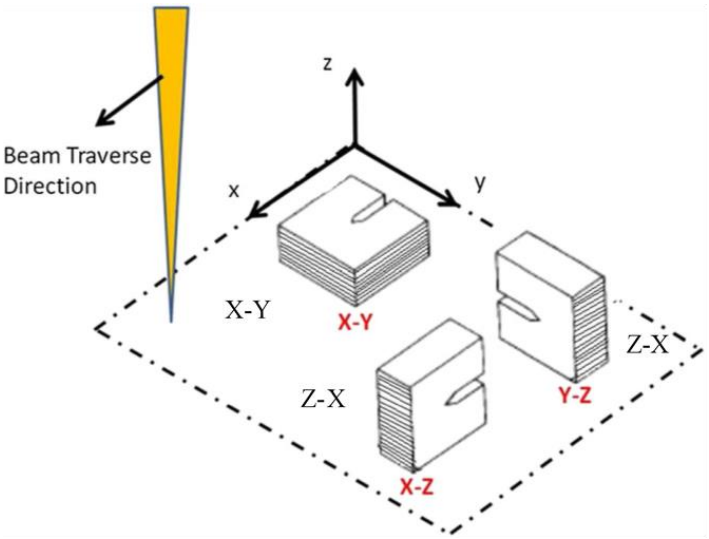

Figure 4-4: Build orientations of Edwards and Ramulu (Edwards & Ramulu, 2015)

4.1.5 Cain

Cain et al (2015) investigated the fatigue crack propagation and fracture toughness of LPBF Ti-6Al-4V. Three build orientations were considered and three conditions investigated, i.e. AF, SR and heat treated (HT). CT specimens were used for this investigation. Details of the specific printing equipment was not mentioned; however, the laser followed a zig zag pattern and rotated 90° per layer. Grade 5 Ti-6Al-4V spherical powder was used with particle sizes ranging between 15-45µm in diameter. FCGR testing conformed to the ASTM E647 standard (ASTM, 2015) and fracture toughness testing conformed to the ASTM E399 standards (ASTM, 2020).

With regards to the fracture toughness in the AF conditions, Cain et al (2015) found that anisotropy existed and mentioned that this could be due to residual stress anisotropy and/or microstructure anisotropy. The results also show that specimens with crack planes perpendicular to build layers produce a larger fracture toughness (in the AF condition). However, Cain et al (2015) did consider residual stress in the crack plane, measured by Vrancken et al (2014). It was found that the specimens with crack planes parallel to the build layer (Z-X orientation) had the largest measured tensile residual stress which was linked to the lowest fracture toughness. The SR condition showed a general improvement in fracture toughness, however, the anisotropic behaviour had now largely diminished. While it was expected to still have anisotropic behaviour in the SR condition, due to maintenance of the columnar grain structure, Cain et al (2015) argued that the SR heat treatment may have: "sufficiently altered the planarity of the grain-to-grain interfaces to reduce grain anisotropy". Interestingly, in the HT conditions, there was an apparent anisotropic behaviour noticed with a 20% difference between the highest and lowest fracture

toughness. In both SR and HT conditions, the specimen with a crack plane parallel to the build layers had the highest fracture toughness.

Similarly, Cain et al (2015) found that the FCGR results had a similar behaviour to that of the fracture toughness with regards to the specimen orientations and AF conditions. In the AF conditions, the X-Y orientation had the lowest FCGR (best) as well as the highest fracture toughness in comparison to the remaining orientations. However, when comparing orientations in the SR conditions, the X-Y orientation's FCGR seemed to have deteriorated compared to the AF counterpart, whereas the remaining orientations had improved their FCGR behaviour. Furthermore, the X-Z and Z-X orientations had a comparable FCGR, similar to the fracture toughness behaviour seen in the SR conditions. When considering the HT conditions, all three orientations have comparable FCGRs with no significant anisotropic behaviour observed. Interestingly, the X-Y orientation's best FCGR was seen to be in the AF conditions, where the remainder of orientations had improved FCGRs in the SR and HT conditions. The reason for this isn't particularly addressed by Cain et al (2015) , but they do mention that the subtle microstructural influences are yet to be investigated.

The FCGRs were compared to that of conventional wrought Ti-6Al-4V (Donachie, 2000) and found that the LPBF produced Ti-6Al-4V was not significantly different between the SR and HT conditions, but a noticeable difference was observed in the AF condition.

This investigation concluded that it gave insight into the anisotropic influence of residual stress in the AF conditions and that the heat treatments, in general, improved the fracture toughness, FCGR and reduced anisotropic effects.

While the argument for residual stress being the factor which causes such a low K_{IC} obtained seems plausible, it is weakened by the fact the K_{IC} values presented in the study are lower than the ΔK for FCGR data. For example, the X-Y AF condition has a K_{IC} of 28 MPa.m$^{0.5}$, however, the ΔK values for FCGR go above 30 MPa.m$^{0.5}$. K_{IC} can be thought of as the K_{max} of ΔK ($K_{max} - K_{min}$). Therefore, K_{IC}, cannot be lower than the FCGR ΔK data. The results do not agree with what is reported in literature.

It should be highlighted that within this study, residual stress is considered the reason for a low fracture toughness, however, in van Hooreweder et al (2012) it is mentioned that it is likely to be due to the brittle microstructure. Furthermore, the improvements in FCGR in the SR and HT conditions are similar to the improvements seen within Leuders et al's (2012) work.

4.1.6 Kunz

Kunz et al (2019) investigated the near-threshold FCGRs as well as Paris regime FCGRs of LPBF Ti-6Al-4V for three build orientations i.e. Z-X, X-Z and X-Y. CT specimens were used and tested in three heat treated conditions of 380, 740 and 900°C. Two *R-ratios* were tested i.e., R = 0.1 and 0.8. Specimens were built on two different EOSINT systems (M270 and M290), using different process parameters. It is mentioned that all three orientations were built using the EOSINT M270 machine while only the Z-X and X-Z specimens were built using the EOSINT M290 machine. However, based on the results, it seems as if M290 specimens were only tested at R = 0.1 in the 740°C condition. The load shedding method was implemented according to the ASTM E647 standard (ASTM, 2015). The fatigue testing was also conducted on two different pieces of fatigue testing equipment and the crack was optically monitored to an accuracy of 0.01mm. This largely suggests that load shedding was implemented manually.

For all conditions and stress ratios, no anisotropic behaviour was observed in the near-threshold FCGRs and Paris regime FCGRs. Furthermore, specimens tested at R = 0.1 from the 740°C condition exhibited the lowest ΔK_{th} ~ 2.7 MPa√m while the 380 and 900°C were largely comparable to each other at ΔK_{th} ~ 3.7 and 3.5 MPa√m, respectively. For the R = 0.8 at 900°C, a ΔK_{th} ~ 2 MPa√m was achieved. Figure 4-5 shows a summary of their results.

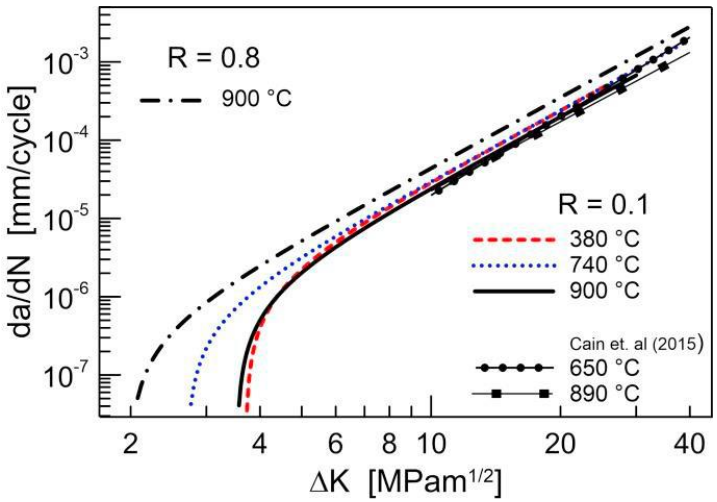

Figure 4-5: Comparison of FCGRs for different heat treatments at R = 0.1 and 0.8 (Kunz et al., 2019)

Kunz et al (2019) attributes the difference in ΔK_{th} in the 380 and 740°C conditions to differences in the microstructure and residual stress between the two conditions.

If one considers the magnitudes of the ΔK_{th} in isolation, i.e. not comparing it to the different conditions, the results are reasonable. However, when comparing it to each

other, the results are unexpected. According to Kunz et al (2019), the 380°C condition is fully α' martensitic while the 740°C condition consists of fine needles of α/α' in a matrix of β phase. This means that the 740°C condition is in a more ductile state and should result in a higher ΔK_{th} than the 380°C condition. It is also likely that there is some grain growth which would have occurred; however, no grain measurements were given. The 900°C condition is described to consist of lamella of ($\alpha + \beta$) phases with locally coarse α grains. Typically, this would further increase ΔK_{th} in comparison to the 380°C condition. However, it is not clear, based on the information presented by Kunz et al (2019), as to what the reasons are for the unexpected results.

4.1.7 Xu

Xu et al (2019) investigated the influence of building direction on the FCGR behaviour of LPBF Ti-6Al-4V. The testing conducted made use of an *in-situ* scanning electron microscope (SEM) to better understand crack initiation and propagation. Three build orientations were selected and are shown in Figure 4-6.

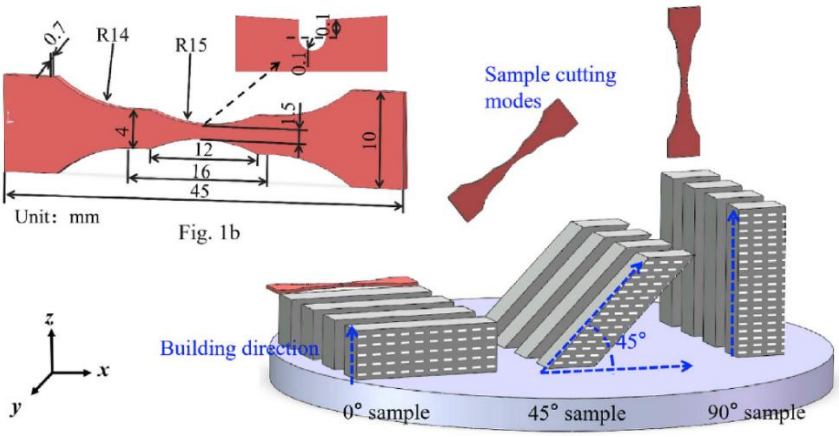

Figure 4-6: build orientations by Xu et al (2019).

This investigation used manufactured specimens on a SLM-280 machine, using a laser power of 450 W, scan speed of 1.2 m.s^{-1}, laser spot size of 50 µm and a hatch spacing of 150 µm. Spherical powdered Ti-6Al-4V material was used ranging between 20-80 µm, with an average of 50 µm in diameter. It is not clear if specimens were first built in blocks, as seen in Figure 4-6, and then wire cut into many specimens per a block, or if one specimen was built out of one block. The specimens underwent a heat treatment of 850°C for two hours. It is not mentioned if the heat treatment was conducted while the specimens were in the block format, attached to the base plate, cut off the base plate or already in the final specimen geometry. According to Xu et al (2019), the annealing heat treatment can greatly eliminate the prior β grain morphology and anisotropy behaviour. However, they did observe a

trace of prior β grains. Furthermore, they described the structure after annealing as basket-weave.

Specimens were polished to eliminate any surface roughness' influence. Thereafter, they were etched to reveal the underlying microstructure at the notch to investigate crack initiation. *In-situ* fatigue tests were conducted at an *R-ratio* of 0.1 and a frequency of 8Hz. Initially, crack length measurements/images were taken at 2000 cycle intervals, but this interval was reduced as the crack length increased (and FCGR).

Based on their explanation of the fatigue test methodology, it would seem that the test was conducted using the constant-load-amplitude method, i.e. conducting a Paris regime type test until failure occurs. In their investigation, they used a NASGRO fitting curve on their data, as shown in Figure 4-7. However, the curve produced a ΔK_{th} based on their data points and not from an actual threshold type test, i.e. load shedding technique. The "ΔK_{th}" observed is greater than 10 MPa.m$^{0.5}$, which is almost double of what is commonly found in the literature. This issue isn't particularly addressed by Xu et al (2019). It is likely that the asymptotic behaviour seen in the fatigue data is due to an artificial threshold: a behaviour observed at the very beginning of a constant-load-amplitude fatigue test. Crack growth rate data increases vertically on a log-log graph, until it reaches the Paris regime portion of the graph, and then proceeds linearly until fast fracture occurs.

The SEM observations showed that cracks were initiated at the machined notches and not from any defect in the vicinity, as shown in Figure 4-8. Further observations showed that most of the small cracks could only propagate between $\alpha + \beta$ grain boundaries, influencing the crack path to deviate as it progressed, causing a "zig-zag" pattern. Closer inspection of α grains show slip band formation.

As the crack increased in length (and cyclic stress intensity), the microstructural influence on the crack path diminished and a more straight crack path was observed. The larger crack also showed formations of shear bands and secondary cracks forming between the $\alpha + \beta$ grain boundaries.

The differences found within FCGRs and values of "ΔK_{th}" of the various build orientations, were concluded to be due to the residual stress and interior defects. It was also concluded that the easiest path for a crack to propagate in (and initiate) is perpendicular to the build direction, i.e. the crack path plane and build layer plane are the same (Z-X as defined in this dissertation). They found that both inter and intra-granular fracture occurred. Based on their microstructure, observations and fatigue data, Xu et al (2019) claimed that α grain colonies can inhibit crack initiation and propagation.

Although some points made by Xu et al (2019) are not agreed with, the appeal of this investigation lies in the *in-situ* SEM fatigue capabilities. The points which are not agreed with: (i) Discussing their results in terms of ΔK_{th} when near-threshold

type testing was not implemented. This result is a false/premature ΔK_{th}. (ii) They perform a stress relief heat treatment (850° for two hours); however, they conclude that part of the reason for anisotropic behaviour in ΔK_{th}, is due to residual stress.

It is a common understanding that at the near threshold FCGR (region I of FCGR curve), microstructural effects have a greater influence on crack propagation than the remainder of the FCGR curve. In this case, Xu et al (2019) showed this happening with the observed "zig-zag" pattern. This is of benefit to this project as one of the reasons in investigating the fatigue threshold (as opposed to any other mechanical property), is that it gives a better insight into the influence of microstructure on crack propagation. As has been seen in the above literature, a common reason behind the variously observed fatigue behaviour is residual stress, microstructure and porosity. Therefore, by investigating the ΔK_{th}, one will be able to draw more insight into what the actual influencing mechanisms are on crack propagation and increase our understanding of these phenomena.

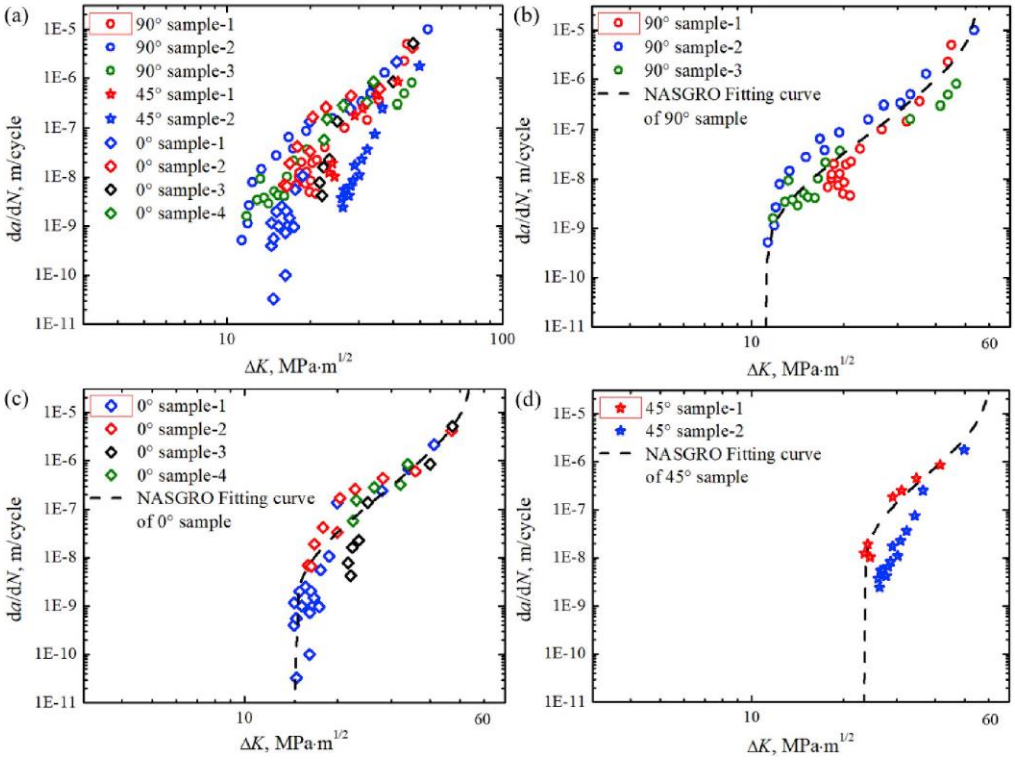

Figure 4-7: Fatigue crack growth rate data of a) all specimens, b) 90° specimens, c) 0° specimens and d) 45° specimens. (Xu *et al.*, 2019)

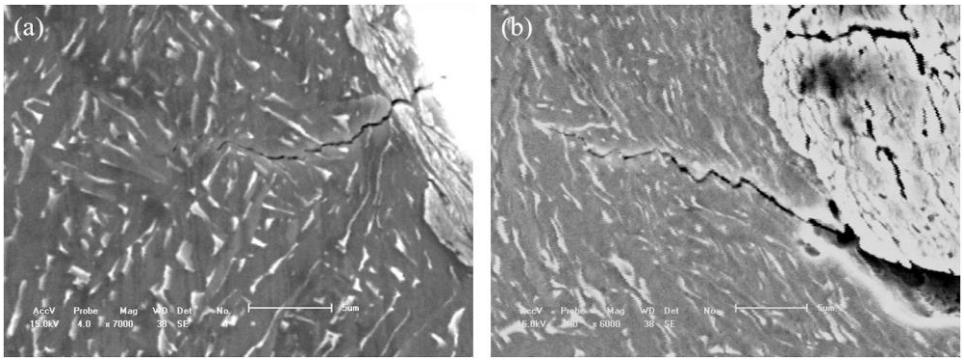

Figure 4-8: Crack path deviations in a) 90° and b) 0° specimen (Xu *et al.*, 2019)**.**

4.1.8 Kumar and Ramamurty (2019)

Kumar and Ramamurty (2019) investigated the microstructural optimisation through heat treatments for enhancing the fracture toughness and fatigue resistance of LPBF Ti-6Al-4V. Four heat treatments were employed. Two above and two below the β transus temperature. Furthermore, four combinations of layer thickness, t, and scan rotation, ϕ, were used i.e., t = 30 or 60 μm and ϕ = 67° and 90°. Manufacturing of specimens were performed on an EOSINT M280 LPBF machine using a Yb: YAG fibre laser. CT specimens were machined from the LPBF manufactured blocks. Two orientations were considered i.e., Z-X and X-Z. The ASTM E647 standard (ASTM, 2015) was employed for the load shedding technique and ΔK was reduced by 10% after every 0.2mm of crack length increments. Kumar and Ramamurty (2019) defined their threshold as $\leq 2 \times 10^{-9}$ m/cycle and designated it ΔK_0 and defined it as the threshold for fatigue crack initiation.

In all heat-treated, layer-thickness and scan-rotation variations, the ΔK_0, ranges from 7.1 to 8.4 MPa.m$^{0.5}$. This is a 34 – 56% increase in comparison to the AF specimens in their previous study, i.e. 5.3 – 5.8 MPa.m$^{0.5}$ (Kumar *et al.*, 2018). There were three noteworthy observations made (i) the ΔK_0 range for all heat treatments, layer thickness, scan rotation and build orientation was not significant, suggesting that the PBG mesostructure has an insignificant effect (ii) the applied heat treatments have a 34 – 56% increase in ΔK_0 in comparison to AF conditions and (iii) no significant anisotropy was observed. In their investigation on AF specimens, Kumar et al's (2018) examination of their threshold results indicated that it is colony size which has a direct influence on ΔK_0.

Kumar and Ramamurty (2019) found that by observing the maximum and cyclic plastic zone size (r_{max} and r_c respectively), it is the lath size which controls the near threshold fatigue behaviour. Their results are higher than those currently found within literature. For example, Leuders et al (2012) obtained ΔK_{th} (ΔK_0) as low as 1.4 MPa.m$^{0.5}$ in the AF condition and 6.1 MPa.m$^{0.5}$ in an annealed condition.

Kumar and Ramamurty (2019) provided great insight into the fatigue behaviour of LPBF Ti-6Al-4V. However, there are some concerns regarding the methodology of fatigue tests. They mentioned that the load shedding technique prescribed by the ASTM E647 (ASTM, 2015) was utilised, however, they designated ΔK_0 (ΔK_{th}) as $\leq 2 \times 10^{-9}$ m/cycle. According the ASTM E647 (ASTM, 2015), ΔK_{th} is for growth rates corresponding to 10^{-10} m/cycle when fitting a straight line through data of growth rates between 10^{-9} and 10^{-10} m/cycle. This means that the ΔK_{th} defined by Kumar and Ramamurty (2019) is an entire order of magnitude different from that defined by the ASTM E647 (ASTM International, 2013) standard. While it is understood that these standards are a guideline and one can deviate from it, Kumar and Ramamurty (2019) did not mention why they deviated from this after proclaiming that they were utilising the ASTM E647 (ASTM, 2015) load shedding technique.

Furthermore, both studies conducted by Kumar et al (2018) and Kumar and Ramamurty (2019) only an *R-ratio* of $R = 0.1$ was considered. Given that their AF and annealed ΔK_0 values are considered higher than what others have reported for AM as well as conventional Ti-6Al-4V, it would be of benefit to consider higher *R-ratios* as well. As previously mentioned in the background section as well as on the work of Leuders et al (2012), $R = 0.1$ is influenced by extrinsic properties. A question that now arises is; How much do extrinsic properties, such as RICC, contribute to the higher ΔK_0 observed and how would a more intrinsic ΔK_0 (at a high *R-ratio*) compare to it as well as those found in literature.

4.1.9 Tarik Hasib

The investigation on near-threshold FCGRs by Tarik Hasib et al (2020) considers the effect of build orientation as well as four conditions, i.e. AF and three heat-treated conditions. Two of the heat-treated conditions are below the β-transus (820°C and 950°C) and are also HIPed and the third is a β-anneal heat treatment (1020°C). The orientations are Z-X, X-Z and a 45° orientation. Testing was conducted using the load shedding technique in accordance to the ASTM E647 standard (ASTM, 2015). Crack measurements were monitored using a back-face strain gauge and a custom software used for data acquisition and machine control. Testing was conducted at $R = 0.1$, however, crack closure was measured using an offset compliance method.

No significant build orientation effects were observed. As expected, the AF conditions had the lowest ΔK_{th} and the higher the heat-treatment temperature was, the higher the ΔK_{th} was, as shown in Figure 4-9.

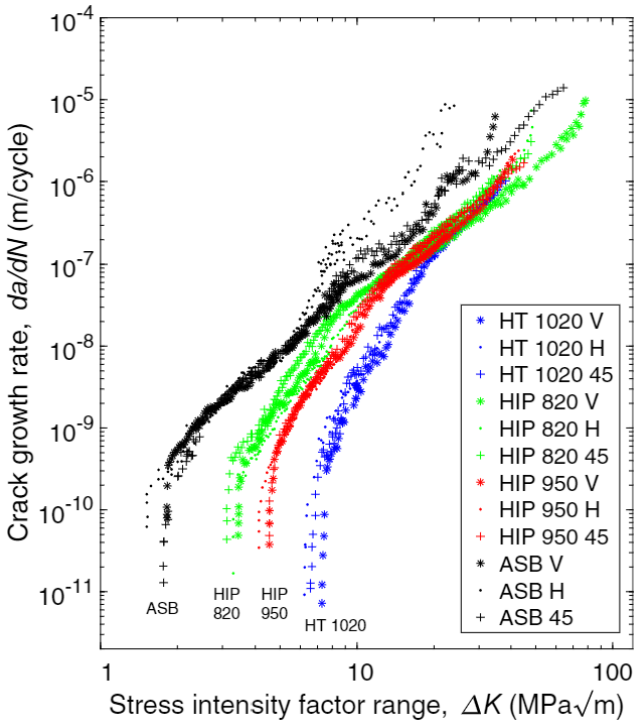

Figure 4-9: FCGR curve of the four conditions and three orientations (Tarik Hasib *et al.*, 2020).

It was found that as the grain size increased (from heat treatments), the ΔK_{th} increased, i.e. the AF condition had the lowest ΔK_{th}, then the HIPed 820°C condition, then the HIPed 950°C condition and the 1020°C condition was the highest. Furthermore, there was no measured crack closure in the AF condition, meaning that the crack was always open throughout the applied load. However, for the heat-treated specimens, the grain size increased with an increase in temperature, resulting in larger crack closure measurements. In addition, the measured fracture surface roughness also increased with an increase in grain size.

Tarik Hasib *et al.* (2020) further used a block slip band model which relates ΔK_{th} to the microstructural length. When using the $\Delta K_{eff,th}$, a more intrinsic ΔK_{th} is observed which is governed by slip transfer across grain boundaries due to the absence of crack closure, as shown in Figure 4-10. The model shows a linear correlation in the characteristic microstructural dimensions and $\Delta K_{th,eff}$.

It was concluded that the most critical factor governing ΔK_{th} was lath thickness. Lath thickness correlated to larger roughness-induced crack closure.

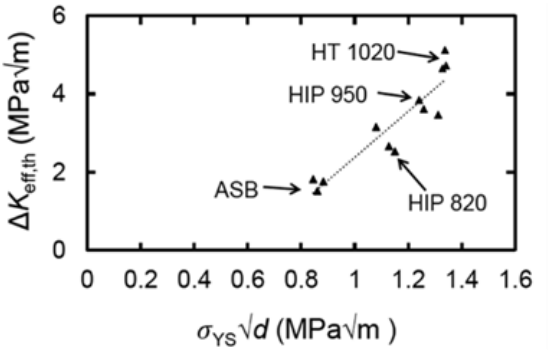

Figure 4-10: Blocked slip model of $\Delta K_{eff,th}$ relationship with microstructural size (Tarik Hasib et al., 2020).

4.2 Summary

There are numerous investigations which consider the fatigue behaviour of LPBF Ti-6Al-4V. A larger portion of these use the *SN*/Wohler approach, which has been shown to be greatly influenced by porosity and surface roughness. The literature addressed above largely focused on LEFM crack propagation techniques as these provide more design capabilities and provide more insight on various mechanisms that may influence fatigue behaviour.

The investigations briefly discussed above have shown various fatigue behaviours in LPBF Ti-6Al-4V. This variation seemed to span the entire FCGR curve, i.e. initiation (threshold), Paris regime and fracture toughness. The general recommendations from investigators are that LPBF Ti-6Al-4V requires an annealing heat treatment to reduce/eliminate residual stress, provide a better microstructure as well as HIP treatment to reduce porosity.

The following points highlight the gaps in the current knowledge derived from the above literature and established the need for the investigation carried out in this dissertation:

- While there are studies such as Leuders et al (2012), Kumar et al (Kumar *et al.*, 2018) and Kumar and Ramamurty (Kumar & Ramamurty, 2019) which investigated if ΔK_{th} does exist, these only considered R = 0.1. Currently, it is only Kunz et al (Kunz *et al.*, 2019) which went beyond R = 0.1 to reduce the crack closure effects and investigate a more intrinsic ΔK_{th} of LPBF Ti-6Al-4V. However, Tarik Hasib et al (Tarik Hasib *et al.*, 2020) measured crack closure which gave insight into a more intrinsic ΔK_{th}.

- In six of the studies presented above, i.e. Leuders et al (2012),Kumar et al (2018), Xu et al (2019), Kunz et al (2019), Kumar and Ramamurty (2019) and Tarik Hasib et al (2020), it is only in Leuders et al (2012), Kunz et al (2019),

and Tarik Hasib et al (2020) that the FCGR actually reached the 10^{-10} m/cycle threshold value as defined by the ASTM E647 (ASTM, 2015). This indicates a very limited amount of research towards ΔK_{th} of LPBF Ti-6Al-4V.

- Various fatigue behaviours have been observed, and generally one or a combination of the same reasons are given, i.e. the behaviour found is due to residual stress, microstructure and porosity. However, apart from porosity, the actual influence of these mechanisms has not been adequately investigated. The example of this is given below:

The point to highlight here is that on the one hand Van Hooreweder et (2012) concluded that the likely reason for low K_{IC} values is due to the brittle microstructure while on the other hand, Cain et al (Cain *et al.*, 2015) gave the likely reason to be residual stress. With regards to FCGRs, Van Hooreweder et (2012) had comparable FCGRs in conventionally manufactured Ti-6Al-4V and concluded that it was the AF LPBF microstructure that was giving rise to the comparable result. Furthermore, Edwards and Ramulu (Edwards & Ramulu, 2015) found that their FCGRs was slower than for that of conventionally manufactured Ti-6Al-4V but did not specify the reason for this, although microstructural reasons were alluded to. In addition, Leuders et al's (2012) AF FCGR is largely weaker (faster) than for conventionally manufactured Ti-6Al-4V, and concluded that residual stress was the primary cause of this. Cain et al (Cain *et al.*, 2015) seems to have a spread in FCGR results due to anisotropic behaviour and gave the reason as anisotropic residual stress behaviour in build orientations.

While all of these reasons are valid, a better understanding of these mechanisms' influence on fatigue behaviour is required. However, no significant study on the specific mechanisms' influence on fatigue behaviour has been investigated. As previously mentioned, a key element of investigating into LPBF Ti-6Al-4V is the qualification of these manufactured components for medical and aerospace applications. Thus, an in-depth understanding of the mechanisms influencing properties such as fatigue is required.

5 Motivation and objectives of thesis

The aim of this chapter is to motivate the investigation and to lay out the objectives It aims to use the summarising points of the previous chapter, to define aims and objectives, for the successful completion of the investigation.

5.1 Motivation

Ti-6Al-4V, along with other (α + β) titanium alloys, can have their mechanical properties manipulated depending on their microstructural state. Furthermore, due to the LPBF process, a unique microstructure is observed resulting in different mechanical properties to those observed in conventionally manufactured Ti-6Al-4V. In addition, adjusting process parameters for LPBF's manufacture can manipulate the microstructure, along with the amount of residual stress and level of porosity, all of which can influence the fatigue properties. This causes a difficulty in determining fatigue properties as there are many variables that influence them.

There are several standardised methods for obtaining fatigue properties such as the *SN* approach (fatigue life), load-shedding (ΔK_{th}) and constant load (Paris regime). Within the literature, a large portion of fatigue investigations regarding LPBF Ti-6Al-4V are conducted using the *SN* approach. The *SN* approach provides the measurement of the material's ability to resist crack initiation as result of fatigue loading. In this method, the cycles to failure contain crack initiation and propagation up to failure. However, it does not distinguish between initiation and propagation to failure. Furthermore, this approach is microstructurally sensitive. From a design perspective, this methodology avoids the problem of fatigue, resulting in parts which are designed in an overly conservative manner, prematurely replaced and thus expensive.

The second largest portion of fatigue information in the literature is the Paris regime. The Paris regime is a material property measuring a crack's ability to propagate through the material (until failure). This methodology is a "fitness for purpose" approach in which a certain amount of fatigue damage is acceptable within the part and requires periodic inspections (NDT testing) to decide on the fitness of the part. In addition, this crack propagation methodology tends to be less microstructurally sensitive than the initiation phase. While the load-shedding approach is the least investigated fatigue property, in recent years there has been an increase in the number of investigations considering this approach. This approach is a measure of the material's ability to resist crack propagation. It is a crack propagation method in which FCGRs are low enough for the crack to be microstructurally sensitive as well as influenced by shear mechanisms as it approaches crack initiation levels.

In the absence of defects and surface roughness, a crack can initiate due to the formation of persistent slip bands (Campbell, 2008). At the initiation stage, the

crack initiates parallel to the slip which is 45° to the principal stress at an approximate rate of 1nm per cycle (10^{-9} m/cycle) (Campbell, 2008). After sufficient crack growth, the stress state at the crack tip dominates the growth and alters the crack growth direction so that it is perpendicular to the loading direction. Furthermore, the crack initiation phase is said to be the dominant phase of the fatigue life cycle of a specimen. Some of the developed models on near-threshold FCGRs are based on the blockage of slip bands by grain boundaries (Tanaka *et al.*, 1981;Anderson, 2005). At the near-threshold crack growth rates (10^{-10} m/cycle), the crack is sensitive to microstructural features and tends to grow along crystallographic planes, resulting in faceted fracture zones on the fracture surface (Anderson, 2005). Investigating the near-threshold FGCRs can be used as a method to identify and gain insight into the fatigue initiation properties of the material.

As previously indicated in Section 4.2, one of the highlighted points is that within the literature on crack initiation there has been both anisotropic behaviour and non-anisotropic behaviour observed in the fatigue life approach. From the above paragraph, in which a description of crack initiation occurring along a slip at 45° to the principal stress, and the discussion in Section 3.4.2 describing the α' laths having a 45° affinity to the build direction, the orientation of the crack plane should be observed. Depending on the observed plane orientation, Ter Haar and Becker (2021) found that the α' affinity is not always 45° but also 0° and 90°. For process parameters which may cause α' laths to have a 45° orientation to the build direction, there is likely to be a difference observed on fracture surfaces for different build orientations (facet formation) in the near-threshold regime, i.e., different crack planes may cause more or less facet formation linked to crack initiation.

As previously mentioned in Section 3.4.1, it is understood that large tensile residual stresses on the surface of the material accelerate the initiation phase of the fatigue life. This is particularly true when other factors that raise stress, such as defects near the surface and surface roughness, are present. However, residual stresses inherent to LPBF processes are tensile on and near the surface and compressive in most of the through thickness. This means that from a fatigue life approach perspective, in which initiation comprises the majority of the life, the tensile stresses on the surface would be more influential than the through thickness' compressive stresses on fatigue life. From a fatigue crack growth perspective, the crack front will experience both tensile and compressive residual stresses throughout its propagation. Some studies on welds have shown that residual stress alters the *K* values which in turn alters the effective *R-ratio* (Beghini & Bertini, 1990; John *et al.*, 2003). In addition, near-threshold FCGRs experience a phenomenon known as crack closure, as described in section 3.3.7. If the residual stress was also to alter the *R-ratio* of LPBF produced Ti-6Al-4V, then it should be observable within the crack closure phenomenon when comparing specimens which contain residual stresses to those that have been stress relieved. As it currently stands, the link between residual stress mechanisms and microstructural morphology mechanisms and their influence on fatigue properties is not well established.

Considering the above, this investigation is concerned with the mechanisms which influence fatigue properties, i.e., what is the effect of microstructure, residual stress and closure mechanisms on fatigue properties. It is believed that by investigating these mechanisms, more insight into the fatigue properties of Ti-6Al-4V will be obtained. The methodology also includes using various build orientations as well stress ratios to consider orientations and closure effects. This was the first investigation on LPBF Ti-6Al-4V to consider crack closure effects.

5.2 Central hypothesis

It is commonly known that the inherent properties of LPBF, i.e., microstructure, residual stress and porosity influence the fatigue properties of LPBF Ti-6Al-4V. However, the specific mechanisms of these have not been adequately investigated, resulting in contradictory conclusions being drawn from various research. This work aims to identify, for the first time, the mechanisms of these inherent LPBF properties as stated in the hypothesis:

If variable R-ratio near-threshold fatigue crack growth rate tests are conducted, then the mechanisms of residual stress, LPBF microstructure's and change in microstructural morphology's influence on fatigue behaviour may be identified. This method reduces extrinsic influencing factors, resulting in a true near-threshold value which can be used for structural integrity purposes.

5.3 Thesis objectives

The objectives of this investigation are aimed at understanding the mechanisms influencing the achievable fatigue properties of LPBF produced Ti-6Al-4V. The objectives can be divided into five categories in order to investigate the respective mechanisms.

1. The first objective is to obtain a near intrinsic ΔK_{th}. This requires variable *R-ratio* testing to reduce/eliminate any closure effects that will result in premature ΔK_{th} values.
2. The second objective requires the variable *R-ratio* tests to be conducted in three build orientations, namely Z-X, X-Z and X-Y.
3. The third objective involves investigating the effect of crack closure on near-threshold behaviour.
4. The fourth objective is to identify the effect of residual stress. This objective requires a comparison between AF and SR conditions. In addition, with the reduction in residual stress, a better observation of the LPBF type microstructure's influence on fatigue crack behaviour is required.
5. The fifth objective is to investigate the improvement in ΔK_{th} after the duplex anneal (DA) heat treatment. Of particular interest between these two conditions is the difference observed in the global "closure free" region as this is more intrinsic to the material's microstructural conditions. This will

give a better understanding of the mechanisms which cause an improvement on near-threshold behaviour.

6. The sixth objective is to identify the role of the unique LPBF Ti-6Al-4V AF microstructure on fatigue behaviour.

5.4 Scope and limitations

5.4.1 Specimen Manufacture

The specimens used in the investigation are limited to those manufactured via the LPBF technique. In particular, the EOSINT M280 is used in the current investigation and is ISO 13485 certified (ISO, 2016). The ISO 13485 certification is for medical devices – quality management systems – requirements for regulatory purposes. Standard process parameters are selected with no intention of optimising parameters for best near-threshold fatigue crack growth behaviour. The selected geometry of specimens is CT.

5.4.2 LPBF material

During the LPBF printing technique the specimen manufacture is liable to various printing defects which typically result in some form of a porosity defect. Defects have been shown to affect mechanical properties. However, the focus is on identifying the influencing mechanisms of residual stress and LPBF microstructure on near-threshold FCGRs.

5.4.3 Structural integrity

While the near-threshold FCGR ΔK_{th} is the value that can be used as a measure of structural integrity, from a fatigue perspective, the focus of the investigation is not specifically the ΔK_{th} value. Rather, it is using a particular method (load-shedding) for obtaining ΔK_{th} to identify the influencing mechanisms.

5.4.4 Threshold testing

The near-threshold testing is conducted in a mode I loading condition. Furthermore, a “quasi”-constant frequency was applied during testing. This means that at the beginning of a test, when FGCRs are in the range of ~ 10^{-8} m/cycle, the frequency is slowly increased from 10Hz to between 60-80Hz and then remains constant for the remainder of the test. However, in-service dynamically loaded components do not only undergo mode I loading nor do they typically experience a constant frequency. Mixed mode conditions and variable frequencies have further adverse effects on the fatigue behaviour of a component.

5.4.5 Long crack

Cracks can typically be divided into three length categories, i.e. a long crack, a short crack and a microcrack. The current investigation only captures fatigue data from the long crack regime and makes observations of microcracks.

5.5 Summary

The above chapter detailed the motivation and objectives of the investigation. It highlighted the importance of establishing a link between the influencing mechanisms of residual stress and AF and SR microstructure on fatigue behaviour. Five objectives were introduced which are aimed at understanding the influencing mechanisms on fatigue behaviour. Thereafter, the scope and limitations were identified.

6 Materials and methods

6.1 Introduction

The previous chapters gave a foundational background to assist in understanding the concept of fatigue. They went further by considering the current literature on LPBF Ti-6Al-4V and fatigue, which establishes the requirement of an experimental investigation in order to meet the aims of the project. The current chapter introduces the experimental details and procedures of the investigation.

This chapter is divided into three parts. The first part considers the information surrounding specimen fabrication, i.e. material, printing equipment and specimen design. Thereafter, the fatigue testing procedure, testing equipment as well as certain critical parameters are detailed. The final part explains miscellaneous/secondary testing such as the various microscopy methods employed, EBSD, and density testing.

6.2 Laser powder bed fusion

6.2.1 Specimen material

The material used in this investigation was Ti-6Al-4V ELI powder. The powder was obtained from TLS Technik GmbH & Co. Powder particles were gas atomised to have a spherical shape and a size distribution of the 10^{th} and 90^{th} percentile which ranged between 23 and 46 μm in diameter, respectively. Using inductively coupled plasma optical emission spectroscopy, the chemical composition of the powder was obtained and is shown in Table 6-1. This composition conforms to the ASTM F3001 “standard specification for additive manufacturing of titanium-6 aluminium-4 vanadium ELI (extra low interstitial) with powder bed fusion” (ASTM, 2014).

Table 6-1: Chemical composition of Ti-6Al-4V ELI powder used in this investigation

Element	Ti	Al	V	Fe	N	O
Chemical composition (wt. %)	Balance	6.34	3.94	0.25	0.006	0.082
ASTM F3001 (ASTM, 2014)	Balance	5.5-6.5	3.5-4.5	0.25	.05	0.13

6.2.2 Specimen manufacture

The manufacturing of specimens was conducted on an EOSINT M280 (EOS GmbH) LPBF printing machine. This machine is equipped with a Yb (Ytterbium) fibre laser of wavelength 1060 – 1100 nm and nominal power of 200W (EOS, 2010). The laser has a Gaussian power distribution and a focal length of 410 mm (EOS, 2010). This machine has a build area of 250 x 250 x 325 mm and platform heating capabilities. As previously mentioned, the printing machine used in this investigation is ISO 13485 certified (ISO, 2016).

The standard parameter settings for Ti-6Al-4V were utilised for this investigation. Parameters included a layer thickness of 30 μm, laser speed of 600 mm/s, laser spot diameter of 100 μm, hatch space of 80 μm and a 175 W Yb-laser setting. Before manufacture, air and moisture is removed from the chamber. Before the air and moisture is removed, the oxygen content is approximately 20%. Thereafter, the chamber is filled with argon, which has purity level of 99.999% with impurities < 10 ppm. During manufacture, the oxygen level was kept at approximately 0.05%. The standard parameter divides the layer into rows with a width of 5mm and each row is scanned individually. A scan rotation of 67° per layer was utilised and no base preheating was in place.

6.2.3 Specimen design

The specimens manufactured for this investigation used the CT specimen design. The CT specimen design follows the ASTM E647 standard (ASTM, 2015). Three orientations were built, namely the XZY, ZXY and XYZ, as previously shown in Figure 4-1 in Chapter 4. These are referred to as Z-X, X-Z and X-Y for the remainder of the dissertation, respectively. The three orientations are selected based on a few criteria:

(i) The crack planes have differences, i.e. the Z-X orientation has a crack plane parallel to build layer, while the X-Z and X-Y has crack planes perpendicular to the build layer.
(ii) The crack propagation in the Z-X orientation experienced an equiaxed PBG while the X-Z and X-Y experienced an elongated PBG structure.
(iii) The per unit area the crack front in the X-Z orientation consumed less PBG structure than the X-Y orientation. This can be seen in Figure 8-3 within Chapter 8.
(iv) The dominant lath angles for the Z-X orientation crack plane were 0° and 90°, whereas in the X-Z and X-Y the dominant lath angle was 45°.
(v) Residual stress levels in all three orientations differed. The crack plane of the Z-X orientation has the highest stress then the X-Z and then the X-Y.

These reasons give a variety of variables such as different PBG structures, different dominant lath angles and different amounts of residual stress within the respective

crack planes, allowing a more critical analysis of the influencing mechanisms. All specimens were wire cut off the base plate in the as-built condition and no base plate heating was implemented.

While three orientations have been selected, it is possible to have more crack planes such as Z-Y, Y-Z and Y-X. However, under the specific scanning strategy employed, these crack planes are redundant. As previously mentioned, a multidirectional scanning strategy was employed in which the scan rotation changed by 67° in each layer i.e., rotation about the normal axis of the XY build plane. As a result of this rotation, the Z-X and Z-Y are the same crack planes, X-Z and Y-Z are the same crack planes, and X-Y and Y-X are the same crack planes.

The specimens were built as individual near-net-shape CT specimens on the baseplate as opposed to large blocks where multiple CT specimens are cut off at different locations. This was specifically done to minimise any residual stress effect that may be caused by build height and geometry. Furthermore, this also ensures that the crack plane of different specimens of the same build orientations were built at the same height as well as have the same residual stress.

The CT specimens were cut off the base plate on a GF Agie Charmilles CA20 EDM machine using a 250 µm wire diameter. Thereafter, the specimens were divided into three groups based on their heat treatments, i.e. i) as-fabricated (AF), ii) stress relieved (SR) and iii) duplex anneal (DA) which leads to a bi-modal microstructure. The heat treatments were as follows:

- As-fabricated – no heat treatment
- Stress relief – 480°C for eight hours followed by a furnace cool
- Duplex anneal – 940°C for two hours. Furnaced cooled to 910°C and held for eight hours followed by a water quench. Aged at 750°C for two hours with a furnace cool. This produces the bi-modal microstructure.

Heat treatments were conducted in a 5 kW Gallenkamp muffle furnace with an inbuilt temperature controller. For a more accurate temperature reading, a type-K thermocouple was inserted into the furnace.

After the heat treatments, specimens were surface ground to remove oxidation and alpha case hardening produced during the heat treatments. Following the necessary heat treatments, the specimens for this investigation were machined to nominally have dimensions of $W = 50$ mm, $B = 6.5$ mm and $a_n = 10$ mm. Holes with a diameter of 12.5 mm were drilled for a sliding fit.

The specimens were then further ground and polished using a Struers Planopol-2 Pedemax-2 automatic grinder, polishing and lapping machine. This process started off using 80grit silicon carbide paper and incrementally increased grit number up

to 1200 grit, to further grind and smoothen the surfaces. The polishing step used a 70% OPS and 30% H_2O_2 solution on a chempad polishing cloth for ten minutes. This was followed by a three-minute water cycle and resulted in a "mirror-like" finish.

6.3 Testing procedure

6.3.1 Testing equipment

The near-threshold FCGR testing equipment was an Instron ElectroPuls E3000 (Instron, Norwood, United States). This is an all-electric test instrument which has both dynamic and static capabilities. The dynamic performance of the equipment is capable of exceeding 100Hz (depending on stiffness of setup, loading required, amongst others). A 5 kN dynacell load cell was utilised but is restricted to approximately 3 kN for dynamic testing.

6.3.2 Test method

Near-threshold FCGR testing conforms to the ASTM E647 standard (ASTM, 2015). The testing procedure utilised both the constant *R-ratio* and K_{max} load shedding techniques. Load was shed at a -0.08mm^{-1} gradient as suggested by the standard. Fatigue testing was conducted on the Instron Electropuls E3000 dynamic tester and used frequencies ranging between 60 - 80Hz. Investigations conducted by Wanhill (1974) and Boyce and Ritchie (2001) showed a negligible effect on ΔK and crack growth rate for frequency vitiations at 0.1, 50 and 1000 Hz. In this investigation, it was assumed, based on the works of Wanhill (1974) and Boyce and Ritchie (2001), that the frequency range of 60-80 Hz will have a negligible effect on the ΔK and crack growth rate results. For the load shedding technique to be implemented, the Instron *da/dN* software was utilised. In addition, for the load-shedding technique to be utilised, a feedback loop of crack length is required by the software to correctly shed the load (at -0.08 mm^{-1}). The crack length was measured using the crack mouth opening displacement (CMOD) compliance technique and periodically checked with visual measurements.

A concern with the load-shedding method was that it is affected by crack closure as well as by the actual load-shedding technique. Premature crack closure results in larger near-threshold FCGRs than what is truly intrinsic to the material. Therefore, for this method to be utilised effectively, one needs to reduce/eliminate these closure effects to obtain the true intrinsic ΔK_{th}. In terms of the load-shedding technique, the issue lies in that after an incremental crack length, the load needs to be incrementally reduced until ΔK_{th} is obtained. However, this makes the method easily susceptible to a plastic build-up/work-hardening region in front of the crack tip which can retard and even arrest the crack, resulting in a premature "ΔK_{th}". This is especially true when crack increments are only achieved optically, and load reduction occurs manually by the user. In order to reduce/bypass this issue, there

are automated methods such as potential drop and compliance methods which can continuously measure the crack and reduce the load accordingly as well as eliminate the possibility of premature crack arrest. In this investigation, the compliance technique was utilised due to the availability of the equipment for this technique.

The R-constant type tests were conducted for test *R-ratios* of 0.6 or less and K_{max} testing occurred for *R-ratios* above 0.6. Figure 6-1 shows how the R-constant (K_{max} and K_{min} varying) and K_{max} (R and K_{min} varying) approach differs with respect to crack closure. For detailed information regarding crack closure, the reader is directed to Section 3.3.7. As can be seen in the R-constant approach from Figure 6-1, as the threshold test progresses, K_{max} and K_{min} reduce such that one or both parameters may become susceptible to crack closure. In the K_{max} approach, however, K_{min} increases throughout the test into a region in which it won't be susceptible to crack closure effects (extrinsic). Typically, to obtain ΔK_{th} at high *R-ratios*, the K_{max} approach is used.

The FCGR data was processed using MATLAB. While the ASTM E647 (ASTM, 2015) defines ΔK_{th} at 10^{-10} m/cycle, in this investigation, values below this level as the FCGR behaviour should also show the typical threshold asymptotic behaviour as seen in Figure 3-13.

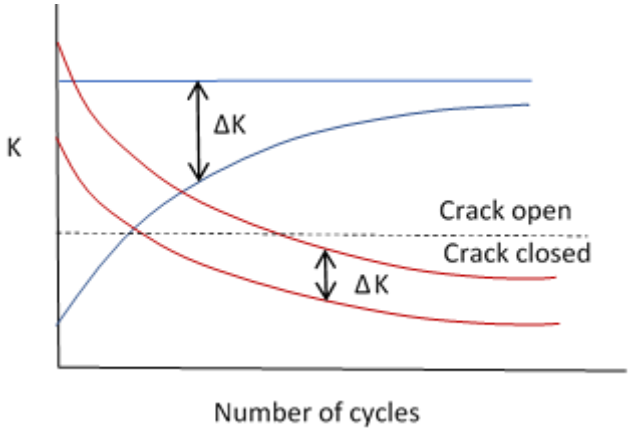

Figure 6-1: *R*-constant (red) versus *Kmax* (blue) approach with respect to crack closure.

6.4 Microscopy

The microscopy work consisted of light microscopy for microstructural analysis and SEM for crack and fractography analysis.

Preparing the specimens for light microscopy work, followed the same procedure set out in section 6.2.3, i.e. grinding and polishing to a mirror like finish. Light microscopy was conducted on an Olympus GX51 light optical microscope

(Olympus Corporation, Tokyo, Japan). Specimens were cut using a Buehler IsoMet low speed micro-slicer. The Micro-slicer was used as it has a diamond tipped blade which does not raise the temperature of the specimen significantly to cause any microstructural distortion. Specimens were then etched using Kroll's reagent of the following composition:

- Distilled water – 100 ml
- HNO_3 – 6 ml
- HF – 3 ml

The etching duration was typically between 5-8 seconds. However, the quality of the etching was investigated visually and by experience which governed whether or not more time under the etchant was required. Individual grain measurements were made using Stream Essential software. A line-intercept method was used to measure the maximum and minimum grain widths with features in Matlab Image processing Toolbox.

Crack profile and fractography analysis were conducted on a Zeiss Merlin SEM (Zeiss, Oberkochen, Germany) with the use of back-scattered electron detectors. For the crack profile investigations, both back scatter detectors as well as secondary electrons were utilised and using a working distance range typically between 6 – 8 mm, the current running through the probe was selected to be 10 nA. The electron high tension was set to 10 kV. For fractographic investigations, similar working distance ranges were utilised as the crack profile investigations, but only secondary electrons were used, not back scatter detectors. The current through the probe was 250 pA with an electron high tension of 10 kV.

EBSD imaging was obtained using two different systems. For the AF and SR conditions it was obtained on a JSM-7001F SEM (JEOL, Tokyo, Japan) with Oxford Instruments HKL-channel 5 software. For the DA condition it was obtained on a Nova 600 NanoLab dual beam SEM (FEI, Oregon, United States). The code used to analyse the EBSD data was initially written by Simonelli (Simonelli, 2014) and later modified by Ter Haar (Ter Haar, 2017). The code makes use of the MTEX toolbox function in MATLAB. This allows for texture analysis of the microstructure in the form of EBSD and pole figure data.

6.4.1 Residual stress

Residual stress measurements were taken on the crack planes of all three orientations, in both of the AF and SR conditions. The contour method, which implements the superposition principal by Bueckner (Bueckner F. H., 1958), was employed. The superposition principal allows for macroscopic residual stress measurements over a region of interest (crack planes).

To implement the contour method, specimens are required to be cut in half along their respective crack planes. Specimens were wire cut on an EDM machine GF Agie Charnilles CA20 (GF Machining Solutions, Biel, Switzerland) using a 250μm wire diameter. The crack plane's contour measurements were conducted on a LK Altera 15.7.6 CMM (Nikon Metrology, Tokyo, Japan) using a Renishaw TP200 touch-trigger probing mechanism (Renishaw, Wotton-under-Edge, United Kingdom). The crack plane contour surfaces were measured in rows and columns with each data point approximately 150μm apart. This approximated to 10000 data points per measured surface. A plane of the specimen's perimeters was also measured so as to realign opposing surfaces for a more accurate stress measurement.

Several steps were required to evaluate the residual stress from the crack plane's contour measurements. The contour measurements were processed using a MATLAB script. The steps to evaluate the residual stress were implemented from Prime and DeWald (2013) and are summarised as follows:

(i) Crack plane contour alignment – the two contour surfaces of one specimen's crack plane are considered to be a mirror image of each other through the crack plane. The two cut surfaces are to be set on the same co-ordinate frame (based on the crack plane in this case). This is done via a rigid body translation and rotation until the two surfaces are facing each other so that they are now mirror images of each other with the crack plane being the "mirror". The perimeter planes allow for the two surfaces to be angled correctly with respect to the crack plane. A zero point was chosen with respect to the specimen breadth midline, the load line, and the average surface height. This allows for any measurements in deviation to be as a result of internal stress deformation as opposed to any alignment issues. The deformed surfaces are "forced back" to a non-deformed state to calculate the stresses

(ii) Shear removal – the shear stresses on the cut surfaces are antisymmetric. By averaging the two cut surfaces, the shear stresses were cancelled out. This left only stresses normal to the crack plane to be computed.

(iii) Noise reduction – there will be some noise in the data which can be attributed to measurement error and surface roughness from the EDM cut. This will affect the residual stress calculation. In order to reduce the noise in data, the contour data was averaged from using data points at 150 μm apart to 500 μm apart. This was smoothed by using a locally weighted linear regression with a span of 10% resulting in ~ 1200 data points (as opposed to initial ~ 10000). This processed data was then used for calculating the residual stress.

A finite element method was used to model one half of a CT specimen. A linear-elastic isotropic material was assumed with properties of E = 116 GPa and ν = 32. This resulted in 66360 hexahedral elements and 219600 degrees of freedom. The height measurements were set as a boundary condition on the cut CT surface while

the lower CT specimen's boundary was fixed. The deformation that is measured is now, computationally, returned to a X-Y surface. The stresses required to return the deformed surface to a X-Y surface is the calculated residual stress in the respective crack planes.

In order to estimate the bias and variance of the described method, the contour method's measurements were applied twice in the AF condition. The difference between these measurements was computed using a pseudorandom Gaussian noise of a 5 μm profiler certainty. As a result of the variance errors such as misalignment, measuring error and unaccounted errors, the estimated bias is 9.4 MPa, the variance 40 MPa and the root mean square error is ~ 50 MPa.

6.4.2 Density testing

Density testing conformed to the ASTM B962 "standard test methods for density of compacted or sintered powder metallurgy (PM) products using Archimedes' principle" (ASTM, 2014). This method makes use of the Archimedes principle of liquid displacement. Measurements were made on a Sartorius Quintix® density measuring kit with a resolution of 0.1mg.

The density of the specimen was then compared to the full density of Ti-6Al-4V of 4.43 $g.cm^{-3}$ (Donachie, 2000). All specimens used in this investigation had a relative density equal to or greater than 99.7 %.

6.4.3 Tensile test

Tensile tests were implemented according to the ASTM E8 "standard test methods for tension testing of metallic materials" (ASTM, 2021) and were conducted on the Criterion Model 44 machine (MTS, Minnesota, USA). The crosshead displacement rate was 0.13mm/min. The specimen gauge diameter was 5 mm and gauge length was 25 mm.

6.5 Summary

This chapter provided the information regarding the experimental methodology behind the investigation.

The investigation made use of Ti-6Al-4V ELI powder which conformed to the ASTM F1580 "standard specification for titanium and titanium-6 aluminium-4 vanadium alloy powders for coatings of surgical implants" (ASTM, 2018). CT specimens were manufactured on an EOSINT M280 LPBF machine using standard settings. Three orientations, namely: Z-X, X-Z and X-Y considered in three conditions i.e. AF, SR and DA.

The near-threshold FCGR testing conformed to the ASTM E647 standard (ASTM, 2015). Tests were conducted on an Instron ElectroPuls E3000 and utilised the load shedding technique for both constant-R and constant K_{max} methodologies. Various *R-ratios* were implemented, and crack lengths monitored using the compliance technique.

The microscopy work consisted of the use of light microscopy, SEM as well as EBSD. Information such as microstructural analysis, crack profiles, fractography and pole figures were obtained.

Residual stress measurements were evaluated using the contour method. This required CMM measurements, specimen alignment, shear removal, noise reduction and the construction of a FE model.

Density and tensile tests were conducted according to the ASTM B962 (ASTM, 2014) and ASTM E8 standards (ASTM, 2021), respectively.

7 Results

7.1 Introduction

The chapter starts off with the microstructural characteristics of AF, SR and DA conditions. This is followed by the residual stress results for the AF and SR specimens. The next sub-section presents the fatigue crack growth rate threshold results for the AF, SR and DA conditions, respectively, in all three orientations. The final section details the fractographic observations.

Chapter 7, Results, and Chapter 8, Discussion, are based on the results of this investigation.

7.2 Microstructure

The three different conditions, AF, SR and DA are depicted in Figure 7-1. Figure 7-2 shows the crystallographic orientations maps and reconstructed PBGs of the AF condition. The crystallographic texture of the PBGs has a strong affiliation to the $\langle \mathbf{001} \rangle_{\boldsymbol{\beta}}$ axes which is parallel to the Z-axis. This is also observed in the (001) pole figure plots in Figure 7-2 (e) and (f). Considering the morphological texture of the PBGs, it is also considered to be morphologically textured in the Z-axis as the columnar-shaped grains are parallel to the Z-axis.

Typically, there are two distinct shapes of the PBG when viewed in two different planes. In the XY plane, i.e. Z-X crack plane, the PBG shape is equiaxed in geometry and approximately 80μm in diameter. In the ZX/ZY plane i.e. X-Z and X-Y crack planes, a columnar structure is observed with the length orientated in the Z-axis direction (build direction) with an approximate length of 200μm and width of 80μm. As a result of the SR and DA heat treatments both being below the β – transus level, no significant morphological change occurs to the PBG. Furthermore, no signs of grain boundary α was observed in the DA condition. The PBG morphological texture in the XY plane is governed by the hatch distance and scan strategy while the ZX/ZY plane is governed by hatch distance, scan strategy, thermal gradient as well as interface velocity. The crystallographic texture of the PBG is governed by the thermal gradient.

The AF LPBF's microstructure in Figure 7-1 (a), contains martensite (needle-shaped transformed β) which is comprised of α' laths typically between 0.5 and 1 μm thick (Vrancken, 2016). Ter Haar and Becker (2018) observed, similar to Yang et al (2016) a hierarchical structure consisting of primary (α_p), secondary, ternary and quartic α' grains. A schematic of the hierarchical α' structure is shown in Figure 7-3. These were measured to have minor axis lengths of 1 – 3 μm, 100 – 900 nm, 10 – 90 nm and less than 10 nm for primary, secondary, ternary and quartic α' grains, respectively. It is observed that there is a strong uniformity for α_p laths to be

oriented at approximately 45° in the Z-direction (build direction), while in the XY plane, the α_p laths do not seem to have such an affinity to the 45° orientation but rather to 0 and 90° (Ter Haar & Becker, 2021).

It is also observed that the α' laths have different aspect ratios when observed in the Z-X or X-Z and X-Y orientations (Ter Haar & Becker, 2021). In addition, the α_p lengths (major axis) span the width of the PBG, as shown in Figure 7-3. The remaining lath orders span the bridge order lath in the hierarchy. The PBG and α' lath shave at least two connections, i.e. a morphological connection and a crystallographic connection. Morphologically, the lath angle affinity may be caused by the combination of $\langle 001 \rangle_\beta$//Z-axis and the $\{334\}_\beta$, $\{344\}_\beta$ habit plane formation of martensitic laths, which causes an approximate 45˚ orientation of primary alpha laths, as shown in Figure 7-3 (Ter Haar & Becker, 2021). This means that the α' lath angle morphology is governed by the PBG crystallographic texture. Crystallographically, the PBG (BCC crystal) and α' (HCP crystal) are connected through the BOR where the $\{110\}_\beta$//$\{0001\}_{\alpha'}$ and $<111>_\beta$//$<1120>_{\alpha'}$ are the preferential crystallographic directions (Kumar *et al.*, 2018; Simonelli, 2014). It should be noted that there are twelve possible variants, as described by Simonelli (2014), and these twelve have also been observed in the LPBF microstructure of this investigation. It is through the BOR that the α_p obtains the fairly weak crystallographic texture. Furthermore, it was found that six of the twelve variants comprised of approximately 70% of the variants observed (Simonelli, 2014). As a result of these twelve possible variants, the LPBF AF microstructure is considered to have a weak crystallographic texture.

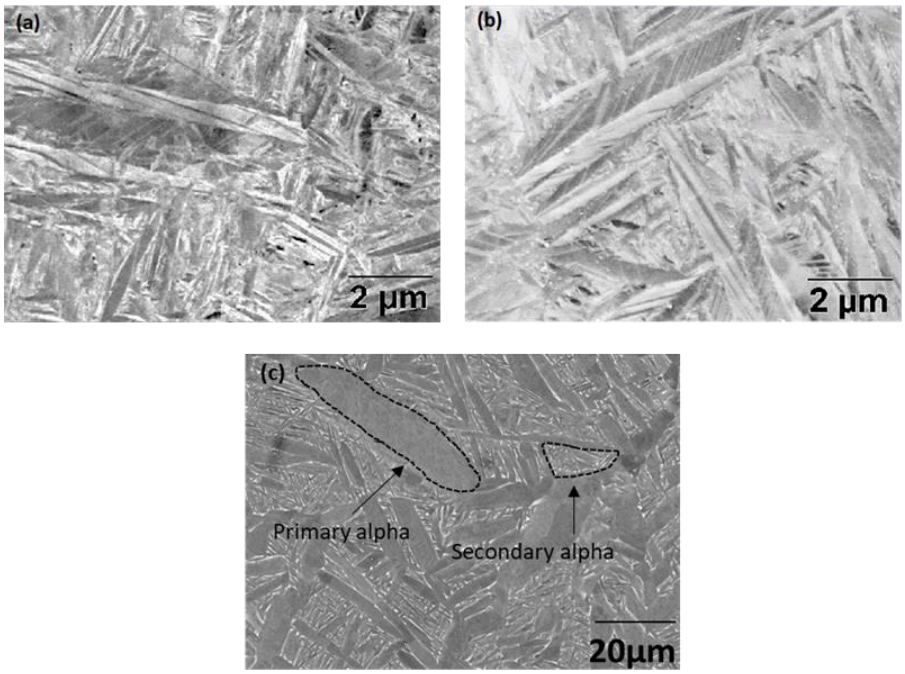

Figure 7-1: Micrographs of (a) AF, (b) SR and (c) DA conditions

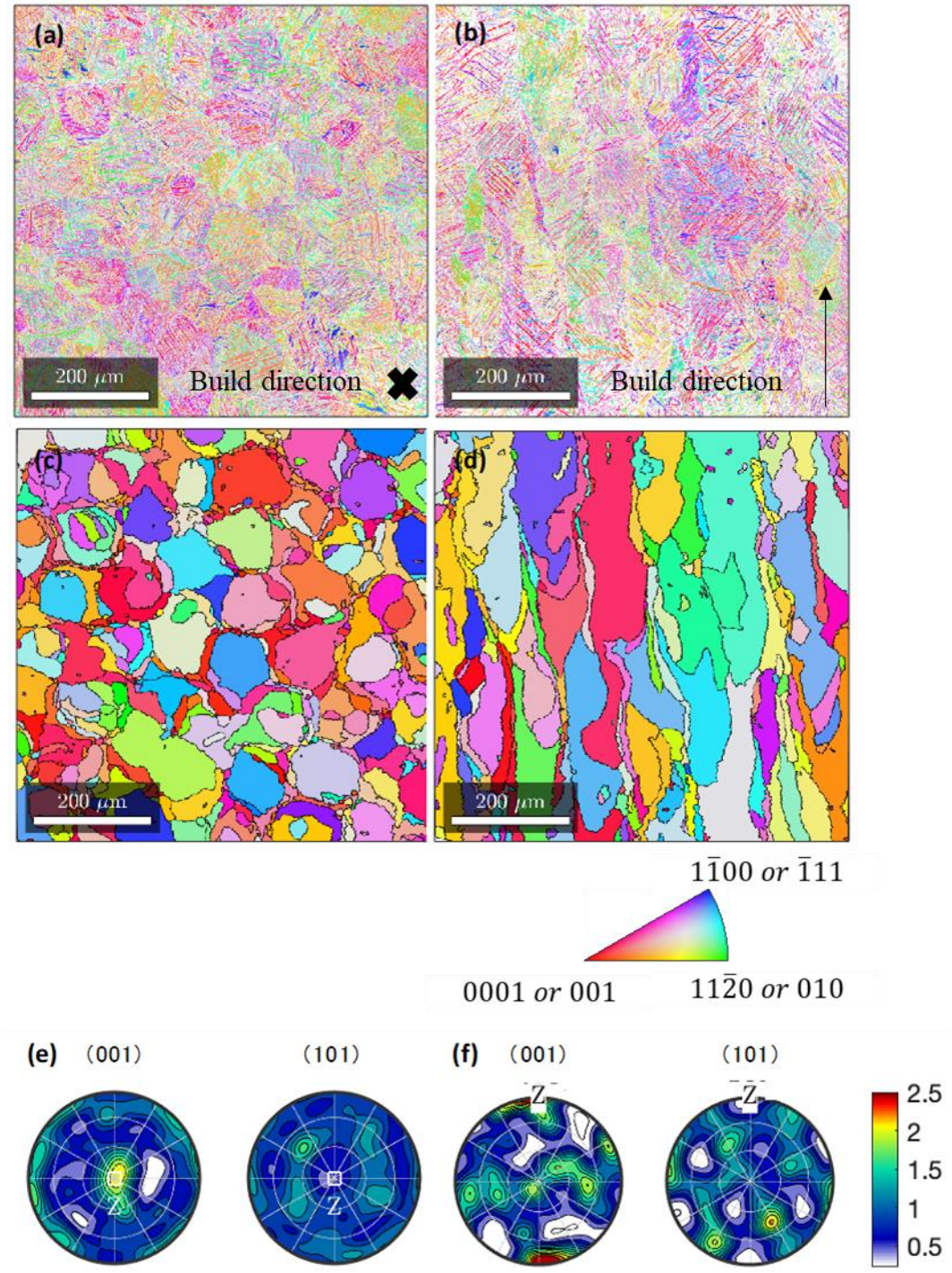

Figure 7-2: EBSD plots of (a) XY and (b) ZX plane with the build directions indicated. The corresponding PBG reconstructions are shown in (c) and (d), respectively. Pole figures of PGB's reconstruction are in (e) the XY and (f) the ZX plane.

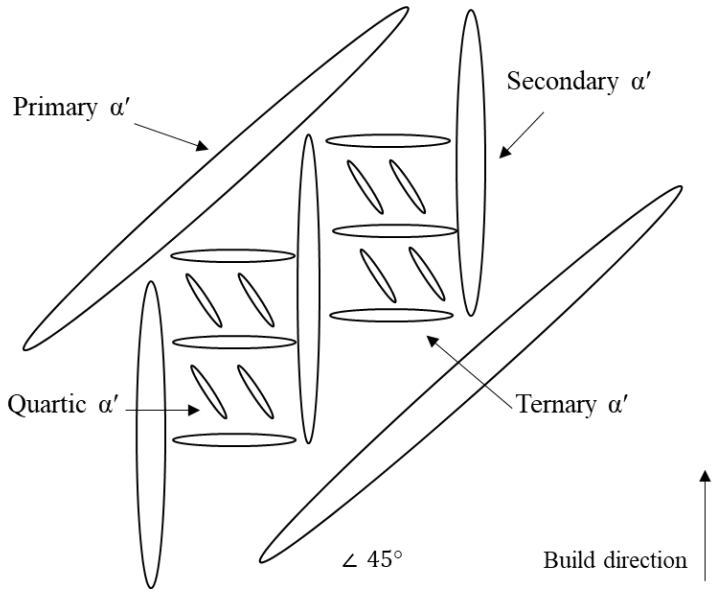

Figure 7-3: Schematic of the hierarchical α' structure, with build direction indicated

After SR, a decrease in the residual stress was measured (discussed later) but with no appreciable change in AF and SR microstructure. This can be seen, qualitatively, in the SEM micrographs in Figure 7-1 (a) and (b). Further observations of a XRD measurement's comparison in Figure 7-4 between AF and SR, shows that β-phase was not detectable. There is, however, a peak shift as well as less peak broadening in the SR compared to the AF condition. The peak shift results in the transformation of α' to α (not completely) and the peak broadening in the relaxation of residual stress and/or dislocation density.

After applying the duplex anneal in the high solid solution temperature region (SSTR), the remaining microstructure is considered to be bi-modal, as shown in Figure 7-1 (c). Once the first annealing step at 910°C for eight hours is complete, a water quench cooling is applied. This results in an initial bi-modal microstructure consisting of α in a matrix of α'. However, the α' is not desired and thus a second anneal in the low SSTR is applied. This results in the α' decomposing into (α + β) lamellae. The initial high SSTR anneal shows that the primary and secondary α' seem to be favoured over the tertiary and quadric α' grains when transforming into lamella α in a matrix of β (Ter Haar & Becker, 2018). The tertiary and quadric α' grains transform into β. The water quench step then transforms the β (from tertiary and quadric α') into α'. As previously mentioned, the newly formed α' is undesirable and is decomposed into secondary (α + β) lamellae with the second annealing step in the low SSTR. The median grain width for primary α is approximately 10 µm and 1 µm for secondary α. The initial needle like primary α' now has a more globular to coarse elongated lamella's α grain morphology. EBSD and pole figures are shown in Figure 7-5 and Figure 7-6.

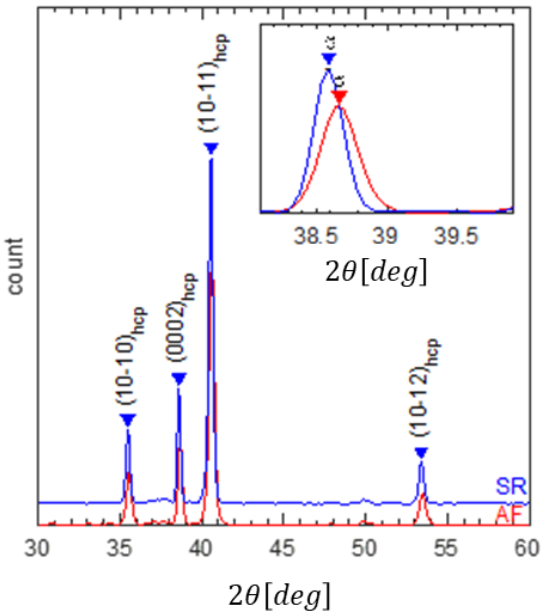

Figure 7-4: XRD plots of AF and SR state.

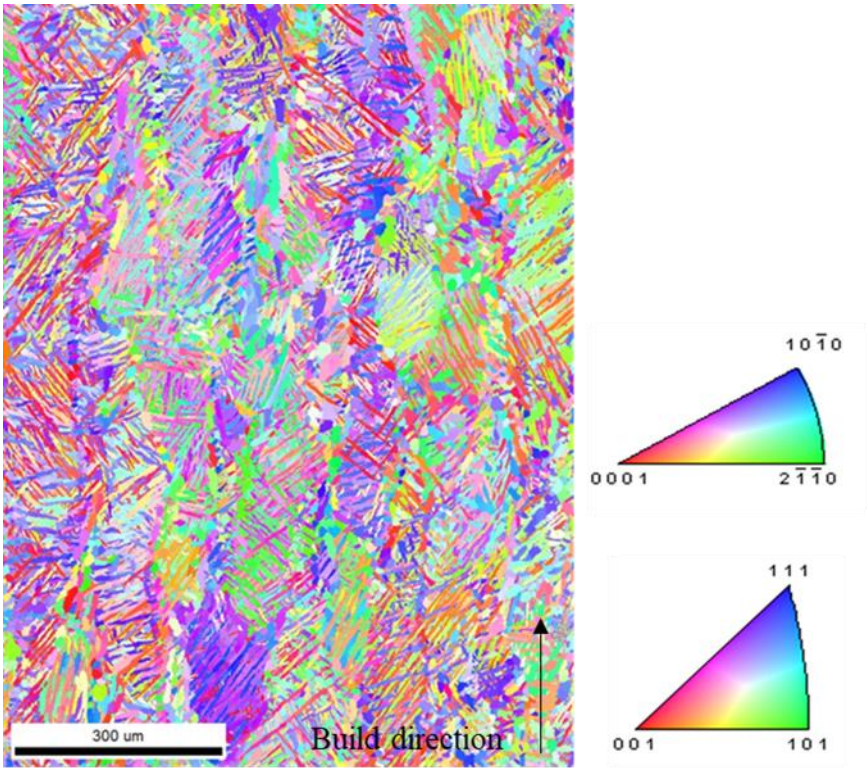

Figure 7-5: EBSD plot of DA condition in the ZX/ZY or X-Z plane, with the build direction indicated.

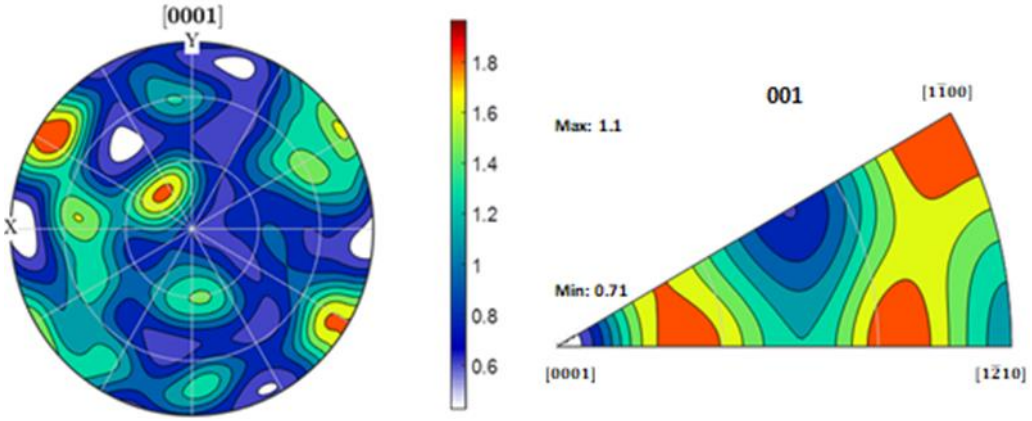

Figure 7-6: Pole figure and inverse pole figure of DA condition.

7.3 Residual stress

The contour residual stress maps are shown in Figure 7-7. It is observed that the AF specimens have larger residual stresses than their SR counterparts. Furthermore, the stresses in both conditions show tensile stresses near the specimen perimeter while compressive stresses are observed through the thickness. The balancing between tensile and compressive stresses are an expected result. In addition, anisotropic behaviour is observed in residual stress. For both AF and SR conditions, the Z-X orientation had the highest residual stresses, then the X-Z and the lowest stresses were observed in the X-Y orientation. The measured maximum tensile residual stresses in the AF condition for Z-X, X-Z and X-Y specimens were 990, 540, and 430 MPa and compressive stress was 380, 190 and 140 MPa, respectively. The tensile residual stress is reduced to a maximum of 200 MPa and compressive of 100 MPa for all three orientations in the SR condition. The residual stress observations align with that found in the literature. Firstly, it was previously observed, using neutron diffraction, that large residual stresses concentrate on the Z-X perimeter of the material while compressive stresses are concentrated through the thickness of the material (Anderson *et al.*, 2018). Secondly, anisotropy of residual stress, in particular, the Z-X orientation (stresses in the Z-direction/build direction) having the largest stresses was also observed (Rangaswamy *et al.*, 2005; Vrancken *et al.*, 2014). In addition to the literature comparison, the maximum measured tensile stress is below the yield strength of the material of approximately 1100 MPa.

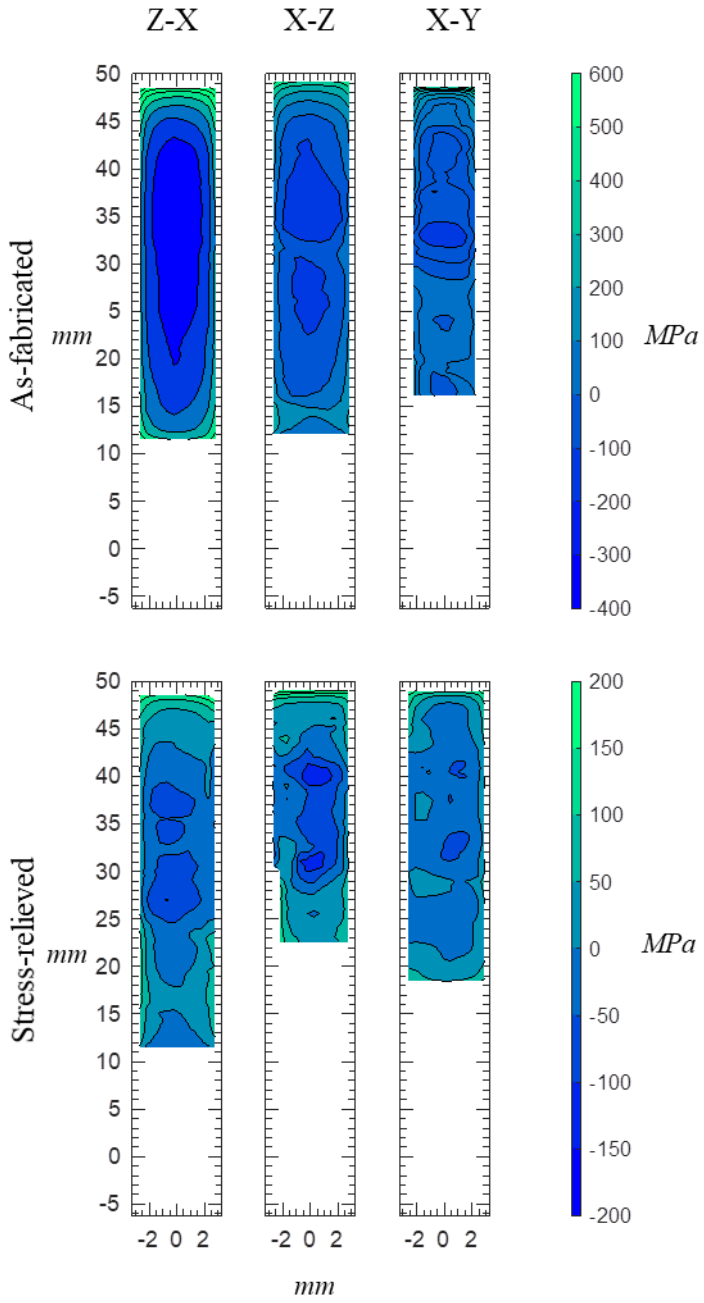

Figure 7-7: Stress values' contour plots for the as-fabricated and stress-relieved conditions, in all three crack planes.

7.4 Fatigue crack growth rate threshold

Figure 7-8 represents the near-threshold fatigue crack growth of the Z-X orientation. These results are for both R-constant and K_{max} approaches as indicated in Figure 7-8. The threshold crack growth rate is defined as 10^{-10} m/cycle, however, in this project, a lower crack growth rate was obtained as not all specimens had displayed the asymptotic behaviour of threshold at 10^{-10} m/cycle. The thresholds have a slight decrease as the *R-ratio* increases. As can be seen in Figure 7-8, there is no threshold for R = 0.1. The *R* = 0.1 test did not yield a threshold result and showed a sporadic behaviour. While it is not entirely clear what caused this behaviour, it is possible that there were localised irregular residual stresses at the crack tip which caused fluctuating crack propagation rates. This behaviour is also observed in the X-Z orientation for *R* = 0.1 in Figure 7-9 (a). For both Z-X and X-Z orientations, the residual stresses were measured to be the highest in these orientations.

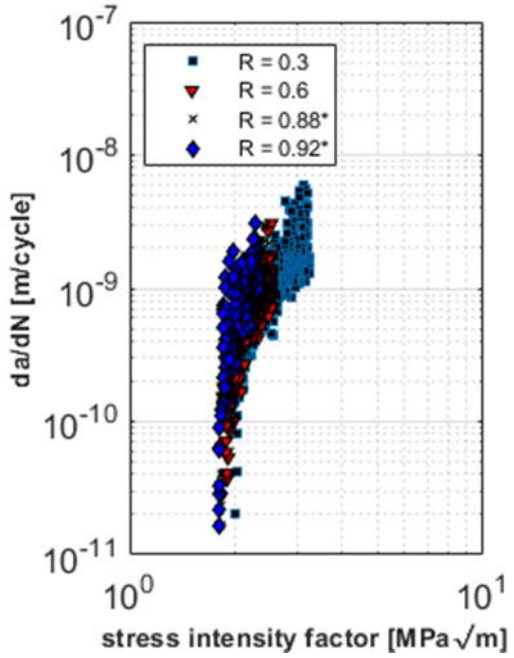

Figure 7-8: Fatigue crack growth rate threshold of the Z-X orientation in the as-fabricated condition. *K_{max} result.

Figure 7-9 (a) represents the near-threshold fatigue crack growth rate of the as-built X-Z orientation specimens. All tests, except the *R* = 0.1, exhibited the asymptotic threshold behaviour with a slight decrease in threshold with an increase in *R*. As previously mentioned, this is likely due to the irregular high residual stress levels which caused the sporadic behaviour observed. However, further investigations are required to confirm this.

Figure 7-9 (b) represents the near-threshold fatigue crack growth rate of the as-built X-Y orientation specimens. It is clearly seen in this orientation that the threshold decreases as the *R-ratio* increases. This orientation also has a threshold for $R = 0.1$. Between the three orientations, the X-Y orientation exhibits the most crack closure effects. While observing the threshold data in the *da/dN* vs ΔK curve form is useful, it is also a cluttered graph with all the data points making up the graph. It is therefore necessary to view the threshold data on a ΔK_{th} vs R graph as well as a ΔK_{th} vs K_{max} graph.

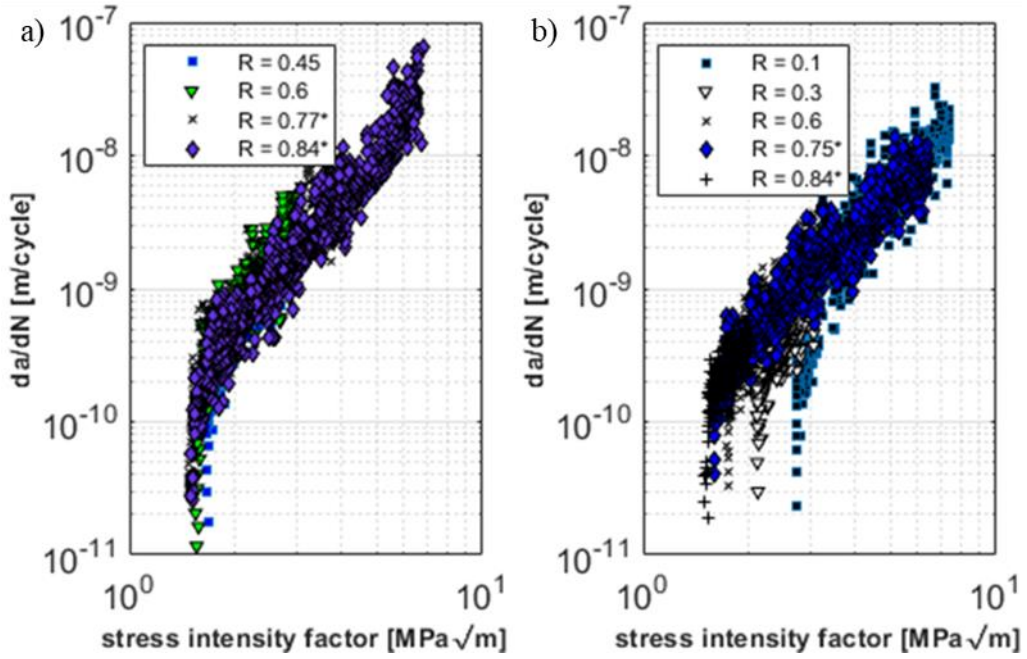

Figure 7-9: Fatigue crack growth rate threshold of the, (a) X-Z orientation and (b) X-Y orientation in the as-fabricated condition. *K_{max} result.

Figure 7-10 (a) shows the graph of ΔK vs R for the as-built specimens in all three orientations. The graph gives a better representation of how ΔK_{th} varies with an increase in R for all three orientations. As seen in Figure 7-10 (a), all three orientations have a decrease in ΔK_{th} for an increasing R, however, the Z-X and X-Z orientation's decrease seems to be less dependent on R than on the X-Y orientation. Both Z-X and X-Z orientations have less than 10 % change in ΔK_{th} for increasing R while the X-Y orientation has an approximately 40 % change. It is likely that the larger residual stress levels in the Z-X and X-Z orientations are an influencing factor in this observed behaviour. Furthermore, the X-Z and X-Y orientations show a convergence to a similar ΔK_{th} at the high R values of approximately 1.5 MPa√m while the Z-X orientation has a slightly higher ΔK_{th} of approximately 1.8 MPa√m.

Figure 7-10 (b) shows the ΔK_{th} vs K_{max} graph for the as-built condition in all three orientations. The areas below the respective curves are regions where no crack

propagation will occur and is limited by a K_{max} of the material's fracture toughness. It is interesting to note that for constant *R-ratio* tests, there is a near vertical decrease in ΔK_{th} with respect to K_{max}, but a near horizontal stagnation in ΔK_{th} for increasing K_{max} when tests are conducted at constant K_{max}. The X-Z decrease is considered as the global "closure affected" region with a K_{max} limit of ~ 3 MPa.√m. The horizontal line, in which we obtain a ΔK_{th} which is independent of K_{max}, is considered to be the global "closure free" region.

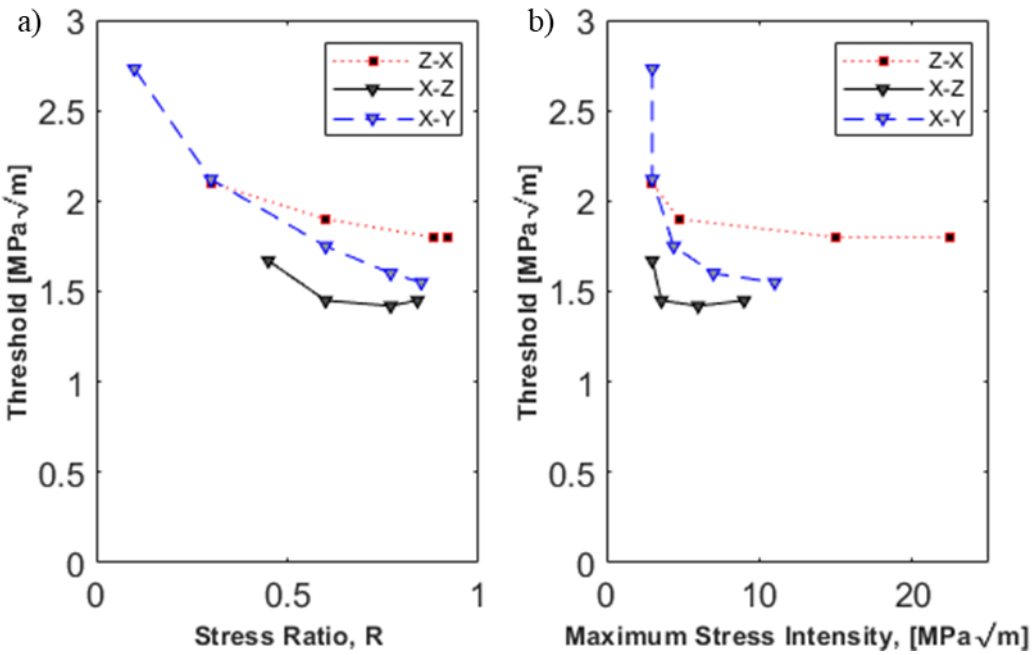

Figure 7-10: Graph of (a) ΔK_{th} vs R and (b) ΔK_{th} versus K_{max} for the as-fabricated specimens

Figure 7-11 shows the near-threshold fatigue crack growth rate of the Z-X orientation in the SR condition. In this condition, the Z-X orientation has produced a ΔK_{th} for R = 0.1. Furthermore, with a decrease in residual stress after the SR heat treatment, a more pronounced crack closure effect can be observed in the results in comparison to the AF condition. The ΔK_{th} for R = 0.1 shows a larger ΔK_{th} than the remaining R values, however, the remaining ΔK_{th} have not significantly changed from the AF conditions.

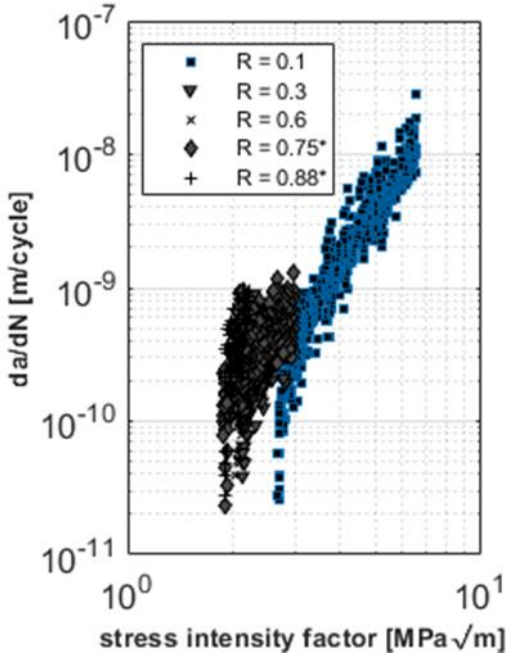

Figure 7-11: Fatigue crack growth rate threshold of the Z-X orientation in the stress relief condition. *K_{max} result.

Figure 7-12 (a) shows the near-threshold fatigue crack growth rate of the X-Z orientation in the SR condition. This orientation and condition show a clear reduction in ΔK_{th} for an increasing *R* than the AF counterpart. It is observed that the final ΔK_{th} for the highest *R* value in the stress relief condition is approximately the same in both the AF and SR condition.

Figure 7-12 (b) shows the near-threshold fatigue crack growth rate for the X-Y orientation in the SR condition. There is a clear decrease in ΔK_{th} as the *R-ratio* increases. This is a similar behaviour observed in the AF counterpart.

Figure 7-13 (a) shows the graph of ΔK_{th} vs *R-ratio* for the SR condition in all three orientations. As seen, both Z-X and X-Z specimens have results at $R = 0.1$. The remainder of ΔK_{th} obtained for the Z-X orientation does not differ significantly from the AF counterpart. When considering the X-Z and X-Y orientations, there are increases in ΔK_{th} compared to the AF counterparts for a given *R-ratio*. However, for the final *R-ratio*, both X-Z and Horizontal orientations converge towards the same ΔK_{th} which is a similar value in the AF condition i.e ~1.5 MPa√m. For the SR condition, both Z-X and X-Z orientations have approximately a 30% decrease in ΔK_{th} for an increasing *R-ratio* compared to the 10% in the AF counterparts. The decrease in ΔK_{th} for the SR X-Y orientation is approximately 50% over the range of *R-ratios* tested in comparison to the approximate 40% decrease in the AF counterpart.

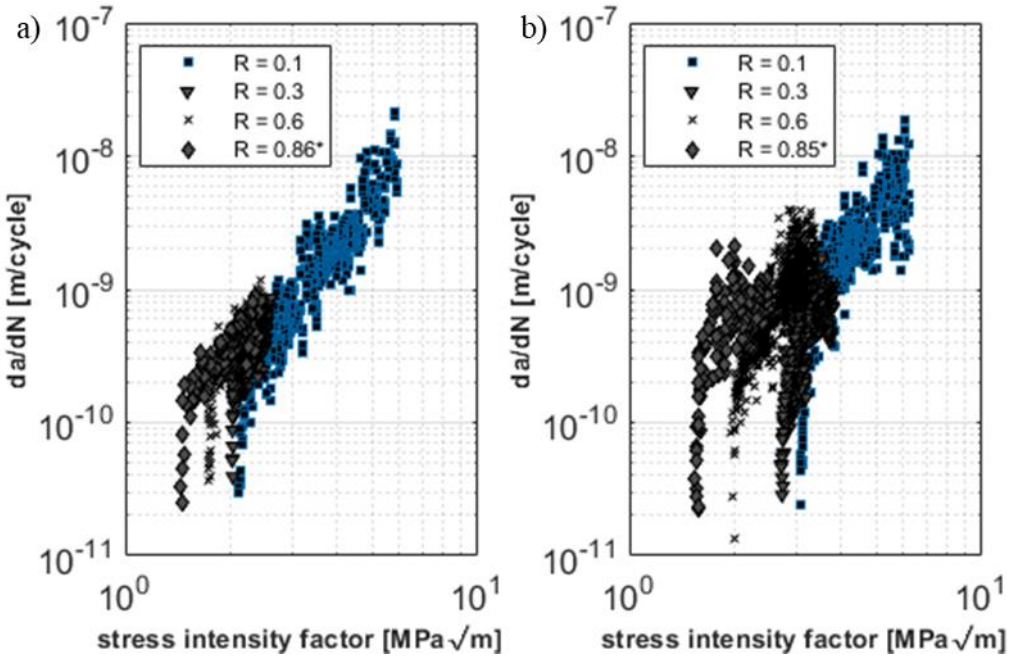

Figure 7-12: Fatigue crack growth rate threshold of the (a) X-Z orientation and (b) X-Y orientation in the stress relief condition. *K_{max} result.

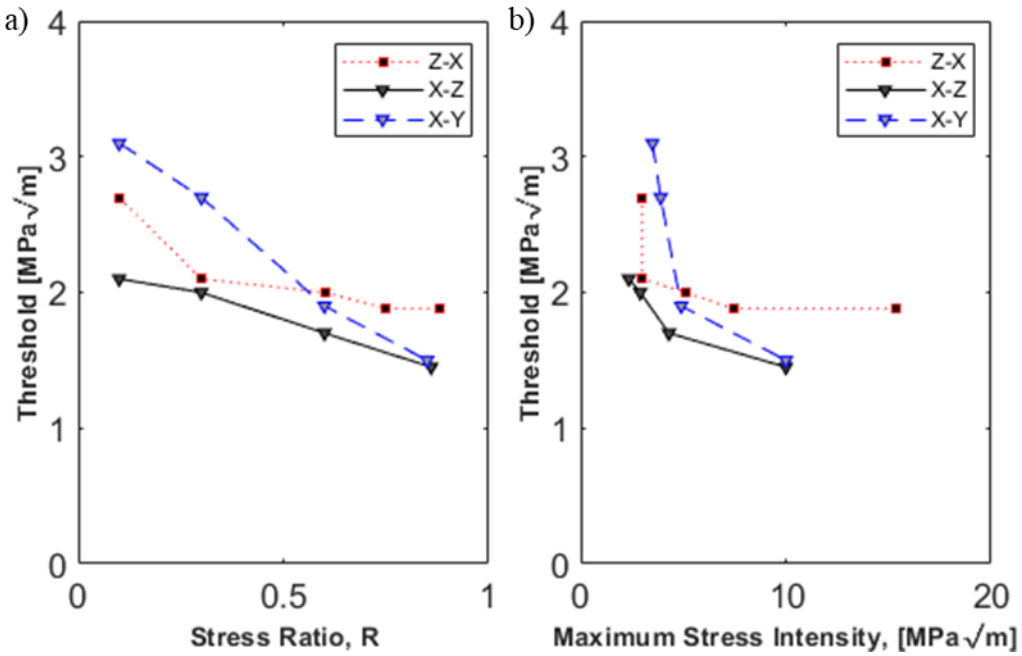

Figure 7-13: Graph of (a) ΔK_{th} versus R and (b) ΔK_{th} versus K_{max} for stress relief specimens

Figure 7-13 (b) shows the ΔK_{th} vs K_{max} graph for the SR specimens. There is no significant difference between this graph and the AF counterpart. The K_{max} limit in the global "closure affected" region is also ~ 3MPa√m.

Figure 7-14 shows the near-threshold fatigue crack growth rate of the Z-X orientation in the DA condition. There is a clear decrease in the ΔK_{th} as the *R-ratio* increases. There is an approximately 52% decrease in ΔK_{th} from the lowest to highest *R-ratio*. The change in microstructural morphology has produced a large increase in ΔK_{th} for all *R-ratios* in the DA condition in comparison to the AF and SR counterparts. For an R = 0.1, the DA condition has an over 100% increase in ΔK_{th} when compared to the SR counterpart. As a result of there being no result for R = 0.1 in the as-built condition, a comparison cannot be made. When comparing the highest *R-ratios* (R = 0.85 in the DA condition) and lowest ΔK_{th} for all three conditions in the Z-X orientation, the DA condition has an approximate 50% increase in ΔK_{th} in comparison to the AF and SR counterparts.

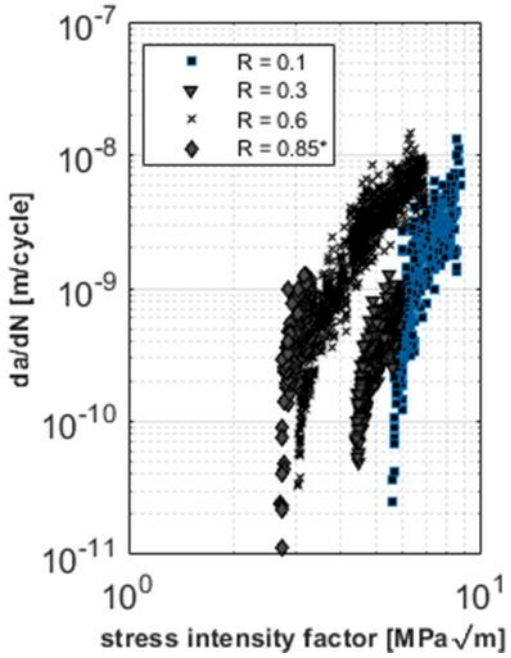

Figure 7-14: Fatigue crack growth rate threshold of the Z-X orientation in the duplex anneal condition. *K_{max} result.

Figure 7-15 (a) shows the near-threshold fatigue crack growth rate of the X-Z orientation in the DA condition. There is a clear decrease in the ΔK_{th} as the *R-ratio* increases. There is an approximately 52% decrease in ΔK_{th} from the lowest to highest *R-ratio*. For an R = 0.1, the bi-modal condition has an approximately 180% increase in ΔK_{th} over that of the SR counterpart. As a result of there being no result for R = 0.1 in the AF condition, a comparison cannot be made. When comparing the highest *R-ratio's* (R = 0.92 for DA) and lowest ΔK_{th} for all three conditions in

the X-Z orientation, the DA counterpart has an over 90% increase in ΔK_{th} compared to that of the AF and SR counterparts.

Figure 7-15 (b) shows the near-threshold fatigue crack growth rate of the X-Y orientation in the DA condition. There is a clear decrease in the ΔK_{th} as the *R-ratio* increases. There is an approximately 40% decrease in ΔK_{th} from the lowest to highest *R-ratio*. For an R = 0.1, the DA condition has an approximately 120% increase in ΔK_{th} comparted to that of the AF counterpart and an approximately 96% increase in comparison to that of the SR. When comparing the highest *R-ratios* (R = 0.91 for DA) and lowest ΔK_{th} for all three conditions in the X-Y orientation, the DA has an over 130% increase in ΔK_{th} when compared to that of the AF and SR counterparts.

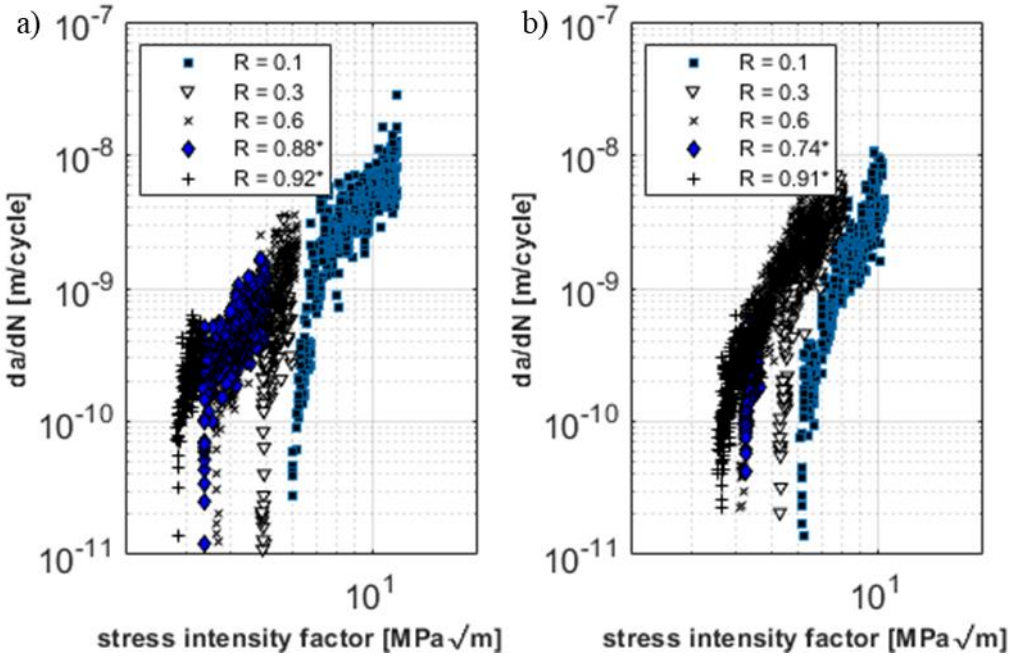

Figure 7-15: Fatigue crack growth rate threshold of the (a) X-Z orientation and (b) X-Y orientation in the duplex anneal condition. *K_{max} result.

Figure 7-16 (a) shows the graph of ΔK_{th} versus R for the DA condition in all three orientations. The ΔK_{th} of the DA condition has a large decrease with respect to an increasing R. Interestingly, in the DA condition, all three orientations have a more similar ΔK_{th} at R = 0.1 in comparison to the SR condition. Furthermore, the manner in which ΔK_{th} decreases as the *R-ratio* increases, up to R = 0.6, is similar in all three orientations. Thereafter, a more noticeable change in behaviour can be observed. and decreases similarly to their highest *R-ratio*. This behaviour is different to that observed in the AF and SR counterparts. The Z-X and X-Z orientation have a ΔK_{th} which reduces down to ~ 2.7 MPa√m and ~3.5MPa√m in the X-Y orientation.

Figure 7-16 (b) shows the relationship between ΔK_{th} and K_{max} for the DA condition in all three orientations. This behaviour also shows a near X-Z decrease in ΔK_{th} for *R-constant* tests in the global "closure affected" region and a near horizontal ΔK_{th} at different K_{max} levels in the global "closure free" region. In the global "closure affected" region for all three orientations, the limiting K_{max} is ~ 6 MPa√m. The global "closure free" intrinsic ΔK_{th} for the Z-X and X-Z orientations is ~ 2.7 MPa√m and ~ 3.5 MPa√m in the X-Y orientation.

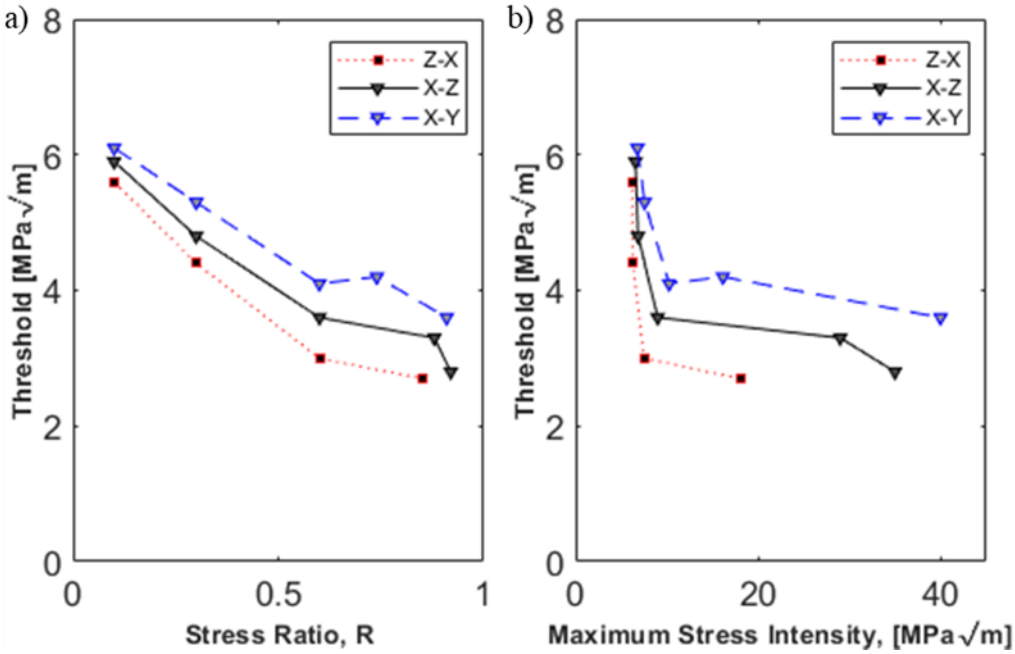

Figure 7-16: Graph of (a) ΔK_{th} versus R and (b) ΔK_{th} versus K_{max} for duplex anneal specimens

7.5 Fractographic analysis

Observations on the fracture surfaces in Figure 7-17 show that the fracture mechanisms are predominantly trans-granular, quasi-cleavage faceted fractures through α_p laths in the AF and SR conditions. This occurs on a localised scale in which the smooth quasi-cleavage facets cause crack deviations on the perimeter of the facet, resulting in crack tortuosity, as seen in Figure 7-17 (d), (e) and (f). It is further observed in Figure 7-17 (g), (h) and (i) that the crack path is largely influenced by α_p laths orientated at ±45°, resulting in crack tortuosity. It is also observed that crack branching and microcracking occur at the secondary and tertiary α laths indicated in Figure 7-17 (g), (h) and (i). In an annealed (850°C for 2 h) condition of LPBF Ti-6Al-4V, Xu et al (Xu *et al.*, 2019) observed crack propagation between "paralleled α laths" which showed a crack direction dependency on the longitudinal axis direction of the α laths. A similar observation has been made in this investigation in which there are very narrow areas parallel to

the load direction of laths, where fine trans-granular fracture mixed with intergranular dimples, are clustered within. It is further observed, on a larger scale, that the crack path is influenced by the PBG morphology. As indicated in Figure 7-17 (a), (b) and (c), the fracture surfaces also contain a PBG boundary shaped fracture, in accordance with the respective orientation, which contains various levels of roughness's within it. It is further observed in Figure 7-17 (a) that large secondary cracks form along PBG and there are visible rachet marks in Figure 7-17 (c), indicating multiple crack paths. These observations indicate that, on a localised scale, crack path influence occurs due to the near crack tip microstructure and, on a larger scale, due to the PBG structure.

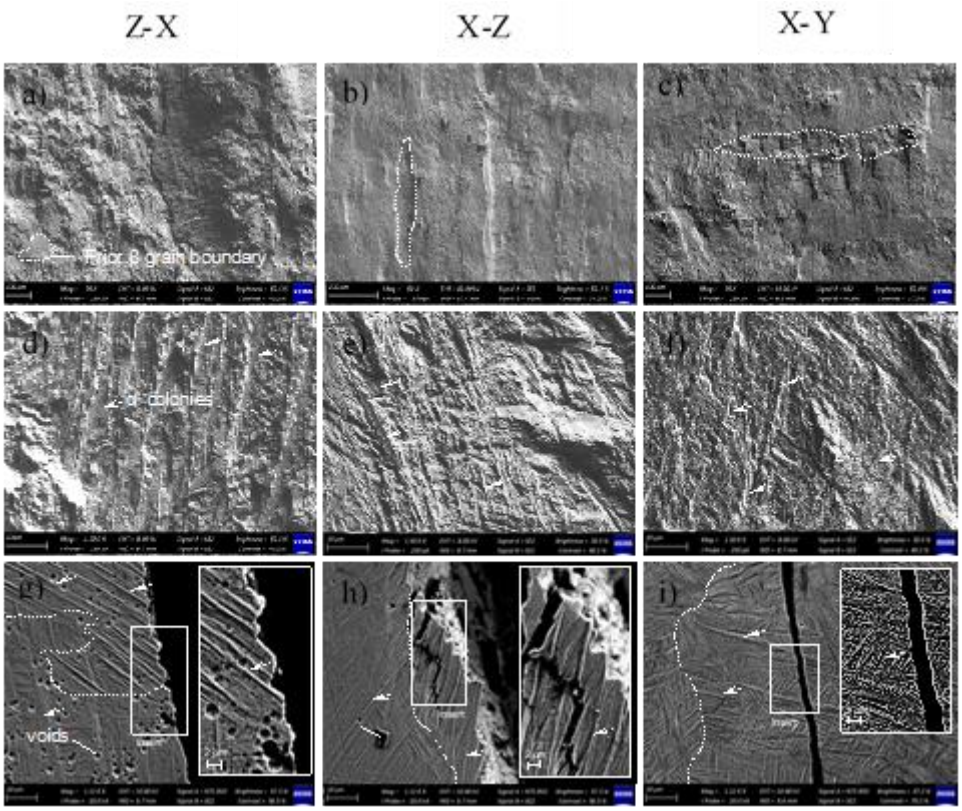

Figure 7-17: Crack profiles in the Z-X, X-Z and X-Y orientations for the AF condition. Fracture surfaces are shown at (a), (b), (c) of PBG outlines, (d), (e), (f) smooth quasi-cleavage facets cause and (g), (h), (i) crack profile images. No differences observed in the SR condition.

In Figure 7-18, the occurrence of slip bands was observed in primary laths near the crack tip. Furthermore, it can be observed that crack deflection has occurred at a primary α′ lath, resulting in crack tortuosity. The slip bands are associated with the crack deflections observed in the primary α′ lath. Porosity voids are also visible in Figure 7-18, however, their effect on crack propagation will not be as significant as

compared to crack initiation (Leuders *et al.*, 2012; Poulin *et al.*, 2019; Becker *et al.*, 2021).

There exists a strong influence of PBG morphology on cracking mechanisms due to the LPBF produced Ti-6Al-4V morphology. It is suggested that primary lath's direct crack growth in retrospect of the asperity levels in roughness between neighbouring PBG. As a result of the hierarchical nature of the LPBF Ti-6Al-4V microstructure, crack paths are predominantly of α_p facets, where secondary and tertiary facets cause secondary crack formations, crack branching and tortuosity due to the differently orientated lath facets. Furthermore, the orientation of columnar PBG means a mixivity in loading and possible roughness induced crack closure effects since the near crack tip crack deflections affect the localised plasticity build-up ahead of the crack tip. In light of the above, it can be concluded that anisotropic behaviour is influenced by both α_p lath orientation and PBG morphology.

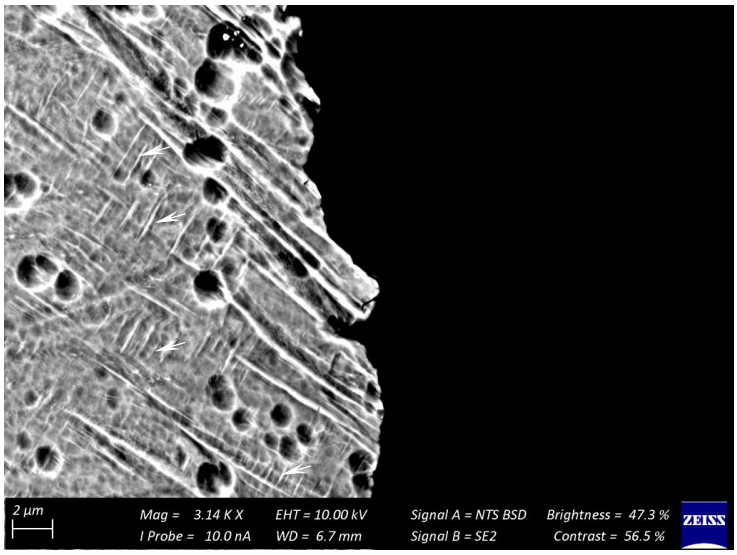

Figure 7-18: Slip bands, indicated with arrows, in primary laths along the crack path

The bi-modal fracture surface also displays a transgranular quasi-cleavage faceted fracture surface, however, due to the larger grain sizes in the DA condition, the facets are larger in the DA condition than in the AF and SR conditions. The larger grains cause larger crack tortuosity which can be observed in the crack paths shown in Figure 7-19. With the now present β phase, there exist α/β interfaces which act as a possible crack deflection barrier. In comparison to the AF and SR fractography, it is apparent that the DA condition has larger crack deflections, crack branching/bifurcation and fracture roughness. However, it is not specifically observed in the DA condition that laths are predominantly orientated at ± 45° as it is in the AF and SR counterparts. On the other hand, while faint, PBG shapes can be observed on the fracture surface with the Z-X orientation showing larger

amounts of faceted fracture than the X-Z and X-Y orientation. This is likely due to the Z-X orientation's crack plane and grain orientation being more favourable for faceted fracture than the X-Z and X-Y orientation. One other difference that is brought about due to the presence of β phase is the ductile fracture observed on non-faceted regions.

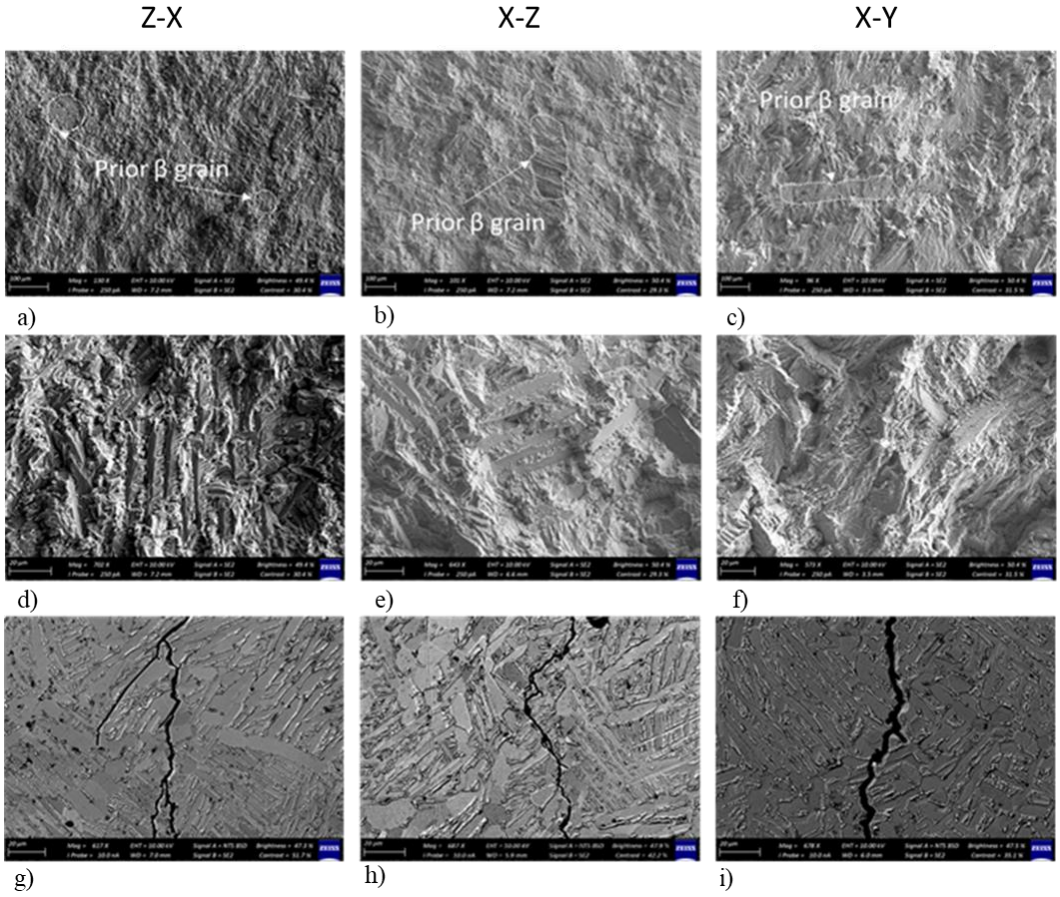

Figure 7-19: Fracture surfaces and crack profiles of Z-X, X-Z and X-Y orientation in the DA condition. (a),(b),(c) shows the prior β grain shapes in the Z-X, X-Z and X-Y orientations respectively. (d), (e), (f) shows faceted facture on the Z-X, X-Z and X-Y orientations, respectively. (g), (h), (i) show the crack path for the Z-X, X-Z and X-Y orientations, respectively

7.5.1 Tensile properties

The tensile properties of the AF, SR and DA conditions are given in Table 7-1 and Figure 7-20 below. The SR condition exhibits the most brittle nature of all three conditions. The formation of extremely fine β precipitates hindered the dislocation movement, resulting in the embrittlement of the microstructure, as confirmed by Ter Haar and Becker (2020). Scanning transmission electron microscopy (STEM) results confirmed the absence of Al_3Ti precipitates. For a more detailed discussion

regarding the ductility of the three conditions, the reader is directed towards the works of Ter Haar and Becker (2018; 2020).

Table 7-1: Tensile properties of the three conditions

	As-built	Stress relief	Bi-modal
Yield strength (σ_y)	1070 ± 21 MPa	1180 ± 21 MPa	880 ± 6 MPa
Ultimate tensile strength (σ_u)	1210 ± 8 MPa	1290 ± 4 MPa	946 ± 7 MPa
Elongation (ε_f)	8.9 ± 0.8 %	6.6 ± 0.1 %	18.7 ± 1.4 %
Hardening ratio	1.13	1.09	1.08

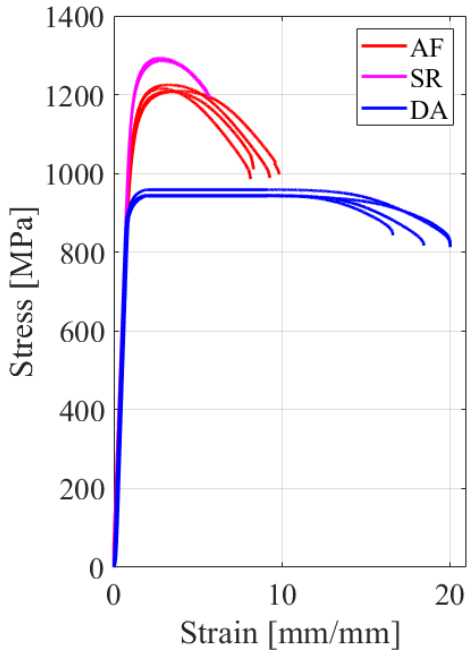

Figure 7-20: Stress-strain curve for the AF, SR and DA conditions.

7.6 Summary

This chapter presented the results of the different aspects in the investigation. The microstructure showed that the PBG lengths had an affiliation to the build direction. The PBG shows an equiaxed shape in the Z-X orientation and columnar shapes in the X-Z and X-Y orientations. The PBG and α' laths are connected through the BOR resulting in a weak crystallographic texture for α'. The α' lath angle texture forms along the habit planes, which is governed by the PBG crystallographic texture. As a result of the specimen orientation difference, the Z-X orientation has 0 - 90° lath angle dominance while the X-Z and X-Y has a 45° lath angle dominance. Once the SR heat treatment is applied, XRD data showed a peak shift as well as less of a peak

broadening compared to the AF condition. The bi-modal microstructure results in an equiaxed primary α phase and lamellar secondary α in a matrix of β.

For the measured residual stress in the AF condition, tensile stresses amounted to 990, 540, and 430 MPa and compressive stresses were 380, 190 and 140 MPa in the Z-X, X-Z and X-Y orientations, respectively. After the SR heat treatment was applied, the measured tensile residual stress is reduced to a maximum of 200 MPa and compressive of 100 MPa for all three orientations.

For the near-threshold FCGR in the AF condition both Z-X and X-Z orientations have less than 10% change in ΔK_{th} for an increasing *R* while the X-Y orientation has an approximately 40% change. The near-threshold FCGR in the SR condition, both Z-X and X-Z orientations have an approximately 30% decrease in ΔK_{th} for an increasing *R-ratio*. The decrease in ΔK_{th} for the SR X-Y orientation is approximately 50% over the range of *R-ratios* tested. In the DA condition, both Z-X and X-Z orientations have an over 50% decrease in ΔK_{th} for an increasing *R-ratio*, while the X-Y orientation has an approximately 40% decrease in ΔK_{th} for an increasing *R-ratio*. For the highest *R-ratios* and lowest ΔK_{th} for all three conditions in the Z-X orientation, the DA condition has an approximately 50% increase in ΔK_{th} over that of the AF and SR counterparts. In the X-Z orientation, the DA condition has an over 90% increase in ΔK_{th} when compared to that in the AF and SR counterparts. The DA condition in the X-Y orientation has an over 130% increase in ΔK_{th} over that of the AF and SR counterparts.

The fracture mechanisms are predominantly trans-granular, quasi-cleavage faceted fractures through α_p laths in the AF and SR conditions. This fracture mode resulted in crack tortuosity so that the crack path is largely influenced by α_p laths orientated at ±45°, resulting in crack tortuosity. The fracture surfaces also contain PBG boundary shaped fractures, in accordance with the respective orientation, which contains various levels of roughness's within it. The DA fracture surface also displays a trans-granular, quasi-cleavage faceted fracture surface. Facets are, however, larger in the DA condition than in the AF and SR conditions. While faint, PBG shapes can be observed on the fracture surface with the Z-X orientation showing larger amounts of faceted fracture than the X-Z and X-Y orientation.

8 Discussion

The following chapter attempts to interpret the findings brought about in Chapter 7 and discuss it in terms of crack growth mechanisms and crack closure mechanisms. The influence of residual stress is first discussed by comparing the AF and SR conditions. Thereafter the influence of the specific LPBF produced Ti-6Al-4V microstructure is discussed by comparing the AF and SR conditions. The influence of microstructural morphology is then discussed by considering the SR and DA condition. The microstructural morphology discussion is specifically divided into extrinsic and intrinsic mechanisms. The final subsection highlights the differences between LPBF Ti-6Al-4V and conventionally manufactured Ti-6Al-4V.

8.1 Influence of residual stress

It has been mentioned by Leuders et al (2012) that the primary influencing factor on crack growth is residual stress. It is not mentioned, however, what the specific mechanisms of residual stress's influence on crack growth are. Furthermore, it has been shown within welded structures, including friction stir welded Ti-6Al-4V, that residual stress has a significant influence on near-threshold behaviour (Woodtli *et al.*, 1986; Beghini & Bertini, 1990; John *et al.*, 2003). While it is also understood that underlying microstructures determine the near threshold behaviour, the residual stresses influence on near threshold behaviour is to alter the effective value of K (Beghini & Bertini, 1990; Vasudeven *et al.*, 1994; Pippan & Hohenwarter, 2017). The current investigation discusses that the residual stress alters the ΔK and R for LPBF Ti-6Al-4V.

As previously mentioned, the residual stress levels have been shown, in Figure 7-7, to vary within the crack plane depending on the orientation of the specimen. When considering the levels of residual stress with respect to specimen orientation, the highest is in the Z-X orientation, then the X-Z and the lowest measured in the X-Y orientation. This order is kept when observing the measured positive crack tip opening displacements (CTOD) on the crack flanks, as shown in Figure 8-1 (a). It is further observed that the AF conditions have significantly larger CTODs than the SR counterparts. The SR condition's CTOD is largely reduced in comparison to the AF condition's but is apparent enough for measurement. For calculating the opening stress intensity, K_{op}, it was assumed to be a linear elastic fracture mechanics model in order to fit a Williams series (Williams, 1960) for mode I crack opening using a linear least-square approach. The resultant fit and K_{op} is incorporated into the CTOD measurements in Figure 8-1 (a). Equation (8-1) is used to calculate K_{op}:

$$\delta = \frac{4K_{op}^2}{\pi\sigma_y E} \tag{8-1}$$

Where δ is the measured CTOD and E is the Young's modulus.

It was reported by Mercelis and Kruth (2006) and Yadroitsev et al (2015) that the LPBF process results in a non-uniform residual stress distribution. This is in agreement with the current investigations' residual stress distribution as can be seen in Figure 7-7. The measured CTODs are taken from the crack flanks (in a state of plane stress) which are representative of a tensile stress state. However, due to the centre of the specimen being in a state of compression (in a state of plain strain), the measured CTOD's will not be representative for it. In addition, Yadroitsev et al (Yadroitsev & Yadroitsava, 2015) report that the near-tip crack driving force will be affected by the localised fluctuations in the residual stress.

It follows that the calculated K_{op} is not the best representative of a near-tip crack driving force but gives a partial insight into this. One can, therefore, use the calculated K_{op} on a global scale to improve ΔK_{eff} estimates. This is done by assuming a fully opened crack at minimum load, with R that can be adjusted using Equation(8-2) and Equation (8-3) below:

$$R_{eff} = \frac{K_{min} + K_{max}}{K_{max} + K_{op}} \tag{8-2}$$

$$\Delta K_{eff} = \Delta K \tag{8-3}$$

When plotted, this results in a shift in R to the right while ΔK remains unaffected, as shown in the $\Delta K_{eff,th}$ versus R_{eff} plot in Figure 8-1 (b). The results in Figure 8-1 (b) show that there is an excellent agreement between the AF and SR conditions, i.e. the R_{eff} adjustments align the AF condition with the SR condition. This means that the differences observed between the AF and SR conditions in the near-threshold regime, based on Figure 8-1 (b), is accounted for by the influence of residual stresses. In addition, the residual stress influence is more prominent in the low *R-ratio* regimes, where K_{max} is low, and less prominent in the high *R-ratio* regimes, where K_{max} is high. Finally, the residual stresses within a specimen are process dependent, thus ΔK_{th} versus R will vary depending on the LPBF machine being used, the specimen size and geometry being built, amongst other parameters.

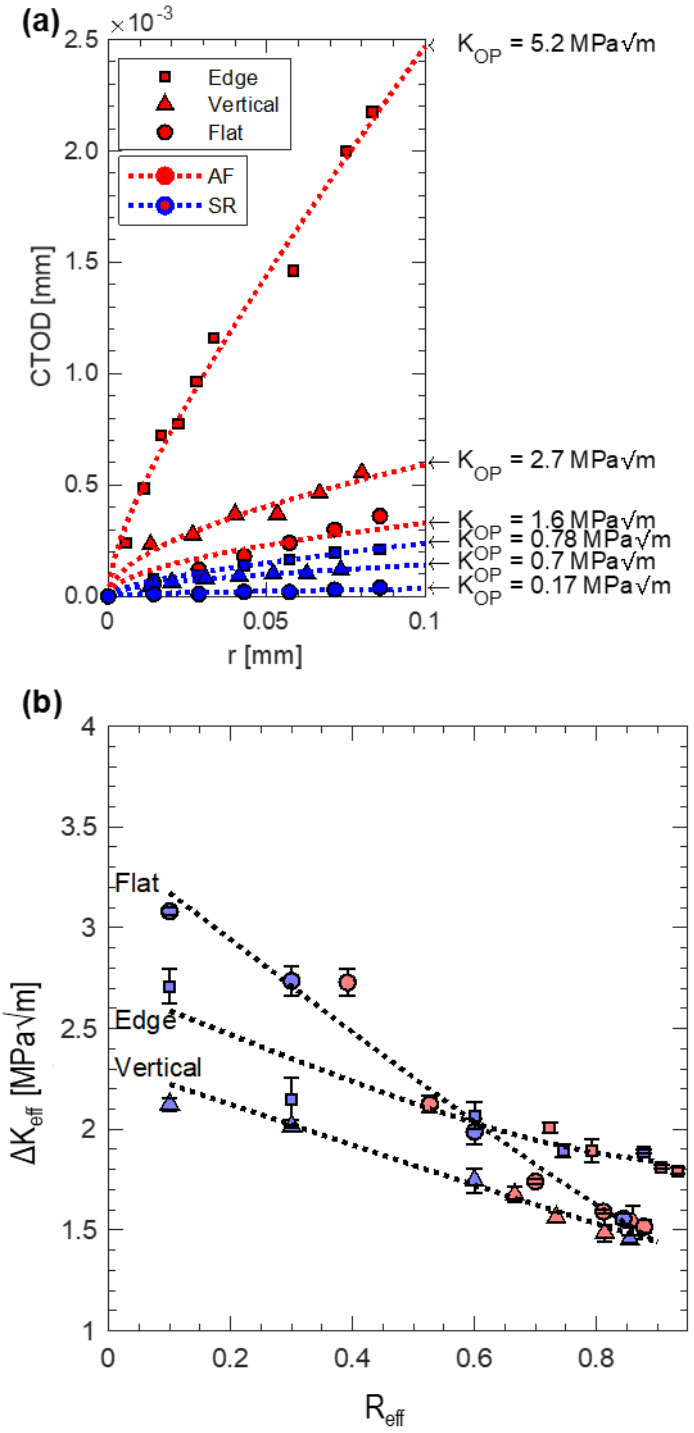

Figure 8-1: (a) CTOD as a function of distance r to the crack tip, and the fitted K_{op} curves. (b) Plot of R_{eff} versus $K_{eff,op}$.

8.2 Influence of LPBF microstructure

Over the past four decades, the complexities of Ti-6Al-4V fracture mechanisms have been an active research topic. It is understood that the complexities of the fracture mechanisms are the result of the two phase nature of Ti-6Al-4V, which cannot be easily modelled (Moore *et al.*, 2017). Of the fracture mechanism's research into Ti-6Al-4V, it has been found that cracking in $\alpha + \beta$ alloys is associated with faceting of unfavourably orientated grains (Bantounas *et al.*, 2009). These facets are commonly in the $\langle a \rangle$ basal plane, and suggest that basal slip is the general cause of crack initiation under fatigue loading conditions (Bantounas *et al.*, 2010). Slip is dependent on the crystallographic orientation of the crystal as well as which slip system is most favourably orientated with respect to the load direction.

There are two factors which slip activation is dependent on:

(i) Schmid factor – a function of grain orientation relative to load direction, and,
(ii) the crystal resolved shear stress required to activate the slip system.

For α phase crystals, the dominant activated slip system is $\langle a \rangle$ basal $\langle 1\bar{1}\bar{2}0 \rangle \{0001\}$, $\langle a \rangle$ prismatic $\langle \bar{1}2\bar{1}0 \rangle \{10\bar{1}0\}$ slip or the first-order $\langle a + c \rangle$ pyramidal $\langle 1\bar{2}1\bar{3} \rangle \{1\bar{1}01\}$ slip (Bantounas *et al.*, 2009). An investigation conducted by Jin and Mall (Jin & Mall, 2003) on a different $\alpha + \beta$ alloy i.e. Ti-6Al-2Sn-4Zr-2Mo-0.1Si, showed that within a colony, individual α laths which are crystallographically aligned tend to behave like a single crystal. This leads to the colonies having long and continuous slips which are accompanied by crack deflection and higher fracture surface roughness. In a study conducted by Qiu et al (Qiu *et al.*, 2016), it was found in α laths that cracks would often propagate along the basal planes while only sometimes along the prismatic planes. This was also confirmed by Bantounas (2009) in which grains orientated between 0 - 90° to the principal loading directions were observed. In addition, Bantounas et al (2009) discuss that it is likely that α grains are likely to cause fatigue crack initiation when orientated favourably for faceted fracture and hence basal slip. This favourable α grain orientation for fatigue crack formation occurs when the c-axis of the grain is orientated between 10° - 66.7° to the principal loading axis. Bantounas et al (Bantounas *et al.*, 2009) draw these conclusions based on the investigation they had conducted in which they compare α texture on fatigue life. They used forged bar, unidirectionally rolled and cross rolled Ti-6Al-4V. It was found that the rolled direction, which causes the grains to be oriented favourably for faceted fracture with respect to load direction, had the lowest fatigue life.

It is observed in the current investigation, in Figure 7-17, that the AF and SR Ti-6Al-4V fracture surfaces also have areas of facet planes. Thus, it is likely that the fatigue cracking mechanisms of LPBF Ti-6Al-4V behave in a similar manner to conventionally manufactured Ti-6Al-4V. This would mean that there is also a preferential fatigue crack propagation along the $\langle \boldsymbol{a} \rangle$ basal planes. As previously

mentioned, with reference to Figure 7-2, the LPBF Ti-6Al-4V has a weak α' crystallographic texture due to the twelve possible variants, however, there is a stronger texture in the $\langle \mathbf{001} \rangle$ || Z direction. This is used to better understand the anisotropic behaviour of AF and SR Ti-6Al-4V.

For the explanation, it is of benefit to differentiate between crystallographic and the inherent LPBF morphological texture. The approach used by Bantounas et al (2009) for crystallographic texture is considered in this analysis. As shown in Figure 8-2 (a), the build planes, and hence the specimen orientations along with the dominant slip systems, are overlaid onto the pole figures. The dominant slip systems are $\langle a \rangle$ basal, $\langle a \rangle$ prismatic and $\langle a + c \rangle$ pyramidal. It is observed that there is good agreement between high Schmidt factors and active slip systems. It is understood that the slip system with the highest Schmidt factor is dominant (Bantounas *et al.*, 2009). Depending on the misorientation angle, a different slip system will be more dominant. Between 0° - 10° the $\langle a + c \rangle$ pyramidal slip is dominant, between 10° - 66.7° the $\langle a \rangle$ basal slip is dominant and between 66.7° - 90° the $\langle a \rangle$ prismatic slip is dominant. With regards to the loading direction for each orientation, the Z-X orientation has a load direction in Z, with reference to the $\{0001\}$ pole figure, while the X-Z and X-Y orientations have a load direction in X, with reference to the $\{11\bar{2}0\}$ pole figure, as seen in Figure 8-2. The respective loading directions both result in a maximum basal Schmid factor at 45°, however, they will have different dominant slip systems. The line of maximum Schmid factor for basal slip as well as the region in which basal slip is favourable, is indicated in Figure 8-2 (a). Comparison between the orientation specific poles, shows a minor difference of 8%. In addition, the number of laths within each dominant slip system is shown in Figure 8-2 (b). In light of the above, it seems that the crystallographic texture influences the near-threshold fatigue crack growth rates to a lesser extent than the morphological texture. The influence of morphological texture will be discussed in Section 8.3.

It is generally agreed upon that the dominant slip systems for Ti-6Al-4V are $\langle a \rangle$ basal, $\langle a \rangle$ prismatic and $\langle a + c \rangle$ pyramidal (Bantounas *et al.*, 2009). However, as to which specific slip system is most dominant is still contested (Lunt *et al.*, 2021). Especially considering that the basal and prismatic slip systems have similar critical resolved shear stress values. Depending on the c/a ratio, this may change which slip system is dominant (Britton *et al.*, 2015). Specifically, in the α′ phase state, the c/a ratio is smaller than if it were in an α phase state. Zhang et al (2020) found the c/a ratio for AF LPBF Ti-6Al-4V, heat treated to 730°C and 900°C, to be 1.5961, 1.5968 and 1.5974, respectively. However, Lunt et al (2021) argues that neighbouring grains has a significant influence on slip system activation and that Schmid factor analysis on its own may not be sufficient to predict the correct slip mode.

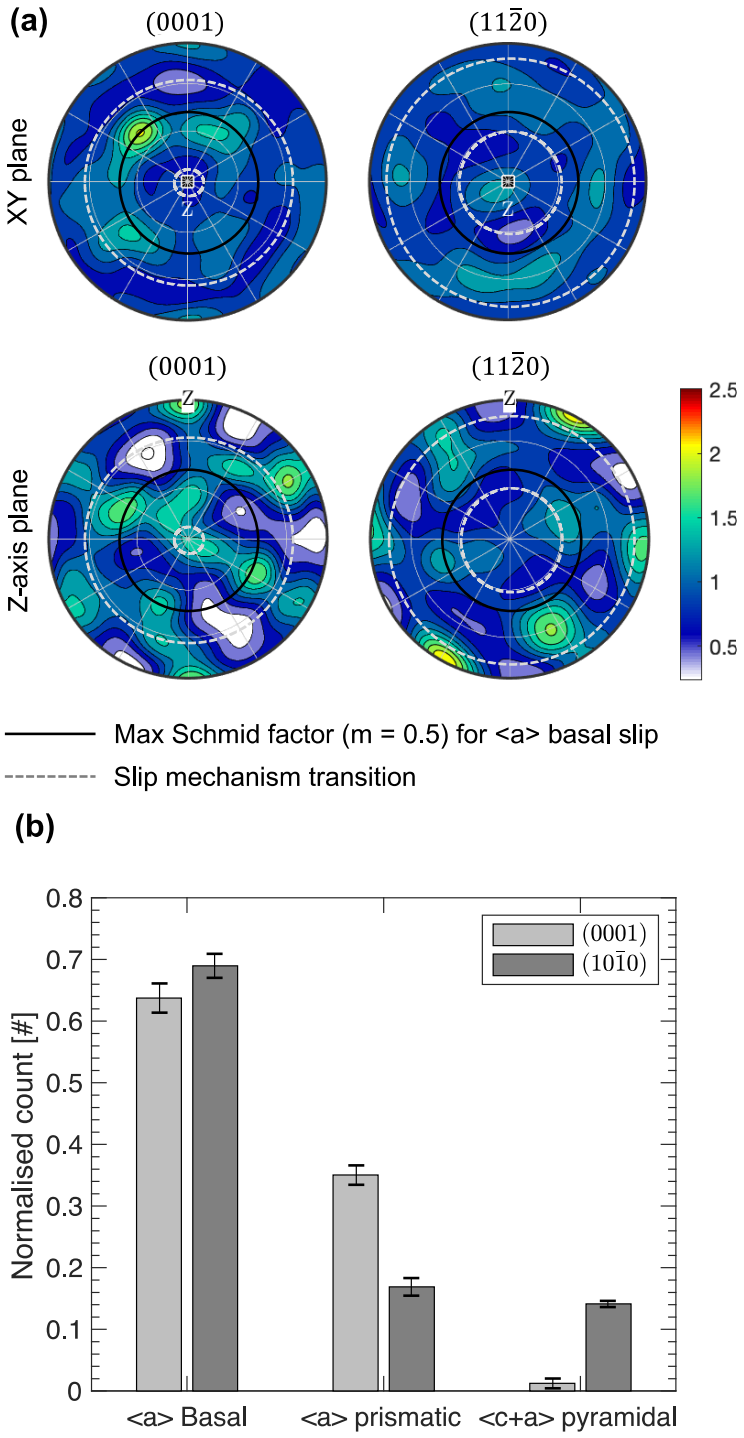

Figure 8-2: Basal (0001) pole figures of XY and Z-axis planes. Overlaid are the boundaries between three slip systems i.e. $\langle a \rangle$ basal, $\langle a \rangle$ prismatic and $\langle a + c \rangle$, and the line of maximum Schmid factor for basal slip. (b) Normalised count of grains oriented for X and Z slip systems as described in (Bantounas *et al.*, 2009).

8.3 Influence of microstructural morphology

The argument of near-threshold fatigue crack growth rates being more influenced by microstructural morphological texture than crystallographic texture, requires a discussion regarding crack closer effects. As has been discussed above, the crack paths are sometimes deflected by the primary α laths. It was similarly reported by Kumar et al (Kumar *et al.*, 2018) where crack deflections occurred at primary α laths and also suggests that the lath thickness plays an important role. Now that a heat treatment has been applied, resulting in a bi-modal microstructure (also larger α grains as well as presence of β phase), a comparison between the AF/SR LPBF Ti-6Al-4V and DA LPBF Ti-6Al-4V microstructural morphologies can be made, to better understand the morphological influence. This is discussed from a crack closure perspective and divided into extrinsic and intrinsic influences.

8.3.1 Extrinsic influence of microstructural morphology

The extrinsic influence on fatigue properties is generally considered as crack closure effects which occur behind the crack tip (Newman, 2000). As previously mentioned, the most influential mechanisms are RICC, PICC and OICC (Zerbst *et al.*, 2016). While OICC may have a significant effect, all testing was conducted in the same environment, thus any differences observed cannot be ascribed to OICC and environmental conditions (Suresh & Ritchie, 1982).

PICC is due to the plastic zone size produced ahead of the crack tip which can result in crack closure behind the crack tip due to large plastic deformation within the plastic wake (Vasudeven *et al.*, 1994). However, the influence of PICC is debated within the literature (Pippan & Hohenwarter, 2017). It is likely that plasticity can be of concern for high magnitude K_{max} type tests, as is conducted in the current investigation (Wang & Müller, 1998). Therefore, issues surrounding plasticity are discussed in section 8.3.2 and 8.5.

The behaviour of extrinsic and intrinsic influence is more observable on the ΔK_{th} versus K_{max} graph in Figure 7-13 (b) and Figure 7-16 (b). For $R < 0.6$, it can be seen that there are significant changes in ΔK_{th} with no significant change in K_{max}. For $R \geq 0.6$, it can be observed that there isn't as much of a significant change in ΔK_{th} as there is in K_{max}. Boyce and Ritchie (2001) also observed this behaviour at $R \sim 0.55$ and described it as a change in some governing mechanism where below this point, the fatigue behaviour is "closure-affected" and above it is "closure-free". The "closure-affected" region would largely be caused by RICC. A study conducted by Newman et al (2003) indicated, analytically and experimentally, that this "closure-affected" region is largely due to asperities near the crack tip (RICC). As previously discussed, the residual stress in the AF condition causes an increase in the applied *R-ratio*, resulting in R_{eff}, as shown in Figure 8-1. Another way of considering this is that due to the crack opening more (from residual stress), there is less RICC being experienced. This is highlighted in the results in Figure 8-1 (b) when the AF condition's R_{eff} is largely in agreement with the SR conditions R_{eff}. It is also assumed

that in the DA condition, no significant residual stress remains, and therefore a full RICC will be experienced in this condition for $R < 0.6$. Therefore, crack closure/opening of the DA condition was not measured in this study, however, the threshold behaviour with increasing *R-ratio* shows similar behaviour to other investigations within regions where closure is and isn't detected (Boyce & Ritchie, 2001; Oberwinkler *et al.*, 2010). Therefore, it is highly likely that the threshold behaviour, particularly in the R-constant approach, is due to RICC.

The results in Figure 7-10 and Figure 7-13 of AF and SR conditions for low *R-ratios*, particularly for the X-Z and X-Y orientations, show that ΔK_{th} has significant differences, but as the *R-ratio* increases, there is a convergence behaviour observed, due to the differences being observed at low *R-ratios*. This is argued from a global "closure-affected" perspective, i.e. RICC. As discussed in Section 8.2, primary α laths act as crack path barriers. These laths tend to fracture in a faceted manner, resulting in a crack path direction change (deflection) as well as crack branching. Overall, this can be summarised as crack tortuosity. It is this crack tortuosity which causes the apparent RICC. It is worth mentioning that RICC is not unique to the LPBF process and significant research has been conducted on it with regards to conventionally manufactured Ti-6Al-4V (Yoder *et al.*, 1979; Döker & Marci, 1983; Beghini & Bertini, 1990; Ravichandran, 1991; Ogawa *et al.*, 1992; Moshier *et al.*, 2001; ZHU *et al.*, 2018). What differentiates LPBF Ti-6Al-4V and conventionally manufactured Ti-6Al-4V, with regards to RICC, is the morphology.

This results in what is perceived to be orientation specific RICC due to the primary α lath dependency on the PBG structure, i.e. PBG governs the primary α lath orientation through the habit planes. For the three orientations, the respective crack planes experience the PBG boundary in three different ways. As has been seen in Figure 7-17 and with respect to the crack growth front, the Z-X orientation has an equiaxed-like PBG shape, while the X-Z orientation propagates parallel to the length of the PBG and the X-Y orientation perpendicular to the length of the PBG. Furthermore, the asperities caused by the primary α lath's influence on the crack path are typically contained within a PBG. This means that, per unit of crack front area, the X-Y orientation experiences the most RICC when compared to any other orientation, i.e. different orientations experience different levels of RICC. A schematic of crack front, perceived PBG shape and dominant primary α lath orientation are illustrated in Figure 8-3, Figure 8-4 and Figure 8-5. This is in agreement with the ΔK_{th} versus R results. Kumar et al (Kumar *et al.*, 2018) had also observed crack deflections along PBG boundaries and primary laths.

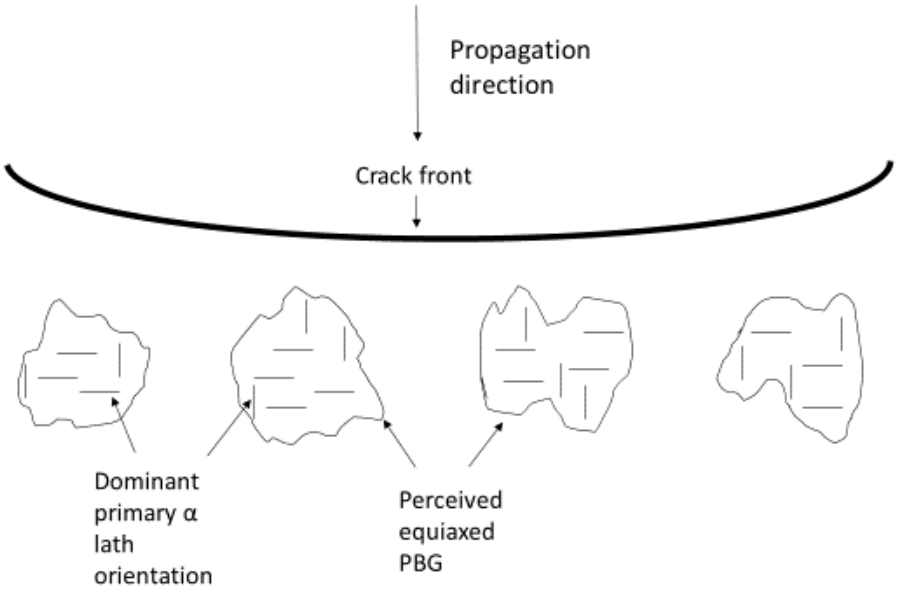

Figure 8-3: Schematic illustration of crack front interaction with PBG in the Z-X orientation as well as the dominant primary *α* lath orientation.

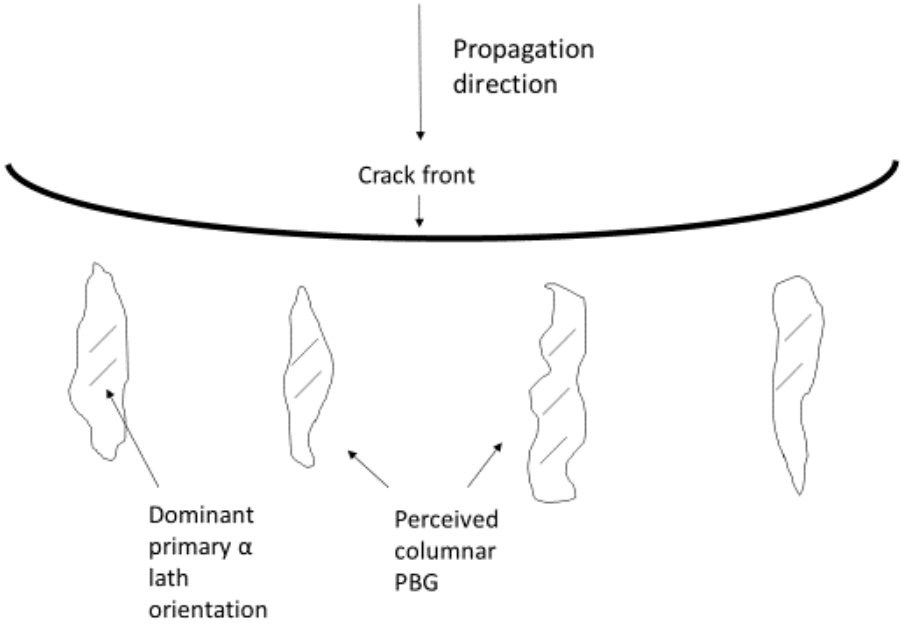

Figure 8-4: Schematic illustration of crack front interaction with PBG in the X-Z orientation as well as the dominant primary *α* lath orientation.

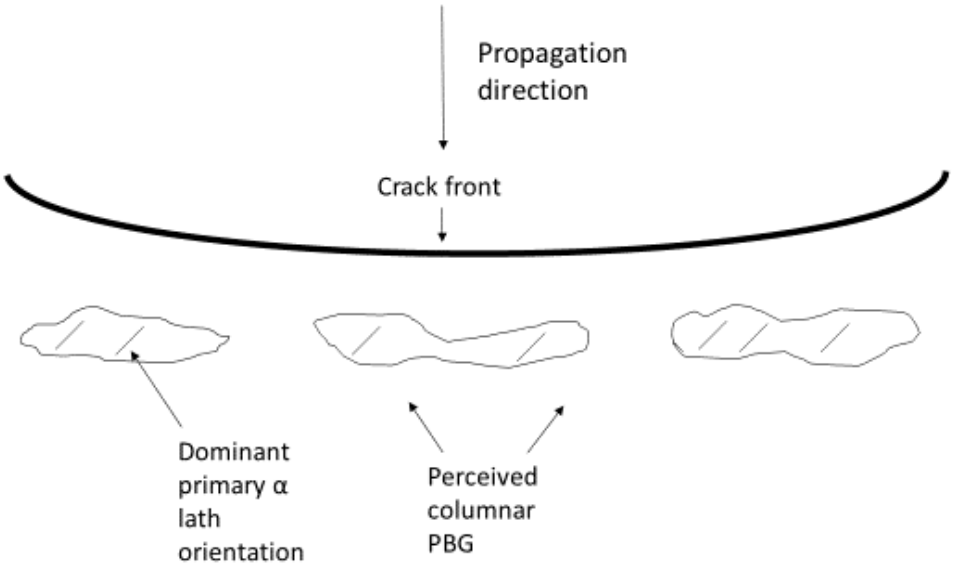

Figure 8-5: Schematic illustration of crack front interaction with PBG in the X-Y orientation as well as the dominant primary α lath orientation.

When considering the bi-modal microstructure, larger amounts of crack path tortuosity, asperities and rough fracture surfaces are observed in comparison to the LPBF microstructure. While there are noticeable differences in ΔK_{th} between the three orientations in the bi-modal microstructure, discussion regarding the differences will be reserved for Section 8.5.

The main microstructural differences between the LPBF microstructure and bi-modal microstructure are as follows: (i) the α/α' grain size and (ii) the β phase. The larger (coarser) grain size of the bi-modal microstructure causes the increase in crack tortuosity, crack deflection as well as crack branching, resulting in a larger ΔKth at a given *R-ratio*. This is a common observation in (α + β) titanium alloys (Krüger *et al.*, 2015). Furthermore, it is observed that the bi-modal microstructure has a more tortuous crack path as well as a rougher fracture surface than LPBF microstructures in Figure 7-17 and Figure 7-19. Tan et al (2015) found in a TC21 titanium alloy under transmission electron microscopy (TEM) observations, that dislocation pile ups occur on the α side of α/β interfaces. This means that during fatigue loading the alpha phase accommodates larger amounts of strain than the β phase (Tan *et al.*, 2015). Their observations also indicated that during fatigue loading, planar slip deformation occurs in the α phase and has been reported by others in various titanium alloys (Huang *et al.*, 2011; Huang *et al.*, 2017). In addition to the highly rough surface, faceted fracturing is also observed. This occurs through crystallographic cracking where aligned α laths behave as a single crystal, resulting in long continuous slips or cracks and observed as facets. While the facet fracture in itself is smooth, the deflections in crack propagation caused by it, results in crack tortuosity. While faceting is also observed in the LPBF conditions, due to the larger grain sizes in the DA conditions, the crack deflections are more

pronounced in the DA condition than in the AF and SR conditions. Further regarding the DA condition, the α_s in a transformed β matrix may not contribute on a large scale to RICC, as the faceting size would be small in comparison to α_p grain size. This was observed by Saxena and Radhakrishnan (1998). With regards to the β phase, there is now an inhomogeneity between crystals (α/β interfaces), which can cause localised strain build-up at the interface and can result in crack deflections. The β phase in itself is fairly ductile which, as discussed by Saxena and Radhakrishnan (1998), contributes to surface roughness through a micro-tearing process. Figure 8-6 shows the roughness observed on a DA fracture surface.

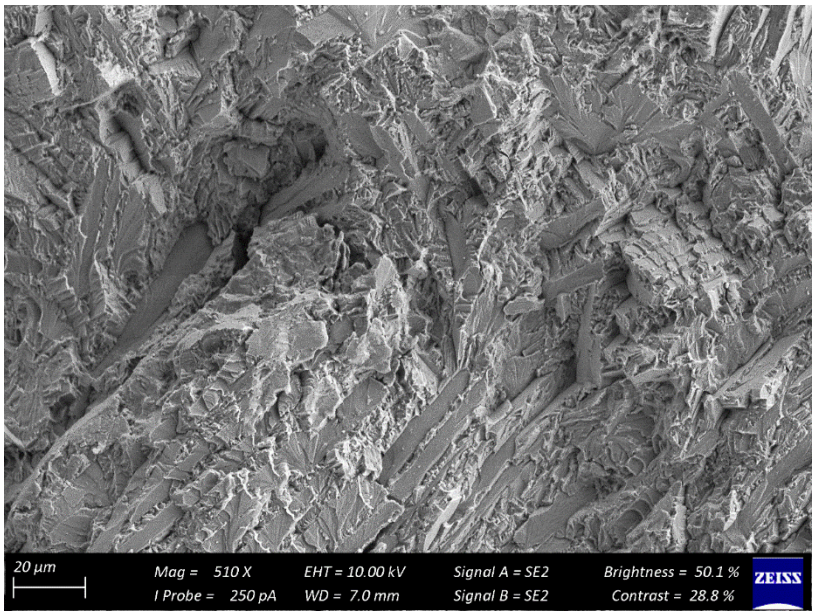

Figure 8-6: Rough fracture surface of the DA condition containing a combination of smooth facets and rough micro-plastic tearing.

While the differences observed in the DA condition's three orientations are to be discussed later, it should be noted that the fracture surface of the Z-X orientation seems to have larger amounts of facetted fractures than the X-Z and X-Y orientations as seen in Figure 7-19.

The α grain size and presence of β phase is considered as a difference between the SR and DA conditions but the PBG boundaries can be considered a similarity between the two. However, while this is a similarity, different observations can be made between the AF/SR and DA conditions:

(i) the PBG in the SR condition plays a role in the orientation of specific crack closure as discussed, and
(ii) in the DA condition, the PBG boundaries are not as easily discernible as in the AF and SR conditions. This is likely due to the increase in ductility of the DA condition.

(iii) Roughness observed in the DA condition does not show a specific containment within PBG boundaries as observed in the AF and SR conditions.

It can be observed in Figure 8-7 and Figure 8-8 that roughness isn't specifically contained to the same extent within a PBG for the DA condition, as it is contained within PBG for the AF and SR conditions. It is therefore likely that the PBGs do not play as significant a role on anisotropic crack closure as has been argued for the AF or SR condition.

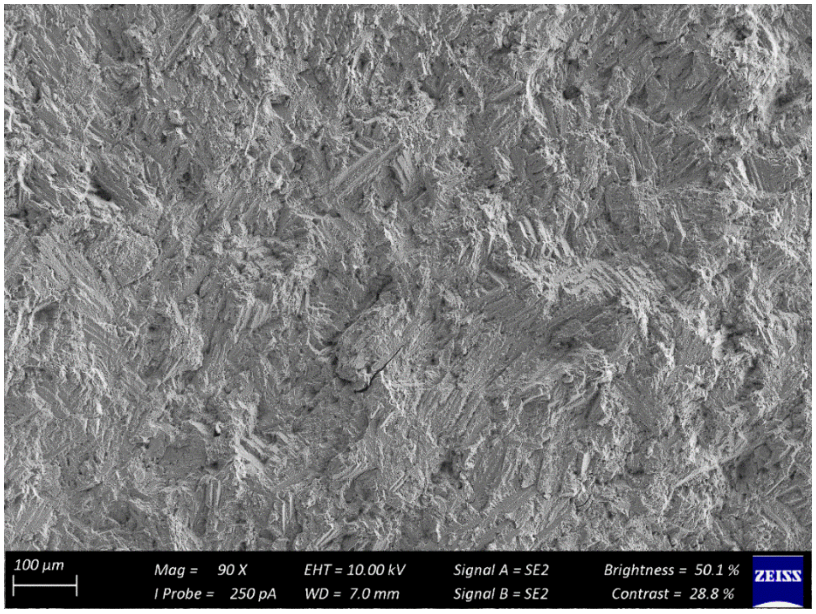

Figure 8-7: Fracture surface of the X-Y orientation in the DA condition with rough fracture not specifically contained within PBGs.

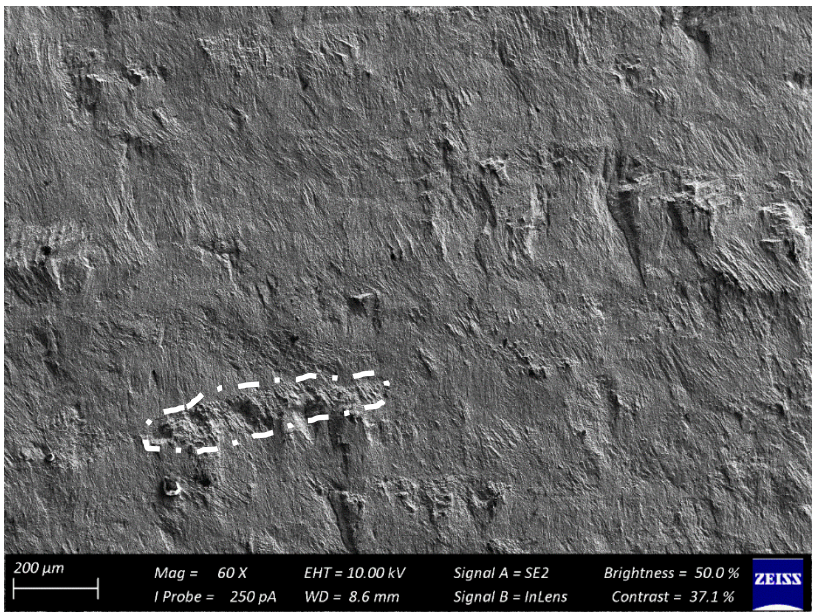

Figure 8-8: Fracture surface of the X-Y orientation in the AF condition with roughness contained with PBG shape.

8.3.2 Intrinsic influence of microstructural morphology

While global "closure-free" of fatigue cracks is occurring above $R \geq 0.6$, and closure mechanisms are generally not detectable anymore (by macroscopic techniques), Davidson (Davidson, 1992) found during in situ SEM fatigue testing, that crack closure was still occurring within 10 µm of the crack tip even though *R-ratios* were above 0.8. This is likely to still be of influence, particularly in the more coarse DA condition. However, this cannot be the only mechanism involved as there is a distinct change in behaviour for $R \geq 0.6$, when considering the ΔK_{th} versus K_{max} graphs.

The study by Kumar et al (Kumar *et al.*, 2018) on LPBF Ti-6Al-4V, discussed that for near-threshold FCGR factors such as cyclic and dynamic plastic zones should be considered. The investigation by Boyce and Ritchie (2001) considered forged bi-modal Ti-6Al-4V and the effects of load ratio on near-threshold FCGRs. Their results showed a K_{max} dependency and while Boyce and Ritchie (2001) mentioned that the precise mechanism was unclear, they noted that it appears to be caused by local plasticity.

It is commonly known within conventionally manufactured Ti-6Al-4V, that plastic deformation behaviours are influenced by factors such as the grain morphology (lamella vs. equiaxed), grain size (fine vs. coarse) and the two phase $\alpha + \beta$ (alpha + beta) structure (Ter Haar & Becker, 2018; Leyens & Peters, 2003). The investigation by Huang et al (2011) considered the cyclic deformation on the bi-modal Ti-5553 alloy. They found that the different microstructural constituents

played different roles in cyclic deformation which occur at different strain levels and different stages of cyclic stresses (Huang *et al.*, 2011). An investigation by Saxena and Radhakrishnan (1998) considered the effect of phase morphology on FCGR behaviour in $\alpha + \beta$ titanium alloy. They investigated variations of elongated and equiaxed α with metastable and transformed β (Saxena & Radhakrishnan, 1998). They concluded that fatigue crack growth resistance in $\alpha + \beta$ titanium alloys are highly influenced by the morphology of the primary α grains and the β phase matrix (Saxena & Radhakrishnan, 1998). However, they added that the extent and nature of the influence at which one of the phase's morphology occurs at, is dependent on the morphology of the other phase, i.e. it depends on which α phase morphology, elongated or equiaxed α, is paired with which β phase morphology, metastable or transformed β (Saxena & Radhakrishnan, 1998).

As previously mentioned, the main microstructural difference in LPBF is the bi-modal microstructure of: (i) α/α' grain size, and (ii) presence of β phase. However, regarding intrinsic influences, the mechanisms are not related to crack roughness, but rather the plastic flow properties of the microstructure. The α' phase is a brittle structure. This is due to the high dislocation density within an α' lath which inhibits plastic flow and increases the strength (Kumar & Ramamurty, 2019). In turn, this results in a faster crack propagation due to less energy being dissipated through plastic flow (Suresh, 1998; Kumar *et al.*, 2018). Kumar and Ramamurty (2019) and Ter Haar and Becker (2021) mention the hardness of the α' lath located at the PBG and the poor slip α' - α' transmissibility both internally and across PGB, which inhibits plastic flow. This is also observed within this investigation where fracture surfaces highlight the PBG boundaries. It is also likely that the primary α' lath, in the AF and SR conditions, plays a more dominant role in the intrinsic near-threshold behaviour than the remainder of the AF's hierarchical structure as the primary α' achieves the highest plastic strain (Ter Haar & Becker, 2021).

The α', α and β phases have different levels of strength and ductility. The low levels of threshold obtained for the AF and SR conditions are attributed to the brittle fine needle-shaped α' martensitic microstructure and dominant trans-granular quasi-cleavage microstructure. The brittle microstructure results in less plastic flow and therefore less energy dissipation. In the DA condition, both α and β phases are present, which are more ductile than the α' phase, larger amounts of plastic flow and energy dissipation, resulting in higher ΔK_{th} values.

Another mechanism associated with the β phase can be considered to be an overlap between extrinsic and intrinsic crack shield mechanisms, i.e. crack tip blunting (Saxena & Radhakrishnan, 1998; Liu & Pons, 2018). Some have described crack tip blunting as an extrinsic mechanism; however, it seems to be more of an overlap mechanism between extrinsic and intrinsic. During cyclic loading, as the crack tip opens (tearing) and extends, the crack tip becomes blunt (Aswath, 1991; Davidson *et al.*, 1991) whereas when the crack tip closes, this resharpens the crack tip. This crack tip blunting is more of a ductile phenomenon, which is enhanced by an increase in the ductility of a material. Furthermore, for the near-threshold FCGR

regime, a coarser grain microstructure has been linked to an increase in ΔK_{th} (Nalla, Boyce, *et al.*, 2002; Leyens & Peters, 2007; Leuders *et al.*, 2012; Becker *et al.*, 2021). Therefore, crack tip blunting is likely to be more pronounced within the DA condition as opposed to the more brittle AF and SR microstructure conditions, resulting in the DA condition having a larger ΔK_{th} than the LPBF conditions. Saxena and Radhakrishnan (1998) reported that the crack tip blunting is caused by the ductile β phase. The differences observed in orientation for the DA condition are discussed in Section 8.5.

In light of the above on extrinsic and intrinsic influences, both types of influences rely on the morphological texture of the material. However, different mechanisms are employed for the two types of influences. For the extrinsic influences, the differences in morphological texture between AF, SR and DA conditions result in different levels of crack tortuosity and thus different levels of RICC. Whereas in the intrinsic type, the difference's morphological texture between the AF, SR and DA conditions results in differences in plastic flow and energy dissipation. It should be noted that at low *R-ratios*, both intrinsic and extrinsic closure mechanisms are being experienced, while at high *R-ratios* the extrinsic mechanisms have been largely reduced.

8.4 Critical parameters

Using the results and the above discussion, one can derive the two parameter approaches' critical parameters. The intrinsic fatigue crack growth rate threshold for both the AF and SR specimens was ΔK_{th} ~ 1.8 MPa√m in the Z-X orientation and ΔK_{th} ~ 1.5 MPa√m in both X-Z and X-Y orientations. Tarik Hasib et al (Tarik Hasib *et al.*, 2020) obtained a ΔK_{th} ~ 1.52 MPa√m and ΔK_{th} ~ 1.82 MPa√m at R = 0.1 in the Z-X and X-Z orientations, respectively, for their AF condition. However, they measured the K_{cl} via the compliance technique to obtain a ΔK_{eff} and found that there was no measurable crack closure from this technique, i.e. the crack was open for the entire range of $K_{min} - K_{max}$. This means that their $\Delta K_{th} = \Delta K_{eff,th}$. This is somewhat in agreement with the current investigation as there was a lack of dependency on *R-ratio* in the Z-X and X-Z orientation, with less than 10% change in ΔK_{th} with respect to the *R-ratio*. Leuders et al (2012) obtained similar threshold values of ΔK_{th} = 1.7 MPa√m and ΔK_{th} = 1.4 MPa√m at R = 0.1 in the Z-X and X-Z orientations, respectively, for the AF condition. Given that it was found in this investigation that the Z-X and X-Z orientation don't exhibit a pronounced dependency on *R-ratio* and Tarik Hasib (2020) measured no crack closure in the same orientations in the AF condition, it is possible that the same may apply to Leuders et al (2012) with respect to *R-ratio*. Interestingly, the investigation by Kumar et al (Kumar *et al.*, 2018) obtains threshold values between ΔK_{th} = 5.3 – 5.8 MPa√m, depending on the various process parameters that were selected in their study as well as in the SR state (650°C for three hours). However, their near-threshold values were reported at ~ $2\ x\ 10^{-9}\ m/cycle$. This is an entire order of magnitude higher from the defined threshold crack growth rate of $1\ x\ 10^{-10}\ m/$

$cycle$, as defined by the ASTM E647 standard (ASTM, 2015). Furthermore, it is observed in the current investigation, the investigation by Tarik Hasib et al (2020) as well as the investigation by Leuders et al (2012) that the typical threshold-asymptotic-behaviour, i.e. X-Z decrease in crack growth rate at a constant ΔK, generally only starts in the lower levels of the $10^{-10}\ m/cycle$ magnitude. This means that there may be a significant decrease in the reported ΔK_{th} of Kumar et al (2018) which will decrease in accordance to the Paris law, until the threshold-asymptotic-behaviour is reached.

An intrinsic critical K_{max} of ~ 3 MPa√m was measured in the AF and SR conditions. This K_{max} value is considered the lowest-K_{max} stress intensity required as the crack driving force in order to break crack tip bonds. Interestingly, the measured intrinsic K_{max} does not show an observable dependency on orientation as the intrinsic ΔK_{th} showed. It is likely that this may be due to the nature of the brittle martensitic microstructure in the AF and SR conditions. However, in order for a fatigue crack to propagate, dynamic loading is required. The previously mentioned intrinsic thresholds, i.e. for AF and SR specimens, were ΔK_{th} = 1.8 MPa√m in the Z-X orientation and ΔK_{th} = 1.5 MPa√m in both X-Z and X-Y orientations and these are also required. Both the intrinsic K_{max} and intrinsic ΔK_{th} parameters need to be fulfilled in order for a crack to propagate. However, this is based on the material of this investigation, which may differ from another investigation using different process parameters on the LPBF Ti-6Al-4V. This is observed within Tarik Hasib et al (2020) as well as Leuders et al (2012) in which, what can be considered as their intrinsic K_{max}, is below 2 MPa√m. As a result of the differences in scan strategy, the effect on PBG may cause differences in the primary α' lath aspect ratio, which in turn can result in a different fatigue behaviour. Furthermore, minor differences in O, N and H in the chemical composition of the Ti-6Al-4V powder may also have a role in observing some differences in mechanical properties.

Considering the DA condition, the intrinsic ΔK_{th} for the Z-X and X-Z orientations ~ 2.7 MPa√m and ~ 3.5 MPa√m in the Z-X orientation, the possible reason for the difference in the X-Y orientation will be discussed in Section 8.5 below. This is approximately a 50% increase in intrinsic ΔK_{th} for the Z-X orientation, 80% for the X-Z orientation and 130% for the X-Y orientation. It was discussed in Section 8.3.2, above, that the increase in ΔK_{th} was due to the increase in α grain size and the presence of the β, which ultimately increases the plastic flow and energy dissipation properties of the material. Interestingly, for all three orientations, the intrinsic critical K_{max} is ~ 6 MPa√m.

One of the theories on near-threshold FCGRs is the blocked slip band model (Li, 1996; Tarik Hasib *et al.*, 2020). It relates the ΔK_{th} to the microstructural length scale and yield strength. The concept behind this model is that the propagation of a crack occurs due to the transfer of slip from one grain to the next. However, this is typically more apparent in finer grained materials. The relationship of this model is as follows:

$$\Delta K_{th} \propto \sigma_y \sqrt{d} \tag{8-4}$$

Where d is the α lath thickness. The relationship in Equation (8-4) is plotted in Figure 8-9 and uses the ΔK_{th} obtained at the highest *R-ratio* for all three conditions and orientation. The plot shows a somewhat linear relationship between AF, SR and DA conditions.

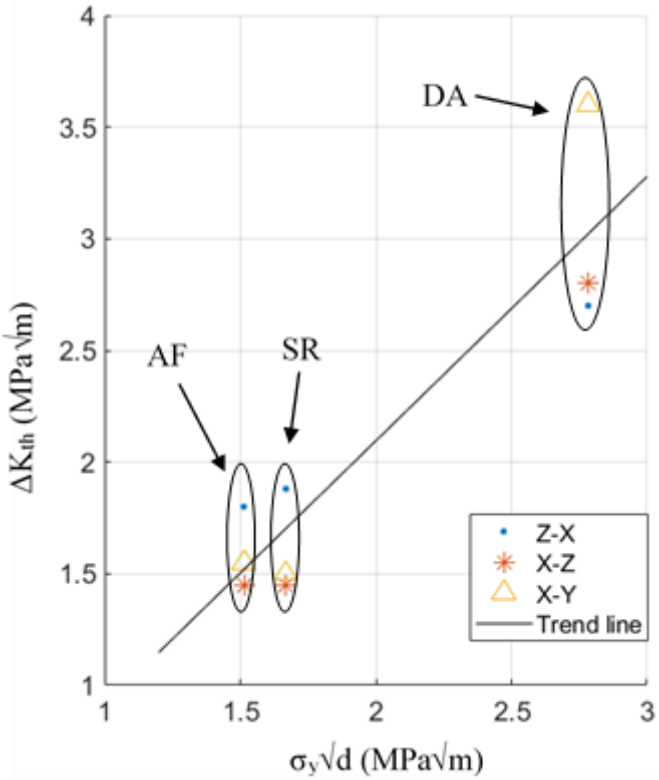

Figure 8-9: The relationship between ΔK_{th} and the microstructural characteristic dimension.

8.5 Comparison to conventional Ti-6Al-4V

The similarity between conventionally manufactured and LPBF Ti-6Al-4V is that chemically, the materials are the same. The main differences between conventionally manufactured and LPBF Ti-6Al-4V is the starting microstructure, residual stress and porosity. It is well established that porosity acts as crack initiation sites (Li *et al.*, 2016; Tammas-Williams *et al.*, 2017; Agius *et al.*, 2018). Residual stress has been shown to reduce crack closure (increase *R-ratio*) as has been discussed earlier. The material's microstructure is what can be elaborated on.

Anneal heat treatments change the morphology of the LPBF microstructure and reduces the variants (transformation occurs) which results in a stronger texture but retains the PBG boundary. By conducting appropriate heat treatments, LPBF Ti-6Al-4V can obtain a similar morphology to conventionally manufactured Ti-6Al-4V, i.e. one can obtain lamellar, bimodal and equiaxed microstructures in LPBF Ti-6AL-4V, albeit with a PBG boundary. However, due to the starting microstructure in LPBF being different to conventionally manufactured, the size of the grains may differ. Furthermore, the presence of PBG in LPBF Ti-6Al-4V is typically not found within conventionally manufactured Ti-6Al-4V.

Bantounas et al (2009) investigated the fatigue behaviour in forged bars of Ti-6Al-4V which had been cross-rolled and unidirectionally rolled. They observed an influence of α grain orientation and fatigue performance, i.e. the more unfavourable the grains are orientated, the weaker the fatigue performance. It was found that Ti-6Al-4V with the least amount of a basal slip regime had the longest fatigue life and those with the largest amount of a basal slip regime had the shortest fatigue life.

Oberwinkler et al (2010), considered two types of forgings, namely V-shape and side pressed pancake forging, along with a mill anneal and solution treatment, which were compared to an as-received feedstock billet. The as-received feedstock billet has no crystallographic texture (globular equiaxed) (Lütjering, 1998; Oberwinkler *et al.*, 2010). From the fatigue life perspective, the textured material had similar fatigue strengths to each other and also had greater fatigue strengths than the non-textured material. While Oberwinkler et al (2010) links this to the α grain size and (α + β) content, it is also likely that the forgings produced less favourable grain orientations for crack initiation in comparison to the feedstock billet. This would be in agreement with the work of Bantounas et al (2009). With regards to near-threshold FCGRs, the reverse occurs, i.e., the globular equiaxed material has the largest ΔK_{th} while the textured material had the lowest. Oberwinkler et al (Oberwinkler *et al.*, 2010) linked this to the α grain size and the connectivity of α regions. This in itself may be extended to the flow properties of the material, i.e., morphology.

In the current investigation it was discussed that microstructure can be differentiated as having crystallographic and morphological texture. It was further discussed that anisotropic effects on ΔK_{th} were influenced to a greater extent by the morphological texture than by the crystallographic texture. What seems to be evident when considering the works by Bantounas et al (2009) and Oberwinkler et al (2010) and the current investigation is that crystallographic texture manifests its influence more prominently in the resistance to crack initiation regime (fatigue life) whereas the morphological texture influence is more prominent in the resistance to crack propagation regime (ΔK_{th}). However, in the current investigation, along with Oberwinkler et al (2010) and Boyce and Ritchie (2001), various *R-ratios* were considered. In all three studies, the general trend shows a fairly large scatter band in ΔK_{th} at low *R-ratios*, for various microstructural conditions, and a smaller scatter band in ΔK_{th} at high *R-ratios* (0.7 in Oberwinkler et al (2010) and 0.92 in the current

investigation). This behaviour is shown in Figure 8-10. It is hypothesised that for a large variation of the *R-ratio* in the near-threshold FCGRs regime, morphological texture has a larger influence than crystallographic texture, but at very high *R-ratios*, the influence of morphological texture seems to diminish. This is more evident in the works of Boyce and Ritchie (2001).

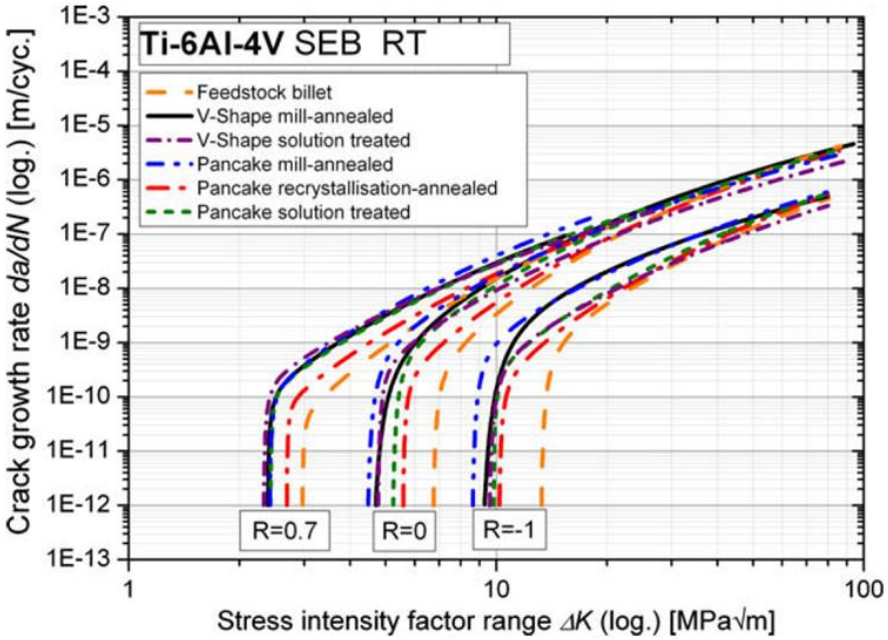

Figure 8-10: Near-threshold graph at various *R-ratios* with a smaller ΔK_{th} scatter band at *R* = 0.7 than at *R* = 0 and -1 (Oberwinkler *et al.*, 2010).

The investigation conducted by Boyce and Ritchie (2001) used *R-ratio* that extended to above 0.97. In Boyce and Ritchie's work (2001), which also considers forged material but compared bi-modal structures with lamellar structures, they found that at very high load ratios, any difference in crack growth resistance (observed at lower *R-ratios*) was eliminated. While the specifics of why the behaviour of the threshold of conventionally manufactured Ti-6Al-4V is like this at high *R-ratios* is not currently understood, it is possible that under high enough *R-ratios*, LPBF Ti-6Al-4V may behave in the same way. However, further investigation is required to support this. For both microstructures in Nalla et al (2002), it is understood that these were made from the same forged material. It is possible, based on the work of Bantounas et al (2009), that because Nalla et al (2002) used the same forged material for the different microstructures, the crystallographic texture in the two structures should be similar. It is then likely that due to the crystallographic texture of the two microstructures that this resulted in comparable ΔK_{th} values at very high *R-ratios*. However, an in-depth investigation is required to confirm this.

With regards to the AF and SR conditions, it is typically welded structures within conventionally manufactured Ti-6Al-4V which produce fine acicular microstructure in the heat affected zone (HAZ) that can be compared to LPBF Ti-6Al-4V. The HAZ results in lower structural integrity than the parent material (John *et al.*, 2003). This is also observed in the investigation by John et al (2003) in which friction stir welded conventionally manufactured Ti-6Al-4V obtained a ΔK_{th} ~ 1.7 MPa√m, comparable to that obtained for LPBF Ti-6Al-4V. They further obtained a similar critical K_{max} of ~ 3 MPa√m to the LPBF Ti-6Al-4V of this investigation.

In the work of Nalla et al (2002), they obtained a "worst case scenario" ΔK_{th} of ≈ 1.9 MPa.m$^{0.5}$ for their bi-modal microstructure. However, in the current investigation, ~ 3.5 MPa√m and 2.7 MPa√m were obtained. It is generally accepted that factors such as grain size, morphology, colony size, lath size, α_p content (volume fraction), amongst others, affect the fatigue properties of Ti-6Al-4V (Wu *et al.*, 2013b; Kumar *et al.*, 2018). Furthermore, Oberwinkler et al (2010) showed that the ΔK_{th} is not only influenced by the α grain size, but also by the connectivity of α regions. This resulted in forged and solution treated microstructures producing lower ΔK_{th} values than the feedstock billet (equiaxed), which had separated α grains. It is also likely that the differences in the α region's connectivity between Nalla et al (Nalla, Boyce, *et al.*, 2002) and the current study has a role to play. Oberwinkler (2010) defines the connectivity of α regions as the ratio of mean size of interconnected α regions , α_{ic}, and the mean size of the primary α grain size, α_p. Oberwinkler (2010) also obtained ΔK_{th} for bi-modal structures at R = 0, ΔK_{th} ≈ 5.1 MPa.m$^{0.5}$ for pancake bi-modal and ≈ 4.8 MPa.m$^{0.5}$ for V-shape bi-modal structures. At R = 0.7, ΔK_{th} ≈ 2.3 MPa.m$^{0.5}$ for both bi-modal shapes. While the ΔK_{th} in this study is higher than that of Oberwinkler (Oberwinkler *et al.*, 2010), the results are fairly comparable. It is likely that the differences in grain size, shape, volume fraction, precipitates, amount of basal slip regime and α grain connectivity all play an influential role in causing the differences observed.

What differentiates LPBF Ti-6Al-4V from conventionally manufactured Ti-6Al-4V is the PBG morphology and its influence on the primary α' lath's morphology. It was shown by Ter Haar and Becker (2021) that within the XY-plane and ZX/ZY plane, that α' lath parameters, such as lath length and width (therefore, aspect ratio) differ. While there is a strong affinity for lath's angle to form at 45° to the Z-axis, this is more dominant in the ZX/ZY plane whereas in the XY plane ~ 0° and ~ 90° is more dominant. These dominant lath angles, in different crack planes, will play a role in anisotropic effects. Interestingly, Ter Haar and Becker (2021) found that after applying a beta anneal, the PBG morphological texture was altered, however, the crystal texture remained unchanged. They further explained that this may cause the ~ 45° lath angle to remain unchanged after the anneal as well. Whereas with wrought material undergoing a beta anneal, nucleation and growth occurs at newly unstrained and differently textured PBGs (Pilchak *et al.*, 2018; Ter Haar & Becker, 2021).

As previously discussed, primary α' laths act as barriers which have predominantly faceted crack growth resulting in crack tortuosity and RICC. The complexity of LPBF produced Ti-6Al-4V is that process parameters influence the AF PBG morphology. This in-turn can affect the primary α' laths (length and thickness) due to its dependency on PBG morphology. The studies by Kumar et al (2018) and Cepeda-Jimenez et al (2020) showed that by adjusting the LPBF process parameters for Ti-6Al-4V, they were able to vary the size and morphology of PBG, which in turn altered the size and texture of the α/α' laths. From a crack propagation perspective, this can have implications on both extrinsic and intrinsic properties. Depending on what the morphological change is, the α/α' lath morphology (based on the PBG morphology) can reduce or increase RICC. Furthermore, the PBG morphology can be near equiaxed in both XY and ZX/ZY crack planes, such as is the case with Kumar et al (Kumar *et al.*, 2018). This will alter the perceived PBG shape by the crack front and reduce the anisotropy observed in this investigation along with investigations found in the literature. From an intrinsic perspective, which has been described earlier as being influenced by plastic flow and energy dissipation properties of the microstructure, properties may also be altered. However, it should be noted that while equiaxed PBGs can be achieved, resulting in the same lath aspect ratio in XY and ZX/ZY planes, one may still retain the PBG crystallographic texture.

The crystallographic texture will cause the lath orientation to be textured at a specific angle. Ter Haar and Becker (2021) propose that both crystallographic and morphological texturse generally contribute to anisotropic deformation behaviour. Furthermore, due to poor α'-α' slip transmissibility, Ter Haar and Becker (2021) argue that PBG boundaries inhibit deformation. This means that for a near-equiaxed PBG shape in the Z-X orientation crack plane (XY plane) and columnar PBG shape in the X-Z and X-Y crack planes (ZX/ZY plane), the Z-X orientation crack front would have a higher density of PBG and therefore a lower amount of deformation compared to the remaining orientations. The lower amount of deformation means that there is less plastic flow and energy dissipation, resulting in a lower ΔK_{th}, i.e. anisotropic behaviour. However, if all crack planes were to perceive a near-equiaxed PBG shape, as is the case in Kumar et al (Kumar *et al.*, 2018), this would reduce anisotropic behaviour in the intrinsic regimes. While the above explanation uses the concept of the columnar PBG changing to a near-equiaxed PBG shape due to process parameters, this is just used as an example. The idea is that any change of the columnar PBG morphology, whether it be made longer/shorter or wider/thinner, and the resultant effect on the primary α' lath morphology, can have implications on both extrinsic and intrinsic influences of near-threshold behaviour.

With regard to differences in anisotropic behaviour between the AF and SR conditions and the DA condition, there isn't a specific convergence behaviour observed in the DA condition as has been observed in the AF and SR conditions. In AF and SR conditions, specifically the X-Z and X-Y orientation, from low *R-ratios* to high, there was a convergence behaviour observed. In the DA condition, anisotropic behaviour manifests itself more prominently above $R = 0.3$, i.e. more so

in the global "closure-free" region. Kumar and Ramamurty (2019) also observed the reduction of anisotropic behaviour after the annealing process. It is explained that due to the hard α' phase along the PBG boundaries, strain localisation occurs, which results in the observed anisotropic behaviour. As previously mentioned, certain areas of the AF and SR fracture surface highlighted the PBG shape fracture. These PBG fractures were somewhat observable on the bi-modal fracture surface but were not as distinct as the LPBF conditions. This is likely due to the transformation into α/β microstructure, which results in less stress localisation because of higher ductility (Kumar & Ramamurty, 2019).

With regards to anisotropy observed in the DA condition, the X-Y orientation had the largest near-threshold FCGRs while the Z-X orientation had the lowest. There are two main observable differences between these orientations on their fracture surfaces:

(i) The Z-X orientation has larger amounts of faceted fractures, and
(ii) Perceived PBG orientation.

As previously mentioned, faceted fracture has been linked to lower resistance to fatigue crack initiation. It is then likely that the increased faceted fracture observed is one of the reasons for a lower ΔK_{th} in the Z-X orientation than in the X-Y orientation. It is possible that the cyclic plastic zone and it's interaction with the characteristic PBG morphology's interaction with the crack front may also influence the near-threshold FCGRs via stress dispersion. The plastic zone size for plain strain conditions is computed by:

$$r_p = \frac{1}{6\pi}\left(\frac{K}{\sigma_y}\right)^2 \tag{8-5}$$

Where K is the K_{max} and σ_y is the yield strength. For the Z-X orientation in the DA condition, this results in a plastic zone size of ~ 23 μm, ~ 88 μm in the X-Z and ~ 115 μm in the X-Y orientations. While the X-Y orientation has the largest ΔK_{th} in the DA condition as well as the largest plastic zone size, the X-Z orientation with a nearly four times larger plastic zone size as the Z-X orientation, has a similar ΔK_{th}.

With regards to the DA condition, the X-Z orientation's near-threshold FCGRs are somewhat in between the Z-X and X-Z orientation for most *R-ratios*. One observes similar faceting fracture to that of the X-Y orientation, i.e. less faceting than the Z-X orientation. This may be one of the reasons why the X-Y orientation has a somewhat larger near-threshold FCGRs than the Z-X orientation. Furthermore, with less observable faceting in the X-Z and X-Y orientation, there is more ductile tearing on these two orientations than in the Z-X orientation which may also contribute to the observable differences in ΔK_{th}. However, at a large enough *R-ratio*, the X-Z orientation's ΔK_{th} is comparable to that of the Z-X orientation.

This, to an extent, is an expected near-threshold behaviour based on the earlier discussion on the scatter band of ΔK_{th} for different Ti-6Al-4V microstructures and forging directions reducing as the *R-ratio* increases. It should be mentioned that it takes a larger *R-ratio* for the X-Z orientation to achieve a similar ΔK_{th} than the Z-X orientation. With regards to the PBG boundary shape interacting with the crack front, the orientation of it differs between the Z-X (equiaxed) and X-Z orientations (elongated in crack direction). However, the crack front will experience a similar amount of PBG per unit length, i.e. the width/diameter of the PBG. Based on the above discussion relating to Nalla et al (2002) and Oberwinkler (Oberwinkler *et al.*, 2010), it is likely that under a larger *R-ratio*, i.e. $0.95 > R > 0.99$, the X-Y orientation's ΔK_{th} will become more comparable to that of the Z-X and X-Z orientation. However, further investigation is required to observe if this will be the case.

8.6 Electron beam powder bed fusion

The study by Galaragga et al (2017) focused on FCGR and FCGR threshold of AF and HT electron beam powder bed fusion (EBPBF) Ti-6Al-4V. Galaragga et al (2017) investigated two build orientations in which the crack plane was (i) parallel and (ii) perpendicular to build direction. Two conditions were investigated, namely (i) AF and (ii) β-annealed. The investigation was conducted on CT specimens according to the ASTM E647 standard (ASTM, 2015). Furthermore, the effect of stress ratio was considered by conducting tests at three different stress ratios, i.e. 0.1, 0.5 and 0.8. The main aim of Galaragga et al's (2017) investigation was to better understand the relationship between FCGR and the EPBF Ti-6Al-4V microstructures.

Microstructurally, there are both similarities and differences between LPBF and EPBF. The main similarity between the two is that both techniques produce columnar prior β grains which are oriented in the build direction. The main difference between the two is that LPBF produces brittle martensitic α' laths within the prior β grain whereas EPBF produces an $\alpha + \beta$ lamellar structure within the prior β grain. This $\alpha + \beta$ lamellar structure is typically Widmanstätten, also known as a basketweave pattern. It should be noted that the prior β grain morphology transforms from columnar to equiaxed when it undergoes a β anneal heat treatment.

Galaragga et al (Galarraga *et al.*, 2017) found that the X-Z orientation had, on average, a 15% higher ΔK_{th} than the Z-X orientation in the AF condition for all *R-ratios* tested. They used an adjusted compliance ratio technique to evaluate crack closure levels and found that the X-Z orientation experienced more RICC than the Z-X orientation in the AF condition. It was argued that the larger experienced RICC was due to the crack's interaction with the orientation of prior β grains and build layers which intensified crack tortuosity, resulting in a more energy demanding X-Z orientation. Based on the arguments from the current dissertation, it is also likely

that variations in residual stress in the orientations may cause the Z-X orientation's crack to open more and experience less RICC.

When comparing the near-threshold fatigue crack growth rate results between EPBF and LPBF, it is found that the EPBF Ti-6Al-4V, in both Z-X and X-Z orientations, have superior ΔK_{th} values than the LPBF Ti-6Al-4V of this study, as well as that of Tarik Haseb et al (2020) and Leuders et al (2012). This is likely due to the larger $\alpha + \beta$ lamellar structure as well as the presence of β which results in larger RICC as well as better energy dissipation, causing higher ΔK_{th} in the EPBF Ti-6Al-4V. Galaragga et al (2017) also found that the prior β grain in EBPBF Ti-6Al-4V influenced the crack path. In addition, Galaragga et al (2017) also found that crack paths are influenced by scanning layers, resulting in the layers affecting the crack path more in the X-Z orientation than the (perpendicular scan layers) Z-X (parallel scan layers). However, this observation is typically not found within LPBF studies, including the current investigation.

The β-anneal heat treatment resulted in a 35-45% increase in ΔK_{th} compared to the AF counterparts. The transformation of the microstructure eliminated the anisotropy behaviour observed in the AF condition and also considerably increased the RICC experienced. These changes were related to the coarsening of the microstructure and resulted in an increase in RICC. Typically, within LPBF Ti-6Al-4V, when an annealing heat treatment is applied (above or below the β transus), increases above 30% in ΔK_{th} are observed. Within the current study, Tarik Hasib (2020), Leuders et al (2012) and Kumar et al (Kumar & Ramamurty, 2019), all observe increases in ΔK_{th} after annealing.

8.7 Laser direct energy deposition

Zhai et al (2016) investigated FCGR and FCGR-thresholds of laser direct energy deposition (LDED) Ti-6Al-4V. Two build orientations were considered, namely: X-Z and Z-X. The conditions considered were AF and HT. However, two different build parameters were also considered in order to better understand the microstructural mechanisms' influence. In this study, they considered two *R-ratios*, i.e. 0.1 and 0.8.

It was found that the laser engineered net shaping (LENS) Ti-6Al-4V, for both low power (LP) and high power (HP) as well as AF and HT, produced a lower K_{th} than that of mill annealed equiaxed Ti-6Al-4V. Zhai et al (2016) concluded that it was the α phase morphology which was the controlling factor due to the HP (coarser α phase morphology) having a higher K_{th} and lower FCGR than the LP (fine α' phase morphology) condition. After the α' decomposition through the annealing step, it was found that the time at temperature did not alter the size and morphology of the α, which made no significant change to the ΔK_{th} and Paris regime between AF and HT. As a result of there being no significant change in α grain size and morphology, it is expected that no significant change in ΔK_{th} should be observed. It was further

observed that crack propagation parallel to the prior β grains and perpendicular to the build layers caused more tortuosity in the crack path, leading to larger RICC effects.

Zhai et al (2016) further observed microstructurally-small crack behaviour. It was found that the propagation of small cracks causes acceleration and retardation of FCGR in long cracks. Furthermore, small cracks were found to be influenced by prior β grains as barriers. In addition, Zhai et al (2016) show that small crack propagations occur at lower ΔK's than the long crack ΔK_{th}. They highlight the importance of considering small crack behaviour when using FCGR in design.

Comparing the LENS Ti-6Al-4V with the EBPBF Ti-6Al-4V, shows that the EBPBF produces larger ΔK_{th} values than that of the LENS material. LENS Ti-6Al-4V, in comparison to the LPBF Ti-6Al-4V of this study, has similar ΔK_{th} values in the AF condition. The reason for the similarities with LPBF and differences to EPBF is because of the α phase morphology and size. Both LPBF and LENS have a fine α' phase with no presence of β, while the EPBF does not have α' phase present and has larger α phase grains as well as β phase present. In both the works of Galaragga et al (Galarraga *et al.*, 2017) and Zhai et al (Zhai *et al.*, 2016), they have observed that the build layer boundaries have a noticeable influence on the fatigue crack path, however, this hasn't specifically been observed/investigated in the fatigue behaviour of LPBF Ti-6Al-4V. Interestingly, LENS layer thickness is typically an order of magnitude (100's microns) larger than LPBF and EPBF (typically 10's of microns). It may be of value for LPBF Ti-6Al-4V research to investigate build layer boundaries and the influence on fatigue behaviour.

8.8 Application

Typically, the ΔK_{th} is used for applications in fatigue design purposes. With regards to LPBF (and AM in general), the concern lies in the inherent porosity/defects found within LPBF material which act as stress raisers/crack initiation sites. Leuders et al (2012) found 0.23% porosity in LPBF specimens while Kasperovich and Hausmann (2015) found 0.08% after applying optimised manufacturing settings. These pores and defects are typically gas and a lack of fusion pores (Liu & Shin, 2019). While some pores (gas pores) tend to have spherical shapes, lack of fusion pores tend to have irregular shapes with sharp tips (Anderson, 2003). This means that while some porosity exists, its shape can also influence its stress raising capabilities in comparison to another porosity (Anderson, 2003). Furthermore, factors such as the position of the pore relative to the surface, pore tip radius, pore size and interaction with surrounding pores are all influencing factors (Anderson, 2003).

Even though flaws pose a problem for fatigue crack initiation, for simplicity and the unavailability of fracture mechanics solutions for complex geometries, flaws are ideally characterised based on their planar shape (Anderson, 2003). Typically, the SIF can be formulated as:

$$\Delta K = Y\sigma\sqrt{\pi a} \tag{8-6}$$

Where Y is a geometric function, σ is the applied stress and a is the crack length. Equation (8-6) can be adjusted as shown by Cao et al (2018):

$$\Delta K = Y\sigma(\pi\sqrt{area})^{1/2} \tag{8-7}$$

Where *area* is the characteristic planar area obtained through flaw characterisation. If $\Delta K > \Delta K_{th,eff}$, a crack will initiate from the flaw, propagate and eventually fracture. Equation (8-7) can be further manipulated to use the $\Delta K_{th,eff}$ obtained in this study, with typical fatigue stresses under service conditions in order to obtain a threshold area, A_{th},. This A_{th} gives the area of a flaw which should not be exceeded under operational loads if crack initiation (from a defect) is not part of the "fitness of purpose" of the structure.

Furthermore, various structural integrity assessment procedures typically assume a mode I loading crack propagation scenario even though mix-mode loading may be present (Anderson, 2003). By using these structural integrity assessment procedures such as BS 7910 (previously PD 6493), SINTAP, API 579 and ASME, amongst others, one is able to assess the flaw for the structure's "fitness of purpose" as well as the structure's defect tolerance. By knowing the ΔK_{th}, operating loads and flaw characteristics, one will be able to determine whether or not the flaw will produce a crack which will propagate and eventually cause fatigue failure. Furthermore, there are structures which can tolerate crack propagation up to a certain level in which information from the Paris regime and fracture toughness can be used. It should be noted that a significant amount of information regarding the Paris regime and fracture toughness data is available from the author of this investigation and multiple additional literature sources. However, with all conventionally manufactured methods, a defect free material is never truly achieved. Therefore, a "living with defects" approach is typically used through the various structural integrity assessment procedures. With regards to LPBF produced material, in this case Ti-6Al-4V, a similar approach will likely be utilised as opposed to aiming to remove all defects caused by the manufacturing process. Thus, by obtaining a near-intrinsic ΔK_{th}, calculations can be made to know whether or not the current typical levels of defects are acceptable for the required damage tolerant design methodologies.

8.9 Summary

Chapter 8 attempted to provide the meaning and relevance of the obtained results. With regards to residual stress, it was shown that larger residual stresses produced larger crack tip openings, i.e. orientations with larger residual stress had larger crack tip openings. This in turn alters the applied ΔK and *R-ratio*. When accounting for

the effect of residual stress, based on the crack openings in the AF condition, both AF and SR condition's near-threshold FCGRs show excellent agreement. Furthermore, it was observed that the residual stress influence is more prominent in the low *R-ratio* regimes, where K_{max} is low, and less prominent in the high *R-ratio* regimes, where K_{max} is high. The AF and SR condition's microstructure shows similarities to conventionally manufactured Ti-6Al-4V in that fracture surfaces have areas of faceted planes, i.e., similar cracking mechanisms.

For the different orientations considered in the AF and SR conditions, there were no significant differences observed in the crystallographic texture. Therefore, it is likely that the influence on near-threshold FCGR behaviour is due to the morphological texture. The microstructural morphology's influence on near-threshold FCGRs is considered from a crack closure perspective and is broken into extrinsic and intrinsic mechanisms. The extrinsic mechanisms are related to the global "closure-affected" region in which RICC is the main closure mechanism discussed. The RICC is due to the primary α lath dependency on the PBG structure. More specifically, the asperities caused by the primary α lath influence on the crack path are typically contained within a PBG which mean that per unit of crack front area, different orientations experience different levels of RICC. The DA conditions larger amounts of crack path tortuosity and as a result asperities and rough fracture surfaces are observed in comparison to the AF and SR conditions. Reducing crack closure sufficiently, a global "closure-free" regime can be obtained in which the intrinsic influence of microstructural morphology can be assessed.

The intrinsic mechanisms were argued from a plastic flow property of the microstructure's perspective. The α' phase for the AF and SR conditions is a brittle structure which inhibits plastic flow. Furthermore, it is observed to have poor slip α' - α' transmissibility both internally and across PGB, which also inhibits plastic flow. In the DA condition, both α and β phases are present, which are more ductile than the α' phase which results in larger amounts of plastic flow and energy dissipation, resulting in higher ΔK_{th} values. Furthermore, it is likely that the DA condition undergoes crack tip blunting due to its ductile nature in comparison to the AF and SR conditions. It was found that an intrinsic critical K_{max} of ~ 3 MPa$\sqrt{m}$ was measured in the AF and SR conditions and an intrinsic threshold of ΔK_{th} ~ 1.8 MPa$\sqrt{m}$ in the Z-X orientation and ΔK_{th} ~ 1.5 MPa$\sqrt{m}$ in both X-Z and X-Y orientations. In the DA condition, all three orientations have an intrinsic critical K_{max} ~ 6 MPa$\sqrt{m}$. The intrinsic ΔK_{th} for the Z-X and X-Z orientation were found to be ~ 2.7 MPa$\sqrt{m}$ and ~ 3.5 MPa$\sqrt{m}$ in the X-Y orientation.

9 Conclusions

This research project set out to investigate near-threshold FCGRs of LPBF produced Ti-6Al-4V in the AF, SR and DA conditions for three build orientations. It was the first investigation to consider the crack closure effects on near-threshold FCGRs using LPBF produced Ti-6Al-4V. Through investigating near-threshold FCGRs, the influencing mechanisms of residual stress and microstructure on fatigue behaviour was identified. The key conclusions are summarised as follows:

- The influencing mechanism of the unique LPBF Ti-6Al-4V microstructure on fatigue behaviour was identified and shown, for the first time, through fractographic images. In particular, it showed that the relationship between the PBG and α' laths are the sources of crack closure. In turn, this identified the reason for the dependency on build orientation behaviour (anisotropy) observed in the AF and SR conditions. The source of the anisotropy comes from RICC from the perceived PBG structure in the respective crack planes. This is specifically apparent in the lower *R-ratio* regime where a global "closure-affected" regime is present. In addition, the typical crack closure behaviours on ΔK_{th} at low *R-ratios* were observed, i.e. as the *R-ratio* increases, ΔK_{th} decreases.

- The DA condition does not show a pronounced reliance on the PBG role's in the orientation of specific crack closures at low *R-ratios*, as with the AF and SR conditions. However, the typical crack closure behaviour on ΔK_{th} at low *R-ratios* was more pronounced in the DA condition because of the larger α grains and presence of the β phase. This resulted in rougher fracture surfaces and more tortuous crack paths due to a larger grain size, larger facets and α/β interfaces.

- The influencing mechanism of residual stress on the fatigue behaviour of LPBF Ti-6Al-4V was identified. In particular, it was shown that residual stress caused crack opening. This results in an increase in the *R-ratio* and causes a reduction in crack closure effects. The reduction in crack closure effects were more prominently observed in the ΔK_{th} results for the Z-X and X-Z orientations. There is also link to orientation dependency on residual stress where the Z-X orientation was shown to have the largest residual stress, then the X-Z and the lowest levels in the X-Y orientation.

- The near-threshold fatigue crack growth mechanism is predominantly governed by transgranular quasi-cleavage mechanisms. More specifically, quasi-cleavage facets resulting in crack tortuosity. The crack path is predominantly on primary α' facets and secondary and tertiary α' facets result in crack branching.

- In the DA condition, the Z-X orientation showed the most faceted regions on the fracture surface and for all *R-ratios* had the lowest ΔK_{th} than the remaining orientations. The X-Z orientation obtained a comparable ΔK_{th} as the Z-X

orientation, but at a higher *R-ratio*. The X-Y orientation had the highest ΔK_{th} and is likely to achieve a comparable ΔK_{th} to the remaining orientations at higher *R-ratio*s.

- For the AF and SR conditions a critical intrinsic K_{max} ~ 3 MPa.m$^{0.5}$ and an intrinsic ΔK_{th} ~ 1.6 ± 0.2 MPa.m$^{0.5}$ was found. In the DA condition, the critical parameters improved to K_{max} ~ 6 MPa.m$^{0.5}$ in all three orientations and ΔK_{th} ~ 2.7 MPa.m$^{0.5}$ in the Z-X and X-Z orientations and ΔK_{th} ~ 3.5 MPa.m$^{0.5}$ in the X-Y orientation.

9.1 Future work

Regarding the near-threshold FCGR behaviour, there are a few aspects in which future investigations may lead to valuable insights within this topic.

From a statistical point of view, it would be advisable to conduct repetition tests in order to gain more confidence in the test results.

One of the discussion points in Chapter 8 explains that at high *R-ratios* (~ 0.98), different morphologies obtained the same ΔK_{th}. Thus, conducting near-threshold tests at such large *R-ratios* would provide further insight into a more intrinsic ΔK_{th} with different morphologies. Furthermore, conducting this with specimens manufactured by different techniques, while trying to keep the same morphology, i.e. across all manufacturing methods and tests of bi-modal, equiaxed and lamellar morphology. In this way, crystallographic texture should be different across the various manufacturing methods.

Initially, fatigue life (*SN* approach) and digital image correlation (DIC) on near-threshold FCGR were to be a part of this dissertation. However, these topics are large within themselves and could form another PhD on their own. The fatigue life approach can be combined with the near-threshold FCGR data of this dissertation and provide a Kitgawa-Takahashi (KT) diagram which provides an envelope of no crack initiation and crack initiation.

Furthermore, Nicolas Macallister, has already published work (Macallister *et al.*, 2021) in a peer-reviewed journal on FCG parameters using the fatigue data from this dissertation. Their work uses the NASGRO model and has to consider the influence of microstructure, residual stress, and specimen orientation, which was obtained from this dissertation. The NASGRO model considers the entire crack growth rate curve, i.e. the near-threshold regime, the Paris regime, and fracture toughness. Furthermore, it incorporates *R-ratios* into its model, which means factors which affect *R-ratio*, such as residual stress and crack closure, can also be incorporated into the model.

References

Agius, D., Kourousis, K., Wallbrink, C. (2018) A Review of the As-Built SLM Ti-6Al-4V Mechanical Properties towards Achieving Fatigue Resistant Designs. Metals. 8(1), 75.

Ahmed, T., Rack, H.J. (1998) Phase transformation during cooling a + b titanium alloys. Material Science and Engineering A. 243(1–2), 206–211.

Airways (2020) Aloha airlines flight 243 incident, 32 years later. Airways magazine. [online]. Available from: https://airwaysmag.com/airlines/32-years-aloha-flight-243-accident/ [Accessed August 18, 2021].

Al-Bermani, S.S., Blackmore, M.L., Zhang, W., Todd, I. (2010) The origin of microstructural diversity, texture, and mechanical properties in electron beam melted Ti-6Al-4V. Metallurgical and Materials Transactions A: Physical Metallurgy and Materials Science. 41(13), 3422–3434.

Anderson, L.S., Venter, A.M., Vrancken, B., Marais, D., van Humbeeck, J., Becker, T.H. (2018) Investigating the Residual Stress Distribution in Selective Laser Melting Produced Ti-6Al-4V using Neutron Diffraction. In Mechanical Stress Evaluation by Neutron and Synchrotron Radiation. pp. 73–78.

Anderson, T.L. (2003) Flaw Characterization. In I. Milne, R. Ritchie, & B. Karihaloo, eds. Comprehensive Structural Integrity. Elsevier Science Ltd, pp. 227–242.

Anderson, T. L. (2005) Fracture Mechanics: Fundamentals and Applications, Third Edition. Third Edit. Boca Raton: CRC Press LLC.

André, V., Henriques, R., Paulo, P., Campos, D., Alberto, C., Cairo, A., Carlos, J. (2005) Production of Titanium Alloys for Advanced Aerospace Systems by Powder Metallurgy. Materials Research. 8(4), 443–446.

Arakere, N.K., Goswami, T., Krohn, J., Ramachandran, N. (2002) High temperature fatigue crack growth behavior of Ti-6Al-4V. High Temperature Materials and Processes. 21(4), 229–236.

ASTM B962-17, Standard Test Methods for Density of Compacted or Sintered Powder Metallurgy (PM) Products Using Archimedes' Principle, ASTM International, West Conshohocken, PA, 2017, DOI: 10.1520/B0962-17, www.astm.org

ASTM E8 / E8M-21, Standard Test Methods for Tension Testing of Metallic Materials, ASTM International, West Conshohocken, PA, 2021, DOI: 10.1520/E0008_E0008M-21, www.astm.org

ASTM E399-20a, Standard Test Method for Linear-Elastic Plane-Strain Fracture Toughness of Metallic Materials, ASTM International, West Conshohocken, PA, 2020, DOI: 10.1520/E0399-20A, www.astm.org

ASTM E561-20, Standard Test Method for KR Curve Determination, ASTM International, West Conshohocken, PA, 2020, DOI: 10.1520/E0561-20 , www.astm.org

ASTM E647-15e1, Standard Test Method for Measurement of Fatigue Crack Growth Rates, ASTM International, West Conshohocken, PA, 2015, DOI: 10.1520/E0647-15E01, www.astm.org

ASTM F1580-18, Standard Specification for Titanium and Titanium-6 Aluminum-4 Vanadium Alloy Powders for Coatings of Surgical Implants, ASTM International, West Conshohocken, PA, 2018, DOI: 10.1520/F1580-18,www.astm.org

ASTM F3001-14, Standard Specification for Additive Manufacturing Titanium-6 Aluminum-4 Vanadium ELI (Extra Low Interstitial) with Powder Bed Fusion, ASTM International, West Conshohocken, PA, 2014, DOI: 10.1520/F3001-14, www.astm.org

Aswath, P.B. (1991) No Title. In W. O. Soboyejo, T. S. Srivatsan, & D. L. Davidson, eds. Conference on Fatigue and Fracture of Ordered Intermetallics Materials. Warrendale, PA: TMS, pp. 329–339.

Avcu, Y.Y., Yetik, O., Guney, M., Iakovakis, E., Sınmazçelik, T., Avcu, E. (2020) Surface, subsurface and tribological properties of ti6al4v alloy shot peened under different parameters. Materials. 13(19), 1–22.

Babu, B. (2008) Physically based model for plasticity and creep of Ti-6Al-4V. Lulea University of Technology.

Bache, M. (2003) A review of dwell sensitive fatigue in titanium alloys: the role of microstructure, texture and operating conditions. International Journal of Fatigue. 25(9–11), 1079–1087.

Bantounas, I., Dye, D., Lindley, T.C. (2009) The effect of grain orientation on fracture morphology during high-cycle fatigue of Ti-6Al-4V. Acta Materialia. 57(12), 3584–3595.

Bantounas, I., Dye, D., Lindley, T.C. (2010) The role of microtexture on the faceted fracture morphology in Ti-6Al-4V subjected to high-cycle fatigue. Acta Materialia. 58(11), 3908–3918.

Basak, A., Das, S. (2016) Epitaxy and Microstructure Evolution in Metal Additive Manufacturing. Annual Review of Materials Research. 46(1), 125–149.

Becker, Thorsten Hermann, Dhansay, N.M. (2020) Influence of porosity on the fatigue life of laser powder bed fusion–produced Ti6Al4V. Material Design & Processing Communications. 3(1), 1–7.

Becker, Thorsten H., Dhansay, N.M. (2020) Influence of porosity on the fatigue life of laser powder bed fusion – produced Ti6Al4V. Material Design & Processing Communications. (January), 1–7.

Becker, T.H., Dhansay, N.M., Haar, G.M. Ter, Vanmeensel, K. (2020) Near-threshold fatigue crack growth rates of laser powder bed fusion produced Ti-Aal-4V. Acta Materialia. 197, 269–282.

Becker, T.H., Kumar, P., Ramamurty, U. (2021) Fracture and fatigue in additively manufactured metals. Acta Materialia. 219(xxxx), 117240.

de Beer, D., du Preez, W., Greyling, H., Prinsloo, F., Sciammarella, F., Trollip, N., Vermeulen, M., Wohlers, T. (2016) A South African Additive Manufacturing Strategy. Department of Science and Technology, 1–92.

Beghini, M., Bertini, L. (1990) Fatigue crack propagation through residual stress fields with closure phenomena. Engineering Fracture Mechanics. 36(3), 379–387.

Benedetti, M., Torresani, E., Leoni, M., Fontanari, V., Bandini, M., Pederzolli, C., Potrich, C. (2017) The effect of post-sintering treatments on the fatigue and biological behavior of Ti-6Al-4V ELI parts made by selective laser melting. Journal of the Mechanical Behavior of Biomedical Materials. 71(February), 295–306.

Bertram Broberg, K. (1999) Elastostatic cracks. In Cracks and fracture. Academic Press, pp. 99–246.

Boyce, B.L., Ritchie, R.O. (2001) Effect of load ratio and maximum stress intensity on the fatigue threshold in Ti-6Al-4V. Engineering Fracture Mechanics. 68, 129–147.

Boyer, R., Collings, E., Welsch, G. (1994) Materials Properties Handbook: Titanium Alloys. Ohio: ASM International.

Boyer, R.R. (1996) An overview on the use of titanium in the aerospace industry. Materials Science and Engineering. Materials Science and Engineering: A. 213(1–2), 103–114.

Britton, T.B., Dunne, F.P.E., Wilkinson, A.J. (2015) On the mechanistic basis of deformation at the microscale in hexagonal close-packed metals. Proceedings of the Royal Society A: Mathematical, Physical and Engineering Sciences. 471(2178), 1–29.

Brooks, H.L., Rennie, A.E.W., Abram, T.N., McGovern, J., Caron, F. (2012) Variable Fused Deposition Modelling - Analysis of benefits, concept design and

tool path generation. Innovative Developments in Virtual and Physical Prototyping - Proceedings of the 5th International Conference on Advanced Research and Rapid Prototyping. (September), 511–517.

Bueckner F. H. (1958) The Propagation of Cracks and the Energy of Elastic Deformation. Transaction of the ASME, Series E. 80(6), 1225–1230.

Burgers, W.G. (1934) On the process of transition of the cubic-body-centered modification into the hexagonal-close-packed modification of zirconium. Physica. 1(7–12), 561–586.

Cain, V., Thijs, L., Van Humbeeck, J., Van Hooreweder, B., Knutsen, R. (2015) Crack propagation and fracture toughness of Ti6Al4V alloy produced by selective laser melting. Additive Manufacturing. 5, 68–76.

Campbell, F. (2008) Fatigue. In Elements of Metallurgy and Engineering Alloys. ASM International, pp. 244–264.

Cao, Fei, Zhang, T., Ryder, M.A., Lados, D.A. (2018) A Review of the Fatigue Properties of Additively Manufactured Ti-6Al-4V. Jom. 70(3), 349–357.

Cao, Xiaojian, Xu, L., Xu, X., Wang, Q. (2018) Fatigue fracture characteristics of Ti6Al4V subjected to ultrasonic nanocrystal surface modification. Metals. 8(1), 1–13.

Carvill, J. (1993) Strengths of materials. In J. Carvill, ed. Mechanical Engineer's Data Handbook. Butterworth-Heinemann, pp. 1–55.

Cepeda-Jiménez, C.M., Potenza, F., Magalini, E., Luchin, V., Molinari, A., Pérez-Prado, M.T. (2020) Effect of energy density on the microstructure and texture evolution of Ti-6Al-4V manufactured by laser powder bed fusion. Materials Characterization. 163(September 2019), 1–9.

Chan, K.S., Koike, M., Mason, R.L., Okabe, T. (2013) Fatigue life of titanium alloys fabricated by additive layer manufacturing techniques for dental implants. Metallurgical and Materials Transactions A: Physical Metallurgy and Materials Science. 44(2), 1010–1022.

Davidson, D. (1992) The Experimental Mechanics of Microcracks. In J. Larsen & J. Allison, eds. STP1149 Small-Crack Test Methods. West Conshohocken, PA, pp. 81–91.

Davidson, D.L., Campbell, J.B., Page, R.A. (1991) The initiation and growth of fatigue cracks in a titanium aluminide alloy. Metallurgical Transactions A. 22(2), 377–391.

Debroy, T., Wei, H.L., Zuback, J.S., Mukherjee, T., Elmer, J.W., Milewski, J.O., Beese, A.M., Wilson-heid, A., De, A., Zhang, W. (2018) Progress in Materials

Science Additive manufacturing of metallic components – Process , structure and properties. . 92, 112–224.

Dhansay, N.M. (2015) Fracture Mechanics Based Fatigue and Fracture Toughness Evaluation of SLM Ti-6Al-4V. University of Cape Town.

Döker, H., Marci, G. (1983) Threshold range and opening stress intensity factor in fatigue. International Journal of Fatigue. 5(4), 187–191.

Donachie, M.J. (2000) Titanium: A Technical Guide. 2nd Editio. D. Mj, ed. ASM International.

Dunne, F., Rugg, D., Walker, A. (2007) Lengthscale-dependent, elastically anisotropic, physically-based hcp crystal plasticity: Application to cold-dwell fatigue in Ti alloys. International Journal of Platicity. 23(6), 1061–1083.

Dunstan, M.K., Paramore, J.D., Fang, Z.Z., Ligda, J.P., Butler, B.G. (2020) Analysis of microstructural facet fatigue failure in ultra-fine grained powder metallurgy Ti-6Al-4V produced through hydrogen sintering. International Journal of Fatigue. 131.

Edwards, P., O'Conner, A., Ramulu, M. (2013) Electron beam additive manufacturing of titanium components: Properties and performance. Journal of Manufacturing Science and Engineering, Transactions of the ASME. 135(6).

Edwards, P., Ramulu, M. (2015) Effect of build direction on the fracture toughness and fatigue crack growth in selective laser melted Ti-6Al-4-‰V. Fatigue and Fracture of Engineering Materials and Structures. 38(10), 1228–1236.

Edwards, P., Ramulu, M. (2014) Fatigue performance evaluation of selective laser melted Ti-6Al-4V. Materials Science and Engineering A. 598, 327–337.

Ekberg, A. (2004) Fatigue crack propagation. Chalmers.

EOS GmbH (2010) Technical Description EOSINT M 280. , 1–33.

Everaerts, J. (2017) Fatigue crack initiation and facet formation in Ti-6Al-4V wires. . (February).

Everaerts, J., Verlinden, B., Wevers, M. (2016) The influence of the alpha grain size on internal fatigue crack initiation in drawn Ti-6Al-4V wires. Procedia Structural Integrity. 2, 1055–1062.

Fatemi, A. (2006) FUNDAMENTALS OF LEFM AND APPLICATIONS TO FATIGUE CRACK GROWTH. Class Lecture, College of Engineering, University of Toledo.

Ferrar, B., Mullen, L., Jones, E., Stamp, R., Sutcliffe, C.J. (2012) Gas flow effects on selective laser melting (SLM) manufacturing performance. Journal of Materials Processing Technology. 212(2), 355–364.

Frazier, W.E. (2014) Metal additive manufacturing: A review. Journal of Materials Engineering and Performance. 23(6), 1917–1928.

Galarraga, H., Warren, R.J., Lados, D.A., Dehoff, R.R., Kirka, M.M. (2017) Fatigue crack growth mechanisms at the microstructure scale in as-fabricated and heat treated Ti-6Al-4V ELI manufactured by electron beam melting (EBM). Engineering Fracture Mechanics. 176, 263–280.

Gibson, I., Rosen, D.W., Stucker, B.E. (2010) Additive Manufacturing Technologies: Rapid Prototyping to Direct Digital Manufacturing. In Springer. pp. 1–16.

Gladush, G.G., Smurov, I. (2011) Physics of laser materials processing. Berlin: Springer, Berlin, Heidelberg.

Glavicic, M.G., Kobryn, P.A., Bieler, T.R., Semiatin, S.L. (2003) An automated method to determine the orientation of the high-temperature beta phase from measured EBSD data for the low-temperature alpha-phase Ti-6Al-4V. Material Science and Engineering A. 351(1–2), 258–264.

Gong, H., Rafir, K., Starr, T., Stucker, B. (2012) Effect of defects on fatigue tests of as-built Ti-6Al-4V parts fabricated by selective laser melting. Solid Freeform symposium.

Ter Haar, G.M. (2017) Selective Laser Melting-produced Ti6Al4V: Influence of annealing strategies on crystallographic microstructure and tensile behaviour. South African Journal of Industrial Engineering. 27(December), 158.

Ter Haar, G.M., Becker, T.H. (2020) Low temperature stress relief and martensitic decomposition in selective laser melting produced Ti6Al4V. Material Design & Processing Communications. (November 2019), 2–7.

Ter Haar, G.M., Becker, T.H. (2018) Selective laser melting produced Ti-6Al-4V: Post-process heat treatments to achieve superior tensile properties. Materials. 11(1).

Ter Haar, G.M., Becker, T.H. (2021) The influence of microstructural texture and prior beta grain recrystallisation on the deformation behaviour of laser powder bed fusion produced Ti–6Al–4V. Materials Science and Engineering A. 814(November 2020), 141185.

Hemmerdinger, J. (2021) Fuel did not feed PW4000 engine fire following engine failure: NTSB. FlightGlobal. [online]. Available from: https://www.flightglobal.com/safety/fuel-did-not-feed-pw4000-engine-fire-following-engine-failure-ntsb/142754.article [Accessed April 26, 2021].

Hines, J.A., Lütjering, G. (1999) Propagation of microcracks at stress amplitudes below the conventional fatigue limit in Ti-6Al-4V. Fatigue and Fracture of Engineering Materials and Structures. 22(8), 657–665.

Van Hooreweder, B., Moens, D., Boonen, R., Kruth, J.-P., Sas, P. (2012) Analysis of Fracture Toughness and Crack Propagation of Ti6Al4V Produced by Selective Laser Melting. Advanced Engineering Materials. 14(1–2), 92–97.

Huang, C., Zhao, Y., Xin, S., Tan, C., Zhou, W., Li, Q., Zeng, W. (2017) High cycle fatigue behavior of Ti–5Al–5Mo–5V–3Cr–1Zr titanium alloy with lamellar microstructure. Materials Science and Engineering A. 682(September 2016), 107–116.

Huang, J., Wang, Z., Xue, K. (2011) Cyclic deformation response and micromechanisms of Ti alloy Ti-5Al-5V-5Mo-3Cr-0.5Fe. Materials Science and Engineering A. 528(29–30), 8723–8732.

International Standard Organisation (2015) Additive manufacturig - General principles - Part 2: Overview of process categories and feedstock. , (ISO Standard 17296-2:2015) 1–8. https://www.iso.org/standard/61626.html

International Standard Organisation (2016) Medical devices – Quality management systems – Requirements for regulatory purposes. (ISO Standard 13485:2016). 1-36. https://www.iso.org/standard/59752.html

ISO / ASTM52900-15, Standard Terminology for Additive Manufacturing – General Principles – Terminology, ASTM International, West Conshohocken, PA, 2015, DOI: 10.1520/ISOASTM52900-15, www.astm.org

ISO / ASTM52921-13(2019), Standard Terminology for Additive Manufacturing—Coordinate Systems and Test Methodologies, ASTM International, West Conshohocken, PA, 2019, DOI: 10.1520/ISOASTM52921-13R19, www.astm.org

Ivanova, S.G., Biederman, R.R., Sisson, R.D. (2002) Investigation of fatigue crack initiation in Ti-6Al-4V during tensile-tensile fatigue. Journal of Materials Engineering and Performance. 11(2), 226–231.

Jeanette Clark (2012) R5bn titanium industry planned for SA by 2020. Moneyweb Holdings Ltd. [online]. Available from: http://www.moneyweb.co.za/archive/r5bn-titanium-industry-planned-for-sa-by-2020/ [Accessed March 4, 2016].

Jin, O., Mall, S. (2003) Effects of microstructure on short crack growth behavior of Ti-6Al-2Sn-4Zr-2Mo-0.1Si alloy. Materials Science and Engineering A. 359(1–2), 356–367.

John, R., Jata, K. V., Sadananda, K. (2003) Residual stress effects on near-threshold fatigue crack growth in friction stir welds in aerospace alloys. International Journal of Fatigue. 25(9–11), 939–948.

Karihaloo, B., Xiao, Q.Z. (2003) Linear and Nonlinear Fracture Mechanics. Comprehensive Structural Integrity. 2, 81–212.

Kasperovich, G., Haubrich, J., Gussone, J., Requena, G. (2016) Correlation between porosity and processing parameters in TiAl6V4 produced by selective laser melting. Materials and Design. 105, 160–170.

Kasperovich, G., Hausmann, J. (2015) Improvement of fatigue resistance and ductility of TiAl6V4 processed by selective laser melting. Journal of Materials Processing Technology. 220, 202–214.

Kelly, S.M., Kampe, S.L. (2004) Microstructural evolution in laser-deposited multilayer Ti-6Al-4V builds: Part II. Thermal Modeling. Metallurgical and Materials Transactions A: Physical Metallurgy and Materials Science. 35 A(6), 1869–1879.

Khairallah, S.A., Anderson, A.T., Rubenchik, A.M., King, W.E. (2017) Laser powder-bed fusion additive manufacturing: Physics of complex melt flow and formation mechanisms of pores, spatter, and denudation zones. Additive Manufacturing Handbook: Product Development for the Defense Industry. m, 613–628.

Kong, C., Tuck, C., Ashcroft, L., Wildman, R., Hague, R. (2011) High density Ti-6Al-4V via SLM processing: microstructure and mechanical properties. In Proceedings of the 22nd Annual International Solid Freeform Fabrication: An Additive Manufacturing Conference,, 475–483.

Krüger, L., Grundmann, N., Trubitz, P. (2015) Influence of Microstructure and Stress Ratio on Fatigue Crack Growth in a Ti-6-22-22-S alloy. Materials Today: Proceedings. 2(0), S205–S211.

Kruth, J.-P., Mercelis, P., Vaerenbergh, J. Van, Froyen, L., Rombouts, M. (2005) Binding mechanisms in selective laser sintering and selective laser melting. Rapid Prototyping Journal. 11(1), 26–36.

Kumar, P., Prakash, O., Ramamurty, U. (2018) Micro-and meso-structures and their influence on mechanical properties of selectively laser melted Ti-6Al-4V. Acta Materialia. 154(May), 246–260.

Kumar, P., Ramamurty, U. (2019) Microstructural optimization through heat treatment for enhancing the fracture toughness and fatigue crack growth resistance of selective laser melted Ti–6Al–4V alloy. Acta Materialia. 169(March), 45–59.

Kunz, L., Pokorný, P., Konečná, R., Nicoletto, G. (2019) Propagation of long fatigue cracks in Ti6Al4V alloy produced by direct metal laser sintering. Procedia Structural Integrity. 17, 222–229.

Ladewig, A., Schlick, G., Fisser, M., Schulze, V., Glatzel, U. (2016) Influence of the shielding gas flow on the removal of process by-products in the selective laser melting process. Additive Manufacturing. 10, 1–9.

Lawson, L., Chen, E.Y., Meshii, M. (1999) Near-threshold fatigue : a review. International Journal of Fatigue. 21, 15–34.

Leuders, S., Thöne, M., Riemer, A., Niendorf, T., Tröster, T., Richard, H. a., Maier, H.J. (2012) On the mechanical behaviour of titanium alloy TiAl6V4 manufactured by selective laser melting: Fatigue resistance and crack growth performance. International Journal of Fatigue. 48, 300–307.

Leyens, C., Peters, M. (2007) Titanium and Titanium Alloys: Fundamentals and Applications. C. Leyens & M. Peters, eds. John Wiley & Sons.

Leyens, C., Peters, M. (2003) Titanium and Titanium Alloys. D. C. (DLR-G. A. C. Leyens & D. M. (DLR-G. A. Peters, eds. Wiley-VCH Verlag.

Li, P., Warner, D.H., Fatemi, A., Phan, N. (2016) Critical assessment of the fatigue performance of additively manufactured Ti-6Al-4V and perspective for future research. International Journal of Fatigue. 85, 130–143.

Li, X.D. (1996) Dislocation pile-up model of fatigue thresholds for 2024- and 7075-alike aluminium alloys. Theoretical and Applied Fracture Mechanics. 24(2), 165–179.

Liu, D., Pons, D.J. (2018) Crack propagation mechanisms for creep fatigue: A consolidated explanation of fundamental behaviours from initiation to failure. Metals. 8(8).

Liu, S., Shin, Y.C. (2019) Additive manufacturing of Ti6Al4V alloy: A review. Materials and Design. 164.

Lunt, D., Thomas, R., Atkinson, M.D., Smith, A., Sandala, R., da Fonseca, J.Q., Preuss, M. (2021) Understanding the role of local texture variation on slip activity in a two-phase titanium alloy. Acta Materialia. 216, 117111.

Lütjering, G. (1998) Influence of processing on microstructure and mechanical properties of (α+β) titanium alloys. Materials Science and Engineering: A. 243(1–2), 32–45.

Lutjering, G., Williams, J. (2007) Titanium. 2nd ed. B. Derby, ed. Springer US.

Ly, S., Rubenchik, A.M., Khairallah, S.A., Guss, G., Matthews, M.J. (2017) Metal vapor micro-jet controls material redistribution in laser powder bed fusion additive manufacturing. Scientific Reports. 7(1), 1–12.

Macallister, N., Vanmeensel, K., Becker, T.H. (2021) Fatigue crack growth parameters of Laser Powder Bed Fusion produced Ti-6Al-4V. International Journal of Fatigue. 145(December 2020), 106100.

Matthews, M.J., Guss, G., Khairallah, S.A., Rubenchik, A.M., Depond, P.J., King, W.E. (2016) Denudation of metal powder layers in laser powder bed fusion processes. Acta Materialia. 114, 33–42.

Mercelis, P., Kruth, Jean-Pierre (2006) Residual stresses in selective laser sintering and selective laser melting. Rapid Prototyping Journal. 12(5), 254–265.

Molaei, R., Fatemi, A. (2018) Fatigue Design with Additive Manufactured Metals: Issues to Consider and Perspective for Future Research. Procedia Engineering. 213(2017), 5–16.

Molaei, R., Fatemi, A., Sanaei, N., Pegues, J., Shamsaei, N., Shao, S., Li, P., Warner, D.H., Phan, N. (2020) Fatigue of additive manufactured Ti-6Al-4V, Part II: The relationship between microstructure, material cyclic properties, and component performance. International Journal of Fatigue. 132(October 2019).

Moore, J.A., Barton, N.R., Florando, J., Mulay, R., Kumar, M. (2017) Crystal plasticity modeling of β phase deformation in Ti-6Al-4V. Modelling and Simulation in Materials Science and Engineering. 25(7), 075007.

Moshier, M. a., Nicholas, T., Hillberry, B.M. (2001) Load history effects on fatigue crack growth threshold for Ti–6Al–4V and Ti-17 titanium alloys. International Journal of Fatigue. 23, 253–258.

Murakami, Y., Endo, M. (1994) Effects of defects, inclusions and inhomogeneities on fatigue strength. International Journal of Fatigue. 16(3), 163–182.

Murakami, Y., Kodama, S., Konuma, S. (1989) Quantitative evaluation of effects of non-metallic inclusions on fatigue strength of high strength steels. I: Basic fatigue mechanism and evaluation of correlation between the fatigue fracture stress and the size and location of non-metallic inclusions. International Journal of Fatigue. 11(5), 291–298.

Murakami, Y., Usuki, H. (1989) Quantitative evaluation of effects of non-metallic inclusions on fatigue strength of high strength steels. II: Fatigue limit evaluation based on statistics for extreme values of inclusion size. International Journal of Fatigue. 11(5), 299–307.

Murr, L.E., Quinones, S. a, Gaytan, S.M., Lopez, M.I., Rodela, a, Martinez, E.Y., Hernandez, D.H., Martinez, E., Medina, F., Wicker, R.B. (2009) Microstructure

and mechanical behavior of Ti-6Al-4V produced by rapid-layer manufacturing, for biomedical applications. Journal of the mechanical behavior of biomedical materials. 2(1), 20–32.

Nalla, R.K., Boyce, B.L., Campbell, J.P., Peters, J.O., Ritchie, R.O. (2002) Influence of Microstructure on High-Cycle Fatigue of Ti-6Al-4V : Bimodal vs . Lamellar Structures. . 33(March).

Nalla, R.K., Campbell, J.P., Ritchie, R.O. (2002) Effects of microstructure on mixed-mode , high-cycle fatigue crack-growth thresholds in Ti-6Al-4V alloy. Fatigue and Fracture of Engineering Materials and Structures. 25(6), 587–606.

Newman, John A (2000) The Effects of Load Ratio on Threshold Fatigue Crack Growth of Aluminum Alloys. Virginia Polytechnic Institute and State University.

Newman, J.A., Riddell, W.T., Piascik, R.S. (2003) Analytical and Experimental Study of Near- Threshold Interactions Between Crack Closure Mechanisms. . (May).

Niinomi, M., Akahori, T., Eylon, D. (1999) Fatigue crack initiation and fatigue life prediction of Ti–6Al–4V ELI. In R. Boyer, D. Eylon, & G. Lutjering, eds. Fatigue behaviour of titanium alloys. TMS, pp. 307–314.

Oberwinkler, B. (2011) Modeling the fatigue crack growth behavior of Ti-6Al-4V by considering grain size and stress ratio. Materials Science and Engineering A. 528(18), 5983–5992.

Oberwinkler, B., Riedler, M., Eichlseder, W. (2010) Importance of local microstructure for damage tolerant light weight design of Ti-6Al-4V forgings. International Journal of Fatigue. 32(5), 808–814.

Ogawa, T., Ohya, K., Tokaji, K. (1992) Ti-6Al-4V合金の疲労き裂進展特性に及ぼす組織の影響.pdf. Journal of the Society of Materials Science, Japan. 41(463), 502–508.

Panwisawas, C., Qiu, C.L., Sovani, Y., Brooks, J.W., Attallah, M.M., Basoalto, H.C. (2015) On the role of thermal fluid dynamics into the evolution of porosity during selective laser melting. Scripta Materialia. 105, 14–17.

Paris, P., Erdogan, F. (1963) A Critical Analysis of Crack Propagation Laws. Journal of Basic Engineering. 85D, 528–534.

Peters, J.O., Luetjering, G. (2001) Comparison of the fatigue and fracture of α+β and β titanium alloys. Metallurgical and Materials Transactions A. 32A(NOVEMBER), 2805–2818.

Pilchak, A.L., Sargent, G.A., Semiatin, S.L. (2018) Early Stages of Microstructure and Texture Evolution during Beta Annealing of Ti-6Al-4V. Metallurgical and Materials Transactions A: Physical Metallurgy and Materials Science. 49(3), 908–919.

Pippan, R., Hohenwarter, A. (2017) Fatigue crack closure: a review of the physical phenomena. Fatigue and Fracture of Engineering Materials and Structures. 40(4), 471–495.

Poulin, J.R., Kreitcberg, A., Terriault, P., Brailovski, V. (2019) Long fatigue crack propagation behavior of laser powder bed-fused inconel 625 with intentionally-seeded porosity. International Journal of Fatigue. 127(June), 144–156.

du Preez, W.B., Booysen, G. (2016) Advances In Ti6Al4V Additive Manufacturing in South Africa. Proceedings of the 13th World Conference on Titanium. 2, 1323–1329.

Prime, M.B., DeWald, A.T. (2013) The Contour Method. In Practical Residual Stress Measurement Methods. pp. 109–138.

Qiu, J., Feng, X., Ma, Y., Lei, J., Liu, Y., Huang, A., Rugg, D., Yang, R. (2016) Fatigue crack growth behavior of beta-annealed Ti-6Al-2Sn-4Zr-xMo (x = 2, 4 and 6) alloys: Influence of microstructure and stress ratio. International Journal of Fatigue. 83, 150–160.

Rack, H.J., Qazi, J.I. (2006) Titanium alloys for biomedical applications. Materials Science and Engineering: C. 26(8), 1269–1277.

Rangaswamy, P., Griffith, M.L., Prime, M.B., Holden, T.M., Rogge, R.B., Edwards, J.M., Sebring, R.J. (2005) Residual stresses in LENS® components using neutron diffraction and contour method. Materials Science and Engineering A. 399(1–2), 72–83.

Ravichandran, K.S. (1991) Near threshold fatigue crack growth behavior of a titanium alloy: Ti-6A1-4V. Acta Metallurgica Et Materialia. 39(3), 401–410.

Ritchie, R., Davidson, D., Boyce, B., Campbell, J., Roder, O. (1999) High-cycle fatigue of Ti-6Al-4V. Fatigue Fracture of Engineering Materials and Structures. 22(7), 621–631.

Ritchie, R.O. (2005) Incomplete self-similarity and fatigue-crack growth. International Journal of Fracture. 132(3), 197–203.

Rombouts, M., Kruth, J.P., Froyen, L., Mercelis, P. (2006) Fundamentals of selective laser melting of alloyed steel powders. Cirp annals-manufacturing …. 1(1), 4–9.

Santos, E.C., Shiomi, M., Osakada, K., Laoui, T. (2006) Rapid manufacturing of metal components by laser forming. International Journal of Machine Tools and Manufacture. 46(12–13), 1459–1468.

Saxena, V.K., Radhakrishnan, V.M. (1998) Effect of phase morphology on fatigue crack growth behavior of α-β titanium alloy - A crack closure rationale. Metallurgical and Materials Transactions A: Physical Metallurgy and Materials Science. 29(1), 245–261.

Schütz, W. (1996) A history of fatigue. Engineering Fracture Mechanics. 54(2), 263–300.

Shiomil, M., Yamashital, T., Materials, E. (2004) Residual Stress within Metallic Model Made by Selective Laser Melting Process. CIRP Annals - Manufacturing Technology. 53(1), 195–195.

Simonelli, M. (2014) Microstructure evolution and mechanical properties of selective laser melted Ti-6Al-4V. Loughborough University.

Simonelli, M., Tse, Y.Y., Tuck, C. (2014) On the texture formation of selective laser melted Ti-6Al-4V. Metallurgical and Materials Transactions A: Physical Metallurgy and Materials Science. 45(6), 2863–2872.

Singla, A.K., Banerjee, M., Sharma, A., Singh, J., Bansal, A., Gupta, M.K., Khanna, N., Shahi, A.S., Goyal, D.K. (2021) Selective laser melting of Ti6Al4V alloy: Process parameters, defects and post-treatments. Journal of Manufacturing Processes. 64(November 2020), 161–187.

Sistiaga, M.L.M. (2019) Selective Laser Melting of 316L and Hastelloy X. Katholieke Universiteit Leuven.

Stoffregen, H.A., Butterweck, K., Abele, E. (2013) Fatigue analysis in selective laser melting: review and investigation of thin-walled actuator housings. Solid Freeform Fabrication (SFF) symposium, 635–650.

Suresh, S. (1998) Fatigue of materials. Second edi. The press syndicate of the univeristy of cambridge.

Suresh, S., Ritchie, R.O. (1982) A geometric model for fatigue crack closure induced by fracture surface roughness. Metallurgical Transactions A. 13(9), 1627–1631.

Tait, R.B. (2012) Fatigue/Fracture Mechanics. Class Lecture, Department of Mechanical Engineering, University of Cape Town.

Tammas-Williams, S., Withers, P.J., Todd, I., Prangnell, P.B. (2017) The Influence of Porosity on Fatigue Crack Initiation in Additively Manufactured Titanium Components. Scientific Reports. 7(1), 1–13.

Tan, C., Fan, Y., Sun, Q., Zhang, G. (2020) Improvement of the crack propagation resistance in an α + β titanium alloy with a trimodal microstructure. Metals. 10(8), 1–11.

Tan, C., Li, X., Sun, Q., Xiao, L., Zhao, Y., Sun, J. (2015) Effect of α-phase morphology on low-cycle fatigue behavior of TC21 alloy. International Journal of Fatigue. 75, 1–9.

Tanaka, K., Nakai, Y., Yamashita, M. (1981) Fatigue growth threshold of small cracks. International journal of fracture. 17, 519–533.

Tarik Hasib, M., Ostergaard, H.E., Li, X., Kruzic, J.J. (2020) Fatigue crack growth behavior of laser powder bed fusion additive manufactured Ti-6Al-4V: Roles of post heat treatment and build orientation. International Journal of Fatigue, 105955.

Thijs, L. (2014) Microstructure and texture of metal parts produced by Selective Laser Melting. KU Leuven.

Thijs, L., Verhaeghe, F., Craeghs, T., Humbeeck, J. Van, Kruth, J.-P. (2010) A study of the microstructural evolution during selective laser melting of Ti–6Al–4V. Acta Materialia. 58(9), 3303–3312.

Torries, B., Imandoust, A., Beretta, S., Shao, S., Shamsaei, N. (2018) Overview on Microstructure- and Defect-Sensitive Fatigue Modeling of Additively Manufactured Materials. Jom. 70(9), 1853–1862.

Totten, G.E. (2008) SPOTLIGHT FATIGUE CRACK. Advanced Materials & Processes. (May), 39–41.

Vasudeven, A.K., Sadananda, K., Louat, N. (1994) A review of crack closure, fatigue crack threshold and related phenomena. Materials Science and Engineering A. 188(1–2), 1–22.

Vilaro, T., Colin, C., Bartout, J.D. (2011) As-fabricated and heattreated microstructure of the Ti–6Al–4V alloy processed by selective laser melting. Metallurgical and Materials Transactions A 42,. 10, 3190–3199.

Vrancken, B. (2016) Study of Residual Stresses in Selective Laser Melting. Katholieke Universiteit Leuven.

Vrancken, B., Cain, V., Knutsen, R., Van Humbeeck, J. (2014) Residual stress via the contour method in compact tension specimens produced via selective laser melting. Scripta Materialia. 87, 29–32.

Wang, S.H., Müller, C. (1998) Fatigue crack closure and crack growth behaviour in a titanium alloy with different microstructures. Journal of Materials Science. 33(18), 4509–4516.

Wanhill, R. (1974) Environment and frequency effects during fatigue crack propagation in Ti-2.5Cu (IMI 230) sheet at room temperature. Corrosion-NACE, 28–35.

Williams, M.L. (1960) The bending stress distribution at the base of a stationary crack. Journal of Applied Mechanics, Transactions ASME. 28(1), 78–82.

Woodtli, J., Muster, W., Radon, J.C. (1986) Residual stress effects in fatigue crack growth. Engineering Fracture Mechanics. 24(3), 399–412.

Wu, G.Q., Shi, C.L., Sha, W., Sha, A.X., Jiang, H.R. (2013) Effect of microstructure on the fatigue properties of Ti-6Al-4V titanium alloys. Materials and Design. 46, 668–674.

Wu, Z., Kou, H., Tang, L., Chen, W., Han, X., Deng, Y., Tang, B., Li, J. (2020) Microstructural effects on the high-cycle fatigue and fracture behaviors of Ti-6Al-4V alloy. Engineering Fracture Mechanics. 235(April).

Wycisk, E., Solbach, A., Siddique, S., Herzog, D., Walther, F. (2014) Effects of Defects in Laser Additive Manufactured Ti-6Al-4V on Fatigue Properties. Physics Procedia. 56, 371–378.

Xu, W., Brandt, M., Sun, S., Elambasseril, J., Liu, Q., Latham, K., Xia, K., Qian, M. (2015) Additive manufacturing of strong and ductile Ti-6Al-4V by selective laser melting via in situ martensite decomposition. Acta Materialia. 85, 74–84.

Xu, Z.W., Liu, A., Wang, X.S. (2019) The influence of building direction on the fatigue crack propagation behavior of Ti6Al4V alloy produced by selective laser melting. Materials Science and Engineering A. 767(August).

Yadollahi, A., Shamsaei, N. (2017) Additive manufacturing of fatigue resistant materials: Challenges and opportunities. International Journal of Fatigue. 98, 14–31.

Yadroitsev, I., Yadroitsava, I. (2015) Evaluation of residual stress in stainless steel 316L and Ti6Al4V samples produced by selective laser melting. Virtual and Physical Prototyping. 10(2), 67–76.

Yang, J., Yu, H., Yin, J., Gao, M., Wang, Z., Zeng, X. (2016) Formation and control of martensite in Ti-6Al-4V alloy produced by selective laser melting. Materials & Design. 108, 308–318.

Yoder, G.R., Cooley, L.A., Crooker, T.W. (1979) Quantitative analysis of microstructural effects on fatigue crack growth in widmanstätten Ti-6A1-4V and Ti-8Al-1Mo-1V. Engineering Fracture Mechanics. 11(4), 805–816.

Zerbst, U., Vormwald, M., Pippan, R., Gänser, H.P., Sarrazin-Baudoux, C., Madia, M. (2016) About the fatigue crack propagation threshold of metals as a design

criterion - A review. Engineering Fracture Mechanics. 153(November 2014), 190–243.

Zhai, Y., Lados, D.A., Brown, E.J., Vigilante, G.N. (2016) Fatigue crack growth behavior and microstructural mechanisms in Ti-6Al-4V manufactured by laser engineered net shaping. International Journal of Fatigue. 93, 51–63.

Zhang, D., Wang, L., Zhang, H., Maldar, A., Zhu, G., Chen, W., Park, J.S., Wang, J., Zeng, X. (2020) Effect of heat treatment on the tensile behavior of selective laser melted Ti-6Al-4V by in situ X-ray characterization. Acta Materialia. 189, 93–104.

ZHU, Y., XIONG, J., LV, Z., ZHAO, Y. (2018) Testing and evaluation for fatigue crack propagation of Ti-6Al-4V/ELI and 7050-T7452 alloys at high temperatures. Chinese Journal of Aeronautics. 31(6), 1388–1398.

Zuo, J.H., Wang, Z.G., Han, E.H. (2008) Effect of microstructure on ultra-high cycle fatigue behavior of Ti-6Al-4V. Materials Science and Engineering A. 473(1–2), 147–152.

Appendix A Near-threshold results

A.1 As-fabricated results

Table 9-1: Near-threshold results for AF condition

	R-ratio	ΔK_{th} (MPa√m)	K_{max} (MPa√m)
AF, Z-X	0.3	2.1	3
AF, Z-X	0.6	1.9	4.75
AF, Z-X	0.88	1.8	15
AF, Z-X	0.92	1.8	22.5
AF, X-Z	0.45	1.67	3
AF, X-Z	0.6	1.45	3.6
AF, X-Z	0.77	1.42	6
AF, X-Z	0.84	1.45	9
AF, X-Y	0.1	2.73	3
AF, X-Y	0.3	2.12	3
AF, X-Y	0.6	1.75	4.4
AF, X-Y	0.77	1.6	7
AF, X-Y	0.85	1.55	11

A.2 Stress relief results

Table 9-2: Near-threshold results for SR condition

Orientation	*R-ratio*	ΔK_{th} (MPa√m)	K_{max} (MPa√m)
SR, Z-X	0.1	2.7	3
SR, Z-X	0.3	2.1	3
SR, Z-X	0.6	2	5.1
SR, Z-X	0.75	1.88	7.45
SR, Z-X	0.88	1.88	15.4
SR, X-Z	0.1	2.1	2.35
SR, X-Z	0.3	2	2.9
SR, X-Z	0.6	1.7	4.3
SR, X-Z	0.86	1.45	10
SR, X-Y	0.1	3.1	3.5
SR, X-Y	0.3	2.7	3.9
SR, X-Y	0.6	1.9	4.9
SR, X-Y	0.85	1.5	10

A.3 Duplex anneal results

Table 9-3: Near-threshold results for DA condition

Orientation	*R-ratio*	ΔK_{th} (MPa√m)	K_{max} (MPa√m)
DA, Z-X	0.1	5.6	6.2
DA, Z-X	0.3	4.4	6.28
DA, Z-X	0.6	3	7.5
DA, Z-X	0.85	2.7	18
DA, X-Z	0.1	5.9	6.56
DA, X-Z	0.3	4.8	6.85
DA, X-Z	0.6	3.6	9
DA, X-Z	0.88	3.3	29
DA, X-Z	0.92	2.8	35
DA, X-Y	0.1	6.1	6.77
DA, X-Y	0.3	5.3	7.57
DA, X-Y	0.6	4.1	10.25
DA, X-Y	0.74	4.2	16.15
DA, X-Y	0.91	3.6	40

```
%% Contour method stress computation.
```

Appendix B MATLAB code for residual stress calculation

```
% Thorsten Becker, 2020
% Revision 2
%clear all;
close all; clc

%% Import data into Matlab's workspace.
% Input data (units of mm)
load EdgeAB
% load EdgeSR
% load VerticalAB
% load VerticalSR
%load FlatAB; adjids=find(s1Contour(:,1)<=-22.7494);
s1Contour(adjids,3)=s1Contour(adjids,3)-0.023;
% load FlatSR
% Surface 1 data
s1c=s1Contour;
s1p1=s1FrontFace(:,1:3);
s1p2=s1LeftFace(:,1:3);
s1p3=s1BackFace(:,1:3);
s1p4=s1RightFace(:,1:3);
% Surface 2 data
s2c=s2Contour;
s2p1=s2FrontFace(:,1:3);
s2p2=s2LeftFace(:,1:3);
s2p3=s2BackFace(:,1:3);
s2p4=s2RightFace(:,1:3);

%% Script inputs
% Approximate spacing between measurement points
GridSpacing=0.5;
% Specimen dimensions (units of mm).
W=50;
B=6.5;
% Elastic properties (units of N/mm^2).
E=117e3;    % Young's Modulus.
v=0.32;     % Poisson's ratio.
% Initial values;
s1ROI=1:size(s1c,1);
s1tx=0; s1ty=0; s1tz=0;
s1thx=90; s1thy=90; s1thz=0;
s2ROI=1:size(s2c,1);
s2tx=0; s2ty=0; s2tz=0;
s2thx=90; s2thy=90; s2thz=0;
% Figure
figure('Name','Data');%,'ToolBar','none','MenuBar','none')
% Show Data.
s1tab=uitab('Title','Surface 1'); s1ax=axes(s1tab);
hold(s1ax,'on')
plot3(s1ax,s1Contour(:,1),s1Contour(:,2),s1Contour(:,3),'b.');
box('on'); grid('minor'); daspect([max(daspect)*[1,1],1]);
view(3);
xlabel('X [mm]'); ylabel('Y [mm]'); zlabel('Z [mm]');
```

```
s2tab=uitab('Title','Surface 2'); s2ax=axes(s2tab);
hold(s2ax,'on')
plot3(s2ax,s2Contour(:,1),s2Contour(:,2),s2Contour(:,3),'b.');
box('on'); grid('minor'); daspect([max(daspect)*[1,1],1]);
view(3);
xlabel('X'); ylabel('Y'); zlabel('Z');
s1axleg=legend(s1ax,'Raw Data');
s2axleg=legend(s2ax,'Raw Data');
rotate3d on

%% Select region of interest.
disp('Select ROI.')
[s1ROI,s2ROI]=selectROIgui(s1c,s2c,GridSpacing);
% Show Data.
plot3(s1ax,s1c(s1ROI,1),s1c(s1ROI,2),s1c(s1ROI,3),'y.');
plot3(s2ax,s2c(s2ROI,1),s2c(s2ROI,2),s2c(s2ROI,3),'y.');
set(s1axleg,'String',[s1axleg.String(1:end-1),{'Selected Data'}]);
set(s2axleg,'String',[s2axleg.String(1:end-1),{'Selected Data'}]);
drawnow

%% Step1. Align Data: Translation in x, y, z and rotation about x,
y, z.
disp('Align data.')
[s1c,s1p1,s1p2,s1p3,s1p4,s1O]=AllignData(s1c,s1p1,s1p2,s1p3,s1p4,s
1ROI);
[s2c,s2p1,s2p2,s2p3,s2p4,s2O]=AllignData(s2c,s2p1,s2p2,s2p3,s2p4,s
2ROI);
% Specimen size
[~,~,~,s1W,s1B]=FitPerimeter(s1p1,s1p2,s1p3,s1p4);
[~,~,~,s2W,s2B]=FitPerimeter(s2p1,s2p2,s2p3,s2p4);
% Display allignment data.
S={'S1','S2'}';
Width=[s1W,s2W]';Breadth=[s1B,s2B]';
Centroid=[s1O(1:3);s2O(1:3)];
Theta=rad2deg([s1O(4:6);s2O(4:6)]);
disp(table(S,Width,Breadth,Centroid,Theta))
% Show Data.
plot3(s1ax,s1c(s1ROI,1),s1c(s1ROI,2),s1c(s1ROI,3),'r.');
plot3(s2ax,s2c(s2ROI,1),s2c(s2ROI,2),s2c(s2ROI,3),'r.');
set(s1axleg,'String',[s1axleg.String(1:end-1),{'Alligned Data'}]);
set(s2axleg,'String',[s2axleg.String(1:end-1),{'Alligned Data'}]);
drawnow

%% Step2. Mirror Data.
s1c=[+s1c(:,1),+s1c(:,2),+s1c(:,3)];
s2c=[+s2c(:,1),-s2c(:,2),+s2c(:,3)];
% Show Data.
plot3(s1ax,s1c(s1ROI,1),s1c(s1ROI,2),s1c(s1ROI,3),'g.');
plot3(s2ax,s2c(s1ROI,1),s2c(s1ROI,2),s2c(s1ROI,3),'g.');
set(s1axleg,'String',[s1axleg.String(1:end-1),{'Mirrored Data'}]);
set(s2axleg,'String',[s2axleg.String(1:end-1),{'Mirrored Data'}]);
drawnow

%% Step3. Regularise data.
disp('Regularise data.')
% Regularise to have the same gridded X & Y position data.
```

```
[X,Y,S1,S2,MASK,DataSize]=regularise(s1c,s2c,GridSpacing,s1ROI,s2R
OI);
% Show Data.
S12tab=uitab('Title','Surface 1&2'); S12ax=axes(S12tab);
hold(S12ax,'on')
surf(S12ax,X,Y,S1.*MASK,'FaceAlpha',0.5);
surf(S12ax,X,Y,S2.*MASK,'FaceAlpha',0.5);
box('on'); grid('minor'); daspect([max(daspect)*[1,1],1]);
view(3);
xlabel('X [mm]'); ylabel('Y [mm]'); zlabel('Z [mm]');
legend(S12ax,'Regularised Data')
drawnow

%% Step4. Average Contours
disp('Averaged Contour.')
% Average Contours.
Sa=((S1+S2)/2).*MASK;
% Show Data.
Satab=uitab('Title','Averaged Surface'); Saax=axes(Satab);
hold(Saax,'on')
mesh(Saax,X,Y,Sa,'FaceAlpha',0.3);
box('on'); grid('minor'); daspect([max(daspect)*[1,1],1]);
view(3);
xlabel('X [mm]'); ylabel('Y [mm]'); zlabel('Z [mm]');
legend('Averaged contour data')
drawnow

%% Step5. Smooth data over ROI.
disp('Smooth data.')
% Set up fittype and options for smoothing.
options=fitoptions('Method','LowessFit' );
options.Robust='LAR';
options.Span=0.15;
% Smooth data.
[fitresult,gof]=fit([X(~isnan(MASK)),Y(~isnan(MASK))],Sa(~isnan(MA
SK)),'loess',options);
Sas=reshape(fitresult([X(:),Y(:)]),DataSize).*MASK;
%Sas=Sas-nanmean(Sas(:));
% Show Data.
surf(Saax,X,Y,Sas);
legend('Averaged contour data','Smoothed contour data')
drawnow

%% Step6. FE discretisation.
disp('FE discretisation.')
% FE domain.
[p.x,p.y,p.z]=meshgrid(unique(X),unique(Y),0:GridSpacing:0.6*W);
FEDataSize=size(p.x);
FEMASK=repmat(MASK,1,1,FEDataSize(3));
% Boundary conditions, displacement.
u.x=nan(FEDataSize); u.x(:,:,end)=0;
u.y=nan(FEDataSize); u.y(:,:,end)=0;
u.z=nan(FEDataSize); u.z(:,:,end)=0; u.z(:,:,1)=-Sas;
% Boundary conditions, force.
f.x=nan(FEDataSize);
f.y=nan(FEDataSize);
```

```
f.z=nan(FEDataSize);
% Compute stresses.
[u,f,~,s]=gridFEA(u,f,GridSpacing,FEMASK,'E',E,'v',v,'ComputeStres
s','On');
% Stress surface
Residualstress=s.zz(:,:,1);
Residualstress=Residualstress-nanmean(Residualstress(:));

%% Steplot results
% Shift x-axis to approximatly allign with loading pins.
Xa=X+0.375*W;
% plot data
figure('Name','Computed surface
stress.');%,'ToolBar','none','MenuBar','none');
%int=linspace(min(Residualstress(:)),max(Residualstress(:)),10);
%int=linspace(-600,600,10);
%Residualstress(Residualstress<-300)=NaN;
contourf(unique(Xa),unique(Y),Residualstress);
axis('equal'); colorbar;
xlim([-0.125*W,+W]);
ylim([-B/2,+B/2]);
%xlabel('X [mm]');
%ylabel('Y [mm]');
set(gca,'FontSize',14)
c2=colorbar('FontSize',12);
caxis([-500,300])
grid('minor'); box on;
drawnow

%% Save data
ii=5;
%residualstress(ii).Condition='As-build';
residualstress(ii).Condition='Stress-relieved';
residualstress(ii).Geometery='CompactTension';
% residualstress(ii).Orientation='Edge';
% residualstress(ii).Orientation='Vertical';
residualstress(ii).Orientation='Flat';
residualstress(ii).Machine='EOSM280';
residualstress(ii).TestType='ContourMethod';
residualstress(ii).DataSize=size(p.x(:,:,1));
residualstress(ii).X1=p.x(:,:,1)+0.375*W;
residualstress(ii).X2=p.y(:,:,1);
residualstress(ii).X3=p.z(:,:,1);
residualstress(ii).U3=u.z(:,:,1);
residualstress(ii).S33=Residualstress;
residualstress(ii).S33max=max(Residualstress(:));
residualstress(ii).S33min=min(Residualstress(:));

clearvars -except residualstress

%% ---Support Functions--- %%

function pos=importKULeuvenData(Filename)
% Import settings
Delimiter=';';
```

```
FormatSpec='%s%f%f%f%s%s%[^\n\r]';
fileID=fopen(Filename,'r');
% Import data.
dataArray=textscan(fileID,FormatSpec,'Delimiter',Delimiter,
'TextType','string','EmptyValue',
NaN,'ReturnOnError',false,'EndOfLine', '\r\n');
% Function output
pos(:,1)=dataArray{:,2}; pos(:,2)=dataArray{:,3};
pos(:,3)=dataArray{:,4};
end

function [s1maskids,s2maskids]=selectROIgui(s1,s2,GridSpacing)
% Open figure.
f=figure('Name','Select region of interest (ROI). Double-click to
complete.','MenuBar','none','ToolBar','none');
% Regularised to show using imagesc.
[SX,SY,S1Z,S2Z]=regularise(s1,s2,GridSpacing);
% Show data in figure.
s1ax=subplot(2,1,1); imagesc(unique(SX),unique(SY),S1Z);
s2ax=subplot(2,1,2); imagesc(unique(SX),unique(SY),S2Z);
% Plot properties.
axis([s1ax,s2ax],'equal','tight')
title(s1ax,'Surface 1. Select ROI.');
xlabel(s1ax,'X [mm]');
ylabel(s1ax,'Y [mm]');
c1=colorbar(s1ax); c1.Label.String='Position z [mm]';
grid(s1ax,'minor');
title(s2ax,'Surface 2. Showing selected ROI.');
xlabel(s2ax,'X [mm]');
ylabel(s2ax,'Y [mm]');
c2=colorbar(s2ax); c2.Label.String='Position z [mm]';
grid(s2ax,'minor');
% Set an initial ROI - will not be visable.
S1rect=rectangle(s1ax,'Position',[0,0,0,0],'LineWidth',1,'EdgeColo
r',[0 0 1],'FaceColor',[0 0 0 0.2]);
S2rect=rectangle(s2ax,'Position',[0,0,0,0],'LineWidth',1,'EdgeColo
r',[0 0 1],'FaceColor',[0 0 0 0.2]);
%  Matlab's selection tool.
h=imrect(s1ax);
fcn=makeConstrainToRectFcn('imrect',get(s1ax,'XLim'),get(s1ax,'YLi
m'));
setPositionConstraintFcn(h,fcn)
% Update selection on both surfaces - will now be visable.
p=getPosition(h);
set(S1rect,'Position',p);
set(S2rect,'Position',p);
addNewPositionCallback(h,@(p) set(S1rect,'Position',p));
addNewPositionCallback(h,@(p) set(S2rect,'Position',p));
% Wait for double-click to finish.
pos=wait(h);
% Find masked datapoints.
S1mask=double(s1(:,1)>pos(1)&s1(:,1)<(pos(1)+pos(3))&s1(:,2)>pos(2
)&s1(:,2)<(pos(2)+pos(4)));
S1mask(S1mask==0)=nan;
S2mask=double(s2(:,1)>pos(1)&s2(:,1)<(pos(1)+pos(3))&s2(:,2)>pos(2
)&s2(:,2)<(pos(2)+pos(4)));
```

```
S2mask(S2mask==0)=nan;
% Function output.
s1maskids=find(S1mask==1);
s2maskids=find(S2mask==1);
% Close figure.
close(f);
end


function varargout = gridFEA(varargin)
%GRIDFEA Grid based Finite Element Analysis (FEA) tool.
%   GRIDFEA is an efficient grid based FEA tool with nodes equally
spaced
%   using MESHGRID. GRIDFEA accepts 2D planar (plane stress),
surface
%   (membrane - feature not coded yet) and 3D (volume) data to
folve the
%   equation [K]{u}={f}.
%
%   GRIDFEA requires structured boundary conditions for
displacement (u.x,
%   u.y or u.x, u.y, u.z), force (f.x, f.y or f.x, f.y, f.z), a
mask (size
%   u or f), and gridspacing (scalar as distance between data
points). u,f,
%   and mask are defined using either values or NaNs (i.e. not
given).
%
%   [u,f]=GRIDFEA(u,f,GridSpacing,Mask) computes displacements and
forces
%   for boundary conditions defined in u and f with a grid spacing
of
%   GridSpacing and using a mask. GRIDFEA assumes a default
Young's modulus
%   of 10e3 and Poisson's ratio of 0.25.
%
%   [u,f,e,s]=GRIDFEA(u,f,GridSpacing,mask,'E',E,'v',v,...
%
'ComputeDisplacementGradients','On','ComputeStrain','On',...
%       'ComputeStress','On') defines Young's modulus and
Poisson's ratio
%       and outputs the symmetric strain and stress tensor
respectively.
%
%   Plane stress example:
%       % Define domain.
%       GridSpacing=1;
%       DataSize=[20,40];
%       [p.x,p.y]=meshgrid(0:GridSpacing:DataSize(2)-
1,0:GridSpacing:DataSize(1)-1);
%       mask=ones(DataSize); mask(1:9,21)=nan;
%       % Boundary conditions, displacement.
%       u.x=nan(DataSize); u.x(:,1)=0;
%       u.y=nan(DataSize); u.y(:,1)=0;
%       % Boundary conditions, force.
```

```
%       f.x=nan(DataSize); f.x(2:end-1,end)=100;
f.x([1,end],end)=100/2;
%       f.y=nan(DataSize);
%       % girdFEA
%
[u,f,~,s]=gridFEA(u,f,GridSpacing,mask,'ComputeStress','On');
%       % plot
%       mask(mask==0)=NaN;
%       figure; hold on;
%       surf(p.x+u.x,p.y+u.y,zeros(DataSize).*mask,s.xx)
%
quiver(p.x+u.x,p.y+u.y,f.x,f.y,'k','LineWidth',2,'AutoScaleFactor'
,1)
%       plot(reshape(p.x+u.x,1,[]),reshape(p.y+u.y,1,[]),'.k')
%       % Set figure properties.
%       view(2); axis equal; axis tight; box on; grid on;
%       title('Stress in xx')
%       xlabel('position [mm]'); ylabel('position [mm]')
%       hcb=colorbar; title(hcb,'[MPa]')
%
%   Volume example:
%       GridSpacing=1;
%       DataSize=[20,40,5];
%       [p.x,p.y,p.z]=meshgrid(0:GridSpacing:DataSize(2)-
1,0:GridSpacing:DataSize(1)-1,0:GridSpacing:DataSize(3)-1);
%       mask=ones(DataSize); mask(1:9,21,:)=nan;
%       % Boundary conditions, displacement.
%       u.x=nan(DataSize); u.x(:,1,:)=0;
%       u.y=nan(DataSize); u.y(:,1,:)=0;
%       u.z=nan(DataSize); u.z(:,1,:)=0;
%       % Boundary conditions, force.
%       f.x=nan(DataSize); f.x(2:end-1,end,:)=10;
f.x([1,end],end,:)= 10/2;
%       f.y=nan(DataSize);
%       f.z=nan(DataSize);
%       % girdFEA
%
[u,f,~,s]=gridFEA(u,f,GridSpacing,mask,'ComputeStress','On');
%       % plot
%       mask(mask==0)=NaN;
%       figure; hold on;
%       slice(p.x,p.y,p.z,s.xx,20,10,2)
%
quiver3(p.x,p.y,p.z,f.x,f.y,f.z,'k','LineWidth',2,'AutoScaleFactor
',1)
%
plot3(reshape(p.x,1,[]),reshape(p.y,1,[]),reshape(p.z,1,[]),'.k')
%       % Set figure properties.
%       view(3); axis equal; axis tight; box on; grid on;
%       title('Stress in xx')
%       xlabel('position [mm]'); ylabel('position [mm]')
%       hcb=colorbar; title(hcb,'[MPa]')
%
%   Version:
%       Created by Thorsten Becker, June 2018
```

```
%% Function preamble.
% Check format of input data.
if numel(varargin)<4;  error('Not enough input arguments.'); end
if ~isstruct(varargin{1}); error('u input structure not correct');
end
if ~all(isfield(varargin{1},{'x','y'})); error('u input structure
not correct'); end
if ~isstruct(varargin{2}); error('f input structure not correct');
end
if ~all(isfield(varargin{2},{'x','y'})); error('f input structure
not correct'); end
if ~isnumeric(varargin{3}); error('GridSpacing input not
correct'); end
if ~numel(varargin{3})==1; error('GridSpacing input not correct');
end
if ~isnumeric(varargin{4}); error('Mask input not correct'); end
% Input data dimensions.
if ~isfield(varargin{1},'z')&&~isfield(varargin{2},'z')&&...

ndims(varargin{1}.x)&&ndims(varargin{1}.y)&&ndims(varargin{2}.x)&&
ndims(varargin{2}.y)==2
    % Check if gridded .
    if ~isMeshGrid(varargin{1}.x,varargin{1}.y); error('u not in
gridded format.'); end
    if ~isMeshGrid(varargin{2}.x,varargin{2}.y); error('f not in
gridded format.'); end
    % 2D data.
    UX=varargin{1}.x;
    UY=varargin{1}.y;
    FX=varargin{2}.x;
    FY=varargin{2}.y;
    MASK=varargin{4};
    % Datasize.
    DataSize=[size(UX),1];
    DataType='PlaneStress';
    GridSpacing=varargin{3};
elseif isfield(varargin{1},'z')&&isfield(varargin{2},'z')&&...

ndims(varargin{1}.x)&&ndims(varargin{1}.y)&&ndims(varargin{2}.x)&&
ndims(varargin{2}.y)==2
    % Check if gridded .
    if ~isMeshGrid(varargin{1}.x,varargin{1}.y); error('u not in
gridded format.'); end
    if ~isMeshGrid(varargin{1}.x,varargin{1}.z); error('u not in
gridded format.'); end
    if ~isMeshGrid(varargin{2}.x,varargin{2}.y); error('f not in
gridded format.'); end
    if ~isMeshGrid(varargin{2}.x,varargin{2}.z); error('f not in
gridded format.'); end
    % Membrane data.
    UX=varargin{1}.x;
    UY=varargin{1}.y;
    UZ=varargin{1}.z;
    FX=varargin{2}.x;
    FY=varargin{2}.y;
    FZ=varargin{2}.z;
```

```
    MASK=varargin{4};
    % Datasize.
    DataSize=[size(UX),1];
    DataType='Membrane';
    GridSpacing=varargin{3};
elseif isfield(varargin{1},'z')&&isfield(varargin{1},'z')&&...

ndims(varargin{1}.x)&&ndims(varargin{1}.y)&&ndims(varargin{2}.x)&&
ndims(varargin{2}.y)==3
    % Check dimensions
    if
~isequal(size(varargin{1}.x),size(varargin{1}.y),size(varargin{1}.
z),...

size(varargin{2}.x),size(varargin{2}.y),size(varargin{2}.z),...
            size(varargin{4}))
        error('Input dimensions not equal.')
    end
    % Volume data.
    UX=varargin{1}.x;
    UY=varargin{1}.y;
    UZ=varargin{1}.z;
    FX=varargin{2}.x;
    FY=varargin{2}.y;
    FZ=varargin{2}.z;
    MASK=varargin{4};
    % Datasize.
    DataSize=size(UX);
    DataType='Volume';
    GridSpacing=varargin{3};
else
    error('Input format not correct.')
end
% Function defaults.
default.E=10e3;
default.v=0.25;
default.compstress='Off';
default.compstrain='Off';
default.Seem=ones(DataSize);
p=inputParser;
addOptional(p,'Seem',default.Seem,@(x) isnumeric(x));
addParameter(p,'E',default.E,@isnumeric);
addParameter(p,'v',default.v,@isnumeric);
addParameter(p,'ComputeStress',default.compstress,@ischar);
addParameter(p,'ComputeStrain',default.compstrain,@ischar);
% Parse input arguments.
parse(p,varargin{5:end});
% Material properties.
E=p.Results.E;
v=p.Results.v;
% Ouput options.
SEEM=p.Results.Seem;
compstress=p.Results.ComputeStress;
compstrain=p.Results.ComputeStrain;

%% FEA discretisation.
```

```
switch DataType
    case 'PlaneStress'

[K,u,f,dofids,elids,elmask]=FEA2D(DataSize,UX,UY,FX,FY,GridSpacing
,MASK,SEEM,E,v);
    case 'Membrane'
        error('Membrane feature not coded. On the to-do list.')
    case 'Volume'

[K,u,f,dofids,elids,elmask]=FEA3D(DataSize,UX,UY,UZ,FX,FY,FZ,GridS
pacing,MASK,SEEM,E,v);
end

%% Boundary conditions.
% Check that BCs are defined correctly.
if any(ismember(find(~isnan(u)),find(~isnan(f)))); error('Multiple
boundary conditions defined'); end
% Fixed (displacment) BCs.
fixddofs=find(~isnan(u));
% Free (force) BCs.
freedofs=setdiff(1:numel(u),fixddofs)';
% Set non-defined freedofs to zero. Change to apply gravity, etc.
f(isnan(f))=0;

%% Solve FEA.
% Solve displacements.
if numel(dofids)>1e5
    % For large problem use pcg operator.
    u(freedofs)=pcg(K(freedofs,freedofs),(f(freedofs)-
K(freedofs,fixddofs)*u(fixddofs)),...
        1e-10,1e4,diag(diag(K(freedofs,freedofs))));
else
    % For small problem use backslash operator.
    u(freedofs)=K(freedofs,freedofs)\(f(freedofs)-
K(freedofs,fixddofs)*u(fixddofs));
end
% Solve forces.
f(fixddofs)=K(fixddofs,freedofs)*u(freedofs)+K(fixddofs,fixddofs)*
u(fixddofs);

%% Gridded discretisation.
switch DataType
    case 'PlaneStress'
        U=reshape(u(dofids),2,[]);
        varargout{1}.x=reshape(U(1,:),DataSize);
        varargout{1}.y=reshape(U(2,:),DataSize);
        F=reshape(f(dofids),2,[]);
        varargout{2}.x=reshape(F(1,:),DataSize);
        varargout{2}.y=reshape(F(2,:),DataSize);
    case 'Membrane'
        error('Membrane feature not coded. On the to-do list.')
    case 'Volume'
        U=reshape(u(dofids),3,[]);
        varargout{1}.x=(reshape(U(1,:),DataSize));
        varargout{1}.y=(reshape(U(2,:),DataSize));
        varargout{1}.z=(reshape(U(3,:),DataSize));
```

```
        F=reshape(f(dofids),3,[]);
        varargout{2}.x=(reshape(F(1,:),DataSize));
        varargout{2}.y=(reshape(F(2,:),DataSize));
        varargout{2}.z=(reshape(F(3,:),DataSize));
end

%% Calculate displacement gradients.
% Displacement derivatives.
UXX=zeros(DataSize); UXY=zeros(DataSize); UXZ=zeros(DataSize);
UYX=zeros(DataSize); UYY=zeros(DataSize); UYZ=zeros(DataSize);
UZX=zeros(DataSize); UZY=zeros(DataSize); UZZ=zeros(DataSize);
% Number of elements neighbouring each node.
elnN=zeros(DataSize);
switch DataType
    case 'PlaneStress'
        e1=[-1,1,1,-1]';
        e2=[-1,-1,1,1]';
        Bx=[e2-1,-e2+1,e2+1,-e2-1]/(2*GridSpacing);
        By=[e1-1,-e1-1,e1+1,-e1+1]/(2*GridSpacing);
        % Loop through elements.
        for elnum=1:size(elids,1)
            if elmask(elnum)==1
                % Displacement at nodes [x1,y1,x2,y2,x3,y3,x4,y4].
                elu=u(reshape([dofids(elids(elnum,:)*2-
1)';dofids(elids(elnum,:)*2)'],[],1));
                % Displacment derivatives at nodes
(row=[uxx,uyy,uxy,uyx],col=nodes).
                eldu=[Bx*elu(1:2:end-1),By*elu(1:2:end-1),...
                    Bx*elu(2:2:end)  ,By*elu(2:2:end)  ]';
                % Track number of elements neighbouring each node.
                elnN(elids(elnum,:))=elnN(elids(elnum,:))+1;
                % Gridded displacement derivatives.
                UXX(elids(elnum,:))=UXX(elids(elnum,:))+eldu(1,:);
                UXY(elids(elnum,:))=UXY(elids(elnum,:))+eldu(2,:);
                UYY(elids(elnum,:))=UYY(elids(elnum,:))+eldu(3,:);
                UYX(elids(elnum,:))=UYX(elids(elnum,:))+eldu(4,:);
            end
        end
        % Average nodal data by number of elements neighbouring
each node.
        UXX=UXX./elnN; UXY=UXY./elnN;
        UYX=UYX./elnN; UYY=UYY./elnN;
        % Exclude Mask and Seem nodes.
        varargout{1}.xx=UXX.*MASK;
        varargout{1}.xy=UXY.*MASK;
        varargout{1}.yx=UYX.*MASK;
        varargout{1}.yy=UYY.*MASK;
        % Displacment derivative in ZZ.
        UZZ=v/(v-1)*(UXX+UYY);
        varargout{1}.zz=UZZ;
    case 'Membrane'
        error('Membrane feature not coded. On the to-do list.')
    case 'Volume'
        e1=[-1, 1, 1,-1,-1, 1, 1,-1]';
        e2=[-1,-1, 1, 1,-1,-1, 1, 1]';
        e3=[-1,-1,-1,-1, 1, 1, 1, 1]';
```

```
        Bx= 1/(4*GridSpacing)*[-(e2-1).*(e3-1),(e2-1).*(e3-1),-
(e2+1).*(e3-1),(e2+1).*(e3-1),...
            (e2-1).*(e3+1),-(e2-1).*(e3+1),(e2+1).*(e3+1),-
(e2+1).*(e3+1)];
        By= 1/(4*GridSpacing)*[(e1-1).*(e3-1),-(e1+1).*(e3-
1),(e1+1).*(e3-1),-(e1-1).*(e3-1),...
            -(e1-1).*(e3+1),(e1+1).*(e3+1),-(e1+1).*(e3+1),(e1-
1).*(e3+1)];
        Bz= 1/(4*GridSpacing)*[-(e1-1).*(e2-1),(e1+1).*(e2-1),-
(e1+1).*(e2+1),(e1-1).*(e2+1),...
            (e1-1).*(e2-1),-(e1+1).*(e2-1),(e1+1).*(e2+1),-(e1-
1).*(e2+1)];
        for elnum=1:size(elids,1)
            if elmask(elnum)==1
                % Displacement at nodes
[x1,y1,z1,x2,y2,z2,x3,y3,z3,x4,y4,z4].
                elu=u(reshape([dofids(elids(elnum,:)*3-2)';
                    dofids(elids(elnum,:)*3-1)';
                    dofids(elids(elnum,:)*3  )'],[],1));
                % Displacment derivatives at nodes
(row=[uxx,uyy,uxy,uyx],col=nodes).
                eldu=[Bx*elu(1:3:end-2),By*elu(1:3:end-
2),Bz*elu(1:3:end-2),...
                    Bx*elu(2:3:end-1),By*elu(2:3:end-
1),Bz*elu(2:3:end-1),...
                    Bx*elu(3:3:end)  ,By*elu(3:3:end)
,Bz*elu(3:3:end)  ]';
                % Track number of elements neighbouring each node.
                elnN(elids(elnum,:))=elnN(elids(elnum,:))+1;
                % Gridded displacement derivatives.
                UXX(elids(elnum,:))=UXX(elids(elnum,:))+eldu(1,:);
                UXY(elids(elnum,:))=UXY(elids(elnum,:))+eldu(2,:);
                UXZ(elids(elnum,:))=UXZ(elids(elnum,:))+eldu(3,:);
                UYX(elids(elnum,:))=UYX(elids(elnum,:))+eldu(4,:);
                UYY(elids(elnum,:))=UYY(elids(elnum,:))+eldu(5,:);
                UYZ(elids(elnum,:))=UYZ(elids(elnum,:))+eldu(6,:);
                UZX(elids(elnum,:))=UZX(elids(elnum,:))+eldu(7,:);
                UZY(elids(elnum,:))=UZY(elids(elnum,:))+eldu(8,:);
                UZZ(elids(elnum,:))=UZZ(elids(elnum,:))+eldu(9,:);
            end
        end
        % Average nodal data by number of elements neighbouring
each node.
        UXX=UXX./elnN; UXY=UXY./elnN; UXZ=UXZ./elnN;
        UYX=UYX./elnN; UYY=UYY./elnN; UYZ=UYZ./elnN;
        UZX=UZX./elnN; UZY=UZY./elnN; UZZ=UZZ./elnN;
        % Exclude Mask and Seem nodes.
        varargout{1}.xx=UXX.*MASK;
        varargout{1}.xy=UXY.*MASK;
        varargout{1}.xz=UXZ.*MASK;
        varargout{1}.yx=UYX.*MASK;
        varargout{1}.yy=UYY.*MASK;
        varargout{1}.yz=UYZ.*MASK;
        varargout{1}.zx=UZX.*MASK;
        varargout{1}.zy=UZY.*MASK;
        varargout{1}.zz=UZZ.*MASK;
```

```
end

%% Calculate strain and stress tensor
% Symmetric strain tensor.
if compstress=="On" || compstrain=="On"
    EXX=UXX;
    EYY=UYY;
    EXY=(UXY+UYX)/2;
    if DataType =="PlaneStress"
        EXZ=zeros(DataSize);
        EYZ=zeros(DataSize);
        EZZ=v/(v-1)*(EXX+EYY);
    elseif DataType =="Membrane"
        error('Membrane feature not coded. On the to-do list.')
    else
        EZZ=UZZ;
        EXZ=(UXZ+UZX)/2;
        EYZ=(UYZ+UZY)/2;
    end
    % Store data.
    if compstrain=="On"
        varargout{3}.xx=EXX;
        varargout{3}.yy=EYY;
        varargout{3}.zz=EZZ;
        varargout{3}.xy=EXY;
        varargout{3}.xz=EXZ;
        varargout{3}.yz=EYZ;
    end
end
% Stress tensor.
if compstress=="On"
    SXX=E/(1-v^2)*(EXX+v*(EYY+EZZ));
    SYY=E/(1-v^2)*(EYY+v*(EXX+EZZ));
    SZZ=E/(1-v^2)*(EZZ+v*(EXX+EYY));
    SXY=E/(1-v^2)*(1-v)*EXY;
    SXZ=E/(1-v^2)*(1-v)*EXZ;
    SYZ=E/(1-v^2)*(1-v)*EYZ;
    % Store data.
    varargout{4}.xx=SXX;
    varargout{4}.yy=SYY;
    varargout{4}.zz=SZZ;
    varargout{4}.xy=SXY;
    varargout{4}.xz=SXZ;
    varargout{4}.yz=SYZ;
end

end

function
[K,u,f,dofids,elids,elmask]=FEA2D(DataSize,ux,uy,fx,fy,gridspacing
,mask,seem,E,v)
% FEA2D Computes stiffness matrix (K), displacment fector (u),
force vector
% (f) and degree of freedom ids (dofids) under plane stress
assumption.
```

```
% Number of elements.
nelx=DataSize(2)-1;
nely=DataSize(1)-1;
nel=nelx*nely;
% Element node ids.
[elrow,elcol]=meshgrid(0:nelx-1,0:nely-1);
elid4=elrow*(nely+1)+(nely+1-(elcol));
elid3=elid4+(nely+1);
elid2=elid4+nely;
elid1=elid4-1;
elids=[elid1(:),elid2(:),elid3(:),elid4(:)];
% Dof ids.
xdof=reshape(flipud(reshape((1:prod(DataSize))*2-
1,DataSize)),1,[]);
ydof=reshape(flipud(reshape((1:prod(DataSize))*2,DataSize)),1,[]);
dofids=reshape([xdof;ydof],[],1);
% Mask & Seem elements.
nodmask=find(isnan(mask(:)));
nodseem=find(isnan(seem(:)));
elmask=zeros(nel,4);
elseem=zeros(nel,4);
for elnum=1:prod(nel)
    elmask(elnum,:)=ismember(elids(elnum,:),nodmask);
    elseem(elnum,:)=ismember(elids(elnum,:),nodseem);
end
elmask=double(~any(elmask,2));
elseem=double(~elseem(:,4));
elmask(elmask==0|elseem==0)=1e-12;
% Element stiffness matrix.
A11=[12, 3,-6,-3; 3,12, 3, 0;-6, 3,12,-3;-3, 0,-3,12];
A12=[-6,-3, 0, 3;-3,-6,-3,-6; 0,-3,-6, 3; 3,-6, 3,-6];
B11=[-4, 3,-2, 9; 3,-4,-9, 4;-2,-9,-4,-3; 9, 4,-3,-4];
B12=[ 2,-3, 4,-9;-3, 2, 9,-2; 4, 9, 2, 3;-9,-2, 3, 2];
KE=1/(1-
v^2)/24*([A11,A12;A12',A11]+v*[B11,B12;B12',B11])*gridspacing;
% Global stiffness matrix.
nodenrs=reshape(1:(1+nelx)*(1+nely),1+nely,1+nelx);
edofVec=reshape(2*nodenrs(1:end-1,1:end-1)+1,nelx*nely,1);
edofMat=repmat(edofVec,1,8)+repmat([0,1,2*nely+[2,3,0,1],-2,-
1],nelx*nely,1);
iK=reshape(kron(edofMat,ones(8,1))',64*nelx*nely,1);
jK=reshape(kron(edofMat,ones(1,8))',64*nelx*nely,1);
sK=reshape(KE(:)*E*elmask',64*nelx*nely,1);
K=sparse(iK,jK,sK);
K=(K+K')/2;
% Displacement & force dofs.
u(dofids)=reshape(reshape([reshape(ux,1,[]);reshape(uy,1,[])],[],1
),1,[]); u=u';
f(dofids)=reshape(reshape([reshape(fx,1,[]);reshape(fy,1,[])],[],1
),1,[]); f=f';
end

function
[K,u,f,dofids,elids,elmask]=FEA3D(DataSize,ux,uy,uz,fx,fy,fz,grids
pacing,mask,seem,E,v)
```

```
% FEA3D Computes stiffness matrix (K), displacment fector (u),
force vector
% (f) and degree of freedom ids (dofids) for 3D data. Adabted from
"An
% efficient 3D topology optimization code written in Matlab", Kai
Liu,
% Andrés Tovar, 25 June 2014 see https://top3dapp.com/

% Number of elements.
nelx=DataSize(2)-1;
nely=DataSize(1)-1;
nelz=DataSize(3)-1;
nel=nelx*nely*nelz;
% Element node ids.
elzid=(nelx+1)*(nely+1);
[elii,eljj,elkk]=meshgrid(0:nelx-1,0:nely-1,0:nelz-1);
elid1=(elkk)*(nelx+1)*(nely+1)+(elii)*(nely+1)+(nely+1-(eljj));
elid2=elid1+(nely+1);
elid3=elid1+nely;
elid4=elid1-1;
elid5=elid1+elzid;
elid6=elid2+elzid;
elid7=elid3+elzid;
elid8=elid4+elzid;
elids=[elid1(:),elid2(:),elid3(:),elid4(:),elid5(:),elid6(:),elid7
(:),elid8(:)];
% Dof ids.
xdof=reshape(flipud(reshape((1:prod(DataSize))*3-
2,DataSize)),1,[]);
ydof=reshape(flipud(reshape((1:prod(DataSize))*3-
1,DataSize)),1,[]);
zdof=reshape(flipud(reshape((1:prod(DataSize))*3,DataSize)),1,[]);
dofids=reshape([xdof;ydof;zdof],[],1);
% Mask & Seem elements.
nodmask=find(isnan(mask(:)));
nodseem=find(isnan(seem(:)));
elmask=zeros(nel,8);
elseem=zeros(nel,8);
for elnum=1:prod(nel)
    elmask(elnum,:)=ismember(elids(elnum,:),nodmask);
    elseem(elnum,:)=ismember(elids(elnum,1),nodseem);
end
elmask=double(~any(elmask,2));
elseem=double(~any(elseem,2));
elmask(elmask==0|elseem==0)=1e-12;
% Element stiffness matrix
KE=lk_H8(v)*gridspacing;
nodegrd=reshape(1:(nely+1)*(nelx+1),nely+1,nelx+1);
nodeids=reshape(nodegrd(1:end-1,1:end-1),nely*nelx,1);
nodeidz=0:(nely+1)*(nelx+1):(nelz-1)*(nely+1)*(nelx+1);
nodeids=repmat(nodeids,size(nodeidz))+repmat(nodeidz,size(nodeids)
);
edofVec=3*nodeids(:)+1;
edofMat=repmat(edofVec,1,24)+ ...
    repmat([0 1 2 3*nely+[3 4 5 0 1 2] -3 -2 -1 ...
```

```
    3*(nely+1)*(nelx+1)+[0 1 2 3*nely+[3 4 5 0 1 2] -3 -2 -
1]],nel,1);
% Global stiffness matrix assembly.
iK=reshape(kron(edofMat,ones(24,1))',24*24*nel,1);
jK=reshape(kron(edofMat,ones(1,24))',24*24*nel,1);
sK=reshape(KE(:)*E*elmask(:)',24*24*nel,1);
K=sparse(iK,jK,sK);
K=(K+K')/2;
% Displacement & force dofs.
u(dofids)=reshape(reshape([reshape(ux,1,[]);reshape(uy,1,[]);resha
pe(uz,1,[])],[],1),1,[]); u=u';
f(dofids)=reshape(reshape([reshape(fx,1,[]);reshape(fy,1,[]);resha
pe(fz,1,[])],[],1),1,[]); f=f';
end

function KE = lk_H8(v)
A=[32 6 -8   6 -6 4 3 -6 -10   3 -3 -3 -4 -8;
    -48 0  0 -24 24 0 0  0  12 -12  0 12 12 12];
k=1/144*A'*[1; v];
K1=[k(1)  k(2)  k(2)  k(3)  k(5)  k(5);
    k(2)  k(1)  k(2)  k(4)  k(6)  k(7);
    k(2)  k(2)  k(1)  k(4)  k(7)  k(6);
    k(3)  k(4)  k(4)  k(1)  k(8)  k(8);
    k(5)  k(6)  k(7)  k(8)  k(1)  k(2);
    k(5)  k(7)  k(6)  k(8)  k(2)  k(1)];
K2=[k(9)  k(8)  k(12) k(6)  k(4)  k(7);
    k(8)  k(9)  k(12) k(5)  k(3)  k(5);
    k(10) k(10) k(13) k(7)  k(4)  k(6);
    k(6)  k(5)  k(11) k(9)  k(2)  k(10);
    k(4)  k(3)  k(5)  k(2)  k(9)  k(12)
    k(11) k(4)  k(6)  k(12) k(10) k(13)];
K3=[k(6)  k(7)  k(4)  k(9)  k(12) k(8);
    k(7)  k(6)  k(4)  k(10) k(13) k(10);
    k(5)  k(5)  k(3)  k(8)  k(12) k(9);
    k(9)  k(10) k(2)  k(6)  k(11) k(5);
    k(12) k(13) k(10) k(11) k(6)  k(4);
    k(2)  k(12) k(9)  k(4)  k(5)  k(3)];
K4=[k(14) k(11) k(11) k(13) k(10) k(10);
    k(11) k(14) k(11) k(12) k(9)  k(8);
    k(11) k(11) k(14) k(12) k(8)  k(9);
    k(13) k(12) k(12) k(14) k(7)  k(7);
    k(10) k(9)  k(8)  k(7)  k(14) k(11);
    k(10) k(8)  k(9)  k(7)  k(11) k(14)];
K5=[k(1)  k(2)  k(8)  k(3)  k(5)  k(4);
    k(2)  k(1)  k(8)  k(4)  k(6)  k(11);
    k(8)  k(8)  k(1)  k(5)  k(11) k(6);
    k(3)  k(4)  k(5)  k(1)  k(8)  k(2);
    k(5)  k(6)  k(11) k(8)  k(1)  k(8);
    k(4)  k(11) k(6)  k(2)  k(8)  k(1)];
K6=[k(14) k(11) k(7)  k(13) k(10) k(12);
    k(11) k(14) k(7)  k(12) k(9)  k(2);
    k(7)  k(7)  k(14) k(10) k(2)  k(9);
    k(13) k(12) k(10) k(14) k(7)  k(11);
    k(10) k(9)  k(2)  k(7)  k(14) k(7);
    k(12) k(2)  k(9)  k(11) k(7)  k(14)];
KE=1/((v+1)*(1-2*v))*...
```

```
    [K1  K2  K3  K4;
    K2' K5  K6  K3';
    K3' K6  K5' K2';
    K4  K3  K2  K1'];
end

function isMG=isMeshGrid(X,Y)
% Adapted from Matlab.
if ~ismatrix(X)||isempty(X)||~isequal(size(X),size(Y))
    isMG=false;
elseif
(~isnumeric(X)&&~islogical(X))||(~isnumeric(Y)&&~islogical(Y))
    isMG=false;
end
isMG=true;
end

function [S,P1,P2,P3,P4,O]=AllignData(S,P1,P2,P3,P4,ROI)

% Initial guess
O0=EstimateOrientation(S(ROI,:),P1,P2,P3,P4);
%O0=[O0(1),O0(2),O0(3),O0(4)-pi/2,O0(5)-pi/2,O0(6)];
% Minimisation function
minfun=@(O) objectivefcn(O,S(ROI,:),P1,P2,P3,P4);
% Optimisation
options=optimset('Display','notify');%,'PlotFcns',@optimplotx);
O=fminsearch(minfun,O0,options);
% Rotate data to optimised value.
O=[O(1),O(2),O(3),O(4)-pi/2,O(5)-pi/2,O(6)];
[S,P1,P2,P3,P4]=RotateData(O,S,P1,P2,P3,P4);

% Support functions
    function res=objectivefcn(O,S,P1,P2,P3,P4)
        % Transform data by O.
        O90=[O(1),O(2),O(3),O(4)-pi/2,O(5)-pi/2,O(6)];
        [S,P1,P2,P3,P4]=RotateData(O90,S,P1,P2,P3,P4);
        % Find orientation of rotated data.
        O=EstimateOrientation(S,P1,P2,P3,P4);
        res=norm([O(1),O(2),O(3),O(4)-pi/2,O(5)-pi/2,O(6)]);
    end
end

function [S,P1,P2,P3,P4]=RotateData(O,S,P1,P2,P3,P4)
% Finds the orientation of the contour cut S (z and thx, thy) and
permiter
% P (x,y and thz). S, P1, P2, P3 and P4 are column vectors with x,
% y and z data. x,y,z,thx,thy, thz are stored in O in the same
order.

% Transformation matrix
t=O(1:3);
R=RotationMatrix(O(4:6));
T=[R,t';0,0,0,1];
% Transfrom data
S=T\[S,ones(size(S,1),1)]'; S=S(1:3,:)';
```

```
P1=T\[P1,ones(size(P1,1),1)]'; P1=P1(1:3,:)';
P2=T\[P2,ones(size(P2,1),1)]'; P2=P2(1:3,:)';
P3=T\[P3,ones(size(P3,1),1)]'; P3=P3(1:3,:)';
P4=T\[P4,ones(size(P4,1),1)]'; P4=P4(1:3,:)';

% Support functions
    function R=RotationMatrix(th)
        % QMATRIX   Three-dimensional Euler rotation matrix.
        %   QMATRIX(th) generates a 3x3 (three-dimensional) Euler
rotation matrix
        %   through angles th(1), th(2) and th(3) around the x-
axis, y-axis and
        %   z-axis respectively. th is required to be a 1x3 vector
and is given in
        %   radians.
        %   TH Becker, Stellenbosch University, 2016

        % Initialise
        X=eye(3);
        Y=eye(3);
        Z=eye(3);
        % Rotatioj about x-axis
        X(2,2)=+cos(th(1));
        X(2,3)=-sin(th(1));
        X(3,2)=+sin(th(1));
        X(3,3)=+cos(th(1));
        % Rotation about y-axis
        Y(1,1)=+cos(th(2));
        Y(1,3)=+sin(th(2));
        Y(3,1)=-sin(th(2));
        Y(3,3)=+cos(th(2));
        % Rotation about z-axis
        Z(1,1)=+cos(th(3));
        Z(1,2)=-sin(th(3));
        Z(2,1)=+sin(th(3));
        Z(2,2)=+cos(th(3));
        % Combine
        R=Z*Y*X;
    end
end

function O=EstimateOrientation(S,P1,P2,P3,P4)
% Finds the orientation of the contour cut (z and thx, thy) and
permiter P
% (x,y and thz). S, P1, P2, P3 and P4 are column vectors with x, y
and z
% data. The permiter P1, P2, P3 and P4 need to be in a clockwise
or
% anti-clockwise order. x,y,z,thx,thy, thz are stored in O in the
same
% order.

% Fit Surface (Cut) Data
[O(3),O(4),O(5)]=FitCut(S);
% Fit Perimter Data
[O(1),O(2),O(6)]=FitPerimeter(P1,P2,P3,P4);
```

```
end

% Support functions
function [z,thx,thy]=FitCut(s)
% Fits surface to cut.
% Thorsten Becker, 2020.

sfitdata=fit([s(:,1),s(:,2)],s(:,3),'poly11');
% Surface normal
n=([sfitdata.p10,sfitdata.p01,1]);
n=n/norm(n);
% Orientation
z=sfitdata([0,0]);
thx=atan2(norm(cross(n,[1,0,0])),dot(n,[1,0,0]));
thy=atan2(norm(cross(n,[0,1,0])),dot(n,[0,1,0]));
end
function [cgx,cgy,thz,W,B]=FitPerimeter(FF,LF,BF,RF)
% Fits a rengtangle to data
% Adapted from
http://people.inf.ethz.ch/arbenz/MatlabKurs/node85.html
% Modified by Thorsten Becker, 2020.

% Input data
Px=FF(:,1); Py=FF(:,2);
Qx=LF(:,1); Qy=LF(:,2);
Rx=BF(:,1); Ry=BF(:,2);
Sx=RF(:,1); Sy=RF(:,2);
% Set up least-squares problem.
zp=zeros(size(Px)); op=ones(size(Px));
zq=zeros(size(Qx)); oq=ones(size(Qx));
zr=zeros(size(Rx)); or=ones(size(Rx));
zs=zeros(size(Sx)); os=ones(size(Sx));
A=[ op,zp,zp,zp,Px,+Py
    zq,oq,zq,zq,Qy,-Qx
    zr,zr,or,zr,Rx,+Ry
    zs,zs,zs,os,Sy,-Sx];
[c,n]=clsq(A,2);
% Compute four corners of the rectangle
B=[n,[-n(2),n(1)]'];
X=-B*[c([1,3,3,1])';c([2,2,4,4])'];
% Outputs
% Angle to x-axis
thz=atan(-n(1)/n(2));
% Centroid
cg=mean(X,2)';
cgx=cg(1);
cgy=cg(2);
% Dimensions
d=[pdist([X(:,1),X(:,2)]'),pdist([X(:,2),X(:,3)]')];
W=max(d);
B=min(d);
end

function [c,n]=clsq(A,dim)
% solves the constrained least squares Problem
% A (c n)' ~ 0 subject to norm(n,2)=1
```

```
% length(n) = dim
% [c,n] = clsq(A,dim)
% Adapted from
http://people.inf.ethz.ch/arbenz/MatlabKurs/node85.html
[m,p] = size(A);
if p<dim+1; error ('Not enough unknowns'); end
if m<dim; error ('Not enough equations'); end
m=min(m,p);
R=triu(qr(A));
[~,~,V]=svd(R(p-dim+1:m,p-dim+1:p));
n=V(:,dim);
c=-R(1:p-dim,1:p-dim)\R(1:p-dim,p-dim+1:p)*n;
end

function
[X,Y,Z1,Z2,MASK,DataSize]=regularise(s1,s2,GridSpacing,s1roiids,s2
roiids)
% Check input args. If not given, assume a default.
if nargin==3
    s1roiids=1:length(s1);
    s2roiids=1:length(s2);
end
% Mask
s1mask=zeros(length(s1),1);
s1mask(s1roiids)=1;
s2mask=zeros(length(s2),1);
s2mask(s2roiids)=1;
% Data range.
minx=min([s1(:,1);s2(:,1)]);
maxx=max([s1(:,1);s2(:,1)]);
miny=min([s1(:,2);s2(:,2)]);
maxy=max([s1(:,2);s2(:,2)]);
% regularised X & Y positions.
[X,Y]=meshgrid(minx:GridSpacing:maxx,miny:GridSpacing:maxy);
% Set up interpolant to obtaind Z position at regularised X & Y
positions.
s1int=scatteredInterpolant(s1(:,1),s1(:,2),s1(:,3),'nearest','none
');
s1MASKint=scatteredInterpolant(s1(:,1),s1(:,2),s1mask,'nearest','n
one');
s2int=scatteredInterpolant(s2(:,1),s2(:,2),s2(:,3),'nearest','none
');
s2MASKint=scatteredInterpolant(s2(:,1),s2(:,2),s2mask,'nearest','n
one');
% Obtaind Z position at regularised X & Y positions. Function
output.
Z1=s1int(X,Y);
Z2=s2int(X,Y);
MASK=s1MASKint(X,Y).*s2MASKint(X,Y);
MASK(MASK==0)=NaN;
MASK(:,all(isnan(Z1),1))=NaN;
MASK(all(isnan(Z1),2),:)=NaN;
DataSize=size(X);
end
```